DYNAMIC OPTICAL IMAGING IN BREAST CANCER DETECTION

THE USE OF DYNAMIC OPTICAL IMAGING IN BREAST CANCER DETECTION

by

Kyle Wilson, M.Sc.

Graduate Program in Medical Physics

A thesis submitted in partial fulfillment
of the requirements for the degree of

Doctor of Philosophy

Faculty of Graduate Studies

McMaster University

Hamilton, Ontario

December, 2010

DOCTOR OF PHILOSOPHY (2010)
(Medical Physics)

MCMASTER UNIVERSITY
Hamilton, Ontario

TITLE: The Use of Dynamic Optical Imaging in Breast Cancer Detection

AUTHOR: Kyle Wilson, M.Sc. (McMaster University)

SUPERVISOR: Professor Dr. Gerald Moran

NUMBER OF PAGES: xiii, 208

MCMASTER UNIVERSITY

FACULTY OF GRADUATE STUDIES

CERTIFICATE OF EXAMINATION

Chief Advisor

_____

Examining Board

_____

Advisory Committee

_____

_____

_____

_____

_____

_____

The thesis by

Kyle Wilson, M.Sc.

entitled:

The Use of Dyanmic Optical Imaging in Breast Cancer Detection

is accepted in partial fulfillment of the requirements for the degree of

Doctor of Philosophy

Date_____

_____

Chair of examining committee

ABSTRACT

Breast cancer has affected many women around the world throughout history. In order to recognize and treat the early signs of breast cancer, obtaining high quality images is crucial. A variety of imaging modalities are available for use in breast imaging, including conventional mammography and newer optical imaging techniques. One such optical imaging system is the ComfortScan™, which uses red light to image the breast and was the focus of this study. The objectives include investigating whether performing a large scale clinical trial with the ComfortScan™ would be warranted to further patient care and diagnostics for breast imaging, and determining whether the ComfortScan™ would achieve better correlation to biopsy than mammography alone. An additional goal was to investigate whether the ComfortScan™ system would be beneficial as a mainstream method for a radiologist to diagnose breast cancer risk.

The preliminary study with 19 patients demonstrated that there was no difference in diagnostic information between the near-infrared (NIR) image and mammography ($p>0.05$). Anecdotal evidence suggests cases where mammography disagreed with biopsy, whereas ComfortScan™ agreed, though these were not statistically significant. Based on these encouraging results, a large scale clinical trial was launched to investigate the potential of widespread use of the ComfortScan™. The large scale trial included 126 NIR images and found difference in diagnostic information between NIR and mammography ($p<0.05$). Mammography agreed with biopsy in 18/33 and the ComfortScan™ system agreed with biopsy in 25/33 cases. The sensitivity and specificity for the ComfortScan™ system was 83% and 67%, respectively. The sensitivity and specificity of mammography was 94% and 13%, respectively. This study included a variety of women with varying ages and BIRADS scores, and demonstrated the effective clinical use of a portable, non-ionizing, inexpensive imaging

modality, indicating that the ComfortScan™ system could likely be successful as a mainstream adjunct to mammography.

The potential of using polyvinyl alcohol cryogel (PVA-C) as a breast tissue mimic was investigated and PVA-C was then used to validate the mode of action of the ComfortScan™ system. Two experimental methods reported the absorption coefficients and reduced scattering coefficients of PVA-C. Using a double integrating sphere, the values were $\mu_a = 0.012 \pm 0.002$ mm^{-1} and $\mu_s' = 1.5 \pm 0.2$ mm^{-1} and using steady-state spatially resolved diffuse reflectance, the values were $\mu_a = 0.017 \pm 0.005$ mm^{-1} and $\mu_s' = 1.3 \pm 0.2$ mm^{-1} at 640 nm. These values are comparable to typical absorption coefficients for tissue reported by others.

The mode of action suggested by DOBI (Dynamic Optical Breast Imaging) Medical for the ComfortScan ™ system is that under compression a malignant tumour will highly attenuate light, due to a partial collapse in the tumourous vasculature, resulting in an increased deoxygenation of blood over time. Using a PVA-C breast mimicking phantom, it was shown that by deoxygenating horse blood in a cavity, there was an increase in the attenuation of 640 nm light as compared with the surrounding phantom material; which suggests that the colour representative of malignancies on the ComfortScan™ is caused by deoxygenating blood. Further evidence suggests that the ComfortScan™ system is not recognizing a total collapse of the vasculature and subsequent void of blood from the tumour as the trigger for malignant detection. The mode of action suggested by DOBI Medical is supported by our findings.

Keywords: NIR, breast imaging, cancer, near infrared

CO-AUTHORSHIP

This thesis consists of an introduction, three studies (Chapters 2, 3 & 4), and then an overall conclusion/discussion. The appendix consists of two studies (Appendix I & II) to provide background on the phantom material used in this thesis. Chapter 2 and Appendix I have been accepted with revisions to peer-reviewed scientific journals. Chapters 1, 3, 4 and Appendix II are in preparation for submission to peer-reviewed scientific journals. Currently, K. J. Wilson is the first author on these publications, co-authored by G. Moran, K. Dhamanaskar, T. Minuk, R.T. Thompson, G. Campbell, A. Jegatheesan, C. Seymour, M. Hill, and R. Thornhill. As the primary author of this thesis, K. J. Wilson did the following:

a.) planned all experiments with G. Moran;

b.) applied for and received REB approval for the clinical trial;

c.) corresponded with representatives of DOBI Medical;

d.) performed all maintenance and quality assurance on the ComfortScan™ system;

e.) supervised and taught all technicians to use the ComfortScan™ system;

f.) ensured patient consent was obtained by all study participants;

g.) managed weekly patient throughput for the clinical trial over the course of 2 years;

h.) organized all data to be analyzed by radiologists;

i.) prepared all PVA-C phantoms for measurements;

j.) performed optical measurements for the phantom study on ComfortScan™ system;

k.) performed all statistical analysis;

l.) wrote the first draft of all the manuscripts and incorporated co-authors' changes in all subsequent drafts.

For my family,

ACKNOWLEDGEMENTS

First, I would like to thank my supervisor Gerald Moran, Ph.D., for all the help he has provided during this project. Without him, none of this would have been possible, and for that, I am truly thankful.

I would like to thank Kavita Dhamanaskar, M.D., Colin Webber, Ph.D., Colin Seymour, Ph.D., and Tom Farrell, Ph.D., from my advisory committee for their guidance throughout the course of my studies. All of their comments and suggestions were very helpful for the completion of this project.

Thank you to Gordon Campbell, Ph.D., for his expertise and providing the facilities for the production of PVA-C.

I would like to thank Horizon Medical for allowing the use of the ComfortScan™ system for this study. Also, I would like to thank all the staff at the OBSP at Chedoke Hospital for their help with patient imaging.

I would like to thank my parents, Ron and Margaret, for providing the support throughout my whole life and always being there.

Most importantly I would like to thank my wonderful fiancée, Mandy. Her help and support throughout this Ph.D. have been amazing.

TABLE OF CONTENTS

LIST OF FIGURES

LIST OF TABLES

Chapter 1

INTRODUCTION

Invited to be published, with modifications, in Critical Reviews in BioMedical Engineering as

"A Review of Current and Future Breast Cancer Imaging Techniques"

KYLE J. WILSON[1*], COLIN SEYMOUR[1], GORDON CAMPBELL[2,3], AND GERALD R. MORAN[1,3]

[1]*Medical Physics and Applied Radiation Sciences, McMaster University, Hamilton, Ontario, Canada*

[2]*Integrated Manufacturing Technologies Institute, National Research Council, London, Ontario, Canada*

[3]*Department of Medical Biophysics, University of Western Ontario, London, Ontario, Canada*

Word Count: 21 335

*Correspondence to: Kyle J. Wilson, Medical Physics and Applied Radiation Sciences, McMaster University, 1280 Main St. W., Hamilton, Ontario L8S 4K1, Canada. Phone: 905 525-9140 Ext. 26876 E-mail: wilsokj2@mcmaster.ca

LIST OF ABBREVIATIONS

ACR	American college of radiology
AEC	automatic exposure control
ALARA	as low as reasonably achievable
CAD	computer assisted detection
CAR	Canadian association of radiologists
CW	continuous wave
DQE	detective quantum efficiency
EIT	electrical impedance tomography
ER	estrogen receptor
FCC	fibrocystic changes
FDPM	frequency domain photon migration
FTC	freeze/thaw cycle
Hb	deoxyhemoglobin
HbO_2	oxyhemoglobin
InGaAs	indium gallium arsenide
MRI	magnetic resonance imaging
MTF	modulation transfer function
NEQ	noise equivalent quanta
NOS	infiltrating carcinoma not otherwise specified
NST	infiltrating carcinoma of no special type
PbS	lead sulfide
PET	positron emission tomography
PR	progesterone receptor
PVA	polyvinyl alcohol
PVA-C	polyvinyl alcohol cryogel
SNR	signal to noise ratio
QTH	quartz tungsten halogen
TDPM	time domain photon migration
TNM	primary tumour (T), regional lymph nodes (N), distant metastases (M)
US	ultrasound

BACKGROUND

1.1 INTRODUCTION

With an estimated 20 300 women diagnosed with breast cancer in 2010 [1], there is a significant need for research in the diagnosis and treatment of this disease. The human breast has always held a revered place in art, history and literature; beyond that of merely biological function [2]; even though the primary purpose of the organ is to produce milk for the live young. Nevertheless, the plague of cancer has continued to assail the breast during the course of history. Many ancient groups have portrayed breast tumours, as early as 3000 years B.C. when the Egyptians used hieroglyphics printed on papyrus, and the Greek and Roman physicians referred to breast tumours in their Hippocratic writings. These accounts have continued into modern times [3-7].

Philosophies for the treatment of breast cancer have moved through four unique schools of thought. In the earliest times, treatment of breast cancer was not regularly performed because it was believed that surgery would only aggravate the condition. Subsequently, cancer began to be recognized as a systemic disease which could be treated with surgery in the short term, but surgery would not abolish the cancer. The next stage reversed what was previously thought, and described cancer as a localized disease, not one that affected the whole body, which meant that local treatments were expected to restore the patient to health. Eventually, a more thorough understanding of breast cancer in modern times has allowed for combined localized and whole-body treatments[8]. While contemporary medicine has increased the range of treatments available for breast cancer patients, early detection is crucial to increase the likelihood of positive outcomes. Customary screening methods such as mammography have been shown to miss up to 10% of malignant lesions, necessitating the development of alternate methods of screening, such as optical breast imaging [9] or contrast enhanced MRI, for those women identified as high risk.

1.2 BREAST BIOLOGY

While the breast seems to be quite a well studied organ, there is a complex biology associated with the mammary glands. Visible on the anterior chest, the mammary glands are modified sweat glands of the skin, with the primary purpose, as previously mentioned, to feed live infant young. Classified into ductal and lobular units which all come together at the tip of the nipple, the mammary gland is comprised of up to 20 different glands. A series of changes occur in the ducts and alveoli during puberty, and the breasts continue to grow into adulthood and, if pregnancy occurs, an additional phase of development will take place. While usually thought of as an exclusively female organ, interestingly, males actually have a similar breast to pre-pubescent females, which consists only of ductal structures[10].

1.2.1 Development

The development of the mammary gland is quite unique, as it begins as an external sac attached to one place on the skin, and thickens into the eventual mammary gland. Formed from the outermost layer of the embryo, the ectoderm, the beginnings of the mammary gland actually extend from the armpit region (axilla) all the way to the groin (inguinal) area on both sides of the chest. This long formation visible very early in embryonic development, is called a 'milk line'. In the end, the upper and lower sections of the 'milk line' are wasted away, and only the sections over the mid-chest region are left, which is where breasts will eventually grow.

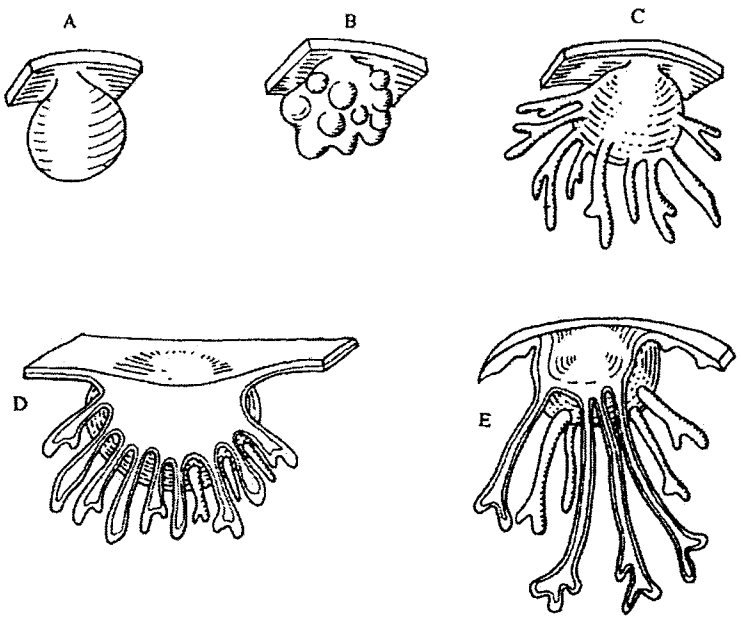

Fig. 1 – Ductal Development [11]

This figure shows the development of the ducts and lobes at an early stage.

When a female infant is born, lobuloalveolar structures are present, but it is not until puberty when hormonal stimulation causes the ducts to form into collecting ducts and terminal duct lobular units. As is true with all embryonic development, irregularities can occur and lead to a variety of conditions. Anomalies in mammary gland development can result in multiple nipples and breasts (polythelia, polymastia), unfinished breast formation (hypomastia), or even the absence of breast tissue, areola and nipple altogether (amastia), although the last condition is quite rare. Extra breast tissue at any site along the former milk line can remain, although this is also quite rare. Cancers occasionally arise in this tissue [12], perhaps due to the predisposition to abnormal cell development.

1.2.2 Anatomy

The anatomy of the breast can be characterized at both a microscopic level, with the cellular arrangements, and macroscopic level by examining the ductal structures.

1.2.2.i Microscopic

At a microscopic level, the breast consists of various types and arrangements of cells. In contrast to typical skin, the skin that overlays the breast contains longitudinal smooth muscle cells, which are necessary during contraction of the ducts to release milk for the young. The areola of the breast, which includes the nipple, is made up of a keratinizing stratified squamous epithelium with high melanin content, and these cells give the areola its characteristic dark colour. The areola also has glands, known as Montgomery's tubercles, which react to stimulation and cause the muscle fibres of the areola to contract, which prepares the nipple for milk release by lifting up the tip of the nipple.

Important for milk production, the lactiferous ducts have irregular walls and a squamous epethelial cell layer quite close to the nipple. These cells and the undulating walls of the ducts provide a large surface area, which ensures a high flow of milk. The cells change as one examines the tissues of the ducts and sinuses further away from the nipple. Simple columnar epithelial cells line the primary ducts, and as the ducts are found deeper and deeper into the breast tissue, the cells change again. The smaller ductal units and ductules, which break off of the duct canal are lined by epithelial cells and an outer layer of mesenchymal myoepithelial cells. The ductules eventually end in terminal lobular units, and terminal ducts can experience intraductal hyperplasia, which is a benign breast disease where cells grow beyond that which is normally seen in a particular tissue type. Intraductal hyperplasia is the one of the few types of breast disease associated with an increased risk of breast cancer[8], and it will be discussed further in section 1.3 "Breast Cancer". Figure 2 depicts the ductal arrangements.

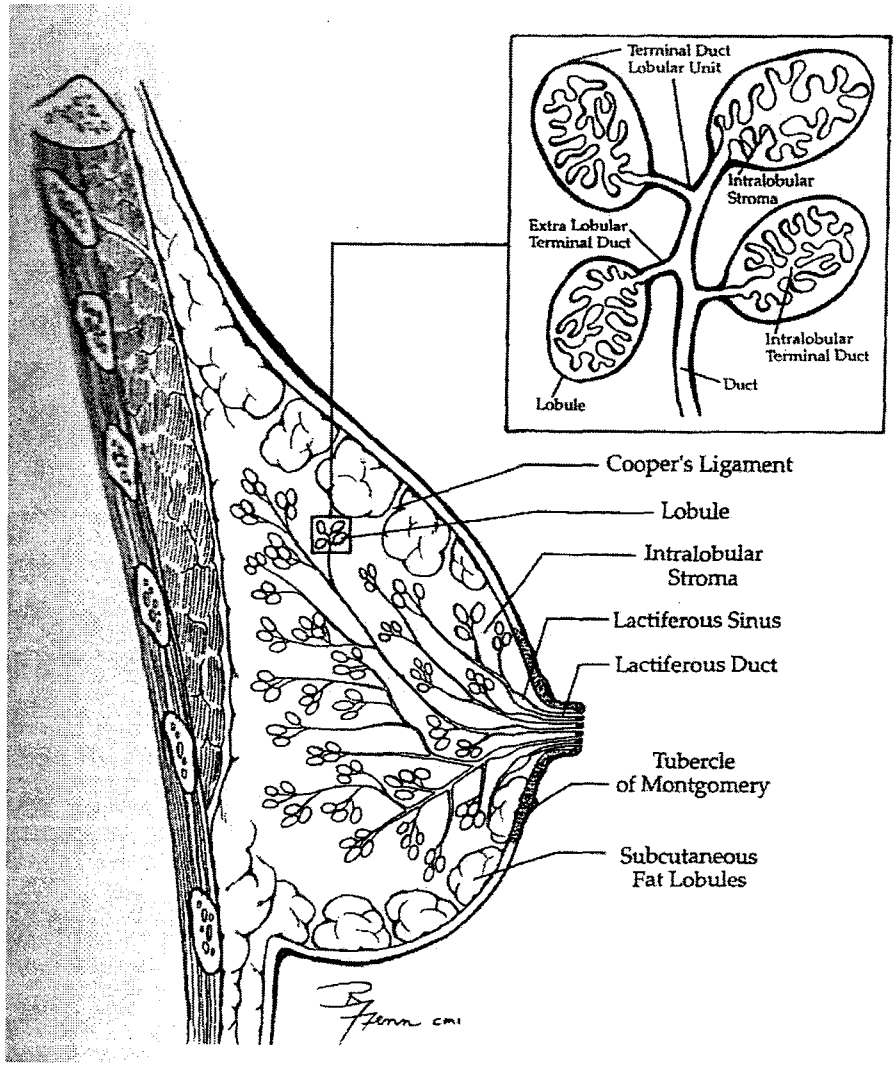

Fig. 2 – Breast Anatomy [8]

This figure shows the location of the various parts of the breast. The range in diameter for the ductules and ducts is 0.3 to 0.6 mm.

1.2.2.ii Macroscopic

The arrangement of breasts on the chest can vary from woman to woman, and some breasts are widely separated on the chest, while others may actually blend together near the sternum. The amount of body fat a woman has will, in part, determine the volume of her breasts[8]. Underneath the fatty tissues,

the glandular structures are found wrapped around the pectoral muscle, straddling the sternum and below the clavicle.

The most easily distinguishable characteristic of the macroscopic breast is the breast volume. Individual breast volume varies extensively among female populations, and can even vary when comparing the right to the left breast in the same individual up to 50%. Published in the Journal of the American Society of Plastic Surgeons, Loughry [13] examined a sample population to determine the average breast volume to be 405 mL, but individual measurements varied from 21 mL to almost 2 litres. In addition, Malini *et al.* determined that breast volume can fluctuate during the menstrual cycle up to 36% [14]. The lowest breast volumes were found during menstrual cycle days 9 to 17, and the difference is likely attributed to water volume changes, which have been measured using MRI [15].

The structural integrity of the mammary gland is determined by the connective tissue surrounding the mammary gland. The purpose of the connective tissue layer, called the pectoral fascia, is to resist mechanical tension and unnecessary movement of the breast as a result of muscular and motion-based activities. Underneath the connective tissues, the lobular units are found, and they are the most active units in all of the breast tissues. Each breast is estimated to have up to 100,000 lobules, which are the crucial components for milk production. Details of the process of milk synthesis will be described in section 1.2.3 'Physiology.'

The overall shape of the breast is determined by the suspensory ligaments, which stretch between the lobes and the skin and keep the mammary gland securely fastened. These special suspensory ligaments are called Cooper's ligaments and a particularly important area that the Cooper's ligaments are found is near the undersurface of the breast, where they create the natural boundary of the breast from the chest wall, called the inframammary fold. A crowded bunch of Cooper's ligaments are found at this fold, and it permits mobility of the breast on the chest wall for ease of infant feeding.

The macroscopic anatomy of the breast as described, including breast volume, shape and structural integrity, can interfere with some surgical procedures. Difficulties can be encountered during mastectomy attempts, since the ducts and lobules are relatively close to the surface of the skin, especially near the nipple. If breast tissue remains after the procedure, the risk of breast cancer still exists, and in many cases where the nipple is preserved after mastectomy, residual breast tissue was found to have a higher likelihood of developing breast cancer [16-18].

Moving from that which can be seen of the macroscopic breast, such as the volume and structure, to the inner workings of the breast, the major blood supplies for the breast comes from the lateral thoracic and the internal mammary arteries. The internal mammary artery serves the more interior components of the mammary gland, while the outermost parts are easily accessed by the lateral thoracic artery, which is also appropriately called the external mammary artery. The very deepest layers of the breast are supplied by smaller arteries, which have to go through the pectoral muscle to reach the breast tissue. Figure 3 shows the arterial network in the breast.

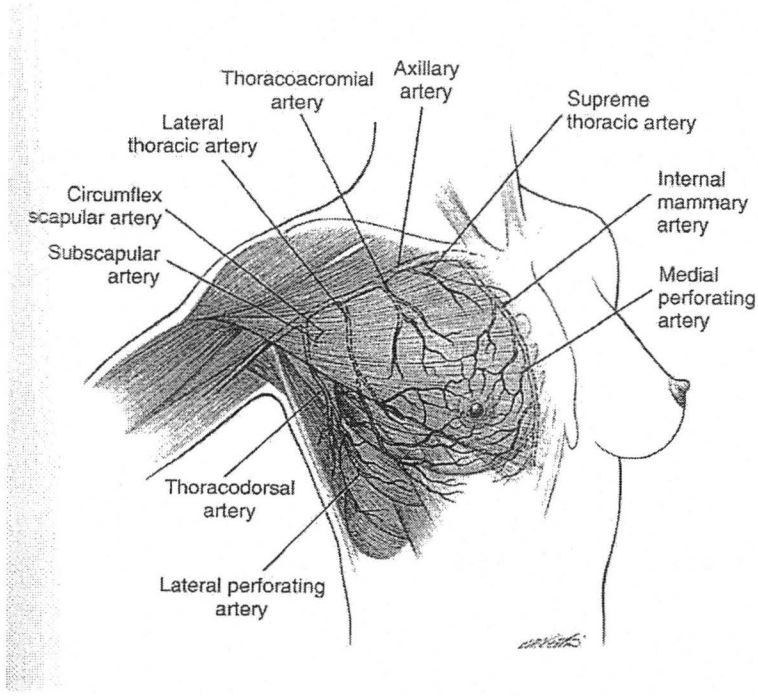

Fig. 3 –Arteries of the Breast [8]

This figure shows the location of the various arteries found in the breast.

The veins in the breast form their own patterns quite close to the skin and actually do not follow the arterial framework, especially near the areola. Figure 4 demonstrates the venous network. During lactation, when both arteries and veins expand and blood flow increases, women with especially thin skin will demonstrate a characteristic pattern [19]. This characteristic pattern visible through transparent skin is shown in Figure 5.

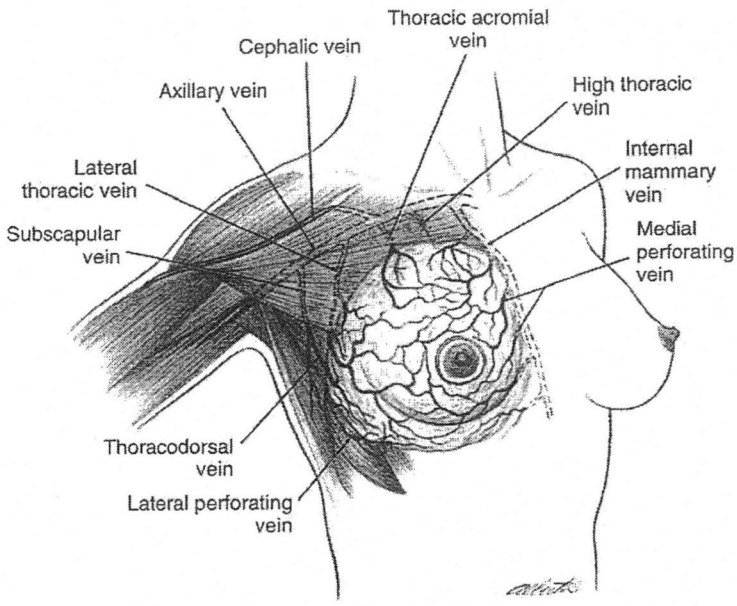

Fig. 4 – Veins of the Breast [8]

This figure shows the location of the various veins found in the breast.

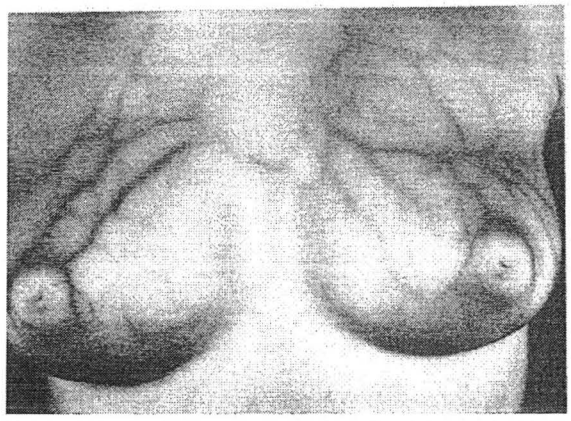

Fig. 5 – Venous Pattern through Transparent Skin [8]

This figure shows an example of a woman with transparent skin. An obvious venous pattern is seen.

Breast lymph, as with all other lymph in the body, must drain before mixing back with blood. In the breast, lymph drains toward the axillia, or armpit region, and also to a lesser extent, drains toward the internal mammary nodes. Due to the high probability of metastases in the lymph nodes, understanding

the organization of the axillary nodes is of utmost importance for surgery. Figure 6 shows the location of the lymph nodes and the travel of lymph in and around the breast.

It has been shown previously that after 216 axillary dissections, the average number of axillary lymph nodes found was 24 [8], whereas Fisher and Slack reported that the mean number of axillary nodes was 17. Fisher and Slack's data came from 2768 patients who underwent radical mastectomy, which is the complete removal of the breast, the chest muscle and adjacent axillary nodes, and they found patients had one to three metastases in the axillary nodes. When patients had a higher average number of nodes, as high as 21, four or more nodes were found to contain metastases [20]. It can be inferred that an increased number of nodes correlates with a more active lymphatic system, which can increase the likelihood of metastases.

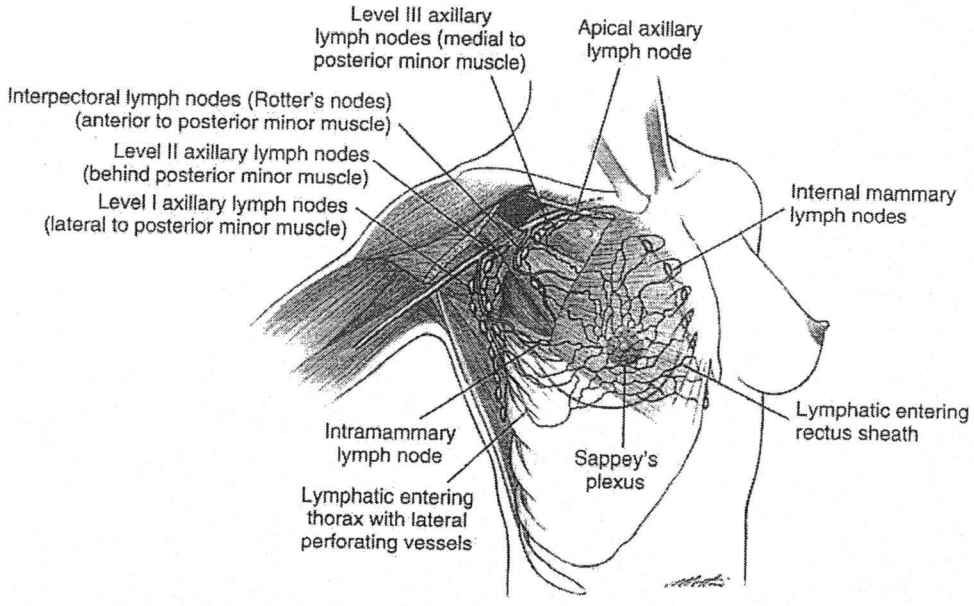

Fig. 6 – Lymph Nodes of the Breast [8]

This figure shows the location of the various lymph nodes associated with the breast.

Classification of the axillary nodes was suggested by anatomists Pickren *et al.* [21] who divided the nodes into four categories: i) the highest nodes, or those closest to the clavicle, ii) the interpectoral nodes,

found between the pectoralis major and pectoralis minor muscles, iii) the lower axillary vein category, from the bottom of the pectoralis minor to the lateral limits of the breast, and iv) the central category [21]. Representative of the controversy experienced by researchers attempting to classify the lymphatic system, and in contrast to Pickren's groupings, surgeons and pathologists have developed their own classification system for grouping axillary nodes by their location relative to the pectoralis minor muscle [8]. Level I is specified for nodes on the outer side of the pectoralis minor muscle. Level II consists of nodes behind the pectorialis minor, and level III describes nodes on the inner side of the muscle. In general, the classification by surgeons and pathologists mimics the order in which cancer cells are likely to infiltrate the axillary lymph nodes.

The speculated interactions between the lymphatic and vascular systems are explained by studies from B. Fisher[22, 23] and E. Fisher[24, 25], which relate to the development of breast cancer. Figure 7 attempts to show their theory about how tumour cells spread throughout the body.

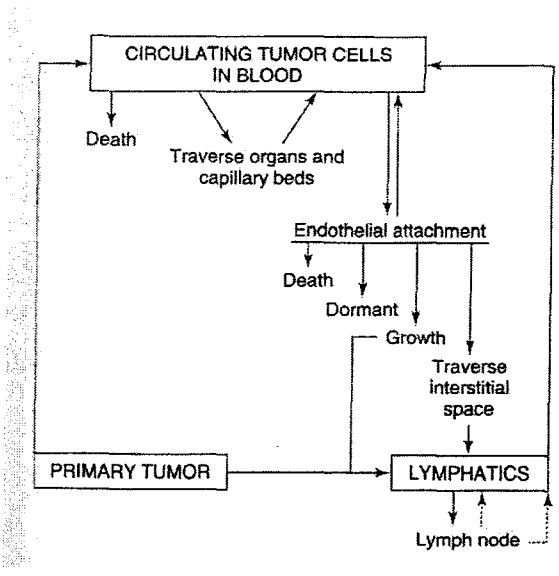

Fig. 7 – Lymphatic and Vasculature Systems[8]

This figure shows the relationship between the lymphatic and vasculature system. These complex relationships are vital in understanding the spread of cancer.

The studies by Fisher develop the idea that tumour cells can be found going between the lymphatic and vascular systems, and their studies suggest that any cells that circulate in the blood can eventually be found in the lymph as they pass through tissues, and likewise, cells in the lymph can enter into the blood. As breast cancer progresses, venous blood samples have shown more circulating cancer cells detected in the blood[26], but for a tumour to actually grow in one location, cells must stop circulating and attach to the endothelial layer of the lymph nodes, ducts or the other tissues to begin localized tumour formation.

The above explanation of the micro and macro anatomy of the breast, including the organization of the ducts and lobes of the breast, the vascular and lymphatic systems will aid in understanding its function, which follows in section 1.2.3.

1.2.3 Physiology

Many factors play a role in the normal physiology of the breast, including protein kinases and growth factors, with a large influence being played by hormones. Hormones direct the control of proliferation and apoptosis of cells in the breast [11] and regulate the structure, size and activity of breast tissues. One of the most important functions of hormones is their instigation of milk secretion in the epithelial cells of a postpartum woman. The influence of hormones on milk secretion is evident even in newborns, whose breasts may secrete their own fluid in response to hormone stimulation, called 'witches'milk.' Hormones continue to be important through the development of ducts at puberty, and the ongoing growth and differentiation of the various breast tissues. Table 1 shows the response of ducts to various hormones.

Table 1 – Effects of Hormones on the Breast [8]

Hormone	Effects
Estrogen	Required for ductal growth during adolescence
	Required for lobuloalveolar growth during pregnancy
	Not necessary for maintenance of lactation or "secretion"
	Required to prime progesterone receptor induction
Progesterone	Required for lobuloalveolar differentiation and growth
	Not necessary for ductal formation
	Probable mitogen in "normal" estrogen-primed breast
Testosterone	Causes mesenchymal destruction of mammary epithelium during critical period of testosterone sensitivity
	Inhibits estrogen action, suppresses estrogen and progesterone receptor levels
Glucocorticoid	Required for maximal ductal growth
	Nonessential but enhances lobuloalveolar growth during pregnancy
Insulin	Enhances protein synthesis of mammary epithelium
	Enhances ductal alveolar growth
	Required for secretory activity with glucocorticoid and prolactin
	Associated with mitoses
Prolactin	Required for lactogenesis and maintenance of lactation
	Stimulates epithelial growth after parturition
Human placental lactogen	Able to substitute for prolactin in epithelial growth and differentiation
	Stimulates alveolar growth and lactogenesis in second half of pregnancy
Growth	Required for ductal growth in adolescence
	May contribute to lobuloacinar growth during pregnancy
Thyroid	Increases epithelial secretory response to prolactin
	Nonessential for ductal growth; may enhance glandular-acinar growth
Oxytocin	Causes contraction of myoepithelial cells, which produce milk ejection

The most sensitive parts of the breast tissue to hormone changes are the secretory units of the alveolar glands, which promote growth or regression of the breast tissue in response to the hormone direction. A second important hormone response is by the specialized smooth muscle cells called myoepithelial cells, surrounding the alveoli. When those smooth muscle cells contract in response to hormonal stimulation, milk gets emptied from the lobes into the lactiferous ducts. Lactation is the primary function of the breast and as such, will be discussed in a dedicated section 1.2.3.i below.

Puberty is of considerable importance for hormone stimulation from estrogen originating in the ovary, which results in significant growth of the breasts; however, further development of the breasts is dependent on numerous other hormones. The development of the ducts requires the presence of prolactin, hydrocortisone, growth hormone and insulin, whereas the presence of progesterone leads to the development of terminal ducts and the alveoli to secrete milk. After the onslaught of hormonal changes induced by puberty, the rest of the mature life of the breast is rather dormant, unless pregnancy requires a phase of rapid growth. A phase that follows childbirth is that of lactation to produce milk for the young,

until such time that milk is no longer required and a stage of regression occurs. The last major change in the physiology of the mammary gland is atrophy during menopause, which results in the cessation of the ability to produce milk. Interestingly, an inhibitory effect on the breast tissue is seen with testosterone, which is the hormone present largely in males, and to a lesser degree in females, which will stop the growth of breasts in males, or in females with increased levels of testosterone. The corresponding anatomical changes that occur during the aforementioned phases are discussed in detail below.

After puberty, the lobes and ducts of the breast are cushioned by connective and adipose tissues, but it is not until pregnancy that the most significant proliferation of cells occurs to prepare for the breasts' ultimate function - lactation. The sudden hyperplasia which occurs prior to childbirth is counterbalanced later in pregnancy by a hypertrophy of alveolar cells, together with a decrease in fat and fibrous connective tissue to return the breast tissue to equilibrium. Interesting changes occur at the cellular level during lactation, and the cells which line the interior of the alveolar sacs become more columnar, and begin to secrete cellular components into the alveolar lumen. Protein products leave the cells by exocytosis, while lipids are actively transported out of the cells. The most important anatomical change in response to hormone stimulation in the breast is that from the latched infant, which triggers cell contractions to force fluids from the alveolar ducts into the lactiferous ducts and eventually, exits the breast into the infant's mouth.

After the termination of breast feeding, the regression and resulting degeneration occurs in the absence of infant feeding, and any residual milk products are reabsorbed by surrounding tissues. The breast begins to turn in on itself, and fat and connective tissue start to fill in the remaining space. Menopause also results in a similar process of atrophy; however, hyalinization follows the degeneration of the alveoli and intralobular ducts. Hyalinization is the process by which normal cellular structures become replaced with hyaline, a translucent material with glassy collagen fibers, and could more simply be described as

degeneration. Menopause signifies the end of the biologically useful life of the breasts and is the stage after which no further lactation can occur.

1.2.3.i Lactation

Lactation is the principal function of the breast and the pinnacle in breast physiology. While the primary function of the lactating breast is to ensure the newborn young are appropriately fed, a secondary function is achieved by establishing an interval between subsequent births, since many mothers do not ovulate or undergo menstrual periods during lactation. Interestingly as such an innate function, lactation can occasionally be stimulated by continuous suckling , either in women without previous childbirths who are not pregnant, or also in men [27, 28].

This important process is induced and regulated by a series of well orchestrated hormonal events, including nine months of increasing progesterone, estrogens, and lactogen levels, in anticipation of this crucial function [29]. Several hormone triggers initiate milk production, but most important is a fall in progesterone levels, which only occurs when the development of the breast is ready for milk [30]. In addition to progesterone, prolactin is another important hormone for lactation, and its function is to drive the synthesis and secretion of milk into the alveoli. Prolaction is also responsible for regulating milk production volume, in accordance with infant demand, but this function can be inhibited by high levels of progesterone present during pregnancy. In nursing mothers, the hormone levels of estrogen and prolactin will decrease more slowly than in a non-nursing mother[31, 32]. Even with low levels of prolactin, lactation can still occasionally occur with only the marked decrease in progesterone after childbirth [33]. The last hormone that plays an important role in the contraction of epithelial cells to actually eject the milk is oxytocin, which activates reflexes in the brain from the suckling infant stimulus. While many hormones are critical in milk production, it is evident that progesterone, prolactin and oxytocin play particularly significant roles.

Each gram of alveolar tissue produces about 1 to 2 mL of milk per day [11] and the ingredients of milk, including lactose, milk proteins and fat, must be sufficient to nourish the infant, while including all components necessary for proper development. Many hormones and growth factors are also found in milk and breast-feeding women should be cognoscente of the types of hormones or other influences they consume, as they will likely be passed onto the child. Studies have shown many drugs can have adverse effects on nursing infants, including antidepressants, aspirin, oral contraceptives, or cough medications [34-36]. The primary milk proteins are casein, β-lactoglobulin, and α-lactalbumin, with casein as the most prevalent at 40% [37]. While the protein and fat components are important, the composition of milk must change with the changing demands of the growing infant. Colustrum, which is a type of milk with high milk fat, protein and immunoglobulins to protect against disease, is produced in the first 5 days of lactation, to deliver nutrients to the newborn in a concentrated volume. Once the small digestive system of the newborn becomes more developed, milk containing higher lactose levels is secreted for further growth and strength.

The importance of considering lactation in a discussion of breast imaging techniques stems in part, from the concern that a breastfeeding mother receiving dose from ionizing radiation, such as through a mammogram, may potentially harm the infant in the passage of milk. Studies by Luick and Mazrimas on udders of cattle irradiated with a cobalt-60 source, producing gamma rays and an absorbed dose of 7.5 to 18 Gy demonstrated that beyond a particular threshold dose, detectable differences were found in the milk. Beyond the threshold dose of 5 to 7.5 Gy, enzyme inhibition was observed in the cattle's fresh milk [38]. Considering the dose for normal diagnostic procedures is only up to 20 mGy, it seems unlikely that these low levels of ionizing radiation will have any effect on the milk delivered to human infant young. Interestingly, a non-ionizing source of radiation is actually being used to enhance lactation in women who struggle to dilate blood vessels during milk production. Far-infrared radiation was commended for its warming and dilating effects on the breast and allowed 75% of women with poor lactation (n=36) to successfully breastfeed their young until weaning [39].

In addition to the concern for radiation during breastfeeding, the link between breastfeeding and cancer has also been well studied. While some research neglects to find a significant relationship between cancer risk factors and breastfeeding [40], several other studies suggest that the length of time a woman spends breastfeeding actually decreases her risk of breast cancer by as much as 4.3% with every month spent breastfeeding [41, 42]. There may, however, be an increased risk of malignancy in those women who already have benign lesions before becoming pregnant and beginning to breastfeed. Since fibroadenomas can become enlarged with the proliferation of other breast tissue during pregnancy, these benign lesions may eventually become malignant [43].

1.3 BREAST CANCER

Breast cancer touches many lives, and it is said that one in nine women will develop breast cancer at some point[44], and over 5000 Canadian women will die of breast cancer every year [44]; thus, the impact of this disease on our society is substantial. The ability to use modern imaging techniques to detect cancer during regular screenings should decrease the risk of mortality, since early detection has been shown to find cancers at earlier stages, before they begin to exhibit symptoms. If detection takes place after symptoms are already presented, the tumour is likely larger and may have already spread through the lymphatic system, increasing the severity of the disease. Even though the current detection tests save many lives each year, more lives could be saved if more women participated in routine screening examinations [45].

1.3.1 Benign Lesions

There are many different types of benign breast conditions, so many that they cannot all be explained in detail, but a few of which will be mentioned below. Mammary duct ectasia where the ducts beneath the nipple become inflamed and blocked, can result in discharge and may require the eventual removal of the duct if it cannot be treated with antibiotics. A papillary neoplasm is a tumour that can grow within the duct

and also lead to duct blockage and nipple discharge. Fibroepithelial tumours, consisting of epithelial tissue and mesenchymal tissues, and nipple diseases can all affect the overall health of the breast, but by far the most common benign conditions are fibrocystic changes[11], affecting more than 50 percent of women with breasts determined irregular through palpation examination [11]. Given their prevalence and importance in understanding benign breast lesions, fibrocystic changes will be discussed in detail in this section.

1.3.1.i Fibrocystic Changes

Fibrocystic changes (FCC) are not considered actual breast disease, but rather encompass a variety of non-cancerous changes to the mammary gland that are considered extraordinary occurrences [46]. Fibrocystic changes have been well studied and documented [47-94], and include various types of cysts, which are sacs enclosed by a membrane full of air, fluids or semi solid materials (but not pus – that is an abscess). Also included in fibrocystic changes are metaplasias, where one cell is replaced by another cell type during a period of cellular stress, and hyperplasias, where cell growth occurs beyond that which is normally seen. More additions to the list of fibrocystic changes include alternations to the stromal or connective tissues and mild adenosis, which is an abnormal number or density of lobes [95-120]. At least 40 different terms[11] have been used to describe benign lesions, but the most common definition is 'fibrocystic disease.' This term includes not only all of the lesions described above, but also includes a variety of proliferative lesions, such as sclerosing adenosis, where extra tissue starts developing in the lobules, or papillomatosis, which is a wart-like growth that can puncture ducts. Including such a broad range of conditions in a single definition unfortunately implies that all of the mammary gland alterations originate from a similar pathophysiological process, which is false.

The earliest description of FCC was recorded in 1846 and is credited to Sir Benjamin Brodie [63] who used the term 'benign cystic disease.' As the understanding of FCC has progressed, the treatments for breast cancer have adapted to correspond with new knowledge. In the 1920's, there was growing concern

that epithelial hyperplasia might be a precursor of carcinoma, so it was not uncommon to perform unnecessary mastectomy in these cases. It was not until Bloodgood reviewed 1200 cases of carcinoma and 800 benign breast lesions, that he concluded cystic disease is not normally associated with carcinoma [61]. Bloodgood's discovery forced surgeons to adopt more conservative treatments and vastly decreased the number of superfluous mastectomies for fibrocystic changes, although Foote *et al.* challenged many of Bloodgood's observations in the mid 1940's in attempt to clarify the definitions of FCC and establish statistical significance with data [76]. Many years of debate between pathologists and surgeons followed to attempt to define FCC[65, 68], until 1986 when the Cancer Committee of the College of American Pathologists finally proposed that "the fibrocystic process in the breast is not a disease, but rather an exaggerated physiologic phenomenon" because of its frequency in breast tissues [87]. Of particular importance is the distinction made by this Committee to separate FCC from proliferative lesions, since the latter lesions are associated with an increased risk of ensuing carcinoma[87].

While it is difficult to quantify the true occurrence of FCC since it is so immensely prevalent, it has been estimated that more than one third of women between 20 and 45 years of age have clinical evidence of FCC on routine physical examinations[92, 93, 101]. Cellular evidence of FCC has been identified in 54% of autopsies of clinically normal breasts[77], 34% of normal breasts after biopsy [94], and 40% of cancer bearing breasts[111]. Interestingly, FCC is not always clinically obvious, since evidence of cystic changes has not only been acknowledged in 61% of autopsy specimens with clear evidence of FCC, but also in 58% of breasts with a normal appearance[55].

While perhaps not always clinically possible to grossly identify FCC, it may be possible to narrow down the likely patient population. Fibrocystic changes generally plague premenopausal women who are 20 to 50 years old and a staggering 70 to 75% of women with FCC are in their mid 30's and 40's[119]. FCC prone breasts may be diffusely dense in addition to the expected connective tissue proliferation. Furthermore, many women with FCC have menstrual abnormalities, have never had children and may

report a history of spontaneous abortions. Women with FCC likely do not take oral contraceptives; on the contrary, women who take or have ever taken oral contraceptives have been reported to be at a reduced risk for FCC[105].

FCC has been observed clinically in three stages. The first stage, usually observed in the middle to late 20's, is referred to as 'mazoplasia,' which is characterized by premenstrual breast swelling and tenderness [94, 119]. The second stage as women enter their 30's, is referred to with various names including, 'the stage of adenosis', 'the multinodular breast', or 'Schimmelbusch's disease'. This stage is recognizable by multiple firm nodules, plaques, and lumps, and is accompanied by premenstrual pain and increased breast tenderness. Finally, the third stage occurs as the patient enters her 40s, and breast pain and tenderness become a constant and debilitating problem. Large cysts and lumps are easily discovered with routine examination, and about 20% of women complain of axillary tenderness.

After menopause, the risk of FCC decreases dramatically. Ovarian estrogen secretion becomes negligible, and only in women who use estrogen replacement therapy is the risk of postmenopausal FCC a factor [115]. According to Bassler [57], approximately 25% of postmenopausal women from 60 to 80 years of age have FCC at autopsy, but only 10% showed previous symptoms. In addition to age, the risk of developing FCC increases with ovarian dysfunctions with related estrogen hormone imbalances. Estrogens cause proliferation of connective tissue, and the development of ductal epithelial cells. To support the correlation between FCC and increased levels of estrogen, Geschikter [78] postulated that breast nodules were caused by hyperestrogenism using animal models. He narrowed his scope to suggest that hormonal imbalances during the luteal phase were the crucial factor, as long as this still resulted in hyperestrogenism. Using large doses of estrogen, Geschikter was able to induce adenosis in rats, and subsequently, other investigators have validated the role of hormonal fluctuations in the induction of FCC [89].

Hyperestrogenism has also been implicated in stromal fibrosis, the proliferation of the connective tissue cells[116], which causes the obstruction of ductules. With the increase in estrogen, continual epithelial

cell development begins to obstruct the ductules, and cysts develop near the obstruction. The majority of cysts do not exceed 1 to 2mm in size; however, larger cysts can be up to 1 to 2cm in diameter, and have been observed in 20 to 40% of patients with fibrocystic changes [119]. The fluid inside a cyst contains proteins, hormones, glucose, cholesterol, and minerals, and calcification of this fluid takes place in 25% of the cases [119].

Popular media has advocated that methylxanthine, found in coffee, cola drinks, and chocolate may contribute to poor health [121-123]. While it has been supported by some research that fibrocystic changes are linked to the intake of methylxanthine [99], still other studies have demonstrated that avoidance of these substances appears to have no effect on the development of fibrocystic changes[119].

While it is perhaps not coffee that causes cancer, many investigators have looked at the relationship between cystic disease and cancer [56, 67, 70, 71, 82-85, 88, 90, 109, 117, 120]. While there are differing viewpoints on whether FCC is truly a precursor to carcinomas, investigators tended to arrive at different conclusions regarding the implication FCC as a cancer risk factor, depending on the number of cases of epithelial hyperplasia included in each study. The disconnect could conceivably be due to the inclusion of all degrees of hyperplasia when defining FCC. Women with FCC have been shown to have double or up to five times higher risk for developing breast carcinoma when they have FCC, as compared to the general population. Some of the highest risks of carcinoma are due to overgrowth of epithelial cells, or epithelial hyperplasia [67, 83-85, 88, 109, 120]. Remarkably, it has been shown that mild degrees of hyperplasia, defined as an epithelial proliferation of up to four cells deep, are ordinary in the breast and do not represent a significant risk factor [102]; therefore, it is only severe hyperplasias which are of significant concern for the development of carcinoma.

While there are several methods of classifying benign breast diseases, the Cancer Committee of the College of American Pathologists [87] has classified patients into three major risk categories for carcinoma: i) no increased risk, incorporates fibrocystic changes such as cysts or mild epithelial hyperplasia, which is

unexpected cell growth in the epithelial cells ii) slightly increased risk (1.5-2.0 times), is for patients with intraductal hyperplasia without a biopsy that shows malignancy, or for patients with sclerosing adenosis[124], and finally, iii) moderately increased risk (4-5 times) includes those with atypical intraductal hyperplasia, which is when the cells lining the lactiferous ducts begin growing more than expected. By dividing his subjects using the above risk categories, Mongeau *et al.* [100] found carcinoma in only 5% of category one lesions (no increased risk). In general, the risk for development of carcinoma subsequent to FCC is not strikingly different than that of the general population; therefore, no particular treatment or subsequent visits are required for patients with FCC.

Even though there is no special treatment for FCC to minimize the risk of the development of carcinoma, some women may still desire treatment for symptomatic relief. Nonsurgical treatment such as oral contraceptives[62] prevent progression of the FCC and have been used with success rates up to 90%[53, 62, 75]. Giving oral progesterone during the luteal phase of the menstrual cycle has also shown improvements in 80-85% of FCC patients[91, 95, 97, 119] and a variety of other hormones treatments, such as bromocriptine [50, 60, 73, 96], danazol [59, 81, 114], and tamoxifen [108, 110] have also been used with varying degrees of success.

Surgical intervention for the treatment of FCC is rarely necessary, and total mastectomy should not be considered as a serious option for FCC management. A drastic choice, mastectomy seldom removes all breast tissue, usually leaving up to 5%[113]. One study even demonstrated that total mastectomy leaves behind breast tissue within the superficial pectoralis major muscle and the lower skin flap[113]. Even small amounts of tissue left behind can result in subsequent carcinoma[74, 79, 106]. Furthermore, mastectomies give the patient a false sense of security, and may prevent her from properly examining the breast to detect future abnormalities.

1.3.2 Malignant Lesions

In contrast to benign lesions, malignant lesions are cancerous and, if inadequately treated, may eventually result in serious health complications. The classification usually used for breast carcinomas is based on their presumed origin in either the ducts or the lobes of the breast. Ductal and lobular carcinomas have been well studied and there is agreement in the scientific community that carcinomas originate in the terminal ductal or lobular unit. While there are several types of malignant breast lesions which target particular cell types, the infiltrating or invasive ductal carcinoma is the most common type of malignant lesion found in the breast and will be described in detail in the section below.

1.3.2.i Infiltrating Ductal Carcinoma

Infiltrating ductal carcinoma, also known as infiltrating carcinoma, is the most common type of breast cancer in women [125]. Diagnosis of infiltrating carcinoma is made by exclusion, when lesions cannot otherwise be classified as another type of breast carcinoma[126]. Categories include 'not otherwise specified' (NOS) [127], or 'no special type' (NST)[128]; however, the pattern of infiltration must be present in 90% of the tumour sample. Accounting for 47 to 75% of all invasive breast carcinomas[125, 129, 130], infiltrating breast carcinoma frequency has varied in different countries depending on the diagnostic criteria used.

The drive toward earlier detection of breast lesions has decreased the incidence of many conditions that reflect advanced stages of malignancy and changed prognosis patterns[131, 132]. Attributes such as skin fixation, which is the inability of the skin to move independently of surrounding tissue, swelling, 'peau d'orange', which is when the breast represents the look and texture of an orange peel, nipple retraction, or ulceration are some of the features visible during advanced stages of malignancy. The presentation of infiltrating duct carcinoma is usually as a mass, generally detected by women in their 50s during self-examination or by mammography. Usually, about 2-3cm in size on palpation, the tumour may, in fact, be substantially larger and occupy a considerable portion of the breast.

On a macroscopic scale, infiltrating ductal carcinoma is either a mass with rounded, well defined borders, or stellate in appearance, with invasive and outstretched protrusions, which radiate into surrounding breast tissue. The latter is referred to as 'scirrhous carcinoma', or 'stellate carcinoma'[133], and is more common than the rounded lobular mass, accounting for two thirds of lesions. Tumour size can vary tremendously, ranging from a few millimeters to more than 14cm. The greater the size of tumour, the more developed the tumour is and the worse the prognosis. Accurate documentation of tumour size is very important and is therefore recorded in three dimensions, but with irregular shapes, accurate measurements are sometimes difficult. Occasionally, the tumour sample is cross-sectioned to maximize the dimension of the specimen before recording the measurements.

As with FCC, radical mastectomy was the most common treatment for infiltrating ductal carcinoma until the 1960's. Some studies began to recommend more conservative treatments, such as local excision or irradiation for some early variants of breast carcinoma [134, 135], and a gradual shift occurred toward modified mastectomies. Eventually, even less radical treatments followed, such as partial mastectomy, quadrantectomy, and finally lumpectomy[134, 136-139]. For some patients with disease not localized to a specific region in the breast, total mastectomy remains the preferred treatment.

By combining some therapies, such as postoperative irradiation to mastectomy, or adjuvant chemotherapy, the risk of recurrences drops dramatically. In one study, the risk of recurrence among 856 women who did not receive additional therapies dropped from 32% to 9% among 852 women who did receive such therapy [140]. Supplemental radiation can also increase the probability of survival free of disease, and a study demonstrated that at 10 years post-mastectomy, the disease-free survival increased from 38% among those who did not receive radiation to 48% among those who did[140]. Increases in disease-free survival was irrespective of tumour size, number of positive nodes, or grade of cancer [140]. Combinatory therapies seem to provide modest success in improving breast cancer outcomes, and as such, the National Institutes of Health Consensus Conference held in June 1990 [141] suggested that breast

conservation treatments should be pursued for a majority of patients with early stages of breast cancer. They concluded that breast preservation "is preferable because it provides survival rates equivalent to those of total mastectomy and axillary dissection while preserving the breast"[141]. Breast preservation is an important factor to consider in meeting patient preferences, improving cosmetology, and for positive psychosocial progress after treatment.

While patient preference and cosmetics are important considerations, there are certain tumour characteristics that determine the ultimate decision for treatment. Conservation therapy, also called a lumpectomy, segmental or partial mastectomy, can be performed to excise a primary tumour and 1cm of adjacent breast tissue, and the majority of patients can be successfully treated by this approach[141]. Conservative therapy is usually followed by radiotherapy with 45-50 Gy to reduce the risk of recurrence, and ensure that the outer margins of the tumour region are free of residual cancerous cells. Occasionally, re-excision may be necessary [142], or in some cases, total mastectomy.

Not all women are good candidates for conservation therapy. Tumours with features that increase the likelihood of recurrence, such as multicentric malignancies or diffuse mammographically detected microcalcifications, may preclude some women from the breast conservation approach. Furthermore, large tumours relative to the size of the breast will result in poor cosmetic results for some women, so conservation therapy would be redundant. Some women have collagen vascular disease, which has been reported to develop immense fibrosis and disfiguration as a result of radiotherapy, so conservation treatments followed by radiotherapy would not be an option [141]. Nevertheless, if a woman has small tumours ($\leq$1cm in diameter) and no spread to the lymph nodes, she would be a particularly good candidate for conservative therapy, as her prognosis is excellent and adjuvant chemotherapy is not required. In addition to conservative treatments and mastectomy, there are many other ways that can be used to treat breast cancer. While a popular option for prostate cancer, brachytherapy can also be used to treat other cancers such as breast, lung, and cervical cancer [143].

1.3.3 Male Breast Lesions

With the presence of a rudimentary mammary gland, males can acquire breast cancer just the same as women; yet, the incidence of breast lesions in males, especially malignant ones, is quite low, making up only 1% of all breast cancer cases[144]. From birth to puberty, there is very little difference between male and female breast development[145]; however, as a male reaches adulthood, the mammary gland becomes a vestigial organ and a dense connective tissue surrounds the ducts. The lobes found in female breasts are absent in males, and microscopically, the male breast resembles that of a prepubertal girl.

While there are many lesions common to the female breast that cannot be present in the male breast due to simple physiology, gynecomastia is a malignant lesion almost exclusive to the male breast, and results in proliferation of the both the ducts and stroma simultaneously. Holleb [146] estimated the breakdown of breast lesions in elderly men to be 65% gynecomastia, 25% carcinoma, and 10% other benign breast lesions. Any other lesions common to both sexes are morphologically impossible to differentiate.

1.3.4 Staging of Breast Cancer

Staging of breast cancer is crucial when evaluating tumour progression and determining the appropriate course of treatment. Establishment of the stage of cancer may be purely clinical, based on the physical examination, mammograms, and scans together[147, 148]. Size, mobility and any skin changes will be visible with a physical examination; however, to identify the pathologic stages requires a tissue specimen from the tumour or axillary nodes [148]. The clinical stage and the pathologic stage do not always correspond to one another, but one benefit of pathologic staging is the certainty it provides about the severity of the lesions. One of the oldest and most widely used systems for staging of carcinomas is termed TNM. First proposed in 1954, the TNM system divides tumours into stages based on evaluation

of the primary tumour (T), the regional lymph nodes (N), and distant metastases (M) [8]. Pathologic staging can also use this classification system, but requires the pTNM guidelines.

Table 2 – TNM Clinical Classification[11]

TNM Clinical Classification

T—Primary Tumor

TX Primary tumor cannot be assessed

T0 No evidence of primary tumor

Tis Carcinoma in situ: intraductal carcinoma, or lobular carcinoma in situ, or Paget's disease of the nipple with no tumor

Note: Paget's disease associated with a tumor is classified according to the size of the tumor.

T1 Tumor 2 cm or less in greatest dimension

T1mic Microinvasion 0.1 cm or less in greatest dimension (1)

T1a More than 0.1 cm but not more than 0.5 cm in greatest dimension

T1b More than 0.5 cm but not more than 1 cm in greatest dimension

T1c More than 1 cm but not more than 2 cm in greatest dimension

T2 Tumor more than 2 cm but not more than 5 cm in greatest dimension

T3 Tumor more than 5 cm in greatest dimension

T4 Tumor of any size with direct extension to chest wall or skin

Note: Chest wall includes ribs, intercostal muscle, and serratus anterior but not pectoral muscle

T4a Extension to chest wall

T4b Edema (including peau d'orange), ulceration of the skin of the breast, or satellite skin nodules confined to the same breast

T4c Both 4a and 4b, above

T4d Inflammatory carcinoma (2)

Notes: (1) Microinvasion is the extension of cancer cells beyond the basement membrane into the adjacent tissues with no focus more than 0.1 cm in greatest dimension. When there are multiple foci of microinvasion, the size of only the largest focus is used to classify the microinvasion. (Do not use the sum of all the individual foci.) The presence of multiple foci of microinvasion should be noted as it is with multiple larger invasive carcinomas.

(2) Inflammatory carcinoma of the breast is characterized by diffuse, brawny induration of the skin with an erysipeloid edge, usually with no underlying mass. If the skin biopsy is negative and there is no localized measurable primary cancer, the T category is pTX when pathologically staging a clinical inflammatory carcinoma (T4d). Dimpling of the skin, nipple retraction, or other skin changes, except those in T4b and T4d, may occur in T1, T2 or T3 without affecting the classification.

N—Regional Lymph Node

NX Regional lymph nodes cannot be assessed (eg, previously removed)

N0 No regional lymph node metastasis

N1 Metastasis to movable ipsilateral axillary node(s)

N2 Metastasis to ipsilateral axillary node(s) fixed to one another or to other structures

N3 Metastasis to ipsilateral internal mammary lymph node(s)

M—Distant Metastasis

MX Distant metastasis cannot be assessed

M0 No distant metastasis

M1 Distant metastasis

The categories M1 and pM1 may be further specified according to the following notation:

Pulmonary	PUL	Bone marrow	MAR
Osseous	OSS	Pleura	PLE
Hepatic	HEP	Peritoneum	PER
Brain	BRA	Adrenals	ADR
Lymph nodes	LYM	Skin	SKI
Others	OTH		

Table 3 – pTNM Pathological Classification[11]

pTNM Pathological Classification

pT—Primary Tumor

The pathologic classification requires the examination of the primary carcinoma with no gross tumor at the margins of resection. A case can be classified pT if there is only microscopic tumor in a margin.

The pT categories correspond to the T categories.

Note: When classifying pT, the tumor size is a measurement of the invasive component. If there is a large in situ component (e.g. 4 cm) and a small invasive component (e.g. 0.5 cm), the tumor is coded pT1a.

pN—Regional Lymph Nodes

The pathologic classification requires the resection and examination of at least the low axillary lymph nodes (Level I) (see p. 38). Such a resection will ordinarily include six or more lymph nodes.

- pNX Regional lymph nodes cannot be assessed (not removed for study or previously removed)
- pN0 No regional lymph node metastasis
- pN1 Metastasis to movable ipsilateral axillary node(s)
  - pN1a Only micrometastasis (none larger than 0.2 cm)
  - pN1b Metastasis to lymph node(s), any larger than 0.2 cm
    - pN1bi Metastasis to 1–3 lymph nodes, any more than 0.2 cm and all less than 2.0 cm in greatest dimension
    - pN1bii Metastasis to 4 or more lymph nodes, any more than 0.2 cm and all less than 2.0 cm in greatest dimension
    - pN1biii Extension of tumor beyond the capsule of a lymph node metastasis less than 2.0 cm in greatest dimension
    - pN1biv Metastasis to a lymph node 2.0 cm or more in greatest dimension
- pN2 Metastasis to ipsilateral axillary lymph nodes that are fixed to one another or to other structures
- pN3 Metastasis to ipsilateral internal mammary lymph node(s)

pM—Distant Metastasis

The pM categories correspond to the M categories.

G Histopathologic Grading

- GX Grade of differentiation cannot be assessed
- G1 Well differentiated
- G2 Moderately differentiated
- G3 Poorly differentiated
- G4 Undifferentiated

R Classification

The absence or presence of residual tumor after treatment may be described by the symbol R. The definitions of the R classification are:

- RX Presence of residual tumor cannot be assessed
- R0 No residual tumor
- R1 Microscopic residual tumor
- R2 Macroscopic residual tumor

Pathologic classification can also be performed using a stage grouping system, which corresponds to the TNM system, as above. Stage I cancers are tumours up to 2cm in diameter and show no evidence of metastases. Stage II cancers are tumours between 2cm and 5cm in diameter and may have some involvement of the axillary nodes, but have not metastasized to distant regions. Stage III cancers are tumours of any size, where the lymph nodes are fused into an axillary mass (IIIa), or tumours where there is extension to the chest wall, or skin involvement (IIIb). Finally, stage IV cancer includes any tumour with distant metastases[149]. Depending on the stage of cancer, a woman might be recommended for a conformational biopsy.

Table 4 – Stages[11]

	Stage Grouping		
Stage 0	Tis	N0	M0
Stage I	T1(1)	N0	M0
Stage IIA (1)	T0	N1	M0
	T1	N1(2)	M0
	T2	N0	M0
Stage IIB	T2	N1	M0
	T3	N0	M0
Stage IIIA	T0	N2	M0
	T1	N2	M0
	T2	N2	M0
	T3	N1, N2	M0
Stage IIIB	T4	Any N	M0
	Any T	N3	M0
Stage IV	Any T	Any N	M1

Note: (1) T1 includes T1mic. (2) The prognosis of patients with pN1a is similar to that of patients with pN0.

1.3.5 Diagnosis of Breast Cancer

The gold standard for diagnosis of breast cancer is performing a biopsy of the sample. A biopsy is the removal of a sample of tissue, and subsequent examination under a microscope to determine the presence or absence of cancerous cells. To determine if a biopsy is needed, images of the breast must be taken to identify suspicious regions and narrow down the area from which the biopsy should be excised (see conventional breast imaging section 1.4.1). While there are various methods of biopsy, including needle core, vacuum assisted incision, and excisional methods like surgery, the most widely used by the Ontario Breast Screening Program (OBSP) are needle core biopsies.

1.3.5.i Needle Core Biopsies

Large core needle biopsies have correctly identified over 95% of carcinomas [150-152]. Often times, more than one core biopsy sample is needed for an accurate diagnosis. Large mass lesions can usually be diagnosed with 5-6 cores, whereas some smaller lesions can be completely encompassed in one core sample[153, 154]. While a core biopsy in and of itself has significant value in identifying and diagnosing a lesion, one must keep in mind that it is a sample of a larger area, and additional tissue should be reviewed for a more complete diagnosis. An atypical intraductal hyperplasia could become an in situ carcinoma after further review, and a papillary lesion may sample an area with features of ductal carcinoma in situ (DCIS). New imaging techniques, such as the ComfortScan™ system have been shown to correlate well with needle core biopsy results[155]. Any unsatisfactory, suspicious, or atypical change detected from the core biopsy should be followed by an excisional biopsy.

1.3.5.ii Excisional Biopsy

An excisional biopsy removes the tumour and some surrounding breast tissue, as compared to an incisional biopsy, which removes only a slice of usually large tumours. Normally performed in the

outpatient department of the hospital under local anaesthetic, the excisional biopsy sample gets delivered to the pathologist shortly after removal. The specimen should have particular orienting features identified, such as a localization wire[156] and radiopaque dye[157, 158], which aid in excising the appropriate area. Excisional biopsy may be preferred over disruptive techniques such as needle aspiration, or core biopsy, since these may tear the tissue and dislodge cells in the mammary stroma. Generally, dislodgement of benign cells is not of concern; however, dislodgement of in situ carcinoma cells results in diagnostic difficulty because they can mimic invasive cancer cells[159-162]. By identifying displaced cells as granulation tissue, or as coming from a hemorrhage or needle tract can help to discriminate truly invasive cells [163].

1.4 CONVENTIONAL BREAST IMAGING

Before a biopsy can be performed, a detailed image of the breast with a suspicious region of interest (ROI) must be obtained. Routine imaging of the breast will ensure early detection and treatment of any suspicious lesion. The three most popular breast imaging techniques are mammography, ultrasound and magnetic resonance imaging (MRI). Mammography is the standard practice and conventional imaging technique for routine detection of breast cancer, as outlined by the Canadian Association of Radiologists (CAR) and American College of Radiology (ACR) standards of care [164, 165]. Ultrasound is mainly used for image guided needle core biopsies and MRI is reserved for high-risk patients or hard to image patients owing to its high cost. If breast density is increased due to increased fibroglandual tissue, then the attenuation of x-rays in this normal tissue becomes comparable to that of malignant tissue, thereby precluding the successful use of mammography. In this case, MRI would be the favoured alternative.

1.4.1 Mammography

Mammography is a breast imaging technique which uses X-rays to produce images of the internal structures of the breast. The goal of routine mammographic screening is to detect breast cancer earlier and allow for more successful treatments. Because fine detail is needed to properly locate and assess

breast lesions, mammography is perfectly suited, as it produces images with high spatial resolution[149]. X-ray attenuation differences, or in other words, the contrast between normal and diseased breast tissues, are very small, so high quality mammography must enhance those differences to provide high contrast resolution[149]. In order to achieve high quality images useful in a clinical setting, many components are required. Figure 8 depicts the components of a typical mammography unit.

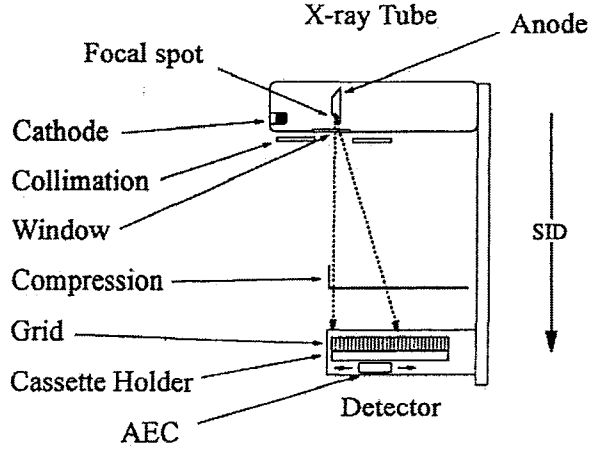

Fig. 8 – Mammography Unit [149]

This figure shows set up of a typical mammography unit. AEC represents the automatic exposure control.

Every component of the imaging sequence plays an integral role in the development of the final image, and ultimately, the detection of breast cancer[149].

1.4.1.i Breast Compression

Breast compression is required to approximate a uniform thickness for the x-ray beam to pass through to achieve optimal exposure for plain film mammography. The breast cannot be imaged in its normal conical shape because the exposure required to image the thick part of the breast nearest to the chest wall, would lead to overexposure of the thin nipple region[166]. A move toward digital

mammography would likely lessen the degree of compression required, since variations in exposure can be corrected[166]. On the other hand, a lack of compression would compromise digital images in other ways, such as increased scatter, which may preclude the reduction in compression[149]. Achieving uniform exposure is not the only reason for breast compression, and others are listed in the table below [149]. The discomfort associated with breast compression is a leading reason that women do not pursue routine mammography screening recommendations, so any procedure that could lessen the degree of compression would likely see successes in adherence to screening routines[149].

Table 5 – Reasons for Breast Compression [149]

REASONS FOR BREAST COMPRESSION
1. To hold the breast away from the chest wall, permitting the projection of all the tissues onto the detector without the interfering noise of the other structures of the thorax
2. To reduce blur due to motion by physically holding the breast motionless
3. To reduce the dose needed to image the breast by reducing the thickness of the tissue through which the radiation must pass
4. To further reduce dose and motion because the shorter exposure time needed to image a thinned structure avoids dose increases due to reciprocity law failure when using film/screen systems with long exposure times. This also reduces the likelihood of motion.
5. To separate overlapping structures, facilitating more accurate evaluation
6. To press breast structures closer to the detector to reduce blur from geometric unsharpness and improve the resolution of the system
7. To reduce image-degrading scatter
8. To produce a more uniform thickness and permit more uniform exposure
9. To permit accurate registration of images for computer reconstruction algorithms

1.4.1.ii Digital Mammography

More sophisticated methods of detection have allowed for the advance of digital mammography. The X-ray film is replaced by solid-state detectors, such as amorphous selenium, that are able to convert X-ray photon energy into electronic signals, which will be detected in a similar manner to the CCD camera, described in section 1.5.3.iii. Computer-aided detection (CAD) uses software to identify abnormal areas of the breast which may require further investigation to determine malignancy. More incoming energy, which is detected by the selenium as a result of photons passing through the tissue will

result in a higher electrical signal, and a digital image is constructed according to a corresponding range of grayscale values.

Several companies have begun to market direct digital detectors, such as ANRAD, Canon, GE and Toshiba. ANRAD offers a patented selenium layered digital detector, which boasts faster image acquisition and superior quality than traditional X-ray mammography[167], whereas General Electric (GE) uses a digital flat panel called the GE Revolution™. This cesium iodide scintillator absorbs photons and converts them to light, which enters the silicon panel and converts the light photons into an electrical charge understood by the detector[168]. Digital imaging does not create a vastly different patient experience, and has other benefits such as image manipulation, ease of storage (as compared to traditional X-ray films) and sharing of images across geography.

1.4.1.iii Radiation Dose

As photons pass through the breast tissue on their way to the film, some of the photon's energy is deposited within the tissue. The amount of energy deposition, or the amount of attenuation, is directly related to the radiation dose received by the tissue. Although it has been shown previously that levels of radiation dose for mammography screening are not of particular concern[169], the possibility of malignancies caused by increased exposure to ionizing radiation exists. The breast's exposure to radiation should be minimized as long as the image quality, and thus, detection capability, is not compromised. When delivering radiation to patients, the ALARA (as low as reasonably achievable) principles should be practiced to ensure the minimal possible dose. The ultimate dose delivered to the breast tissue is affected by several factors: i) beam energy, ii) compressed breast tissue thickness, and iii) composition of tissue, for example, the amount of fat or glandular tissue[149]. Largest beam energy results in lower interactions with tissue; whereas, compressed breast tissue allows a smaller path length for energy deposition. Different tissues absorb different amounts of energy; and thus, receive different doses[169].

Since the glandular and ductal tissues are at higher risk of developing malignancies[8] due to high cellular activities, it has been suggested by Hammerstein *et al.* [170] that dose calculations to these areas is of utmost importance. A direct *in vivo* measurement of dose is impossible, since the actual dose delivered is a function of tissue depth; however, direct measurements from a phantom material are possible and can be used to create an *in vivo* model of dose distribution[149]. The phantom material would be used to measure such factors as the half value layer (HVL). The HVL is a measure of beam energy related to the thickness of aluminum needed to attenuate the beam of photons by 50%; therefore, the larger the energy, the higher the corresponding HVL[149].

Radiation dose can be decreased; however, enough photons must still reach the detector to produce a useful image. Recall that thicker screens result in larger amounts of scatter distinguished by the film, since the produced light photons have more time to scatter before reaching the film. Scatter causes a blur in the image, which is detrimental to radiological image evaluation. If scatter in the image was not a concern, mammographic units would have very thick screens in order to detect all photons; thus, improving efficiency and minimizing patient dose. To eliminate patient dose, a high resolution imaging technique without the use of ionizing radiation would be beneficial.

1.4.2 Other Techniques

Currently, there are several other techniques besides mammography, which can be used to image the breast. Ultrasound, which uses high frequency sound waves rather than radiation, is usually used in concert with needle core biopsy to guide the needle, after a positive mammogram result. It can sometimes provide more information about a tumour, and uses the same BIRADS classification as mammography. On the other hand, magnetic resonance imaging (MRI) is reserved for higher risk patients[165], or harder to image patients due to the density of the breast tissue. While not widely used for breast cancer screening due to the exorbitant cost, MRI still provides excellent image quality through

its use of high powered magnetic fields. Electrical impedance tomography (EIT) has a variety of applications[171-175], and uses small currents to measure changes in cell membrane electrical resistivity. Cancer cells have different electrical properties than normal cells, and thus, image contrast is obtained through these differences. Positron emission tomography (PET) uses injected radioactive materials, which are preferentially metabolized by highly active cancer cells and the areas which uptake the radioactive markers appear more brightly due to the emission of photons[176]. This technique is much more invasive than the others due to the injected materials and patient dose, but can be very useful during early detection to determine the precise location of the tumour and decide the best course of treatment. As well, this process may recognize additional metastases appearing during a whole body PET scan. Finally, thermography[177] relies on the heat produced by the cells in the body and detects malignancies through higher blood volume and, therefore, higher temperature in tumours. Thermal patterns produced by this technique can aid in the early detection of breast cancer, but malignancy cannot yet be confirmed without an additional test, such as a biopsy. Table 6 compares the sensitivity, a measure of the number of correctly identified cancers, and the specificity, the number of correctly identified benign conditions, of a number of imaging techniques. A low sensitivity would result in a large number of missed cancers, whereas a low specificity would result in a large number of unneeded biopsies. Equations 1 and 2 provide the equations used to calculate sensitivity and specificity.

$$Sensitivity = \frac{(\#of\_true\_positives)}{(\#of\_true\_positives)+(\#of\_false\_negatives)} \quad (1)$$

$$Specificity = \frac{(\#of\_true\_negatives)}{(\#of\_true\_negatives)+(\#of\_false\_positives)} \quad (2)$$

Table 6 – Sensitivity and Specificity of various Breast Imaging Techniques

Imaging Modality	Sensitivity	Specificity
Mammography	95% [178]	83-88% [179]
MRI	95-100% [180]	37-97% [181]
Ultrasound	56-72% [182]	70-90% [182]
EIT	68-100% [183]	47% [184]
PET	61-93% [185]	79-80% [185]
Thermography	85% [186]	70% [186]

1.4.3 Challenges for Breast Imaging

The difficulty in breast imaging is related to its extreme sensitivity and function as a reproductive organ. Choosing the appropriate imaging technique is of utmost importance; thus, minimizing the exposure to ionizing radiation. It has been postulated that since there is resultant damage to human DNA, ionizing radiation is a cause of carcinogenesis[187]. Most desired in the breast imaging field is a safe, fast, inexpensive technique that uses non-ionizing radiation to the detection of breast lesions. The technique of choice for breast imaging should be highly sensitive and specific to reduce the number of required invasive biopsies. It is also vital that this imaging technique be able to resolve, or at least detect, tumours that are at least 2mm in diameter or less. Tumours of this size are considered to not be of a sufficient size to have begun to spread metastatically throughout the body [11].

1.5 Optical Breast Imaging

One candidate technique is optical breast imaging, which uses light to examine the vasculature of the breast tissue. Since the vasculature of fibroglandular tissue and malignant tissues are different, suspicious malignancies may be more easily identified with optical imaging than with X-ray techniques. There are

several commercially available optical breast imaging units such as: ComfortScan™[188], SoftScan™[189], CTLM-LILA™[190], who have all used optical imaging techniques in hopes of achieving better breast cancer detection.

1.5.1 Interaction of light with material

As light travels through tissue, its path length is governed by the amount of scatter and absorption that occurs. The amount of absorption is described with the absorption coefficient, μ_a, and the amount of scatter is described with the scattering coefficient, μ_s. Both quantities are measured in units of inverse length. If a material has isotropic or uniform scattering, then the scattering coefficient, μ_s, is a good measure of the scatter. Typically, biological materials do not exhibit isotropic scattering, and therefore, the reduced scattering coefficient is used. The reduced scattering coefficient is given in Equation 3.

$$\mu_s' = (1-g)\mu_s \tag{3}$$

where '*g*' provides a measure of the anisotropic properties of the tissue[191]. A highly forward scattering isotropic medium would have a *g* value of zero; however, a completely backscattering medium would have a *g* value of one.

Absorption coefficients, μ_a, vary due to the different concentrations of chromophores in the tissue. The major chromphores in skin are melanin, water, and haemoglobin [192]. Absorption in tissue can be described by Equation 4.

$$\mu_a = \varepsilon \cdot c \tag{4}$$

where μ_a is the absorption coefficient, ε is the molar extinction coefficient and *c* is the concentration of the absorbing species. There are two main types of scatter: i) Rayleigh scattering, ii) Mie scattering. Rayleigh scattering is most common in gases and results in uniform scattering. Rayleigh scattering occurs when the

particle responsible for the scattering of light is smaller in size than the wavelength of the incident light. The amount of scatter is inversely proportional to the 4th power of the wavelength of the incident light; therefore, Rayleigh scattering has a significant effect on smaller wavelengths (blue-violet region). On the contrary, Mie scattering occurs when the scattering particle is of comparable size to the incident light and results in highly forward scattering. Mie scattering would dominate over Rayleigh scattering in tissue. The difference in scattering coefficients and *g* factors was shown by Mourant *et al.* [193-195] to be caused by the differences in refractive indexes of the various cellular components, including cellular fluids, nuclei, and mitochondria. By determining the transmission and reflectance of incident light on the material, then by using reconstruction algorithms, an estimation of the absorption and scattering coefficients is made. Values of these factors typically seen in human tissue are: $5 < \mu_s < 20$ cm^{-1}, $0.01 < \mu_a < 1$ cm^{-1}, and $0.75 < g < 0.99$ cm^{-1}.

A major challenge in optical imaging is that light is highly absorbed and easily scattered in biological tissues. As a result of elevated light attenuation, two problems occur: only small amounts of light can be transmitted through the breast, and complex image reconstruction techniques must be employed. While there are some challenges, when compared to other imaging techniques, there are advantages to using near-infrared (NIR) modalities, such as a faster imaging time and lower cost. In addition, NIR allows for different methods to obtain contrast, such as using HbO_2, Hb, or blood volume.

1.5.2 Near-Infrared Imaging

Near-infrared imaging is an aspect of optical imaging which has shown promise in the field of medicine[196-209], it is a well known imaging technique which is non destructive and shown a rapid imaging time [210]. Near-infrared imaging uses wavelengths in the visible range to the mid infrared region[210]. The NIR region has been identified by the American Society of Testing and Materials (ASTM) to include wavelengths from 780 to 2526 nm, or the corresponding wave numbers 12820-3959 cm^{-1}[210].

The credit for the discovery of the NIR region was given to Herschel in 1800. Herschel used a prism to separate the electromagnetic spectrum and when examining the red region, a temperature increase was found [210]. The popularity in the use of near-infrared devices started in the 1950's[211], and by the 1960's NIRS was being more commonly used for a wide variety of applications which included: i) quality control and product testing in the pharmaceutical industry [210], meat industry for product improvement [212], or medical applications such as imaging or measuring patient oxygen saturation. In the 1980's, a shift towards NIR systems having an array of near-infrared detectors with complex readouts replaced the earlier single detector units[211].

The basic principles of NIR imaging is the measurement of the absorption and scattering properties of the tissue by the transmission of near infrared light. NIR absorption bands are normally: i) broad, ii)overlapping, iii)10-100 times weaker than the mid-IR absorption bands; thus, severely restricting sensitivity [210]. However, low absorption coefficients allow for better depth penetration, thus, the ability to image thicker samples. In imaging strongly absorbing or highly scattering samples a low absorption coefficient is invaluable.

A typical NIR spectrometer has several components: i) light source, ii) monochromator, iii) sample holder, and iv) detector. The light source is normally a tungsten halogen lamp because of its small size and ruggedness. The monochromator selects the narrow band of wavelengths of NIR light which is used for the measurement. The sample holder simply allows the sample to be centered and motionless for the experiment. The detector is used to quantify both the diffuse reflectance: the amount of reflected NIR light from the sample; and the transmittance: the amount of NIR light transmitted through the sample.

There are several types of detectors which include: silicon, indium gallium arsenide (InGaAs), and lead sulfide (PbS). Silicon detectors are small in size, fast, and have a high sensitivity in the near-infrared and short-wavelength infrared (1100-2500 nm) regions[210]. The other two types of detectors, InGaAs and PbS, are usually larger and slower compared to silicon detectors, but they are operable for a larger number

of wavelengths. The most expensive, and best detectors use both silicon and PbS to utilize the speed and size of silicon detectors but have the wavelength range of the PbS (largest wavelength range) detector.

There are several types of sources that can used, some of the more common source include: i) quartz tungsten halogen (QTH) bulbs, ii) light-emitting diodes (LEDs), or iii) lasers. LED, or broadband discrete filter photometer based instruments have a very narrow spectral range[210], usually between 50-100 nm. Specific wavelengths can also be achieved with lasers; however, lasers also offer the user a high energy that can be delivered in ultrashort pulses, beneficial for time domain photon migration (TDPM) NIR systems, one of the 3 main types of NIR imaging systems.

1.5.2.i Frequency-Domain Photon Migration (FDPM) Systems

Frequency domain photon migration systems transmit intensity modulated photons through tissue and measure the change in amplitude and phase. A large advantage of FDPN system is that an independent measure of both the absorption and scattering coefficients can be obtained by examining the change in intensity and the phase shift. Another advantage is that ambient light has minimal effect on the image quality for FDPM systems, and hence environments previously unusable for imaging, such as patient bedside, now can be used. The disadvantage of these systems is high cost.

1.5.2.ii Time Domain Photon Migration (TDPM) Systems

TDPM systems measure the intensity of time lag of pulse laser light as it passes through a material. Similar to the FDPM system described below, TDPM systems provide a measure of the both the absorption and scattering coefficients. Both coefficients can be measured, since both the time lag, and the light intensity is measured; however, the disadvantage of these systems is that they are expensive (even higher than FDPM systems).

1.5.2.iii Continuous Wave (CW) Systems

In continuous wave systems, the incident light intensity is constant with time and the resultant transmitted light intensity is measured. In this system, only the intensity is measured, and therefore, both the absorption and scattering cannot be independently measured. CW systems can be handheld and are the most commonly used in breast cancer detection systems.

The advantages of CW systems are simple instrumentation, and they are inexpensive and portable. The disadvantage of CW systems, as compared to FDPM or TDPM systems, is that there is only limited depth information possible. Since CW systems simply measure the transmitted light intensity, which is a combination of the absorption and scatter within the material, they cannot provide individual measures of both the absorption and scattering coefficients. Less optical contrast is possible, as compared to FDPM or TDPM, because of the lack of time dependent information in the CW system[213, 214]. An exciting new continuous wave NIR breast cancer detection system is the ComfortScan™, which will be discussed in detail in the next chapter.

1.5.2.iv NIR breast imaging

The use of near-infrared light in breast imaging for cancer detection is a new application compared to traditional uses of NIR light, such as spectroscopy or climatology. NIR imaging of the breast works by passing light through the breast and determining the attenuation based on the amount of transmitted light. Hemoglobin is the main attenuator of light in the NIR range, so more attenuation means more blood is present. Since tumours are highly vascularized, more attenuation in a particular area represents a higher likelihood of cancer. NIR light scanning has advantages over conventional mammography, as it uses a much lighter compression than mammography, which is favoured for patient comfort. Furthermore, NIR does not use ionizing radiation, and tissue density is no longer a factor for cancer detection.

There have been many studies involving the use of NIR light for imaging[196-209, 215-239]; many of which were simulations or phantom studies[199, 201, 202, 205, 206, 209, 220, 221, 226, 229, 230, 236]. The simulations and phantom studies served to determine the viability of the NIR imaging technique, and to improve the NIR image. Similar phantom studies need to be performed on the new ComfortScan™ NIR imaging system, to warrant its validity in a clinical setting.

1.5.3 ComfortScan™ Optical Imaging System

A novel, dynamic optical breast imaging technique, the ComfortScan™ system (XinAoMDT Technology Co., LTD, Beijing, China), was developed to be used as an adjunct to mammography in order to increase the likelihood of breast cancer detection. The ComfortScan™ system has shown promising results in previous studies[155, 240-242]. The main difference in the ComfortScan™ system is the unique method in obtaining the image contrast. The image contrast is obtained by examining difference in light transmission with and without compression. No other commercially available near infrared system uses this method for imaging construction.

The previous studies have been performed by a group in France. They have published 3 studies on the usefulness of the ComfortScan™ system[240-242]. The number of patients used in these studies was between 25 and 72. Either BIRADS 4-5 or BIRADS 3-5 were included in these studies. It was said that future work should include normal patients and, therefore, include the full BIRADS range (1-5). Depending on the study, the ComfortScan™ results were compared to mammography, ultrasound, biopsy, or MRI. In our study using the ComfortScan™ system, patients with BIRADS ratings from 1-5 were successfully imaged. Also, the total number of ComfortScan™ images included in the study was 126, which is larger than any previous publication using the ComfortScan™ system.

1.5.3.i Patient Positioning

The ComfortScan™ system, shown in Figure 9, is a light scanning technique using 640nm red light to image the breast.

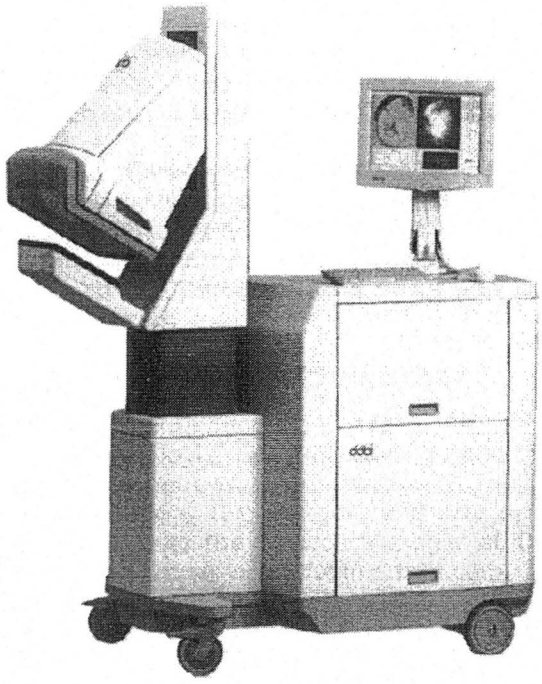

Fig. 9 – ComfortScan™ System

This figure shows the ComfortScan™ system. The patient is positioned on the left side and the technician stands to the right in front of computer monitor.

The technician positions the patient in front of the arm of the ComfortScan™ system. The arm unit can move independently up and down to accommodate different patient heights. The technician then positions the breast on the LED array, which is a square grid consisting of 127 LEDs on a platform angled 30 degrees from the horizontal. A soft air bladder is then lowered onto the top of the breast. The Charge Coupled Device (CCD) camera, located within the soft air bladder above the breast, enables cranial-caudal

imaging of the breast. A real time positioning image can be obtained to check the position of the breast, and an LED check must be performed using the ComfortScan™ software in order to ensure all the LEDs are functional, and make certain that the light intensity passing through the breast is within a normal range. Errors can occur during this LED check if the breast is either too thick (not enough light is transmitted) or too thin (too much light is transmitted). A suspicious ROI can be identified with the ComfortScan™ from a previous mammogram, and the machine will perform a more detailed analysis in this area.

1.5.3.ii Light Emitting Diodes

As are used with the ComfortScan™ LED tray, light emitting diodes (LED) are semiconductor light sources, meaning that the light is produced by the excitation of a semiconductor crystal by introducing the flow of electrical current. An LED is an example of a solid state lighting technology, which means that light is emitted from a piece of solid matter, in comparison to a gas, as in compact fluorescence. An LED is basically a light bulb that is placed in an electrical circuit. There are several advantages to use LED's rather than conventional incandescent light bulbs; LED's have: longer life span, use less electricity, lower annual operating cost, no sensitivity to low temperatures or humidity, low heat emission, and very durable. Currently, LED's are not widely used throughout homes and businesses because of the large initial capital cost.

A luminescent semiconductor is needed for an LED to work properly. A semiconductor is made of an N-type material bonded to a P-type material. An N-type material has extra electrons in the conduction band; whereas, a P-type material has extra holes for electrons to fill the valence band. The applied current across the semiconductor activates the flow of free moving electrons. Once the semiconductor is activated, the electrons will start to fill the holes in the P-type material. In filling these holes, which are at a lower energy orbital, there is excess energy which is emitted in the form of photons. The larger the drop from conduction band to valence band, the larger the energy of the emitted photon.

Below is a figure showing the electron jumping from the N-type material (or conduction band) to the P-type material (or the valance band).

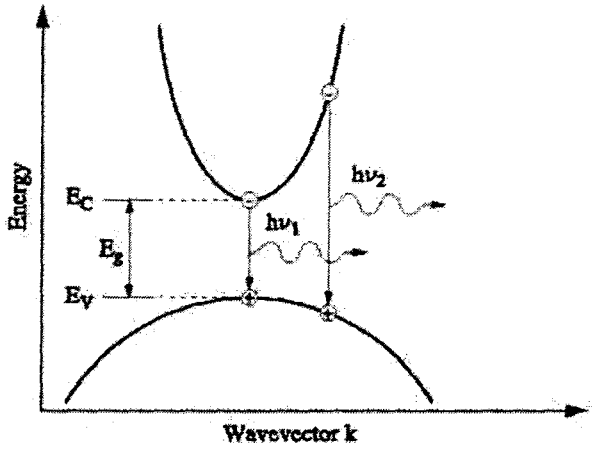

Fig. 10 – LED [243]

This figure shows the energy gap between the conduction and valence bands for N-type and P-type materials. As the drop in energy of the electron is increased, so is the energy of the emitted photon.

The energy of the emitted photon is given in the Equation 5.

$$E_c - E_v = E_g \tag{5}$$

where E_c is the energy of the electron in the conduction band, E_v is the energy of the electron in the valence band, and E_g is the energy of the emitted photon. As the energy gap, or band gap, between the conduction and valence bands increases, so does the energy of the emitted photon. The energy of the emitted photon is related to frequency, as shown in the Equation 6. A higher energy corresponds to a higher frequency (or a smaller wavelength); thus, by changing the energy of the emitted photon the colour of the produced light can be altered.

$$E = hf = \frac{hc}{\lambda} \tag{6}$$

where E is the photon energy, h is Planck's constant ($6.626*10^{-34}$ J·s), c is the speed of light, f is the frequency, and λ is the wavelength.

1.5.3.iii Charge Coupled Device

A charge coupled device (CCD) camera, such as the one within the inflatable soft-membrane of the ComfortScan™, converts received light into electrical charges through a charge coupled device, or semiconductor[244]. The CCD chip is basically an array of small sensors and each sensor is called a pixel. To improve image resolution, the amount of light a single sensor can convert must be considered. The smaller the pixel, the less signal per pixel, and if the signal drops below detectable limits, image quality would be reduced. As long as incident light intensities are high enough, a larger number of pixels are actually beneficial to improve resolution. Once a sensor has converted the maximum amount of light to electrons, the pixel on the produced image is saturated and will not provide any more useful information. The maximum number of incident photons is directly related to the size of the well available to hold the produced electrons. For the ComfortScan™ system the full well capacity is 178,000 electrons. By having sensors which convert more light, better image quality can be achieved.

Quality can be measured using the modulation transfer function (MTF), detective quantum efficiency (DQE) and dynamic range. MTF is a measure of the image resolution. The point at which no more variation in the image intensities can be detected is when the MTF is zero. Equation 7 describes how MTF is calculated.

$$MTF = \frac{I_{max} - I_{min}}{I_{max} + I_{min}} \tag{7}$$

where I_{max} is the maximum intensity, and I_{min} is the minimum intensity.

In comparison to the MTF, the DQE is a measure of the combined effects of both the signal (or intensity) and the noise. Equation 8 describes how the DQE is calculated.

$$DQE = \frac{NEQ}{Q} \tag{8}$$

where Q is the number of x-ray quanta on the detector per unit area, and NEQ, noise equivalent quanta, is a measure of the minimum number of x-ray quanta required to give a specified signal to noise ratio (SNR). The NEQ is simply a more complete description of SNR. Dynamic range is yet another way to measure the quality of an image, and it is the difference between the minimum and maximum detectable values in question. All of the above variables describe different measures of quality and it is important to understand which variable is being measured when reporting 'higher quality' images.

The amount of electrical charge produced is proportional to the amount of light, or photons, received by a sensor. The electrical charge is then converted to a digital signal by using an analog-to-digital converter (ADC), which has a set number of bits. The ADC affects the image resolution by determining the number of available unique brightness output values. The larger the number of bits in the ADC, the larger the number of unique output values. In the ComfortScan™ system the ADC has 12 bits, which corresponds to a resolution of 4096 levels. Through the use of the CCD technology, such as with the ComfortScan™, high quality, low noise images are created. Figure 11 depicts a CCD device and demonstrates its function.

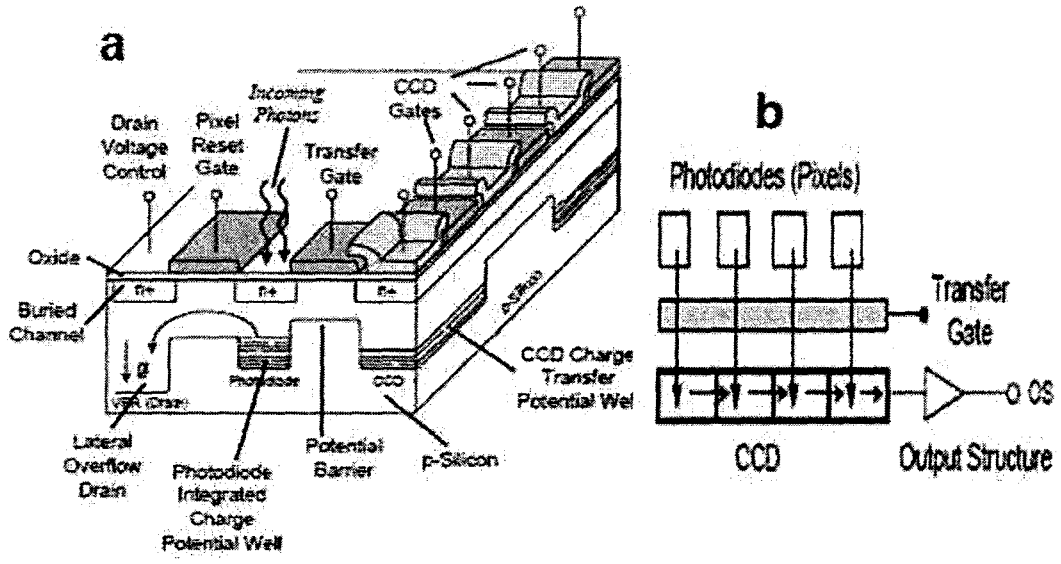

Fig. 11 – Charge Coupled Device[244]

Part 'a' shows the detailed anatomy of a CCD sensor. Part 'b' shows a simplified block diagram of the CCD architecture.

1.5.3.iv Scanning and Analysis

The scan utilizes the LEDs to pass 640 nm light through the breast and detects the transmitted light with a sensitive CCD camera. As the scan starts, a soft air bladder, made of thin silicon, is inflated to apply gentle pressure (5 mmHg) during the first 15 seconds of the scan. The pressure steadily increases to 10 mmHg and images were taken for the next 30 seconds. During the last part of the scan, pressure slowly decreases back to 5 mmHg. A total of 45 images are taken during the 60 second scan.

A dynamic signature for every pixel is obtained using Equation 9.

$$DS(x,y,t) = \frac{I(x,y,t) - I_{ref}(x,y)}{I_{ref}(x,y)} \qquad (9)$$

where $DS(x,y,t)$ is the dynamic signature used for image production, $I(x,y,t)$ is the intensity of transmitted light at various x and y coordinate positions in the image at a certain time point, and $I_{ref}(x,y)$ is the transmitted light intensity at various x and y coordinate positions in the image during the non compression phase of the

imaging sequence. This dynamic signature is intended to highlight changes in light transmission from the reference image, resulting from changes in pressure of the breast.

The dynamic signature is used to produce all 45 images; these images are then shown by the image analysis software as a video. A colour scale can be applied to the range of dynamic signatures to allow for easier image analysis. Green areas correspond to a relatively stable dynamic signature over time, whereas an area of red represents a highly increasing dynamic signature with time. Purple areas represent an highly decreasing dynamic signatures with time. The dynamic signature is related to the increase or decrease in light attenuation with time, which is directly correlated to the volume of blood at a given position. For example, a highly decreasing dynamic signature represents an area where the transmitted light becomes highly attenuated with time. By convention, the image analysis software displays the pressure as decreasing with respect to time. Videos produced from image analysis show how the dynamic signatures change with respect to time; the more purple an area becomes, the higher the likelihood of malignancy. The manufacturer of ComfortScan™ suggests a range of characteristics as indicators of malignancy. Based on these characteristics, a rating scale provided by the manufacturer extending from DOBI 0 to DOBI 5 can be assigned to each suspicious region in an image by a radiologist. Table 7 shows how these DOBI ratings are determined.

Table 7 – Determination of DOBI Ratings

	Benign	Probably Benign	Indeterminate	Probably Malignant	Malignant
Location (Proximity to: nipple and ROI from mammogram)	No blue near the suspicious ROI from mammogram			Blue area is located directly at ROI from mammogram	
Space (Spatial Characteristics)			Diffuse flat blue at ROI	Focal peaked blue at ROI	
Time (Temporal characteristics using ROI curve)		Strong upward trend	Wavy with amplitude 0 to -2	Downward trend with amplitude -2 to -4	Downward trend with amplitude more negative than -4
Context (Lesion Curve vs. Reference Curve)		Very similar curves that are above the x-axis (amplitudes greater than 0)	Variable curve throughout background Lesion not distinctly different	Very dissimilar pattern of curves with consistent background Diverging curves	

Table 7 describes 4 different categories for image evaluation: i) location, ii) space, iii) time, and iv) context. The 'location' characteristic evaluates the proximity of any blue/purple area near the suspicious ROI obtained from a positive mammogram. The 'space' characteristic evaluates if the blue/purple colour is peaked in one precise location or is spread over a larger area. The 'time' characteristic evaluates the extent of the percentage change in the dynamic signature spectrum of the suspicious ROI and a reference area. The 'context' characteristic compares the dynamic signature of the suspicious ROI and the reference area to determine likelihood of malignancy.

Analysis of ComfortScan™ images should be performed by an experienced radiologist, with at least 5 years of experience in breast imaging. In order to compare the DOBI rating scheme to the BI-RADS classification used in mammography, the two scales must be aligned, or normalized. Wilson *et.al* [155] have suggested an adjusted system and carefully aligned the two classifications. This conversion system is shown in Table 3 (section 3.2.4). The higher adjusted rating, the higher the probability of malignancy. A normalized rating of 1 or 2 is benign, and a rating of 3 or 4 would be malignant.

1.6 SUMMARY

A thorough understanding of breast imaging requires an insight into breast biology in order to understand the current limitations of mammography. Early detection of breast cancer results in a higher likelihood of a successful treatment outcome[44]. Using complimentary imaging modalities to mammography increases the sensitivity and specificity of the imaging procedure, and allows for better detection and diagnosis of breast cancer. Optical imaging measures small changes in the vasculature to provide a measure of the likelihood of an abnormality. Specifically, the ComfortScan™ system uses an additional process to further enhance contrast. The additional contrast method is achieved by applying pressure to the breast, and examining any resultant changes in deoxygenation that occur due to the partial collapse of the breast vasculature during compression. The partial collapse of vasculature provides a unique dynamic signature throughout the breast, which can be useful information when determining breast cancer risk. The future of breast imaging is exciting and promising, since the ability to detect breast cancer earlier with a non-ionizing, inexpensive, portable imaging modality is advantageous. Considering the incidence of breast cancer is on the rise, optical imaging brings a new light to the current breast cancer imaging modalities.

1.7 OBJECTIVES OF CURRENT STUDY

[I] To investigate whether performing a large clinical trial with the ComfortScan™ system would be warranted to further patient care and diagnostics for breast imaging.

[II] To determine if the ComfortScan™ system will achieve better correlation to biopsy than with mammography alone.

[III] To determine if the ComfortScan™ system would be beneficial as a mainstream method for a radiologist to diagnose breast cancer risk.

[IV] To evaluate the potential use of PVA-C as a breast mimicking material.

[V] To validate the suggested mode of action of the ComfortScan™ system for detection of malignancies.

1.8 THESIS OUTLINE

This thesis consists of several bodies of work that have been or will be submitted for publication. The introduction, Chapter 1, of this thesis will be modified to include a more thorough review of current and future breast imaging techniques and has been invited to be published in Critical Reviews of Biomedical Engineering. This chapter should provide the needed background on breast anatomy, breast cancer, and various breast imaging modalities to fully understand the body of this thesis.

The body of the thesis consists of 3 chapters. The first is Chapter 2: A pilot study investigating the potential use of dynamic optical breast imaging in breast cancer detection. Chapter 2 uses the ComfortScan™ imaging system to determine the appropriateness of performing a large scale clinical trial. Chapter 2 addresses objective [I]. Chapter 2 has been accepted with revision to Canadian Association of Radiologists Journal as a technical note. The subsequent chapter is Chapter 3: Dynamic optical breast imaging in breast cancer detection. Chapter 3 uses 126 ComfortScan™ images to determine if this system should be used in routine clinical setting to assist in breast cancer detection. Chapter 3 addresses objectives [II] and [III]. The third is Chapter 4: Use of polyvinyl alcohol cryogel as a tissue mimicking phantom for use in near-infrared imaging. Chapter 4 investigates the potential use of PVA-C as a tissue mimicking

phantom and uses PVA-C in the validation of the proposed mode of action of the ComfortScan™ system by DOBI Medical International. Chapter 4 addresses objectives [IV] and [V].

Chapter 5 is a summary of the entire thesis. Important conclusions are reiterated and discussed. In addition, commentary is provided on the potential of the widespread use of the ComfortScan™ system and future directions of the thesis work.

Appendix I and II are manuscripts written by the authors on the properties of PVA-C, a phantom material used in the thesis. These chapters are to provide background knowledge and supplement the reader's understanding of the thesis. Appendix I has been accepted with revisions in Magnetic Resonance Materials Physics, Biology and Medicine.

1.9 REFERENCES

1. Society, C.C. *Breast Cancer Statistics.* 2010 [cited; Available from: www.cancer.ca.
2. Yalom, M., *A history of the Breast.* 1997, New York: Alfred A Knopf.
3. Ackerknecht, E., *History and geography of the most important diseases.* 1965, New York: Hafner Publishing. 162-173.
4. Cooper, W., *The history of the radical mastectomy.* Ann Med History, 1941. **3**: p. 36-53.
5. DeMoulin, D., *A short history of breast cancer.* 1983, Boston: Martinus Nijhoff.
6. Lewison, E., *The surgical treatment of breast cancer: an historical and collective review.* Surgery, 1953. **34**: p. 904-953.
7. Mansfield, C., *Early breast cancer: its history and results of treatment.* Experimental biology and medicine: monographs on interdisciplinary topics, ed. W. A. Vol. 5. 1976, New York: Karger. 2-22.
8. Donegan, W. and J. Spratt, *Cancer of the Breast.* 5th ed. 2002, Toronto: Saunders.
9. IARC. *IARCHandbooks of Cancer Prevention: Breast Cancer Screening.* Screening Techniques [cited.
10. Amenta, P., *Elias-Pauly's histology and human microanatomy.* 1986, New York.
11. Tavassoli, F., *Pathology of the breast.* 2 ed. 1999, Stanford: Appleton & Lange.
12. Siegel, B., et al., *Carcinoma of aberrant breast tissue.* Contemporary Surgery, 1990. **36**: p. 42-44.
13. Loughry, C., *Breast volume measurement of 598 women using biostereometric analysis.* Ann Plastic Surgery, 1989. **22**: p. 380-385.
14. Malini, A., E. Smith, and G. JM, *Measurement of breast volume by ultrasound during normal menstrual cycles and with oral contraceptive use.* Obstet Gynecol, 1985. **66**(4): p. 538-541.
15. Fowler, E., *Cyclic changes in composition and volume of the breast during the menstrual cycle, measured by magnetic resonance imaging.* Br J Ostet Gynaecol, 1991. **97**: p. 595-602.
16. Bowers, D. and C. Radlauer, *Breast cancer of prophylactic subcutaneous mastectomies and reconstruction with Silastic prostheses.* Plast Reconstr Surgery, 1969. **44**: p. 541.
17. Goldman, L. and R. Glodwyn, *Some anatomical considerations of subcutaneous mastectomy.* Plast Reconstr Surgery, 1973. **51**: p. 501.

18. Goodnight, J.Q., IM and D. Morton, *Failure of subcutaneous mastectomy to prevent the development of cancer.* Journal Surg Oncol, 1984. **26**: p. 198-201.
19. Cunningham, L., *The anatomy of the arteries and veins of the breast.* J Surg Oncol, 1977. **9**: p. 71-85.
20. Fisher, E. and B. Fisher, *Number of lymph nodes examined and the prognosis of breast carcinoma.* Surgery Gynecol Obstet, 1970. **131**: p. 79-88.
21. Pickren, J., J. Rube, and H. Auchincloss, *Modification of conventional radical mastectomy: a detailed study of lymph node involvement and follow-up information to show its practicality.* Cancer, 1965. **18**: p. 942.
22. Fisher, B., *Prospects for the control of metastases.* Cancer, 1969. **24**: p. 1263.
23. Fisher, B. and E. Fisher, *The interrelationship of hematogenous and lymphatic tumor cell dissemination.* Surg Gynecol Obstet, 1966. **122**: p. 791.
24. Fisher, E. and B. Fisher, *Experimental studies of factors influencing development of hepatic metastses: XVII, role of thyroid.* Cancer Research, 1966. **26**: p. 2248.
25. Fisher, E. and B. Fisher, *Local lymphoid response as an index of tumor immunity.* Arch Pathol, 1972. **94**: p. 137.
26. Taback, B., *Detection of occult metastatic breast cancer cells in blood by a multimolecular marker assay: correlation with clinical stage of disease.* Cancer Research, 2001. **61**(24): p. 8845-8850.
27. Brown, R., *Relactation with reference to application in developing countries.* Clin Pediatr, 1978. **17**: p. 333.
28. Rosner, M., *Galactorrhea in men.* Journal of the American Medical Association, 1979. **1**: p. 1327.
29. Houdbine, L., *Role of progesterone in the development and activity of the mammary gland.* Progesterone and progestins, ed. C. Bardin, E. Milgrom, and P. Mauvais-Jarvis. 1983, New York: Raven Press. 297-319.
30. Kuhn, N., *Lactogenesis: the search for trigger mechanisms in different species.* Zool Soc London, 1977. **41**: p. 165.
31. Delvoye, P., *The influence of the frequency of nursing and of previous lactation experience on serum prolactin in lactating mothers.* J Biosoc Sci, 1997. **9**: p. 447.
32. Hiba, J., *Hormonal mechanism of milk secretion in the newborn.* Journal of Clinical Endocrinology Metabolism, 1997. **44**: p. 973.
33. Franks, S., R. Kiwi, and J. Nabarro, *Pregnancy and lactation after pituitary surgery.* Br Med J, 1997. **1**: p. 882.
34. Iqbal, M., *Effects of antidepressants during pregnancy and lactation.* Ann Clin Psychiatr, 1999. **11**(4): p. 237-256.
35. Larimore, W. and K. Petrie, *Drug use during pregnancy and lactation.* Primary Care, 2000. **27**(1): p. 35-53.
36. Mitchell, J., *Use of cough and cold preparations during breast feeding.* J Human Lactation, 1999. **15**(4): p. 347-349.
37. Jenness, R., *The composition of human milk.* Semin Perinatol, 1979. **3**: p. 225.
38. Luick, J. and J. Mazrimas, *Biological effects of ionizing radiation on milk synthesis. Effects on milk lipase, esterase, alkaline phosphatase and lactoperoxidase activities 2 III.* Journal of Dairy Science, 1966. **49**(12): p. 1500-1504.
39. Ogita, S., et al., *Effects of far-infrared radiation on lactation.* Ann Physiol Anthropol, 1990. **9**(2): p. 83-91.
40. Helewa, M., et al., *Breast cancer, pregnancy, and breastfeeding.* J Obstet Gynaecol Can, 2002. **24**(2): p. 164-180.
41. Collaborative_Group_on_Hormona_Factors_in_Breast_Cancer, *Breast cancer and breastfeeding: collaborative reanalysis of individual data from 47 epidemiological studies in 30 countries, including 50302 women with breast cancer and 96973 women without the disease.* Lancet, 2002. **July 20: 360**(9328): p. 187-195.
42. Loof-Johanson, M., et al., *Breastfeeding and pronostic markers in breast cancer.* Breast, 2010(Epub Sept 17th).
43. Scott-Conner, C. and S. Schorr, *The diagnosis and management of breast problems during pregnancy and lactation.* Am J Surg, 1995. **170**(4): p. 401-405.

44. Canadian_Cancer_Society_Website. *Breast Cancer Statistics.* 2010 [cited November 2010]; Available from: http://www.cancer.ca/canada-wide/about%20cancer/cancer%20statistics/stats%20at%20a%20glance/breast%20cancer.aspx.
45. American_Cancer_Society. *Breast Cancer: Early Detection -The importance of finding breast cancer early.* 2010 [cited November 2010]; Available from: http://www.cancer.org/Cancer/BreastCancer/MoreInformation/BreastCancerEarlyDetection/breast-cancer-early-detection-importance-of-finding-early.
46. Huseby, R. and L. Thomas *Histological and histochemical alterations in the normal breast tissues of patients with advanced breast cancer being treated with estrogenic hormones.* Cancer, 1954. **7**: p. 54-74.
47. Abrams, A., *Use of vitamin E in chronic cystic mastitis.* N Engl J Med, 1965. **272**: p. 108-1081.
48. Ahmed, A., *Aprocrine metaplasia in cystic hyperplastic mastopathy. Histochemical and ultrastructural observations.* J Pathol, 1975. **115**: p. 211-214.
49. Anastassiades, T., E. Tsakraklides, and J. Gogas, *The histology of fibrocystic disease of the female breast.* Path Res Pract, 1981. **172**: p. 109-129.
50. Anderson, A., J. Larsen, and O. Steenstrup, *Effect of bromocriptine on the premenstrual syndrome. A double blind clinical trial.* Br J Obstet Gynaecol, 1977. **84**(370-374).
51. Angeli, A., H. Bradlow, and L. Dogliotti, *Endocrinology of cystic breast disease.* 1983, New York: Raven Press.
52. Archer, F. and M. Omar, *The fine structure of fibroadenoma of the human breast.* J Pathol, 1969. **99**: p. 113-117.
53. Ariel, I., *Envoid therapy (norethynodrel with mestranol) for fibrocystic disease.* Am J Obstet Gynecol, 1973. **117**: p. 453-468.
54. Azzopardi, J., *Problems in Breast Pathology.* 1979, Philadelphia: WB Saunders. 57-72.
55. Bartow, S., W. Black, and R. Waeckerlin, *Fibrocystic disease: A continuing enigma.* Path Annu, 1982. **17**: p. 93-111.
56. Barwick, K., M. Kashgarian, and P. Rosen, *Clear cel change within duct and lobular epithelium of the human breast.* Path Annu, 1982. **17**: p. 319-328.
57. Bassler, R., *Pathologie der BrustDruse.* 1978, Berlin: Springer-Verlag.
58. Birkett, J., *The disease of the breast.* 1850, London: Longman & Co.
59. Blackmore, W., *Danazol in the treatment of benign breast disease.* J Int Med Res, 1977. **5**: p. 101-108.
60. Blichert-Toft, M., A. Anderson, and O. Henriksen, *Treatment of mastalgia with bromocriptine: A double bind crossover study.* Br Med J, 1979. **1**: p. 237.
61. Bloodgood, J., *The pathology of cronic cystic mastitis of the female breast with special consideration of the blue-domed cysts.* Arch Surg, 1921. **3**: p. 445-542.
62. Brinton, L., M. Vessey, and R. Flavel, *Risk factors for benign breast disease.* Am J Epidemiol, 1981. **113**: p. 203-214.
63. Brodie, B., *Lectures on sero-cystic tumors of the breast.* London Med Gaz, 1846. **25**: p. 808.
64. Bryant, T., *The diseases of the breast.* 1887, London: Cassel & Co.
65. Cowan, D. and T. Herbert, *Involution of the breast in women aged 50 to 104 years: A histopathologic study of 102 cases.* Surg Pathol, 1989. **2**: p. 323-333.
66. David, H., M. Simons, and J. Davis, *Cystic disease of the breast: Relationship to carcinoma.* Cancer, 1932. **17**: p. 957-978.
67. Davis, H., M. Simons, and J. Davis, *Cystic disease of the breast: Relationship to carcinoma.* Cancer, 1964. **17**: p. 957-978.
68. Devitt, J., *Fibrocystic disease of the breast is not premalignant.* Surg Gynecol Obstet, 1972. **134**: p. 803-806.
69. Dixon, J., *Cystic disease and fibroadenoma of the breast: Natural history and relation to breast cancer risk.* Br Med Bull, 1985. **72**: p. 190-192.

70. Dixon, J., *Cystic disease and fibroadenoma of the breast: Natural history and relation to breast cancer risk.* Br Med Bull, 1991. **47**(258-271).
71. Dupont, W. and D. Page, *Risk factors for breast cancer in women with proliferative disease.* N Engl J Med, 1985. **312**: p. 146-151.
72. Dupont, W. and D. Page, *Relative risk of breast cancer varies with tim esince diagnosis of atypical hyperplasia.* Hum Pathol, 1989. **20**: p. 723-725.
73. Durning, P. and R. Sellwod, *Bromocriptine in severe cyclical breast pain.* Br J Surg, 1982. **69**: p. 248-249.
74. Eldar, S., M. Meguid, and J. Beatty, *Cancer of the breast after prophylactic subcutaneous mastectomy.* Am J Surg, 1984. **148**: p. 692-693.
75. Erb, H. and A. Kallenberger, *The action of an oral high dosed oestrogen-progestogen combination on the human breast.* Acta Endocrinol, 1972. **70**: p. 143-155.
76. Foote, F. and F. Stewart, *Comparative studies of cancerous versus noncancerous breast.* Ann Surg, 1945. **121**: p. 197-222.
77. Frantz, V., J. Pickren, and G. Melcher, *Incidence of chronic cystic disease in so-called 'normal breasts.' A study based on 225 postmortem examinations.* Cancer, 1951. **4**: p. 762-783.
78. Geschikter, C., *Diseases of the breast: Diagnosis-pathology treatment.* 2nd ed. 1945, Philadelphia: JB Lippincott. 723-732.
79. Goldman, L. and R. Goldwyn, *Some anatomical considerations of subcutaneous mastectomy.* Plast Reconstr Surg, 1973. **51**: p. 501-505.
80. Golinger, R., *Hormones and the pathophysiology of fibocystic mastopathy.* Surg Gynecol Obstet, 1978. **146**: p. 273-281.
81. Greenblatt, R., W. Dmowski, and V. Mahesh, *Clinical studies with an antigonadotropin-danazol.* Fertil Steril, 1971. **22**: p. 102-112.
82. Haagensen, C., *The relationship of gross cystic disease of the breast and carcinoma.* Surgery, 1977. **185**: p. 375-376.
83. Haagensen, C., *Diseases of the breast.* 1986, Philadelphia: WB Saunders. 250-266.
84. Harrington, E. and G. Lesnick, *The association between gross cysts of the breast and breast cancer.* Breast, 1980. **7**: p. 13-17.
85. Hitchinson, W., D. Thomas, and W. Hamlin, *Risk of breast cancer in women with benign breast disease.* J Natl Cancer Inst, 1980. **65**: p. 13-20.
86. Huseby, R. and L. Thomas, *Histological and histochemical alterations in the normal breast tissues of patients with advanced breast cancer being treated with estrogenic hormones.* Cancer, 1954. **7**(54-74).
87. Hutter, R., *Consensus Meeting: Cancer committee of the college of american pathologists: Is 'fibrocystic disease' of the breast precancerous?* Arch Pathol Lab Med, 1986. **110**: p. 171-173.
88. Jones, B. and J. Bradbeber, *The presentation and progress of macroscopic breast cysts.* Br J Surg, 1980. **67**: p. 669-671.
89. Kier, L., R. Kickey, and W. Keettel, *Endocrine relationships in benign lesions of the breast.* Ann Surg, 1952. **135**: p. 782-790.
90. Kodlin, D., E. Winger, and N. Morgenstern, *Chronic mastopathy and breast cancer.* Cancer, 1977. **39**: p. 2603-2607.
91. Lafaye, C. and B. Aubert, *Action de la pregesterone lecale dans les mastopathies benignes.* J Gynecol Obstet Biol Reprod, 1978. **7**: p. 1123-1139.
92. Leis, H., *Fibrocystic disease of the breast.* J Med Assoc Alabama, 1962. **32**: p. 97-104.
93. Leis, H., *Diagnosis and treatment of breast lesions.* 1970, New York: Medical Examinations Publishing Co.
94. Leis, H. and C. Kwon, *Fibrocystic disease of the breast.* J Reprod Med, 1979. **22**: p. 291-296.
95. London, R., G. Sundaram, and P. Goldstein, *Medical management of mammary dysplasia.* Obstet Gynecol, 1982. **59**: p. 519-523.

96. Mansel, R., P. Preece, and L. Hughes, *A double blind trial of the prolactin inhibitor bromocriptine in painful benign breast disease.* Br J Surg, 1978. **65**: p. 724-727.
97. Mauvais-Jarvis, P., N. Sterkers, and F. Kuttenn, *Traitement des mastopathies benignes par la progesterone, et les progestatifs.* J Gynecol Obstet Biol Reprod, 1978. **7**: p. 477-484.
98. Minkowitz, S., H. Hedayati, and S. Millar, *Fibrous mastopathy. A clinical histopathologic study.* Cancer, 1973. **32**: p. 913-916.
99. Minton, J., M. Poecking, and D. Webster, *Response of fibrocystic disease to caffeine withdrawal and correlation of cyclic nucleotides with breast disease.* Am J Obstet Gynecol, 1979. **135**: p. 157-158.
100. Mongeau, C., P. Madarnas, and L. Majem, *Risk of invasive breast carcinoma in patients with fibrocystic disease. Pathological and epidemiological study.* Path Res Pract, 1987. **182**: p. 528.
101. Niebergs, H., *Cancer Detection and Prevention.* 1977, New York: Marcel Dekker Inc.
102. Page, D., *Cancer risk assessment in benign breast biopsies.* Hum Pathol, 1986. **17**: p. 871-874.
103. Page, D., R. Jensen, and W. Dupont, *Papillary apocrine change of the breast - Cancer risk indication.* Lab Invest, 1994. **70**: p. 26A.
104. Page, D., R. Vander Zwag, and L. Rogers, *Relation between component parts of fibrocystic disease complex and breast cancer.* J Natl Cancer Inst, 1978. **61**: p. 1055-1063.
105. Pastides, H., J. Kaysey, and V. LiVolsi, *Oral contraceptive use and fibrocystic breast disease with special reference to its histopathology.* J Natl Cancer Inst, 1983. **71**: p. 5-9.
106. Pennisi, V., *Subcutaneous mastectomy and fibrocystic disease of the breast.* Clin Plast Surg, 1976. **3**: p. 205-216.
107. Renieri, N., C. Stavropoulos, and X. Kappelou, *Fibrocystic disease of the breast and HLA antigens.* Path Res Pract, 1984. **179**: p. 59-60.
108. Ricciardi, I. and A. Ianniruberto, *Tamoxifen-induced regression of benign breast lesions.* Obstet Gynecol, 1979. **54**: p. 80-84.
109. Roberts, M., V. Jones, and R. Elton, *Risk of breast cancer in women with a history of benign disease of the breast.* Br Med J, 1984. **228**: p. 275-278.
110. Shaaban, M., F. Morad, and A. Hassad, *Treatment of fibrocystic mastopathy by an antiestrogen, tamoxifen.* Int J Gynaecol Obstet, 1980. **18**: p. 348-350.
111. Silverberg, S., A. Chitale, and S. Levitt, *Prognostic implications of fibrocystic dysplasia in breasts removed for mammary carcinoma.* Cancer, 1972. **29**: p. 574-580.
112. Sitruk-Ware, R., N. Sterkers, and P. Mauvais-Jarvis, *Benign breast disease.* Obstet Gynecol, 1979. **53**: p. 457-460.
113. Temple, E., R. Lindsay, and E. Magi, *Technical considerations for prophylactic mastectomy in patients at high risk for breast cancer.* Am J Surg, 1991. **161**: p. 413-415.
114. Tobiassen, J., T. Rasmussen, and A. Doberl, *Danazol treatment of severly symptomatic fibrocystic breast disease and long term follow-up - The Hjorring project.* Acta Obstet Gynecol Scand, 1984. **123**: p. 159-176.
115. Trapido, E., L. Brinton, and C. Schairer, *Estrogen replacement therapy and benign breast disease.* J Natl Cancer Inst, 1984. **73**: p. 1101-1105.
116. Vassar, P. and C. Culing, *Fibrosis of the breast.* Arch Pathol, 1959. **67**: p. 128-133.
117. Veronesi, V. and G. Pizzocaro, *Breast cancer in women subsequent to cystic disease of the breast.* Surg Gynecol Obstet, 1968. **126**: p. 529-534.
118. Vina, M. and C. Wells, *Clear cell metaplasia of the breast: A lesion showing eccrine differentiation.* Histopathology, 1989. **15**: p. 85-92.
119. Vorherr, H., *Fibrocystic breast disease: Pathophysiology, pathomorphology, clinical picture, and management.* Am J Obstet Gynecol, 1986. **154**: p. 161-179.
120. Warren, S., *Relation of chronic mastitis to carcinoma of the breast.* Surg Gynecol Obstet, 1940. **71**: p. 257-273.
121. Ciampa, L. *CNN Food Central Dietitians look at health effects of coffee.* CNN Health 1999 [cited 2010 November]; Available from: http://articles.cnn.com/1999-10-

21/health/9910_21_coffee.health_1_caffeine-intake-three-cups-full-strength-coffee?_s=PM:FOOD.

122. Mann, D. *Study: Chocolate and depression go hand in hand.* 2010 [cited 2010 November]; Available from: http://articles.cnn.com/2010-04-26/health/chocolate.depression_1_chocolate-consumption-depressed-people-chocolate-cake-batter?_s=PM:HEALTH.
123. Vartanian, L., M. Schwartz, and K. Brownell, *Effects of soft drink consumption on nutrition and health: a systematic review and meta-analysis.* American Journal of Public Health, 2007. **97**(4): p. 667-675.
124. Jensen, R., D. Page, and W. Dupont, *Invasive breast cancer risk in women with sclerosing adenosis.* Cancer, 1989. **64**: p. 1977-1983.
125. Rosen, P., *The pathological classification of human mammary carcinoma: Past, present and future.* Ann Clin Lab Sci, 1979. **9**: p. 144-156.
126. World Health Organization, H., *Histologic typing of breast tumors, International histologic classification of tumors.* 1981, Geneva: World Health Organization. 19.
127. Azzopardi, J., *Problems in breast pathology.* 1979, Philadelphia: WB Saunders. 244-274.
128. Page, D. and T. Anderson, *Diagnostic histopathology of the breast.* 1987, New York: Churchill Livingstone. 198-205.
129. Ellis, I., M. Galea, and N. Broughton, *Pathological prognostic factors in breast cancer. II. Histological type. Relationship with survival in a large study with long term follow up.* Histopathology, 1992. **20**: p. 479-489.
130. Fisher, E., R. Gregorio, and B. Fisher, *The pathology of invasive breast cancer. A syllabus derived from findings of the national surgical adjuvant breast project.* Cancer, 1975. **36**: p. 1-85.
131. Fisher, E., C. Redmond, and B. Fisher, *Pathologic findings from the national surgical adjuvant breast and bowel projects (NSABP). Prognostic discriminant for 8 year survival for node-negative invasive breast cancer patients.* Cancer, 1990. **65**: p. 2121-2128.
132. Rosen, D., D. Bell, and T. Flotte, *Pathological predictors of recurrence in stage 1 (T1N0M0) breast cancer.* Am J Clin Pathol, 1982. **788**: p. 817-820.
133. Gallager, H. and J. Martin, *An orientation to the concept of minimal breast cancer.* Cancer, 1971. **28**: p. 1505-1507.
134. Kurtz, J., J. Jacquemier, and J. Thorhorst, *Conservation therapy for breast cancers other than infiltrating ductal carcinoma.* Cancer, 1989. **63**: p. 1630-1635.
135. Wise, L., A. Mason, and L. Ackerman, *Local excision and irradiation: An alternative method for the treatment of early mammary cancer.* Ann Surg, 1971. **174**: p. 392-401.
136. Cedermark, B., J. Askergren, and A. Alveryd, *Breast conserving treatment for breast cancer in Stockholm, Sweden.* Cancer, 1984. **53**: p. 1253-1255.
137. Fisher, B., M. Bauer, and R. Margolese, *Five-year results of a randomized clinical trial comparing total mastectomy and segmental mastectomy with or without radiation in the treatment of breast cancer.* N Engl J Med, 1985. **312**: p. 665-673.
138. Sarrazin, D., M. Le, and J. Rouesse, *Conservative treatment versus mastectomy in breast cancer tumors with macroscopic diameter of 20 millimeters or less. The experience of the Institut GustaveRoussy.* Cancer, 1984: p. 1209-1213.
139. Veronesi, U., A. Banfi, and B. Salvadori, *Comparing radical mastectomy with quadrantectomy, axillary dissection, and radiotherapy in patients with small cancers of the breast.* N Engl J Med, 1990. **305**: p. 6-11.
140. Overgaard, M., P. Hansen, and J. Overgaard, *Postoperative radiotherapy in high risk premenopausal women with breast cancer who receive adjuvant chemotherapy.* N Engl J Med, 1997. **337**: p. 949-955.
141. NIH Consensus Conference, I. *Treatment of early-stage breast cancer.* 1991: JAMA.
142. Anscher, M., P. Jones, and L. Prosnitz, *Local failure and margin status in early stage breast carcinoma treated with conservation surgery and radiation therapy.* Ann Surg, 1993. **218**: p. 22-28.
143. Thomadsen, B.R., et al., *Anniversary Paper: Past and current issues, and trends in brachytherapy physics.* Medical Physics, 2008. **35**(10): p. 4708-4723.

144. Landis, S., et al., *Cancer Statistics.* Cancer J Clin, 1999. **49**: p. 8-31.
145. Neal, M. and B. Simpson, *Diseases of the male breast.* J Mo State Assoc, 1930. **27**: p. 565-570.
146. Holleb, A., H. Freeman, and J. Farrow, *Cancer of the male breast, Parts I and II.* N Y J Med, 1968. **68**: p. 544-656.
147. Chen, Z., D. Wen, and W. Coulson, *Occult metastases in the axillary lymph nodes of patients with breast cancer node negative by clinical and histologic examination and conventional histology.* Dis Markers, 1991. **9**: p. 239-248.
148. Danforth, D., A. Lichter, and M. Lippmann, *The diagnosis of breast cancer.* 1988, Philadelphia: WB Saunders. 50-94.
149. Kopans, D., *Breast imaging.* 3rd ed. 2007, Philadelphia: Lippincott Williams & Wilkins.
150. Elvecrog, E., M. Lechner, and M. Nelson, *Nonpalpable breast lesions: Correlation of stereotaxic large-core needle biopsy and surfical biopsy results.* Radiology, 1993. **188**(435-455).
151. Gardecki, T., B. Hogbin, and D. Melcher, *Aspiration cytology in the preoperative management of breast cancer.* Lancet, 1980. **2**: p. 790-792.
152. Liberman, L., D. Dershaw, and P. Rosen, *Stereotaxic core biopsy of breast carcinoma: Accuracy at predicting invasion.* Radiology, 1995. **194**: p. 379-381.
153. Liberman, L., D. Dershaw, and P. Rosen, *Stereotaxic 14-gauge breast biopsy: How many core biopsy specimens are needed?* Radiology, 1994. **192**(793-795).
154. Mikhail, R., R. Nathan, and M. Weiss, *Stereotactic core needle biopsy of mammographic breast lesions as a viable alternative to surgical biopsy.* Ann Surg Oncol, 1994. **1**: p. 363-367.
155. Wilson, K., et al., *Pilot Study Investigating the Potential use of Dynamic Optical Breast Imaging in Breast Cancer Detection.* Accepted - Canadian Association of Radiologists Journal, 2010.
156. Silverstein, M., P. Gamagami, and R. Rosser, *Hooked wire directed breast biopsy and overpenetrated mammography.* Cancer, 1987. **59**: p. 715-722.
157. Edeiken, S., W. Suer, and S. Vitale, *Needle localization of non-palpable breast lesions using methylene blue.* Breast Dis, 1990. **3**: p. 75-80.
158. Hirsh, J., W. Banks, and J. Sullivan, *Effect of methylene blue on estrogen receptor activity.* Radiology, 1989. **171**: p. 105-107.
159. Groote, A., J. Oosterhuis, and W. Molenaar, *Radiographic imaging of lymph nodes in surfical specimens.* Lab Invest, 1985. **52**: p. 236-239.
160. Tabbara, S., H. Frierson, and R. Fechner, *Diagnostic problems in tissues previously sampled by fine needle aspiration.* Am J Clin Pathol, 1991. **96**: p. 76-80.
161. Tavassoli, F. and J. Pestaner, *Pseudoinvasion in intraductal carcinoma.* Mod Pathol, 1995. **8**: p. 380-383.
162. Youngson, B., L. Liberman, and P. Rosen, *Displacement of carcinomatous epithelium in surgical breast specimens following stereotactic core biopsy.* Am J Clin Pathol, 1995: p. 598-602.
163. Grabau, D., J. Anderson, and H. Gaverson, *Needle biopsy of breast cancer. Appearance of tumor cells along the needle track.* Eur J Surg Oncol, 1993. **19**: p. 826-827.
164. American_College_of_Radiology. *ACR Practice Guidelines & Technical Standards.* . 2010 [cited; Available from: http://www.acr.org/SecondaryMainMenuCategories/quality_safety/guidelines.aspx.
165. Canadian_Association_of_Radiologists. *Canadian Association of Radiologists Standards of Care.* 2010 [cited; Available from: http://www.car.ca/en/standards-guidelines.aspx.
166. Russell, D. and J. Ziewacz, *Pressure in a simulated breast subjected to compression forces comparable to those of mammography.* Radiology, 1995. **194**: p. 383-387.
167. ANRAD. *ANRAD Flat Panel Digital X-Ray Detectors for mammography and more...* 2009 [cited; Available from: www.anrad.com.
168. Healthcare., G. *GE Revolution Digital Detector.* . 2010. [cited; Available from: www.gehealthcare.com.
169. Mettler, F., A. Upton, and C. Kelsey, *Benefits versus risks from mammography: a critical assessment.* Cancer, 1996. **77**: p. 903-909.

170. Hammerstein, G., D. Miller, and M. Masterson, *Absorbed radiation dose in mammography.* Radiology, 1979. **130**: p. 485.
171. Borsic, A., et al., *Electrical impedance tomography reconstruction for three-dimensional imaging of the prostate.* Physiological Measurement. **31**(8): p. S1-S16.
172. Moura, F.S., et al., *Dynamic Imaging in Electrical Impedance Tomography of the Human Chest With Online Transition Matrix Identification.* Ieee Transactions on Biomedical Engineering. **57**(2): p. 422-431.
173. Muders, T., H. Luepschen, and C. Putensen, *Impedance tomography as a new monitoring technique.* Current Opinion in Critical Care. **16**(3): p. 269-275.
174. Rahal, M., et al., *A comparison study of electrodes for neonate electrical impedance tomography.* Physiological Measurement, 2009. **30**(6): p. S73-S84.
175. Rimpilainen, V., et al., *Electrical impedance tomography for three-dimensional drug release monitoring.* European Journal of Pharmaceutical Sciences. **41**(2): p. 407-413.
176. Peart, O., *Mammography & Breast Imaging - Just the Facts.* 2005, United States: The McGraw-Hill Companies Inc.
177. Minkina, W. and S. Dudzik, *Infrared Thermography - Errors and Uncertainties.* 2009, West Sussex, United Kingdon: John Wiley & Sons, Ltd.
178. Timmeman, K., *The specificity and sensitivity of screening mammography and estrogen therapy use*, in *Community Health and Epidemiology.* 1999, Queen's University: Kingston.
179. Sussman, H., *Mammography screening for breast cancer in women under 50 years.* Family Practice, 2000. **17**: p. 272-275.
180. BC_Breast_Cancer_Agency. *MRI (Magnetic Resonance Imaging).* 2010 [cited November 2010]; Available from: http://www.bccancer.bc.ca/HPI/CancerManagementGuidelines/Breast/Diagnosis/MRI.htm.
181. Morris, E., L. Liberman, and D. Ballon, *MRI of occult breast carcinoma in a high risk population.* AJR, 2003. **181**: p. 619-626.
182. Damera, A., et al., *Diagnosis of axillary nodal metastases by ultrasound guided core biopsy in primary operable breast cancer.* Br J Cancer, 2003. **89**(7): p. 1310-1313.
183. Prasad, S., D. Houserkova, and J. Campbell, *Breast imaging using 3D electrical impedance tomography.* Biomed Pap Med Fac Univ Palacky Olomouc Czech Repub, 2008. **152**(1): p. 151-154.
184. FDA, *TransScan T-Scan.* P970033, April 24th, 2002.
185. Ghesani, M., V. Torri, and S. Smith. *PET/CT and a subcentimeter lesion in breast cancer.* Posted June 10, 2009 [cited November 2010]; Available from: http://www.hemonctoday.com/article.aspx?rid=40811.
186. Haberman, J., J. Francis, and T. Love, *Screening a rural population for breast cancer using thermography and physical examination techniques.* Ann NY Acad Sci, 1980. **335**: p. 492-500.
187. Day, N. and C. Brown, *Multistage models and primary prevention of cancer.* J Natl Cancer Inst, 1980. **64**: p. 977-989.
188. Xinaomdt_Medical. *ComfortScan System.* [cited; Available from: http://www.xinaomdt.com/en/.
189. Advanced_Research_Technologies_Incorporated. *SoftScan system.* [cited; Available from: http://www.cadth.ca/index.php/en/hta/reports-publications/health-technology-update/issue4/optical.
190. Imaging_Diagnostic_Systems_Inc. *CTLM-LILA.* [cited; Available from: http://imds.com/products/ctlm/.
191. Welch, A. and M. Van Gemert, *Optical-thermal response of laser irradiated tissue.* 1995, New York: Plenum.
192. Stochel, G., et al., *Bioinorganic Photochemistry.* 2009, West Sussex, United Kingdom: John Wiley & Sons Ltd.

193. Mourant, J., et al., *Light scattering from cells: the contribution of the nucleus and the effects of proliferative status.* J Biomed Opt, 2000. **5**(2): p. 131-137.
194. Mourant, J., et al., *Mechanisms of light scattering from biological cells relevant to noninvasive optical-tissue diagnostics.* Appl Opt, 1998. **37**(16): p. 3586-3593.
195. Mourant, J., et al., *Evidence of intrinsic differences in the light scattering properties of tumorigenic and nontumorigenic cells.* Cancer Cytol, 1998. **84**(6): p. 366-374.
196. Cerussi, A., et al., *In vivo absorption, scattering and physiologic properties of 58 malignant breast tumours determined by broadband diffuse optical spectroscopy.* Journal of biomedical optics, 2006. **11**(4): p. 044005.
197. Choe, R., *Diffuse optical tomography and spectroscopy of breast cancer and fetal brain.* University of Pennsylvania, 2005.
198. Durduran, T., et al., *Diffuse Optical measurement of blood flow in breast tumours.* Optic Letters, 2005. **30**(21): p. 2915-2917.
199. Guo, P., et al., *A combined 2-D ultrasound and NIR imaging system*, in *Proceedings of the IEEE 26th anual NE bioengineering conference.* April 8-9th, 2000. p. 77-78.
200. Nioka, S. and B. Chance, *NIR spectroscopic detection of breast cancer.* Technology in Cancer Research & Treatment, 2005. **4**(5): p. 497-512.
201. No, K., et al. *In vivo breast cancer measurement with a handheld laser breast scanner.* in *The 50th IEEE International Midwest Symposium on circuits and systems (MWSCAC).* 2007. Montreal Marriott Chateau Champlain Hotel.
202. Sao, V., et al. *Breast tumor imaging using NIR LED based handheld continuous-wave imager.* in *IEEE 29th Annual NE Bioengineering Conference.* March 22-23, 2003.
203. Tromberg, B., et al., *Non-invasive measurements of breast tissue optical properties using frequency-domain photon migration.* Philosophical Transactions of the Royal Society of London, 1997. **352**(1354): p. 661-668.
204. Tromberg, B., et al., *Non-invasive in vivo chracterization of breast tumors using photon migration spectroscopy.* Neoplasia, 2000. **2**(1-2): p. 26-40.
205. Xu, C. and Q. Zhu, *Optimal probe design for dual-modality breast imaging*, in *SPIE-optical tomography and spectroscopy of tissue VII.* 2007.
206. Xu, R., B. Qiang, and J. Mao, *Near infrared imaging of tissue heterogeneity: probe design and sensitivity analysis*, in *IEEE: Eng in Med and Biol.* 2005: Shanghai, China.
207. Xu, R., et al., *Development of a handheld near-infrared imager for dynamic characterization of in vivo biological tissue systems.* Applied Optics, 2007. **46**(30): p. 7442-7451.
208. Zhu, Q., N. Chen, and S. Kurtzman, *Imaging tumor angiogenesis by use of combined near-infrared diffusive light and ultrasound.* Optic Letters, 2003. **28**(5): p. 337-339.
209. Zhu, Q., et al., *Imager that combines near-infrared diffusive light and ultrasound.* Optic Letters, 1999. **24**(15): p. 1050-1052.
210. Reich, G., *Near-infrared spectroscopy and imaging: Basic principles and pharmaceutical applications.* Advanced Drug Delivery Reviews, 2005. **57**(8): p. 1109-1143.
211. Sibille, F., *Infrared Dectiection and Imaging.* Reports on Progress in Physics, 1986. **49**(11): p. 1197-1242.
212. Mlcek, J., et al., *Potentials of NIR Spectroscopy in Meat Industry.* Chemicke Listy. **104**(9): p. 855-860.
213. Delpy, D. and M. Cope, *Quantification in tissue near-infrared spectroscopy.* Phil Trans R Soc Lond B, 1997. **352**: p. 649-659.
214. Houston, J., et al., *Sensitivity an ddepth penetration of continuous wave versus frequency-domain photon migration near-infrared fluorescence contrast-enhanced imaging.* Photochem, 2003. **77**: p. 420-430.
215. Bevilacqua, F., et al., *Broadband absorption spectroscopy in turbid media by combined requency-domain and steady-state methods.* Applied Optics, 2000. **1**(39(34)): p. 6498-6507.
216. Cerussi, A., et al., *Sources of absorption and scattering contrast for near-infrared optical mammography.* Academic Radiology, 2001. **8**(3): p. 211-218.

217. Cerussi, A., et al., *Predicting response to breast cancer neoadjuvant chemotherapy using diffuse optical spectroscopy.* Proceedings of the National Academy of Sciences of the United States of America, 2007. **6:104**(10): p. 4014-4019.
218. Cerussi, A., et al., *Spectroscopy enhances the information content of optical mammography.* Journal of biomedical optics, 2002. **7**(1): p. 60-71.
219. Chance, B., et al., *Breast cancer detection based on incremental biochemical and physiological of breast cancers: a six-year, two-site study.* Academic Radiology, 2005. **12**(8): p. 925-933.
220. Chance, B., et al., *Simple AC circuit for breast cancer detection and object detection.* Rev Sci Instrum, 2006. **77**: p. 064301.
221. Chen, N., et al., *Simultaneous near-infrared diffusive light and ultrasound imaging.* Applied Optics, 2001. **40**(34): p. 6367-6380.
222. Chen, N., et al., *Portable near-infrared diffusive light images for breast cancer detection.* Journal of biomedical optics, 2004. **9**(3): p. 504-510.
223. Holboke, M., et al., *Three dimentional diffuse optical mammography with ultrasound localization in a human breast subject.* Journal of biomedical optics, 2000. **5**(2): p. 237-247.
224. Hsiang, D., et al., *Coregistration of dynamic contrast enhanced MRI and broadband diffuse optical spectroscopy for characterizing breast cancer.* Technology in Cancer Research & Treatment, 2005. **4**(5): p. 549-558.
225. Jakubowski, D., et al., *Monitoring neoadjuvant chemotherapy in breast cancer using quantitative diffuse optical spectroscopy: a case study.* Journal of biomedical optics, 2004. **9**(1): p. 230-238.
226. Javachandran, B., et al., *Design and development of a hand-held optical probe toward fluorescence diagnostic imaging.* Journal of biomedical optics, 2007. **12**(5): p. 054014.
227. Lanning, R., *Non-invasive characterization of breast cancer using near infrared optical spectroscopy.* UCI Undergraduate Research Journal II, 1999. **2**: p. 43-49.
228. Liebert, A., et al., *Bed-side assessment of cerebral perfusion in stroke patients based on optical monitoring of a dye bolus by time-resolved diffuse reflectance.* NeuroImage, 2005. **24**(2): p. 426-435.
229. No, K. and C. Ph, *Mini-FDPM and heterodyne mini-FDPM: handheld non-invasive breast cancer detectors based on frequency-domain photon migration.* IEEE Trans Circuits Syst, 2005. **52**: p. 2672-2685.
230. No, K., et al. *HBS: a handheld breast dyne.* in *Procedings of IEEE BioCAS.* November 29 - December 1, 2006. London: The British Library.
231. Shah, N., et al., *Noninvasive functional optical spectroscopy of human breast tissue.* Proceddings of the National Academy of Sciences of the United States of America, 2001. **98**(8): p. 4420-4425.
232. Shah, N., et al., *Spatial variations in optical and physiological properties of healthy breast tissue.* Journal of biomedical optics, 2004. **9**(3): p. 534-540.
233. Shah, N., et al., *Combined diffuse optical spectroscopy and contrast-enhaced magnetic resonance imaging for monitoring breast cancer neoadjuvant chemotherapy: a case study.* Journal of biomedical optics, 2005. **10**(5): p. 051503.
234. Sunar, U., et al., *Noninvasive diffuse optical measurement of blood flow and blood oxygenation for monitoring radiation therapy in patients with head and neck tumors: a pilot study.* Journal of biomedical optics, 2006. **11**(6): p. 064021.
235. Xu, R., et al., *Localization and functional parameter reconstruction of suspicious breast lesions by near infrered/ultrasound dual modal imaging.* Conference Proceedings IEEE End Med Biol Soc, 2005. **5**: p. 4473-4476.
236. Zhu, Q., et al., *Combined ultrasound and near infrared diffusive light imaging.* IEEE Symp Ultrasonics, 2000: p. 1629-1632.
237. Zhu, Q., et al., *Benign versus malignant breast masses: optical differentiation with US-guided optical imaging reconstruction.* Radiology, 2005. **237**(1): p. 57-66.
238. Zhu, Q., et al., *Ultrasound-guided optical tomographic imaging of malignant and benign breast lesions: initial clinical results of 19 cases.* Neoplasia, 2003. **5**(5): p. 379-388.

239. Zhu, Q., et al., *Utilizing optical tomography with ultrasound localization to image heterogeneous hemoglobin distribution in large breast cancers.* Neoplasia, 2005. 7(3): p. 263-270.
240. Athanasiou, A., et al., *Dynamic optical breast imaging: a new technique to visualize breast vessels: comparison with breast MRI and preliminary results.* European Journal of Radiology, 2005. **54**(1): p. 72-79.
241. Athanasiou, A., et al., *Optical Mammography: a new technique for visualizing breast lesions in women presenting non palpable BIRADS 4-5 imaging findings: preliminary results with radiologic-pathologic correlation.* Cancer Imaging, 2007. **7**: p. 34-40.
242. Fournier, L., et al., *Dynamic optical breast imaging: a novel technique to detect and characterize tumor vessels.* European Journal of Radiology, 2009. **69**(1): p. 43-49.
243. Mottier, P., *LEDs for Lighting Applications.* 2009, New York: Wiley.
244. Li, F., *CCD Image Sensors in Deep-Ultraviolet: Degradation Behaviour and Damage Mechanisms.* 2005, Berlin: Springer-Verlag Berlin Heidelberg.

Chapter 2

Pilot Study Investigating the Potential Use of Dynamic Optical Breast Imaging in Breast Cancer Detection

Accepted with corrections to Canadian Association of Radiologists Journal to be published as a Technical Note

KYLE J. WILSON[1*](M.Sc.), KAVITA DHAMANASKAR[2](M.D.), TERRY MINUK[2](M.D.), AND GERALD R. MORAN[1](Ph.D.)

[1]*Medical Physics and Applied Radiation Sciences, McMaster University, Hamilton, Ontario, Canada*

[2]*Diagnostic Imaging Division, Hamilton Health Sciences, Hamilton, Ontario, Canada*

Word Count: 1456

*Correspondence to: Kyle J. Wilson, Medical Physics and Applied Radiation Sciences, McMaster University, 1280 Main St. W., Hamilton, Ontario L8S 4K1, Canada. Phone: 905 525-9140 Ext. 26876, Fax: 905-522-5982, E-mail: wilsokj2@mcmaster.ca

ABSTRACT

Introduction: Considering mammography misses at least 10% of the breast cancers in Canadian women, having a more sensitive, specific, yet inexpensive, quick, and easy to use complimentary imaging modality is essential to reducing the impact of breast cancer. The ComfortScan™ system, a light scanning technique, uses 640 nm light to image the breast. This light scanning technique uses the absorption and scattering properties of tumours and blood to image the breast. The difference in the absorption properties of blood help to determine a likelihood of cancer. One very important aspect of near-infrared imaging is the fact that it does not depend on breast tissue radiological density and this is advantageous when compared to mammography. High fibroglandular tissue density, leading to a dense mammogram, represents a scenario where conventional mammography has a high incidence of failure to detect small cancers.

Purpose: Our objective is to validate the ComfortScan™ system as a complimentary imaging modality to mammography. In an attempt to achieve this objective an initial pilot study with 19 patients is presented.

Methods: A ComfortScan™ image was obtained for all patients and compared to mammogram through use of a normalized rating system.

Results: Analysis of the light scans showed good correlation with mammography and biopsy results. A t-test showed there was no significant difference in diagnostic information when comparing the ComfortScan™ and mammography results ($p<0.05$). The NIR results from 12 patients agreed with mammography, 2 patients agreed with biopsy and disagreed with mammography, and 4 results disagreed with mammography but cannot yet be confirmed as they were not sent for biopsy.

Conclusion:

The results of this pilot study are encouraging and demonstrate that further investigation on the ComfortScan™ system is warranted.

Keywords: DOBI, breast imaging, cancer, Near-infrared

2.1 INTRODUCTION

In Canada, an estimated 23 200 women will be diagnosed with breast cancer in 2010[1]. The accepted breast screening standard is mammography; however, since the attenuation of x-rays by dense tissue and tumourous tissue is similar, it is difficult to detect tumours in dense breasts.

Near-infrared spectroscopy (NIRS) is a well known non-destructive imaging technique with a rapid imaging time[2]. In the ComfortScan™ light scanning technique, light is passed through the breast and the attenuation is determined by detecting the amount of transmitted light. Light in the NIR range is attenuated mainly by the hemoglobin in the blood and, therefore, more attenuation means more blood. Since tumours are highly vascularized, the more attenuation seen in an area represents a higher likelihood of cancer. This light scanning technique has advantages over conventional mammography, in that, it does not use ionizing radiation and the density of the tissue being examined should not affect cancer detection.

2.2 METHODS

2.2.1 Patients

In this preliminary study, 19 patients were examined. The age of the patients was 62 ± 6 [SD] years. DOBI (Dynamic Optical Breast Imaging) scans and mammograms were performed on all patients. Ultrasound guided biopsies were performed on patients as deemed necessary from mammography.

2.2.2 Mammography

All mammograms were performed at Chedoke Hospital (part of Hamilton Health Sciences Centre) in Hamilton, Ontario, Canada through the Ontario Breast Screening Program (OBSP). Two identical GE Senographe Essential [GE Healthcare, Mississauga, Canada] mammography units were used. The mammograms were analyzed by 2 experienced radiologists using the Breast Imaging-Reporting and Data System (BI-RADS) rating[3] (Figure 1).

2.2.3 Dynamic Optical Breast Imaging

DOBI was performed using the ComfortScan system (XinAoMDT Technology Co., LTD, Beijing, China). The ComfortScan system is a light scanning technique using 640nm light to image the breast. The scan utilizes light emitting diodes to pass 640nm light through the breast and detect the transmitted light with a charge coupled device camera. As the scan starts, the soft air bladder is inflated to apply gentle pressure (5 mmHg) during the first 15 seconds of the scan. Next, the pressure is increased to 10 mmHg and images are taken for the next 30 seconds. During the last part of the scan, the pressure is lowered back to 5 mmHg. A total of 45 images are taken during the 60 second scan. A dynamic signature is defined for every pixel using Equation 1.

$$DS(x,y,t) = \frac{I(x,y,t) - I_{ref}(x,y)}{I_{ref}(x,y)} \tag{1}$$

where $DS(x,y,t)$ is the dynamic signature, $I(x,y,t)$ is the transmitted light intensity at a given position and time, $I_{ref}(x,y)$ is the transmitted light intensity at a given position during the non compression aspect of the imaging sequence. The dynamic signature is intended to highlight changes in light transmission ($I(x,y,t)$) with respect to the reference image ($I_{ref}(x,y)$), resulting from changes in pressure of the breast. Based on the changes in dynamic signature, a rating scale provided by the manufacturer extending from DOBI 0-5 was given to each suspicious region in each image by the reading radiologist (Figure 1).

Mammograms were scored using the BIRADS scale, Comfortscans using the DOBI score, however, all comparisons were made using a normalized ranking (Figure 1).

BIRADS	meaning	DOBI Score	interpretation	Normalized
0	Incomplete	0	nipple blue or invalid image	0
1	Negative	1	benign	1
2	Benign	2	likely benign	2
3	Probably Benign	3	low malignant or probably malignant	3
4	Suspicious Abnormality	4	likely malignant	
5	Highly Suspicious of Malignancy	5	malignant (high probability of malignancy)	4
6	Known Biopsy Proven Malignancy			

Figure 1 – Normalized ranking system

2.2.4 Statistics

All statistics were performed using Minitab (Minitab Inc., release 13.20, State College, PA, U.S.A). T-tests were performed to determine if there was a significant difference between the diagnosis from mammography and that of the ComfortScan™ system.

2.3 Results and Discussion

The results of the light scans were evaluated against mammography and biopsy (where available). Some typical cases are discussed.

2.3.1 Case 1 - carcinoma

In Figure 2 a typical carcinoma is shown. The suspicious ROI is the purple circular region. The colour purple represents an area of the breast which has higher light absorption than background.

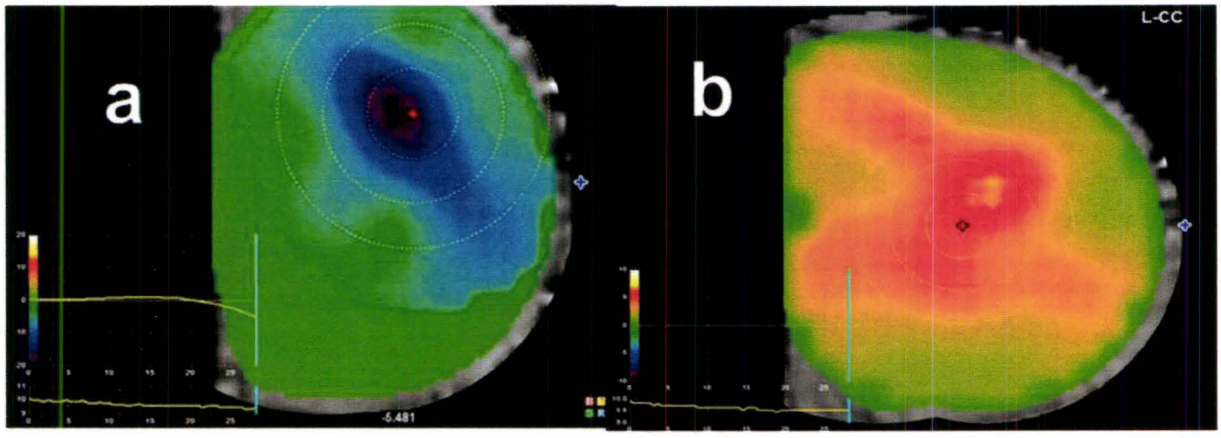

Fig. 2 – ComfortScan™ Image of a) Carcinoma, b) Benign lesion

As the colour of the suspicious ROI becomes a darker purple, the likelihood of cancer increases. The DOBI rating system (Figure 1) is then used to describe if the breast has a benign or has a malignant tumour. A malignant tumour has an increased vasculature which has tortuous properties. With a pressure increase there is a collapse of the tumourous vasculature, trapping blood in the tumourous vasculature[4]. With time, the blood begins to deoxygenate and the ratio of deoxygenated/oxygenated hemoglobin increases. With this increase, there is increased attenuation at 640 nm light, since deoxygenated hemoglobin has a larger molar extinction coefficient when compared to oxygenated hemoglobin at 640 nm[5].

2.3.2 Case 2 – Benign tumour

Figure 2 illustrates a benign finding. The suspicious ROI in this case do not show the presence of blue or purple. The slight red colour represents an area with less light absorption as compared to the background. This implies that there are no regions with a higher light attenuation compared to background, and thus no malignancies.

Images of breasts that show benign findings do not show a significantly decreasing dynamic signature with time. This means that benign breast lesions do not show a significant increase in light attenuation with time. There are 2 reasons for this: i) there is not a significant blood volume increase in the suspicious ROI,

and ii) there is not a tortuous vasculature which collapses with pressure causing an increased deoxyhemoglobin/oxyhemoglobin ratio with time.

The ComfortScan™ system has been shown to have promising results. In this 19 patient study, there was only 1 invalid image. The invalid image was caused by a 'nipple blue' artifact, this means that the suspicious ROI is within 2cm of the nipple. When the suspicious ROI is within 2cm of the nipple the image analysis protocol deems the image to be invalid due to surface artifacts. The rest of the patient's ComfortScan™ ratings matched that of either mammography or biopsy. Overall, there was no significant difference between the diagnosis provided by mammography and that of the ComfortScan™ system ($p>0.05$). There were 2 patients where the NIR results contradicted mammography but agreed with biopsy. Since biopsy is the gold standard for malignancy, these results are very interesting. There were no patients where mammography results contradicted NIR but agreed with biopsy. This study suggests that the ComfortScan™ system could potentially be used in a clinical setting as an adjunct to mammography to provide a more definitive diagnosis.

These preliminary results show that 12 patients agree with mammography. Of those that do not, 2 are in agreement with biopsy results, however 4 cannot yet be confirmed as they were not sent for biopsy (samples sent for biopsy on basis of mammographic findings). A larger study is continuing to demonstrate the benefit of using the ComfortScan™ system in a clinical setting.

2.4 ACKNOWLEDGEMENTS

We would like to thank Horizon Medical for their support with all imaging equipment used in this study

2.5 REFERENCES

1. Canadian_Cancer_Society. *Breast Cancer Stats.* 2010 [cited 2010 August]; Available from: www.cancer.ca.
2. Reich, G., *Near-infrared spectroscopy and imaging: Basic principles and pharmaceutical applications.* Advanced Drug Delivery Reviews, 2005. **57**(8): p. 1109-1143.
3. Liberman, L. and J.H. Menell, *Breast imaging reporting and data system (BI-RADS).* Radiologic Clinics of North America, 2002. **40**(3): p. 409-+.
4. Koukourakis, M.I., *Tumour angiogenesis and response to radiotherapy.* Anticancer Research, 2001. **21**(6B): p. 4285-4300.
5. Kim, J.G. and H. Liu, *Variation of haemoglobin extinction coefficients can cause errors in the determination of haemoglobin concentration measured by near-infrared spectroscopy.* Physics in Medicine and Biology, 2007. **52**: p. 6295-6322.

Chapter 3

Dynamic Optical Breast Imaging in Breast Cancer Detection

To be Submitted to Radiology

KYLE J. WILSON[1*], KAVITA DHAMANASKAR[2], TERRY MINUK[2], AND GERALD R. MORAN[1]

[1]*Medical Physics and Applied Radiation Sciences, McMaster University, Hamilton, Ontario, Canada*

[2]*Diagnostic Imaging Division, Hamilton Health Sciences, Hamilton, Ontario, Canada*

Word Count: 10 257, Figures: 7, Tables: 6

*Correspondence to: Kyle J. Wilson, Medical Physics and Applied Radiation Sciences, McMaster University, 1280 Main St. W., Hamilton, Ontario L8S 4K1, Canada. Phone: 905 525-9140 Ext. 26876 E-mail: wilsokj2@mcmaster.ca

ABSTRACT

Background:

Considering mammography misses at least 10% of the breast cancers in Canadian women, having a more sensitive, specific, yet inexpensive, quick, and easy-to-use complimentary imaging modality is essential to reducing the impact of breast cancer. This light scanning technique uses the absorption and scattering properties of tumours and blood to determine a likelihood of cancer. One very important aspect of near-infrared (NIR) imaging is that it does not depend on breast tissue density, and this is advantageous when compared to mammography. High fibroglandular tissue density, leading to a dense mammogram, represents a scenario where conventional mammography has a high incidence of failure to detect small cancers. The objective was to validate the ComfortScan™ system as a complimentary imaging modality to mammography. Our hypothesis is that by using the ComfortScan™ system as an adjunct to mammography, the clinical diagnosis will be better correlated to the biopsy results.

Methods:

The ComfortScan™ system, a light scanning technique using 640 nm light to image the breast, was used to collect 128 NIR images. A ComfortScan™ dynamic imaging session was performed for all patients and compared to mammography. Mammograms were performed using two identical GE Senographe Essential mammography units. All images were analyzed by 2 experienced radiologists having more than 5 years of breast imaging experience. In those patients requiring a biopsy, as indicated by mammography, the disease state of the tissue was determined by histopathology.

Results:

There was no statistically significant difference between the diagnosis provided by mammography and that of the ComfortScan™ system ($p>0.05$). A total of 33 patients had biopsies. The diagnosis from the NIR images correlated with biopsy in 25/33 patients. The diagnosis from mammography correlated with biopsy

in 19/33 of the patients. Since biopsy is the gold standard of malignancy analysis, these results are very interesting. The NIR results show 80/126 in agreement with mammography diagnosis.

Conclusion:

No statistically significant difference in diagnosis was found between mammography and the ComfortScan™ system ($p>0.05$). The NIR results show 80/126 in agreement with mammography diagnosis. There were 29 NIR malignant findings that disagreed with mammography but no biopsies were available for comparison. Comparing mammography and the ComfortScan™ system in the biopsy population showed that the ComfortScan™ system (specificity 83%) matched biopsy more often than mammography (specificity 13%). Therefore, by introducing the ComfortScan™ system as an adjunct to mammography there would be better agreement between diagnosis and biopsy. This study validates the potential benefits of using the ComfortScan™ system in a clinical setting to give the radiologist more information for better diagnosis of breast cancer.

Keywords: DOBI, breast imaging, cancer, Near-infrared

LIST OF ABBREVIATIONS

AOTFs	acousto-optic tunable filters
BI-RADS	Breast Imaging-Reporting and Data System
DOBI	dynamic optical breast imaging
LED	light emitting diode
LEDs	light emitting diodes
MRI	magnetic resonance imaging
REB	research ethics board
ROI	region of interest
SOP	standard of protocol
US	ultrasound

FULL STUDY - DOBI

3.1 INTRODUCTION

In Canada, an estimated 23 200 women will be diagnosed with breast cancer in 2010[1]. Approximately 1 in 9 women will develop breast cancer in their lifetime[2]. In women, breast cancer ranks as the 4th leading cause of death (5% of all deaths); trailing only ischaemic heart disease (21%), stroke (9%), and lung cancer (5.4%)[2]. Men can also be affected by this disease. The frequency of breast cancer in men compared to women is significantly lower. For every man diagnosed with breast cancer there are approximately 140 women with the disease [2].

There are several different ways to image the breast to determine the likelihood of breast cancer. The most commonly used, and the accepted standard for screening, is mammography. In mammography, an image is obtained by passing ionizing radiation through the breast, and then reading the obtained imaged, called a mammogram, to obtain a measure of tissue attenuation. Since the attenuation of x-rays by dense tissue and tumourous tissue is similar, it is difficult to detect tumours in dense breasts.

Near-infrared spectroscopy (NIRS) is a well known nondestructive imaging technique with a rapid imaging time[3]. NIRS uses wavelengths between the visible range to the mid infrared region [3]. The American Society of Testing and Materials (ASTM) defines the NIR region to be 780-2526 nm, which corresponds to the wave numbers 12820-3959 cm^{-1}[3].

NIRS involves the transmission and detection of near infrared light through a sample. The incident light intensity is higher than the transmitted light intensity due to absorption and scatter caused by the sample. NIR absorption bands are normally: i) broad, ii) overlapping, iii) 10-100 times weaker than the mid-IR absorption bands[3]; and thus, severely restrict sensitivity. On the other hand, the low absorption coefficient allows for better depth penetration which translates into the possibility of imaging thicker samples. Therefore, a low absorption coefficient is very useful in order to image strongly absorbing or highly scattering samples. This allows for the measurement of turbid liquids or solids, which normally is

not possible. Since the transmitted NIR signal will depend on both the absorption and scatter of the sample, both chemical and physical information can be obtained from a single measurement.

Imaging the breast to determine the likelihood of cancer is a relatively new application compared to the other uses of NIR light. With this light scanning technique, light is passed through the breast and the intensity of transmitted light attenuation relative to the initial light intensity is measured. Light in the NIR range is attenuated mainly by the hemoglobin in the blood and, therefore, more attenuation signifies more blood. Since tumours are highly vascularized, an area of higher attenuation represents an area with higher likelihood of cancer. This light scanning technique has advantages over conventional mammography, in that, it uses a much lighter compression than mammography (i.e. it is more comfortable), it does not use ionizing radiation, and the density of the tissue being examined will not affect cancer detection.

There have been many studies involving the use of NIR light for imaging [6-44]; many of which were phantom studies [12, 13, 17, 21, 24, 26-29, 36, 37, 40, 43]. The phantom studies were used to determine the viability of the NIR imaging technique and to improve the NIR image. The work presented in this paper is a clinical trial of the ComfortScan™ system that builds upon preliminary findings of an earlier study [46].

The ComfortScan™ system uses 640 nm light to image the breast in hopes of detecting breast cancer. This system also has a very novel application of pressure. In a mammogram, pressure is used to flatten the breast and hold it in a stable position for imaging. To enhance tumour detection, the ComfortScan™ system applies pressure to the breast. Pressure is applied in order to collapse the tortuous vasculature of the tumour and trap blood near the tumour [47]. In theory, this trapped blood will deoxygenate with time, causing a larger attenuation of NIR light, thus improving the image contrast. To date, publications on the ComfortScan™ system have been limited [46 (our preliminary findings), 48, 49,50]. XinAoMDT Technology Co. [XinAoMDT Technology Co.,Hebei, China] currently owns all rights to the ComfortScan™ system. It is hypothesized that by using the ComfortScan™ system as an adjunct to

mammography there will be better agreement to biopsy results resulting in less unneeded biopsies, and thus, better patient care.

3.2 MATERIALS AND METHODS

3.2.1 Patients

In this study, 128 NIR studies were examined. There were ambient light problems in 2 NIR images; therefore, only 126 NIR images are reported in this paper. The mean age of the patients was 62 ± 8 [SD] years. DOBI (Dynamic Optical Breast Imaging) scans and mammograms were performed on all patients. Ultrasound guided biopsies were available on 33 of the patients. Only patients already returning to the Ontario Breast Screening Program (OBSP) because of a suspicious mammogram were included in this study. Part 1 of this study examines NIR breast images from the breast with a suspicious mammogram; however, for 52 patients the contralateral breast, which was found to be mammographically normal, was also imaged to obtain normal NIR images used in Part 2 of this study. Patients with recent biopsies (within 1 month of light scan) were excluded from the study because of the possibility for abnormal vasculature due to scarring. The breast images were randomly assigned numbers DOBI1-DOBI126 for anonymity and to blind the radiologists to the patients.

3.2.2 Ethics

All procedures carried out for this study were approved by the Research Ethics Board for Hamilton Health Sciences and McMaster University. Informed consent was obtained from all patients participating in this study. The line of patient care was not altered due to any results obtained from the DOBI scans

3.2.3 Mammography

All mammograms were performed at the Chedoke Hospital (part of Hamilton Health Sciences Centre) in Hamilton, Ontario, Canada through the Ontario Breast Screening Program (OBSP). Two identical GE Senographe Essential [GE Healthcare, Mississauga, ON, Canada] mammography units were used. The mammograms were analyzed by 2 experienced radiologists having more than 5 years of breast imaging experience, using the Breast Imaging-Reporting and Data System (BI-RADS) rating[51] . The different BI-RADS classifications are described in Table 1.

Assessment categories of the BI-RADS Classification System

Stage	Result
0	Assessment incomplete. Need additional imaging evaluation.
1	Negative. Routine mammogram in 1 year recommended.
2	Benign Finding. Routine mammogram in 1 year recommended.
3	Probably benign finding. Short interval follow up suggested.
4	Suspicious. Biopsy should be considered.
5	Highly suggestive of malignancy. Appropriate action should be taken.

Table 1 – BI-RADS Classifications

This table shows the various classifications using the BI-RADS classification system. The higher the BI-RADS rating, the higher the probability of malignancy.

3.2.4 Dynamic Optical Breast Imaging

Dynamic Optical Breast Imaging was performed using the ComfortScan system (XinAoMDT Technology Co., LTD, Beijing, China). This system has been tested by another group and has shown promising results [48, 49, 50], using different methods of image analysis.

The ComfortScan system, shown in Figure 1, is a light scanning technique using 640nm red light to image the breast.

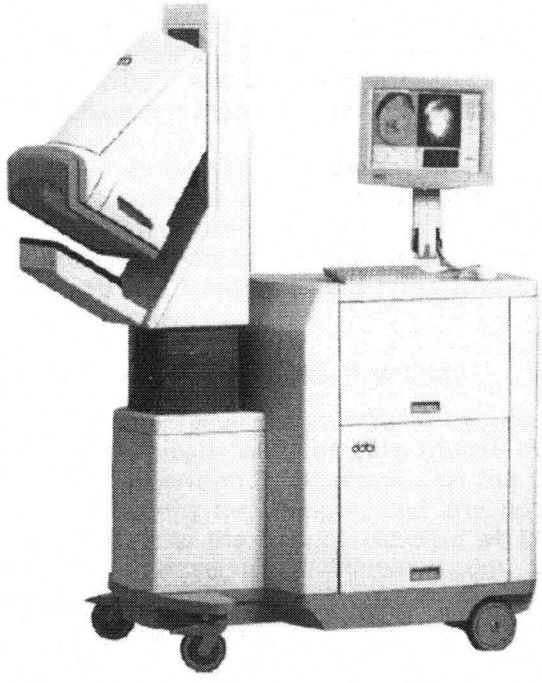

Fig. 1 – ComfortScan System

This figure shows the ComfortScan system that was used in this study. The patient is positioned on the left side and the NIR technician stands to the right in front of computer monitor.

The near-infrared (NIR) technician positioned the patient in front of the arm of the ComfortScan™ system. In order to accommodate different patient heights, the arm unit is able to independently move up and down. The technician then positioned the breast on the LED array, which is positioned in a square grid and consists of 127 LEDs on a platform angled 30 degrees from horizontal. The soft air bladder was then lowered onto the top of the breast. The Charge Coupled Device (CCD) camera, located within the soft air bladder above the breast, enables cranial-caudal imaging of the breast. At this point the patient was instructed to remain still and breathe normally. A real-time positioning image was obtained to check the position of the breast. Next, an LED check was performed using the ComfortScan™ software in order to ensure all the LEDs are functional, and ensure that the light intensity exiting the breast was within a normal

range. Errors can occur during this LED check if the breast is either too thick (not enough light is transmitted), too thin (too much light is transmitted), or improperly positioned. A suspicious Region Of Interest (ROI) marker was placed over the area of interest co-registered by a previous mammogram and, in this region, a more detailed analysis is performed. The suspicious region on the mammogram determines where the suspicious ROI marker is placed on the NIR image.

When the scan started, the soft air bladder, made of thin silicon, was inflated to apply gentle pressure (5 mmHg) during the first 15 seconds of the scan. Next, the pressure was increased to 10 mmHg and images were taken for the next 30 seconds. During the last part of the scan, the pressure was lowered back to 5 mmHg. A total of 45 images were taken during the 60 second scan, and the initial 5 images were used as a baseline. The remaining 40 images make up the dynamic part of the sequence.

A dynamic signature for every pixel was obtained using Equation 2.

$$DS(x,y,t) = \frac{I(x,y,t) - I_{ref}(x,y)}{I_{ref}(x,y)} \tag{2}$$

where $DS(x,y,t)$ is the dynamic signature used for image production, $I(x,y,t)$ is the intensity of transmitted light at the various positions, and $I_{ref}(x,y)$ is the transmitted light intensity at a given position during the non-compression phase of the imaging sequence. The variables x and y represent the pixel position on the 2D NIR image, and t represents the point in time when the image was taken. This dynamic signature highlights changes in light transmission from the reference image resulting from changes in pressure of the breast. The number of LEDs used is determined by breast size and other parameters in the scanning procedure.

Through this process the variations in light transmission over the scan duration, the dynamic signature, is calculated at each pixel. These dynamic signatures can be displayed as an intensity time curve by assigning a region of interest in the image window. A false colour overlay was applied to each of the 2D images based upon these dynamic signatures. The images were then displayed by the image analysis

software as a video, which allows for easier image analysis. A green area corresponds to a relatively stable dynamic signature with time, an area of red would represent a highly increasing dynamic signature with time, and a purple area represents an area of highly decreasing dynamic signatures with time. The dynamic signature is related to the increase or decrease in light attenuation with time, which is related to the volume of blood at a given position. For example, a highly decreasing dynamic signature represents an area where the transmitted light becomes highly attenuated with time. Note that, by convention, the image analysis software (ComfortView™) displays only the compression aspect of the imaging sequence. The videos used in the image analysis show how the dynamic signatures change with respect to time; the more purple an area becomes, the higher the likelihood of malignancy. The manufacturer suggests a range of characteristics of these curves as indicators of malignancy. Based on these characteristics a rating scale provided by the manufacturer extending from DOBI 0 to DOBI 5 was given to each suspicious region in each image by the reading radiologist. Table 2 shows the manufacturers guidelines to determine these DOBI ratings.

	Benign	Probably Benign	Indeterminate	Probably Malignant	Malignant
Location (Proximity to nipple and ROI from mammogram)	No blue near the suspicious ROI from mammogram			Blue area is located directly at ROI from mammogram	
Space (Spatial Characteristics)			Diffuse flat blue at ROI	Focal peaked blue at ROI	
Time (Temporal characteristics using ROI curve)		Strong upward trend	Wavy with amplitude 0 to -2	Downward trend with amplitude -2 to -4	Downward trend with amplitude more negative than -4
Context (Lesion Curve vs. Reference Curve)		Very similar curves that are above the x-axis (amplitudes greater than 0)	Variable curve throughout background Lesion not distinctly different	Very dissimilar pattern of curves with consistent background Diverging curves	

Table 2 – DOBI Rating system

This table shows how the DOBI images were rated. DOBI1 is benign, DOBI2 is probably benign, DOBI3 is intermediate, DOBI4 is probably malignant, and DOBI5 is malignant. A rating of DOBI 0 is given when the suspicious ROI is within 2cm of the nipple. A rating of DOBI0 is called 'nipple blue' and is caused by surface artifacts.

The analysis of all ComfortScan images was performed by an experienced radiologist, with at least 5 years of experience in breast imaging, who was double blinded to the study.

In order to compare the DOBI rating scheme to the BI-RADS classification, the two scales must be aligned, or normalized. To do this, an adjusted system was implemented to carefully align the two classifications. This adjusted rating system allowed for comparison of the light scan (DOBI) and mammography ranking (BIRADS) on the same scale. This conversion system is shown in Table 3, the higher the adjusted rating, the higher the probability of malignancy. A normalized rating of 1 or 2 is benign, and a rating of 3 or 4 would be malignant. Mammograms were scored using the BIRADS scale and ComfortScan™ images using the DOBI score, however, all comparisons were made using the normalized ranking.

BIRADS	meaning	DOBI Score	interpretation	Normalized
0	Incomplete	0	nipple blue or invalid image	0
1	Negative	1	benign	1
2	Benign	2	likely benign	2
3	Probably Benign	3	low malignant or probably malignant	3
4	Suspicious Abnormality	4	likely malignant	
5	Highly Suspicious of Malignancy	5	malignant (high probability of malignancy)	4
6	Known Biopsy Proven Malignancy			

Table 3 – BIRADS/DOBI Conversion

This table shows the table used to convert both the BIRADS and DOBI systems into a normalized rating system.

3.2.5 Biopsy

All biopsies were performed at the Chedoke site of Hamilton Health Sciences in Hamilton, Ontario, Canada by certified radiologists. Samples were fixed in 10% formalin solution and embedded in

paraffin wax for analysis. Analysis was performed in Hamilton Health Sciences Centre by certified pathologists. The pathologist determined the histological type of tissue and characterized the sample as benign or malignant. Biopsy was used as the Gold Standard for breast cancer diagnosis.

3.2.6 Statistics

All statistics were performed using Minitab (Minitab Inc., release 13.20, State College, PA, U.S.A). T-tests were performed to determine if there was a significant difference between the diagnosis from mammography and that of the ComfortScan™ system. Sensitivity and specificity were calculated for all biopsy patients, and was used to produce receiver operating characteristic (ROC) curves (Figure 8-9) to evaluate the performance of mammography and the ComfortScan™ system. Figure 8 has separate ROC curves for both radiologist 1 and 2. Figure 9 has ROC curves of both mammography and the ComfortScan™ system, but a modified rating system was used. The modified rating system consisted of simply rating the suspicious ROI as malignant or benign; thus, it did not include varying degrees of malignancy, as found in Figure 8. Sensitivity and Specificity were calculated with Equations 3 and 4.

$$Sensitivity = \frac{(\#of\_true\_positives)}{(\#of\_true\_positives)+(\#of\_false\_negatives)} \tag{3}$$

$$Specificity = \frac{(\#of\_true\_negatives)}{(\#of\_true\_negatives)+(\#of\_false\_positives)} \tag{4}$$

The area under the curve (AUC) was calculated using the trapezoidal rule; thus, by looking at the average sensitivity between two points and multiplying by the corresponding difference in specificity. The trapezoidal rule is shown in Equation 5.

$$AUC = \frac{TPR_2 - TPR_1 \Big/ 2}{FPR_2 - FPR_1} \tag{5}$$

where AUC is the area under the curve between point 1 and 2 on the ROC curve, TPR is the true positive rate (or sensitivity) at point 1 or 2, FPR is the false positive rate (or 1-specificity) at point 1 or 2.

3.3 RESULTS

The results of the light scans were evaluated against mammography and biopsy (where available). Biopsies were only performed as required by mammographic and/or ultrasound findings, and were not based on ComfortScan™ readings. The ComfortScan™ images were analyzed and read by a radiologist who was blinded to the patient name, mammogram, and pathology results. The results are divided into 2 parts. The first part contains NIR images of patients with known suspicious mammograms visiting for follow up imaging; the second part contains NIR images of the mammographically normal contralateral breast of these patients. In this study 128 NIR images were obtained, 2 were discarded due to technical issues; there were 74 NIR images for part 1, and 52 NIR images for part 2. Three patients could not be imaged due to breast thickness; two patients had breasts too thin causing a "transmitted light intensity too high" error and one patient had breasts too thick causing a "transmitted light intensity too low" error. Below a few typical cases are illustrated before presenting the results for parts 1 and 2.

3.3.1 Case 1 - carcinoma

In Figure 2 the image of a typical carcinoma is shown. Note that the corresponding mammographic image was used to identify the suspicious ROI. The suspicious ROI is the circular region shown in purple. Both the suspicious ROI and nipple position were marked before the NIR scan commenced. The colour purple represents an area of the breast which had higher light absorption than background. When the suspicious ROI showed a colour of dark purple, the likelihood of cancer in that region increases. The dynamic signature of video sequence is shown in the bottom left corner. Notice that there is a highly decreasing dynamic signature over time.

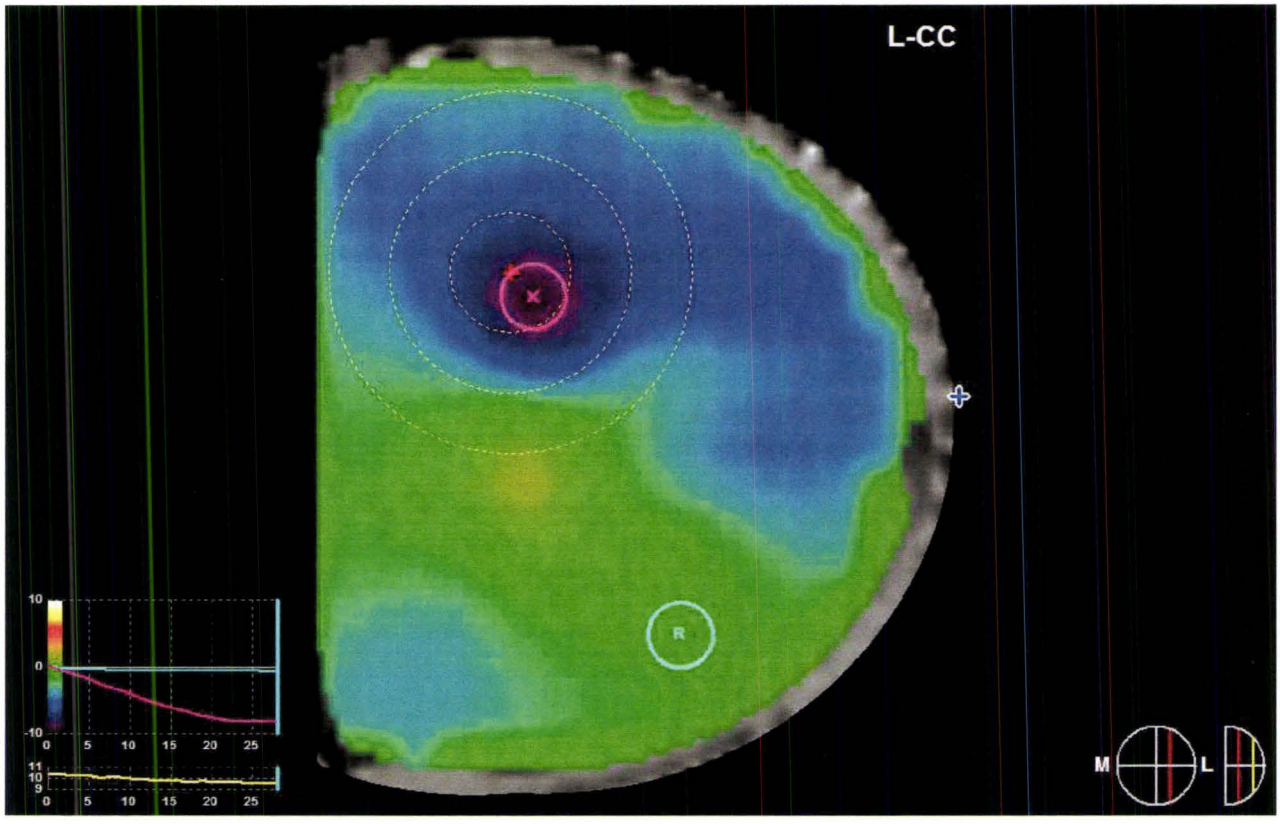

Fig. 2 – NIR Image of Carcinoma

This figure shows a typical image of a malignancy. This image is taken from a series of images which plays as a video. As time progresses the pressure on the breast is decreased, which is seen by the spectrum at the bottom left side of the above image. The other spectrum represents the dynamic signature with respect to time at two different positions in the image. The teal circle ('R') is an area with a relatively stable dynamic signature and used as reference. The purple circle ('x') has a highly decreasing dynamic signature and considered to be an area of high likelihood of malignancy.

3.3.2 Case 2 – Benign tumour

Next, an image with a benign finding is shown in Figure 3. The suspicious ROI in this case does not show the presence of blue or purple. The slight red colour in these images represents an area with less light absorption as compared to background. This implies that there are no regions with a higher light attenuation compared to background, and thus, no malignancies.

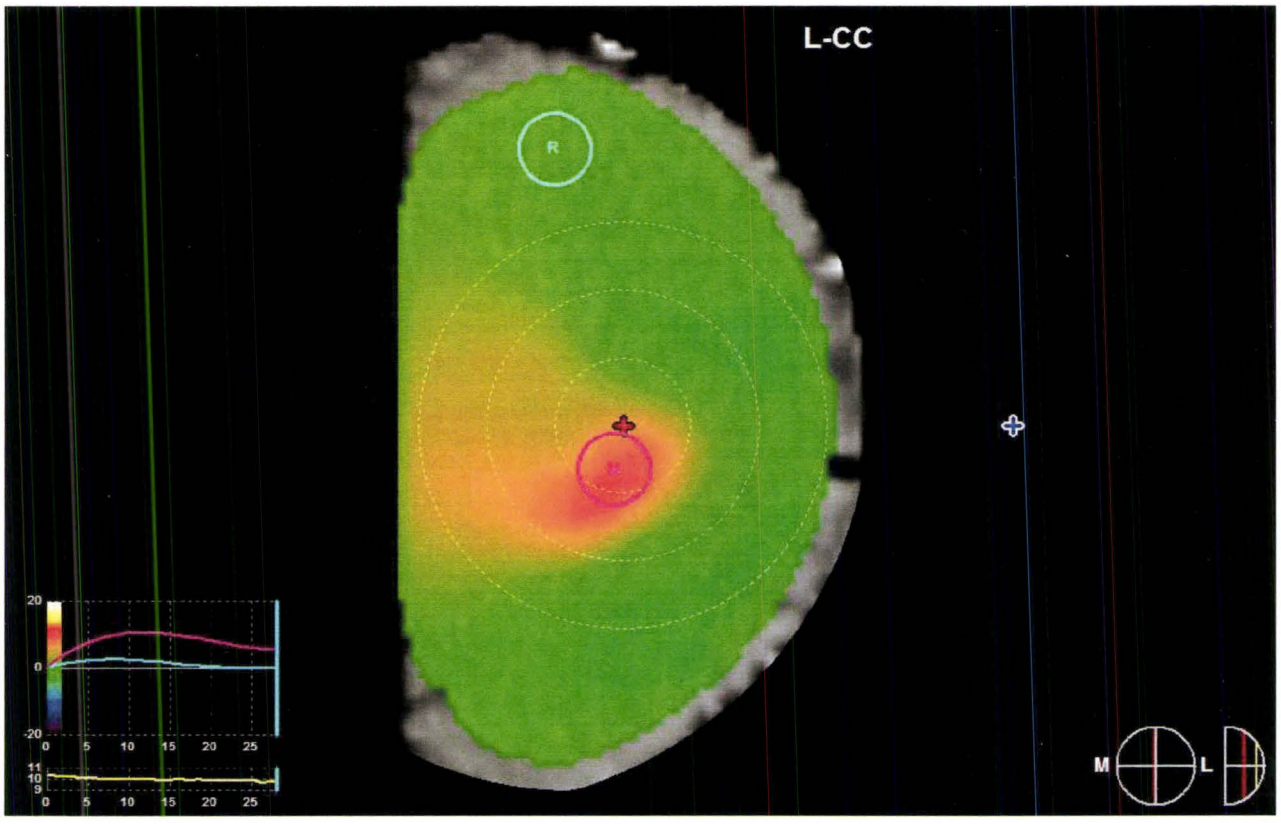

Fig. 3 – NIR Image of Benign Lesion

This figure shows no significant malignant findings. Note, there is no concentrated blue/purple ROI's near or at the anticipated suspicious ROI taken from the mammogram. The teal circle ('R) is a region of relative stable dynamic signature and used as reference. The purple circle ('x') is a suspicious region from the mammogram. Both ROI's in this image have a relatively stable dynamic signature, and thus, the diagnosis would be benign.

3.3.3 Case 3 – "Nipple Blue" Artifact

A sample image illustrating an invalid image and is shown in Figure 4. When the suspicious ROI is too close to the nipple surface, artifacts can be introduced. Note the concentrated region of blue/purple within 2cm to the nipple. This image is inconclusive and cannot be interpreted. This has occurred thus far in 1 out of 126 cases.

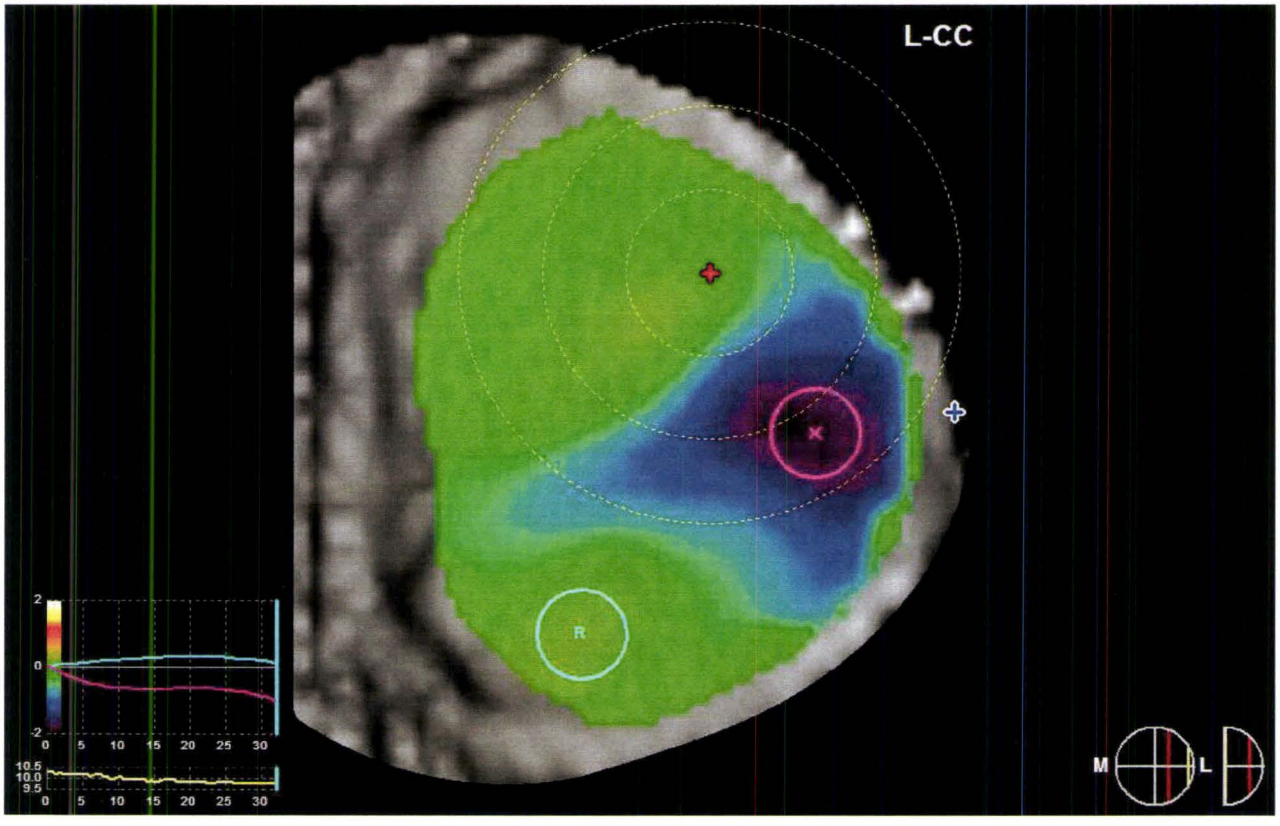

Fig. 4 – NIR Image of an Invalid Image

This figure a 'nipple blue' image taken by the ComfortScan™ system. The proximity (within 2cm) of the suspicious purple area to the nipple causes the DOBI rating on this image to be 'nipple blue'. In other words, the purple area is thought to be an image artifact.

3.3.4 Case 4 – "Blue Bloom" Artifact

Figure 5 shows a typical "blue bloom" image. This 'blue bloom' image was seen in 17 of the 74 ComfortScan™ images from patients with suspicious mammograms, and 20 of the 52 ComfortScan™ images from patients with normal mammograms. The name 'blue bloom' was coined by one of the radiologists reading the ComfortScan™ images. The blue colour is normally associated with malignancy. The difference between a 'blue bloom' and a malignant finding is that 'blue bloom' images have significant blue throughout the entire image; however, malignant images have a well defined peaked area of blue in the image. This study suggests that such an image is the result of a pixel with a transmitted light intensity vastly

different than the rest of the image; this outlier, when its intensity is too high, would cause the rest of the image to be a relatively homogenous blue colour. The above mentioned theory is described in detail later in this chapter. In short, it is believed that a "blue bloom" image (rated as DOBI 0) is indeterminate, and instead, the dynamic signature should be comprehensively evaluated to determine the likelihood of malignancy. The dynamic signature is evaluated using the time and context characteristics that are described in Table 2.

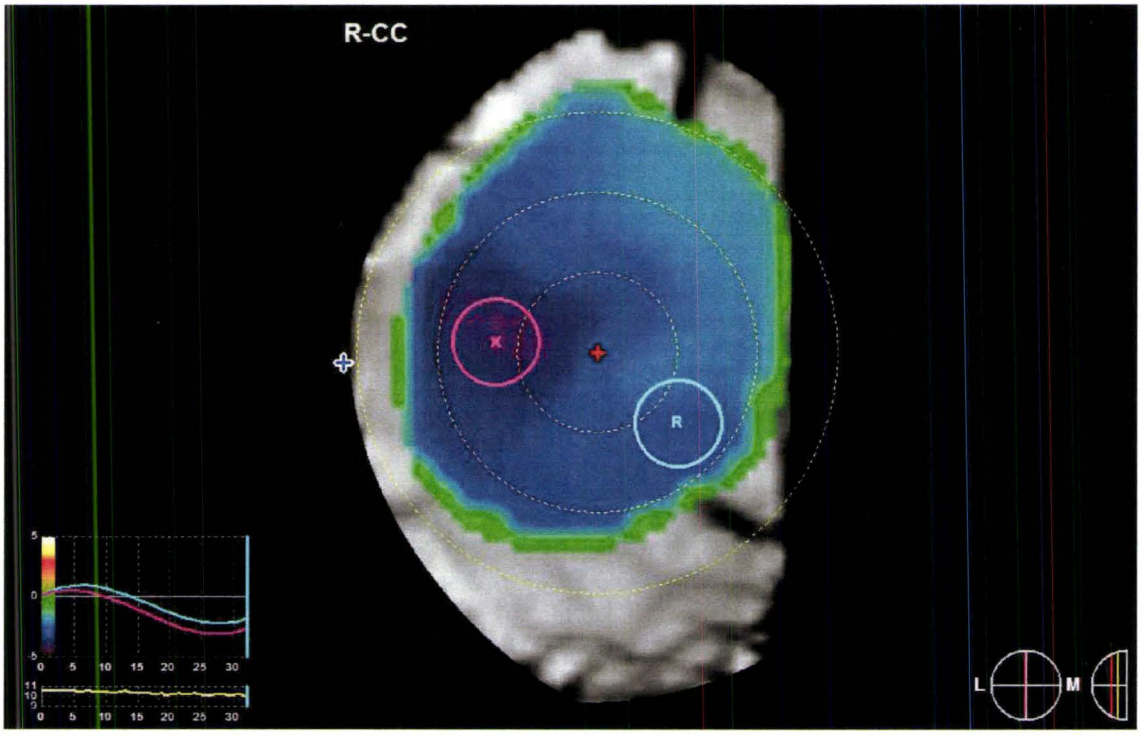

Fig. 5 – NIR of a 'Blue Bloom' Image

A 'blue bloom' image taken by the ComfortScan™ system. There is significant blue colour in the entire image. It is interesting to notice that in this case, the dynamic signatures are relatively constant throughout the image. This suggests that it is indicative of a normal breast since there is no area of highly varying dynamic signature.

3.3.5 Part 1 – Breasts with suspicious mammogram

Below in Figure 6 and Tables 4-6, the DOBI results from the 74 images from Part 1 are compared with the mammography classification. Please note that the numbers given are from the normalized rating system. Figure 6 indicates the number of patients with each score.

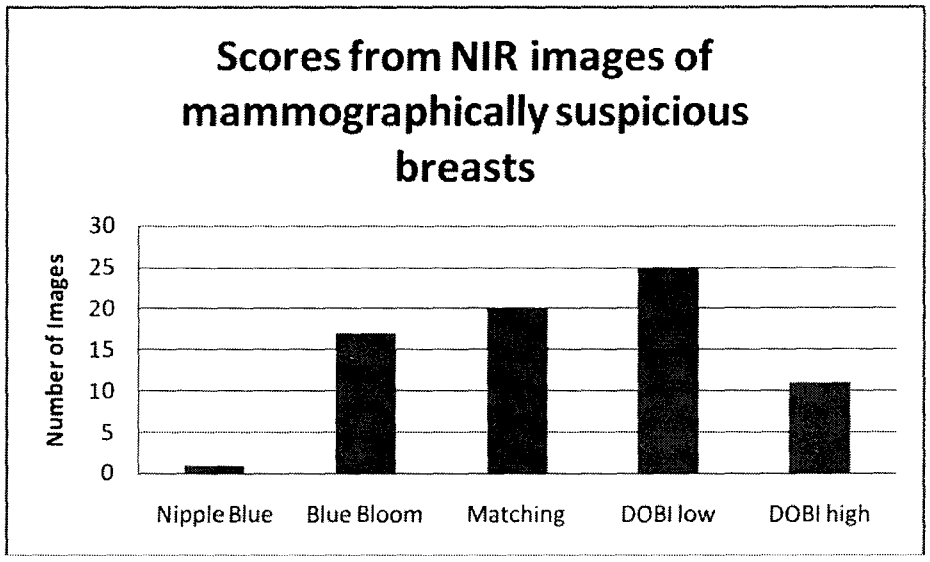

Fig. 6 – Scores from NIR images of mammographically suspicious breasts.

This figure shows the number of NIR images that are in each of the different categories. Nipple blue is an invalid image, 'blue bloom' is believed to be a contrast image introduced in mainly benign lesions.

One patient (out of 126) was reported as an invalid image due to a 'nipple blue' result. It should be noted that the adjusted BIRADS of 2 (normalized score) was associated with a suspicious region that was within 2cm of the nipple. In this NIR image, this suggests that perhaps the nipple blue image was actually correctly identifying a suspicious region. The 17 'blue bloom' images showed significant blue colour throughout the entire image. Based upon the static image presentation, the diagnosis of these patients is indeterminate. However the dynamic characteristics can be used in all 17 cases to assess the disease state of the tissue as indicated in the third and fourth row of table 2. In the final analysis, these "blue bloom"

artifact cases will be categorized as either matching, DOBI low, or DOBI high, based upon their dynamic signature. The 20 'matching' images are those for which the normalized rating for the DOBI and the mammogram were identical. The 25 'DOBI low' images were those where the normalized DOBI rating was lower than the normalized mammography rating; hence, the ComfortScan™ system determined the breast to be less suspicious of abnormality than the mammogram. The 11 'DOBI high' images were those where the normalized DOBI rating was higher than the normalized mammography rating; hence, the ComfortScan™ system determined the breast to be more suspicious than the mammogram.

Clearly, it can be seen by examining Figure 6 that the ComfortScan™ system's results are in disagreement with mammography for some patients. In those mammograms that were suspicious, biopsies were taken and sent to pathology for analysis. Patients with normal mammograms were not asked to undergo a biopsy; therefore, it is impossible to use biopsy for validation for all patients in this study.

In Tables 4 to 6 the normalized DOBI scores and normalized mammography scores are shown, as well as their agreement with pathology (i.e. malignant or benign). Table 5 shows data for patients with normalized DOBI scores lower than normalized mammography scores. In other words, for these suspicious regions, the DOBI generated a more benign finding than mammography. Similarly, Table 6 lists the patients where the DOBI had a higher normalized rating as compared to mammography, indicating that DOBI identified the suspicious region as having a greater likelihood of malignancy as compared to mammography. The last two columns of these tables give a comparison of the DOBI and mammography rating to biopsy. These figures indicate that the ComfortScan™ system's findings were in agreement with the available histological analysis. When compared to histological findings the ComfortScan™ system had an accuracy of 76% and mammography had an accuracy of 58%.

Image #	DOBI Score	Mammogram Score	DOBI correct?	Mammo Correct?
DOBI126	1	1	n/a	n/a
DOBI107	1	1	n/a	n/a
DOBI114	1	1	n/a	n/a
DOBI116	1	1	n/a	n/a
DOBI13	1	1	n/a	n/a
DOBI15	1	1	n/a	n/a
DOBI19	1	1	n/a	n/a
DOBI62	1	1	n/a	n/a
DOBI63	1	1	n/a	n/a
DOBI64	1	1	n/a	n/a
DOBI92	1	1	n/a	n/a
DOBI97	1	1	n/a	n/a
DOBI96	2	2	n/a	n/a
DOBI113	3	3	yes	yes
DOBI18	3	3	n/a	n/a
DOBI32	3	3	n/a	n/a
DOBI47	3	3	yes	yes
DOBI71	3	3	yes	yes
DOBI3	3	3	no	no
DOBI109	4	4	yes	yes
DOBI16	4	4	yes	yes
DOBI20	4	4	no	no
DOBI34	4	4	no	no
DOBI36	4	4	Yes	yes
DOBI43	4	4	Yes	yes
DOBI67	4	4	n/a	n/a
DOBI87	4	4	Yes	yes

Table 4 – Matching Patients

This table shows the results when comparing the rating from the ComfortScan™ system (DOBI rating) and the BIRADS rating to biopsy results. These results are for the patients with normalized (or adjusted) DOBI ratings identical to the normalized BIRADS. Note, n/a means no biopsy information was available because biopsy was not taken. (using the adjusted scoring system)

Image #	DOBI Score	Mammogram Score	DOBI correct?	Mammo Correct?
DOBI55	1	2	n/a	n/a
DOBI57	1	2	n/a	n/a
DOBI74	1	2	n/a	n/a
DOBI79	1	2	yes	yes
DOBI85	1	2	n/a	n/a
DOBI99	1	2	n/a	n/a
DOBI14	1	2	n/a	n/a
DOBI110	1	3	no	yes
DOBI120	1	3	n/a	n/a
DOBI22	1	3	n/a	n/a
DOBI58	1	3	yes	no
DOBI68	1	3	n/a	n/a
DOBI69	1	3	n/a	n/a
DOBI75	1	3	yes	no
DOBI77	1	3	yes	no
DOBI86	1	3	yes	no
DOBI101	1	3	yes	no
DOBI17	1	4	yes	no
DOBI23	1	4	yes	no
DOBI49	1	4	no	yes
DOBI2	2	4	Yes	no
DOBI105	3	4	yes	yes
DOBI38	3	4	yes	yes
DOBI7	3	4	n/a	n/a
DOBI82	3	4	n/a	n/a
DOBI9	3	4	Yes	yes
DOBI4	3	4	Yes	Yes
DOBI8	3	4	Yes	Yes
DOBI6	3	4	Yes	Yes

Table 5 – ComfortScan™ System lower than Mammography

This table shows the results when comparing the rating from the ComfortScan™ system (DOBI rating) and the BIRADS rating to biopsy results. These results are for the patients with normalized (or adjusted) DOBI ratings lower than normalized BIRADS. Note, n/a means no biopsy information was available because biopsy was not taken. (using the adjusted scoring system)

Image #	DOBI Score	Mammogram Score	DOBI correct?	Mammo Correct?
DOBI122	4	1	n/a	n/a
DOBI27	4	2	n/a	n/a
DOBI103	4	3	yes	yes
DOBI10	4	3	no	no
DOBI29	4	3	no	no
DOBI60	4	3	no	no
DOBI12	4	3	no	no
DOBI11	3	1	n/a	n/a
DOBI31	3	1	n/a	n/a
DOBI65	3	1	n/a	n/a
DOBI53	3	2	n/a	n/a
DOBI1	3	2	n/a	n/a
DOBI46	3	1	n/a	n/a
DOBI40	2	1	yes	yes
DOBI124	2	1	n/a	n/a
DOBI45	1	0	n/a	n/a
DOBI118	1	0	no	no

Table 6 – ComfortScan™ System higher than Mammography

This table shows the results when comparing the rating from the ComfortScan™ system (DOBI rating) and the BIRADS rating to biopsy results. These results are for the patients with normalized (or adjusted) DOBI ratings higher than normalized BIRADS. Note, n/a means no biopsy information was available because biopsy was not taken. (using the adjusted scoring system)

In Figure 2, a cancerous finding is shown. As the colour of the suspicious ROI becomes a darker purple with a highly decreasing dynamic signature, the likelihood of cancer increases. The DOBI rating system, shown in Table 2, is then used to determine if the breast is healthy, has a benign tumour, or has a malignant tumour.

In Figure 3 a benign finding is shown. There is no blue or purple area within the ROI shown on the image. The ROI shown on the image is obtained by examining the suspicious areas of the mammogram.

In Figure 4 a typical invalid image is shown.

In Figure 5 a typical "blue bloom" image is shown; this name was coined by one of the radiologists reading the NIR images. One theory is that these images showed significant blue (increased attenuation) throughout because of a contrast issue. The ComfortScan™ system uses an automatic contrast adjustment which identifies the range of pixel intensities and sets the colour scheme accordingly. If there are pixels with very similar intensities, but some pixels that are outliers with higher intensities, this could cause a large number of pixels to seem to exhibit significant attenuation. Also, the colour scheme is applied to all the pixel intensities for a given image; therefore, the colour blue from NIR image to NIR image may not represent the same absolute light attenuation. The colour scheme is a relative measure of light attenuation throughout a given image; this means that the same colour blue in two different NIR images may not in fact represent the same amount of transmitted signal intensity. Having both, some pixels with a higher signal intensity and a small pixel intensity range, could cause the "blue bloom" artifact and in fact represent a NIR image of a normal breast. More work needs to be done in studying this 'blue bloom' artifact and a larger scale clinical trial on mammographically normal breasts should be performed to see the incidence of the 'blue bloom' artifact in this patient population. This theory of 'blue bloom' images representing normal breasts is validated when examining the dynamic signature. The dynamic signatures in two different areas of the image in Figure 5 are very similar. They are both sinusoidal in shape and not highly decreasing. The ComfortScan™ image analysis determines an area has a higher likelihood of malignancy if there is both an area of higher attenuation and a highly decreasing dynamic signature. Therefore, Figure 5 would be deemed as benign through use of the dynamic signature. The dynamic signature should be a larger determinant of malignancy, rather than simply the presence of the colour blue on the image. By examining the dynamic signatures of all 'blue bloom' images, 11 were found to be malignant and 26 were found to be normal. These results were used to determine if the 'blue bloom' images matched, were higher, or were lower than mammography. In Figure 6 the results from part 1 of this study are presented.

Table 4 shows the 27 out of 74 patients where the ComfortScan™ system matched the mammogram; representing 36% of the NIR images taken from the population with initial suspicious mammograms.

The more interesting data is represented in Tables 5 and 6; these are the NIR images which either graded the breast lower than mammography (Table 5), or higher than mammography (Table 6). It was found that 39% of the time the ComfortScan™ graded the breast lower than mammography. When compared to biopsy the light scanning technique was wrong 7% (2/29) of the time, where as mammography was wrong 28% (8/29) of the time. Examining Table 6 shows that the ComfortScan™ system graded the breast higher (i.e. more likely malignant), when compared to mammography, 23% of the time. The light scanning technique, mammography and biopsy all report the same result 17% (3/18) of the time. The light scanning technique and mammography agreed, but disagreed with biopsy 28% (5/18) of the time. It is difficult to obtain numbers and truly evaluate the ComfortScan™ system's performance for NIR images from Table 6 because there is not much biopsy information for these patients. It is impressive that the ComfortScan™ system (accuracy of 76%) had a higher correlation with biopsy as compared to mammography (accuracy of 58%). Mammography showed more false positives. Unfortunately, since biopsy was only performed if the mammogram showed significant risk of malignancy, biopsy results weren't available for all patients. It would be interesting to have biopsy results from patients that show significant risk of malignancy through the ComfortScan™ system but show no risk with mammography. At the time of this study ethics was only granted with the caveat that patient care was not changed. Follow up mammograms were analyzed for the patients in Table 6; still there was no suspicious regions and therefore no biopsies ordered. These patients will be followed over the next few years to see if any abnormalities are seen.

3.3.6 Part 2 – Breasts with normal mammogram

In Figure 7, the DOBI and mammography classifications for the 52 NIR images are represented. All 52 patients had no suspicious regions on their mammogram. The REB approval would not allow for the line of patient care to be altered due to NIR images; thus, no biopsy results are available for these patients. Please note that the numbers given are from the normalized rating system. The 31 'agree' images represent when ComfortScan™ system agreed with the mammographically normal finding. The 21 'disagree' images represent when the ComfortScan™ system disagreed with a mammographically normal finding.

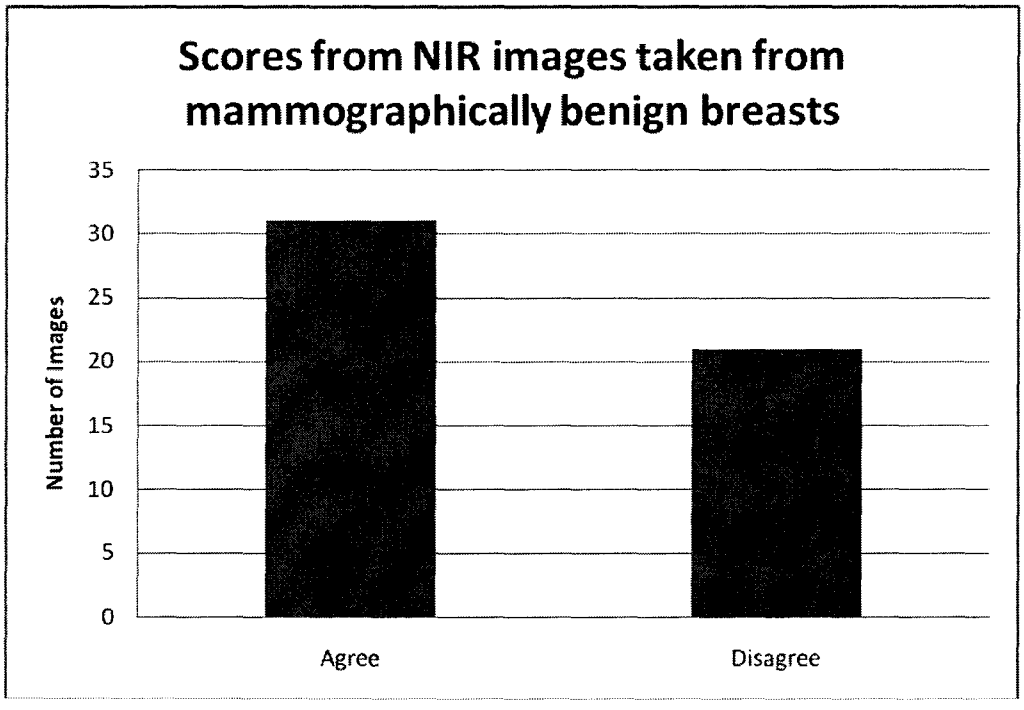

Fig. 7 – NIR images of benign breasts

This figure shows the ratings of the 52 NIR images which had mammographically benign breasts.

There were 20 'blue bloom' images in Part 2. The dynamic signature was evaluated for all 20 and results showed that 15 NIR images were normal and 5 were malignant.

When examining the dynamic signature of all 37 'blue bloom' images (combining those in Part 1 and 2), it was found that 26 were classified as normal and 11 as malignant, by consideration of the dynamic signature. Of the 11 malignancies, as determined by the ComfortScan™ system, 3 were confirmed by biopsy, the rest were not sent to biopsy because all biopsies were ordered based on mammographic findings. Of the 26 normal ComfortScan™ system images, 5 were confirmed through biopsy to be benign, the rest were not sent for biopsy because of normal mammograms.

3.3.7 Reproducibility

The intra-rater reproducibility was examined by re-analyzing 19 patients after all patients were analyzed; the radiologist was blinded throughout this process. To obtain the required sample size of 19, a 1-sample t test was performed using a p value of 0.01, target power of 0.9 and difference of 1. It was found that 15 out of the 19 had identical DOBI ratings. There were 4 ComfortScan™ images that were first found to be malignant and subsequently found to be benign through use of the ComfortScan™ image rating system. In these 4 images, there was no question that there was an area of higher attenuation and decreasing dynamic signature, which could be considered malignant; the reason they were found to be benign in the second analysis was because the ROI that exhibited the area of greater attenuation was found to be too far away from the suspicious ROI marker to cause a malignant rating using the ComfortScan™ image interpretation. One of the image interpretation parameters is to examine the distance of the suspicious ROI from the marker placed in the image by the imaging technologist. If the suspicious ROI on the ComfortScan™ image is further from the marker, the probability of malignancy decreases. In the 4 differing analyses: i) 3 were found to be now consistent with mammography, but no biopsy information was available for comparison, ii) 1 was now inconsistent with a malignant biopsy finding. From this information it was found that it is crucial to not only look at the suspicious ROI marker placed on the NIR image by the technologist; but also, look for any other

incidental malignant findings on the NIR image. It is believed that the suspicious ROI marker may not always be an accurate measure of suspected tumour position. The technologist approximates the tumour position from the suspicious mammogram and places a marker on the NIR image using the ComfortScan™ imaging software. The compression of the ComfortScan™ system and mammography are very different and therefore the position of the marker may be an accurate measure of tumour location.

3.4 DISCUSSION

Using the ComfortScan™ system, the breast can be imaged and the likelihood of cancer can be determined. The ComfortScan™ system uses the differences in optical properties and vascularization of malignant, benign, and healthy breast tissue to obtain image contrast. More importantly, since the images are independent of breast tissue density, it has the potential to be used as an adjunct modality particularly in patients with dense breast parenchyma.

There have been previous studies [46, 48-50] investigating the potential use of the ComfortScan™ system for breast imaging; all were pilot studies, and showed encouraging results. Anthanasiou et al.[48] showed that dynamic optical breast imaging could be a promising tool, when used in conjunction with other imaging modalities, in determining the likelihood of breast cancer. Anthanasiou *et al.* [48] examined 5 positive breast cancers, found using MRI, and mention that further studies with larger patient population are needed to validate this technique. The next study by Anthanasiou *et al.* [50] examined 72 patients with BIRADS rating 4-5 that were scheduled for biopsy. A sensitivity and specificity for the ComfortScan™ system was reported to be 73% and 38%, respectively. These two studies by Anthanasiou et al. [48, 50] used a numeric level of suspicion score, which was related to the colour and maximum transmitted intensity in the ROI, rather than the dynamic signature as described in this paper. Fournier *et al.* [49] performed the most recent study by the Anthanasiou et al. group using the dynamic optical breast imaging system. In the

study by Fournier et al., 47 patients were used in the analysis of this novel light imaging technique. A comparison between mammography and dynamic optical breast imaging was used to determine the validity of the technique. Fournier et al. showed that there is potential to use dynamic optical breast imaging as a tool to distinguish between benign and malignant breast tumours. The study by Fournier et al. used the same dynamic signature analysis as described in this paper. Wilson *et al.* [46 (our group)] performed a pilot study examining the possible use of the ComfortScan™ system as an adjunct to mammography. The encouraging preliminary findings warranted the collection of data shown in this paper.

This study uses the same dynamic optical breast imaging unit as in the above two mentioned studies, and therefore the methods are very similar. The main differences were a larger number of patients were included in this study and results from normal breasts were included (as was suggested previously by Fournier et al. [49]). Our results agree with both Anthanasiou et al. and Fournier et al.; using dynamic optical breast imaging is a promising tool in both the detection of breast cancers and distinguishing between benign and malignant lesions. There was no significant difference between the diagnosis provided by mammography and that of the ComfortScan™ system ($p>0.05$). There were 6 patients where the NIR results contradicted mammography but agreed with biopsy. Since mammography misses up to 10% of breast cancers[53], these results are very interesting. Increasing the sensitivity of mammography would be extremely beneficial in the detection of breast cancer. There were 29 NIR results with malignant findings that disagreed with mammography with no available biopsies. This was due to mammography being the determinant for biopsy requirement. These patients have been followed for 1 year and still no malignant finding on mammography has forced the need for biopsy.

In the 37 'blue bloom' images there are 3 confirmed malignancies through biopsy. The remaining patients had either normal mammograms, or negative biopsies. By examining the dynamic signatures of these images more closely it was found that 26 patients showed normal conditions and 11 showed a high probability of malignancy. The 3 confirmed biopsy results were within the 11 NIR images with high

probability of malignancy. The 5 biopsy confirmed benign results were found within the 26 patients with normal optical dynamic signatures. This suggests that it is crucial to not only look at the presence of blue (or higher attenuation) in the NIR image, but also, critically examine the dynamic signature of any potential suspicious ROI's. It would be beneficial to obtain biopsy results on the 8 patients with abnormal dynamic signatures, but at this time the REB approval forced the line of patient care to be unaltered.

Patients with positive HER2 are at high risk for breast cancer, and therefore, have regular mammographic screening at an early age. This patient population could have an increased risk of radiation induced cancers with time because of the large dose build up over time. A non-ionizing, inexpensive imaging technique for breast cancer detection could prove very useful for these patients.

The use of the ComfortScan™ system on patients with dense breasts could prove to be very beneficial. Normally, with inconclusive mammograms caused by increased breast density are imaged using MRI to examine changes in vascularization. With the cost of MRI being so high, it would be beneficial to have a low cost imaging modality that also uses vascularization to obtain its contrast.

The benefits of using the ComfortScan™ system, that is the ability to increase the sensitivity in breast cancer detection, outweighs the cost to the patient, in terms of an extra scan time of 15 minutes. Perhaps dynamic optical breast imaging will find a place in the clinical setting during routine breast cancer screening.

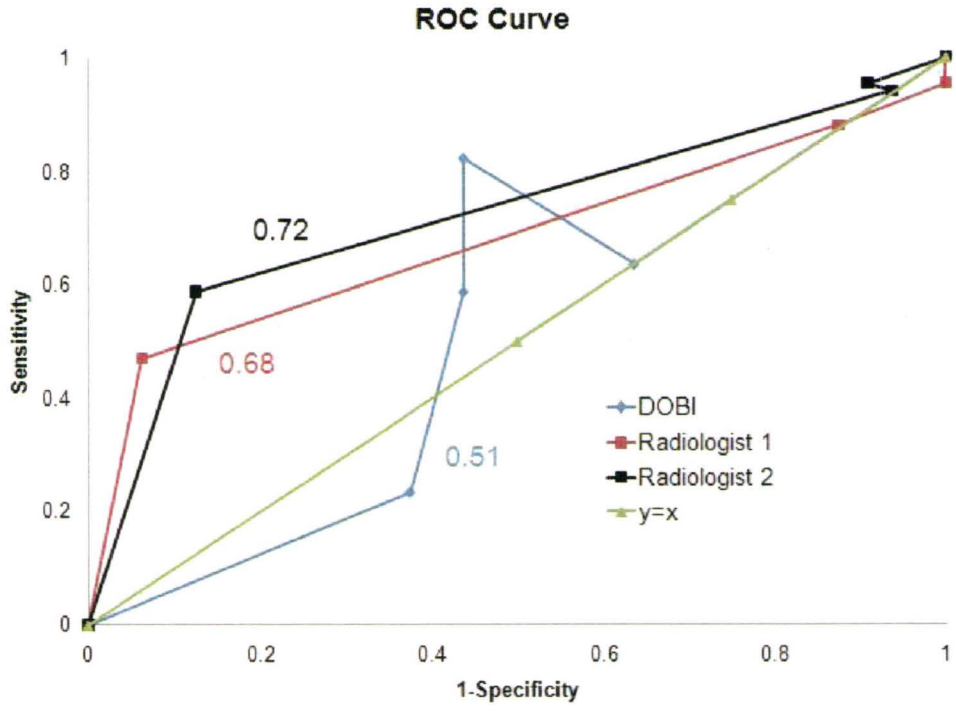

Fig. 8 – ROC Curve

This figure shows an ROC curve to compare mammography and the ComfortScan™ system. A separate ROC curve was produced for both radiologists. The area under the curve is given. The AUC was calculated using the trapezoidal rule. This shows that the ComfortScan™ system does not perform well as a screening tool.

Figure 8 shows a receiver operator characteristic (ROC) curve for mammography using the BIRADS rating system and for the ComfortScan™ system using the DOBI scoring system. This figure suggests that the ComfortScan™ system does not perform well as a screening tool for breast cancer detection. The area under the curve (AUC) for the ComfortScan™ system was 0.51, which is lower when compared to the AUC for either radiologist, 0.72 and 0.68. Therefore, mammography is better (more sensitive) than ComfortScan™ as a screening tool. However the goal here is not to evaluate the Comfortscan system's effectiveness as a screening tool, but rather to gauge its utility as an adjunct to mammography. For instance, all of the patients used to compare the Comfortscan and mammography have already been

prescreened with mammography to have a suspicious lesion. Thus patients are preselected that are mammographically positive. In order to assess the ability of the DOBI (as compared with mammography) to discriminate malignant from benign lesions, the DOBI and BIRADS rating scales were reduced effectively to either a benign or a malignant classification.

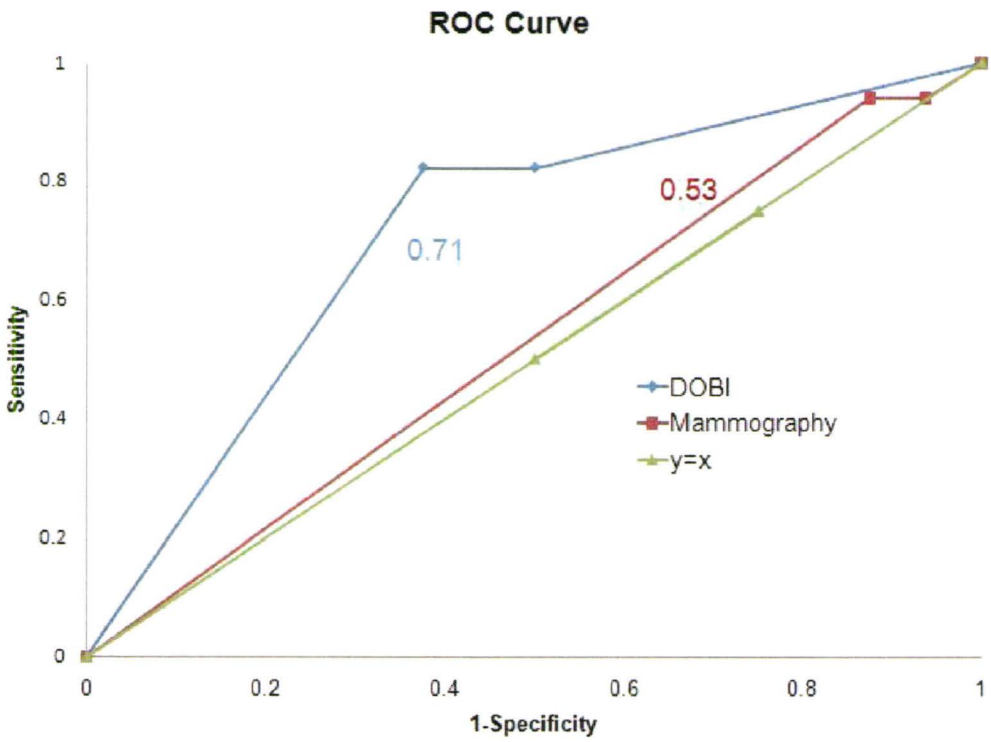

Fig. 9 – ROC Curve with Adjusted Rating System

This figure shows an ROC curve for both mammography and the ComfortScan™ system. These ROC curves, and corresponding AUCs, were obtained using an adjusted rating system. Instead of varying degrees of malignancies, as in the BIRADS rating system, a simple malignant or benign rating system was used.

.

Figure 9 is the corresponding ROC curve using this simplified rating system. The ComfortScan™ system is designed to be used as an adjunct to mammography not as a sole screening modality. Therefore, an ROC analysis which includes ratings of only benign or malignant is more appropriate. The AUC for the ComfortScan™ system is 0.71, whereas, for mammography is 0.53. This suggests that after idenfiying suspicious lesions using mammography, the ComfortScan™ system demonstrates potential in reducing the number of false positives. Therefore, may be some benefit in changing the current clinical practice to use the ComfortScan™ system to evaluate patients following a suspicious mammogram before sending for biopsy.

3.5 CONCLUSION

The ComfortScan™ system has been shown to have promising results. Out of 128 NIR images in this study, there were only 2 unusable images (ambient light issue). Overall, there was statistically significant difference between the diagnosis provided by mammography and that of the ComfortScan™ system ($p<0.05$).

In Part 1, the NIR results showed: i) 1/74 'nipple blue' image, ii) 27/74 matched perfectly with mammography, iii) 29/74 the DOBI rating was lower than mammography, and iv) 17/74 the DOBI was rated higher than mammography. The nipple blue image had significant blue and a decreasing dynamic signature near the nipple. This decreasing dynamic signature suggested malignancy, which was validated through biopsy; however, this image was deemed 'nipple blue' as per the ComfortScan™ image analysis parameter for lesion proximity to the nipple. For the images where NIR and mammography agreed, biopsy results showed that a wrong diagnosis was made 3 times, and a correct diagnosis was made 7 times, the rest of the images were not sent for biopsy. When the DOBI rating was lower than mammography biopsy results revealed: 7/29 both imaging techniques agree with biopsy, 2/29 mammography agreed but NIR disagreed with biopsy, and 8/29 mammography disagreed and NIR

agreed with biopsy. In the images where the DOBI rating was higher than mammography the biopsy results showed: 3/17 both imaging techniques agreed with biopsy, and 5/18 both imaging techniques disagreed with biopsy. There were not many cases sent for biopsy in this last category since mammography, not the ComfortScan™, decided whether or not a biopsy was needed as per REB restrictions. In the 'blue bloom' images: 4/17 were malignant through biopsy, 4/17 were benign through biopsy, and no biopsy results were available for the remaining.

In Part 2 there were: i) 31/52 NIR image agreed with mammography, and ii) 21/52 NIR image disagreed with mammography. None of the image in Part 2 went to biopsy, since the mammogram was normal. Out of the 20/52 'blue bloom' images there were 15 that were rated as normal and 5 that were rated as malignant through use of the dynamic signature.

By examining all 33 biopsy results it was found that the sensitivity and specificity for the ComfortScan™ system was 83% and 67%, respectively. The sensitivity and specificity of mammography was 94% and 13%, respectively. The sensitivity and specificity were calculated as per Equations 3 and 4. Please note that the sensitivity and specificity would be partially skewed due to mammography being the sole determinant for requirement of biopsy. Mammography determined the need for biopsy and, therefore, only patients with suspicious mammograms had a biopsy; this may cause there to be less false negatives and true negatives than the actual number for mammography. Having less false negatives and true negatives than expected would cause an increase in the sensitivity and decrease in the specificity, which could explain the high sensitivity and low specificity for mammography. It is difficult to get a true sense of the specificity of mammography because the number of true negatives cannot be confirmed. Confirming the number of true negatives through biopsy is unethical and since biopsy is the gold standard test, can only be done by waiting several decades and monitoring patient's routine mammograms.

Considering the specificity of the ComfortScan™ system is much greater than that of mammography; this study suggests that the ComfortScan™ system could be potentially used in a clinical setting as an adjunct to mammography to give the radiologist more information to provide a more definitive diagnosis.

3.6 ACKNOWLEDGEMENTS

We would like to thank Horizon Medical for their support with all imaging equipment used in this study. Also, we would like to thank Dr. Al-Douri Faten for her help in analysis of mammogram images. Lastly, we would like to thank you Dr. Zhang from DOBI Medical for all his assistance and lengthy conversations.

3.7 CONFLICTS OF INTEREST

There are no conflicts of interest to declare.

3.8 REFERENCES

[1] Canadian_Cancer_Society. Breast Cancer Stats. 2010 [cited 2010 August 11]; Available from: www.cancer.ca

[2] Gaudette LAS, C.; Altmayer, C.A.; Gao, RN. Trends in Breast Cancer Incidence and Mortality. Health Reports. 1996;8(2):8.

[3] Reich G. Near-infrared spectroscopy and imaging: Basic principles and pharmaceutical applications. Advanced Drug Delivery Reviews. 2005;57(8):1109-43.

[4] Sibille F. Infrared Detection and Imaging. Reports on Progress in Physics. 1986;49(11):1197-242.

[5] Reich, G. Near-infrared spectroscopy and imaging: Basic principles and pharmaceutical applications. Advanced Drug Delivery Reviews. 2005; 57 (8). 1109-1143.

[6] Bevilacqua F, Berger AJ, Cerussi AE, Jakubowski D, Tromberg BJ. Broadband absorption spectroscopy in turbid media by combined frequency-domain and steady-state methods. Applied optics. 2000 Dec 1;39(34):6498-507.

[7] Cerussi A, Hsiang D, Shah N, Mehta R, Durkin A, Butler J, et al. Predicting response to breast cancer neoadjuvant chemotherapy using diffuse optical spectroscopy. Proceedings of the National Academy of Sciences of the United States of America. 2007 Mar 6;104(10):4014-9.

[8] Cerussi A, Shah N, Hsiang D, Durkin A, Butler J, Tromberg BJ. In vivo absorption, scattering, and physiologic properties of 58 malignant breast tumors determined by broadband diffuse optical spectroscopy. Journal of biomedical optics. 2006 Jul-Aug;11(4):044005.

[9] Cerussi AE, Berger AJ, Bevilacqua F, Shah N, Jakubowski D, Butler J, et al. Sources of absorption and scattering contrast for near-infrared optical mammography. Academic radiology. 2001 Mar;8(3):211-8.

[10] Cerussi AE, Jakubowski D, Shah N, Bevilacqua F, Lanning R, Berger AJ, et al. Spectroscopy enhances the information content of optical mammography. Journal of biomedical optics. 2002 Jan;7(1):60-71.

[11] Chance B, Nioka S, Zhang J, Conant EF, Hwang E, Briest S, et al. Breast cancer detection based on incremental biochemical and physiological properties of breast cancers: a six-year, two-site study. Academic radiology. 2005 Aug;12(8):925-33.

[12] Chance B, zhao Z, wen S, Chen Y. Simple ac circuit for breast cancer detection and object detection. Rev Sci Instrum. 2006;77:064301.

[13] Chen NG, Guo P, Yan S, Piao D, Zhu Q. Simultaneous near-infrared diffusive light and ultrasound imaging. Applied optics. 2001 Dec 1;40(34):6367-80.

[14] Chen NG, Huang M, Xia H, Piao D, Cronin E, Zhu Q. Portable near-infrared diffusive light imager for breast cancer detection. Journal of biomedical optics. 2004 May-Jun;9(3):504-10.

[15] Choe R. Diffuse optical tomography and spectroscopy of breast cancer and fetal brain: University of Pennsulvania; 2005.

[16] Durduran T, Choe R, Yu G, Zhou C, Tchou JC, Czerniecki BJ, et al. Diffuse optical measurement of blood flow in breast tumors. Optics letters. 2005 Nov 1;30(21):2915-7.

[17] Guo P, Piao D, Zhu Q, Fikiet J. A combined 2-D ultrasound and NIR imaging system. Proceedings of the IEEE 26th annual NE bioengineering conference; 2000 april 8-9; 2000. p. 77-8.

[18] Holboke MJ, Tromberg BJ, Li X, Shah N, Fishkin J, Kidney D, et al. Three-dimensional diffuse optical mammography with ultrasound localization in a human subject. Journal of biomedical optics. 2000 Apr;5(2):237-47.

[19] Hsiang D, Shah N, Yu H, Su MY, Cerussi A, Butler J, et al. Coregistration of dynamic contrast enhanced MRI and broadband diffuse optical spectroscopy for characterizing breast cancer. Technology in cancer research & treatment. 2005 Oct;4(5):549-58.

[20] Jakubowski DB, Cerussi AE, Bevilacqua F, Shah N, Hsiang D, Butler J, et al. Monitoring neoadjuvant chemotherapy in breast cancer using quantitative diffuse optical spectroscopy: a case study. Journal of biomedical optics. 2004 Jan-Feb;9(1):230-8.

[21] Jayachandran B, Ge J, Regalado S, Godavarty A. Design and development of a hand-held optical probe toward fluorescence diagnostic imaging. Journal of biomedical optics. 2007 Sep-Oct;12(5):054014.

[22] Lanning RT. Non-invasive characterization of breast cancer using near infrared optical spectroscopy. UCI Undergraduate Research Journal II. 1999;2:43-9.

[23] Liebert A, Wabnitz H, Steinbrink J, Moller M, Macdonald R, Rinneberg H, et al. Bed-side assessment of cerebral perfusion in stroke patients based on optical monitoring of a dye bolus by time-resolved diffuse reflectance. NeuroImage. 2005 Jan 15;24(2):426-35.

[24] Liu Q, Luo Q, Chance B. 2D phased array fluorescence wireless localizer in breast cancer detection 2004.

[25] Nioka S, Chance B. NIR spectroscopic detection of breast cancer. Technology in cancer research & treatment. 2005 Oct;4(5):497-512.

[26] No K, PH C. Mini-FDPM and heterodyne mini-FDPM: handheld non-invasive breast cancer detectors based on frequency-domain photon migration. IEEE Trans Circuits Syst. 2005;52(December 12):2672-85.

[27] No K, Xie Q, Chou P, Kwong R, Cerussi A, Tromberg B. In vivo breast cancer measurement with a handheld laser breast scanner. *The 50th IEEE international Midwest symposium on circuits and systems (MWSCAS).* Montreal Marriott Chateau Champlain Hotel 2007.

[28] No K, Xie Q, Kwong R, Cerussi A, Tromberg B, Chou P. HBS: a handheld breast dyne. In Proceedings of IEEE BioCAS; 2006 November 29 - December 1; London: The British Library; 2006.

[29] Sao V, Pourrezaei K, Akin A, Ayaz H. Breast tumor imaging using NIR LED based handheld continuous-wave imager. In: Reisman S FR, Mantilla B, editor. IEEE 29th annual NE bioengineering conference; 2003 March 22-23; 2003. p. 55-6.

[30] Shah N, Cerussi A, Eker C, Espinoza J, Butler J, Fishkin J, et al. Noninvasive functional optical spectroscopy of human breast tissue. Proceedings of the National Academy of Sciences of the United States of America. 2001 Apr 10;98(8):4420-5.

[31] Shah N, Cerussi AE, Jakubowski D, Hsiang D, Butler J, Tromberg BJ. Spatial variations in optical and physiological properties of healthy breast tissue. Journal of biomedical optics.2004 May-Jun;9(3):534-40.

[32] Shah N, Gibbs J, Wolverton D, Cerussi A, Hylton N, Tromberg BJ. Combined diffuse optical spectroscopy and contrast-enhanced magnetic resonance imaging for monitoring breast cancer neoadjuvant chemotherapy: a case study. Journal of biomedical optics. 2005 Sep-Oct;10(5):051503.

[33] Sunar U, Quon H, Durduran T, Zhang J, Du J, Zhou C, et al. Noninvasive diffuse optical measurement of blood flow and blood oxygenation for monitoring radiation therapy in patients with head and neck tumors: a pilot study. Journal of biomedical optics. 2006 Nov-Dec;11(6):064021.

[34] Tromberg BJ, Coquoz O, Fishkin JB, Pham T, Anderson ER, Butler J, et al. Non-invasive measurements of breast tissue optical properties using frequency-domain photon migration. Philosophical transactions of the Royal Society of London. 1997 Jun 29;352(1354):661-8.

[35] Tromberg BJ, Shah N, Lanning R, Cerussi A, Espinoza J, Pham T, et al. Non-invasive in vivo characterization of breast tumors using photon migration spectroscopy. Neoplasia (New York, NY. 2000 Jan-Apr;2(1-2):26-40.

[36] Xu C, Zhu Q. Optimal probe design for dual-modality breast imaging. SPIE-optical tomography and spectroscopy of tissue VII; 2007 February 13; 2007. p. 64340B.

[37] Xu R, Qiang B, Mao J. Near infrared imaging of tissue heterogeneity: probe design and sensitivity analysis. IEEE: Eng in Med and Biol; 2005 September 1-4; Shanghai, China; 2005.

[38] Xu R, Qiang B, Olsen J, Povoski S, Yee L, Mao J. Localization and functional parameter reconstruction of suspicious breast lesions by near infrared/ultrasound dual modal imaging. Conf Proc IEEE Eng Med Biol Soc. 2005;5:4473-6.

[39] Xu RX, Qiang B, Mao JJ, Povoski SP. Development of a handheld near-infrared imager for dynamic characterization of in vivo biological tissue systems. Applied optics. 2007 Oct 20;46(30):7442-51.

[40] Zhu Q, chen N, Guo p, yan S, Piao d. Combined ultrasound and near infrared diffusive light imaging. IEEE Symp Ultrasonics; 2000; 2000. p. 1629-32.

[41] Zhu Q, Chen N, Kurtzman SH. Imaging tumor angiogenesis by use of combined near-infrared diffusive light and ultrasound. Optics letters. 2003 Mar 1;28(5):337-9.

[42] Zhu Q, Cronin EB, Currier AA, Vine HS, Huang M, Chen N, et al. Benign versus malignant breast masses: optical differentiation with US-guided optical imaging reconstruction. Radiology. 2005 Oct;237(1):57-66.

[43] Zhu Q, Durduran T, Ntziachristos V, Holboke M, Yodh AG. Imager that combines near-infrared diffusive light and ultrasound. Optics letters. 1999 Aug 1;24(15):1050-2.

[44] Zhu Q, Huang M, Chen N, Zarfos K, Jagjivan B, Kane M, et al. Ultrasound-guided optical tomographic imaging of malignant and benign breast lesions: initial clinical results of 19 cases. Neoplasia (New York, NY. 2003 Sep-Oct;5(5):379-88.

[45] Zhu Q, Kurtzma SH, Hegde P, Tannenbaum S, Kane M, Huang M, et al. Utilizing optical tomography with ultrasound localization to image heterogeneous hemoglobin distribution in large breast cancers. Neoplasia (New York, NY. 2005 Mar;7(3):263-70.

[46] Wilson K, Dhamanaskar K, Minuk T, Moran G. Pilot Study Investigating the Potential use of Dynamic Optical Breast Imaging in Breast Cancer Detection. Submitted to Canadian Association of Radiologists Journal. 2010.

[47] Samtinoranont M, Rooney F, Ferrari M. Interstitial Stress and Fluid Pressure Within a Growing Tumor. Annals of Biomedical Engineering. 2003. Vol 31. 327-335.

[48] Athanasiou A, Vanel D, Balleyguier C, Fournier L, Mathieu MC, Delaloge S, et al. Dynamic optical breast imaging: a new technique to visualise breast vessels: comparison with breast MRI and preliminary results. European journal of radiology. 2005 Apr;54(1):72-9.

[49] Fournier LS, Vanel D, Athanasiou A, Gatzemeier W, Masuykov IV, Padhani AR, et al. Dynamic optical breast imaging: a novel technique to detect and characterize tumor vessels. European journal of radiology. 2009 Jan;69(1):43-9.

[50] Athanasiou A, Vanel D, Fournier L, Balleyguier C. Optical mammography: a new technique for visualizing breast lesions in women presenting non palpable BIRADS 4-5 imaging findings: preliminary results with radiologic-pathologic correlation. Cancer Imaging. 2007. (7): 34-40.

[51] Liberman L, Menell JH. Breast imaging reporting and data system (BI-RADS). Radiologic Clinics of North America. 2002;40(3):409-+.

[52] Koukourakis MI. Tumour angiogenesis and response to radiotherapy. Anticancer Res. 2001 Nov-Dec;21(6B):4285-300.

[53] Kim JG, Liu H. Variation of haemoglobin extinction coefficients can cause errors in the determination of haemoglobin concentration measured by near-infrared spectroscopy. Physics in Medicine and Biology. 2007;52:6295-322.

[52] IARC. Handbooks of Cancer Prevention: Breast Cancer Screening. B.F. Vainio H, Lyon, IARC Press.

Chapter 4

Use of Polyvinyl Alcohol Cryogel as a Tissue Mimicking Phantom for use in Near-Infrared Imaging

To be submitted to Journal of Biomedical Optics

KYLE J. WILSON[1*], GORD CAMPBELL[3,4], KAVITA DHAMANASKAR[2], TERRY MINUK[2], KEVIN DIAMOND[1,5], AND GERALD R. MORAN[1,3]

[1]*Medical Physics and Applied Radiation Sciences, McMaster University, Hamilton, Ontario, Canada*

[2]*Diagnostic Imaging Division, Hamilton Health Sciences, Hamilton, Ontario, Canada*

[3]*Department of Medical Biophysics, University of Western Ontario, London, Ontario, Canada*

[4]*Integrated Manufacturing Technologies Institute, National Research Council, London, Ontario, Canada*

[5]*Juravinski Cancer Centre, Hamilton, Ontario, Canada*

Word Count: 9946

*Correspondence to: Kyle J. Wilson, Medical Physics and Applied Radiation Sciences, McMaster University, 1280 Main St. W., Hamilton, Ontario L8S 4K1, Canada. Phone: 905 525-9140 Ext. 26876 E-mail: wilsokj2@mcmaster.ca

ABSTRACT

When performing quality assurance and optimizing new technologies, such as the ComfortScan™ system, a realistic tissue mimicking near-infrared (NIR) phantom is extremely valuable. Quality assurance requires a realistic phantom in order to test the imaging device properly to ensure safety. New technologies require a realistic phantom to optimize imaging sequences and to ensure the device is working as expected. Polyvinyl Alcohol Cryogel (PVA-C) is a non-toxic material that has been shown to have characteristics similar to soft tissue for various imaging modalities. Our objective is to demonstrate the effectiveness of PVA-C as a NIR phantom for breast imaging and use it to validate the ComfortScan™ breast imaging system. The hypothesis is that the ComfortScan™ breast imaging system can detect small changes in the concentration of oxy- and deoxy-hemoglobin. A breast phantom was constructed with a small inclusion using PVA-C to test this hypothesis. In an attempt to vary the optical absorption co-efficient of PVA-C, 50μL and 100μL (0.006% and 0.01% by weight) of India ink were added to the 850mL total PVA volume. Two phantoms were constructed for each combination of PVA and India ink: i) a thin film, and ii) a large cylinder. All PVA-C samples underwent 5 freeze/thaw cycles (FTCs). The absorption (μ_a) and reduced scattering coefficients (μ_s') for the India ink PVA-C thin film samples were estimated using a double integrating sphere and a steady-state spatially resolved diffuse reflectance method. Measurements on the ComfortScan™ system were performed on the cylindrical 5 FTC PVA-C phantom with a 1cc cavity located in the central region; this cavity was filled with either: saline, oxygenated equine blood, or deoxygenated equine blood in an attempt to mimic different breast lesions. Using the double integrating sphere method, the optical properties of the 50μL PVA-C sample were $\mu_a = 0.00450 \pm 0.00002$ mm^{-1} and $\mu_s' = 1.2 \pm 0.1$ mm^{-1}, and $\mu_a = 0.012 \pm 0.002$ mm^{-1} and $\mu_s' = 1.5 \pm 0.2$ mm^{-1} for the 100μL thin film sample, at a wavelength of 640 nm (the operational wavelength of the ComfortScan™ system). Steady-state spatially resolved diffuse reflectance measurements were performed on the 100μL cylindrical PVA-C sample; the estimated optical properties were $\mu_a = 0.017 \pm 0.005$ mm^{-1} and $\mu_s' = 1.3 \pm 0.2$ mm^{-1} at 640 nm. The ComfortScan™ system

was used to measure the 640nm light attenuation of the PVA-C phantom and show that: i) saline solution and oxygenated equine blood was less attenuating than the surrounding phantom material; ii) deoxygenation of the equine blood resulted in increased attenuation; and iii) removing equine blood during the compression part of the scan decreased the measured attenuation. With the above information, when evaluating images on the ComfortScan™ system: i) a benign lesion, such as a cyst filled with fluid, would appear less attenuating than a malignant tumour; ii) a malignant tumour, having trapped deoxygenating blood, would result in the strongest attenuation compared to a benign lesion; and iii) the total collapse of the vasculature and void of all blood is not the only source of higher attenuation. This study was performed to independently confirm the methodology of benign and malignant lesion detection using the ComfortScan™ system.

Keywords: DOBI, breast imaging, cancer, Near-infrared

LIST OF ABBREVIATIONS

AOTFs	acousto-optic tunable filters
ASTM	American society of testing and materials
CCD	charged coupled device
EIT	electrical impedance tomography
FTC(s)	freeze/thaw cycle(s)
HCT	hematocrit
LED	light emitting diodeMRImagnetic resonance imaging
NA	numerical aperture
NIR	near infrared
NIRS	near infrared spectroscopy
PVA	polyvinyl alcohol
PVA-C	polyvinyl alcohol cryogel
QTH	quartz-tungsten-halogen
US	ultrasound

4.1 INTRODUCTION

With an estimated 20 300 women diagnosed with breast cancer in 2010 [1], there is significant need for research in the diagnosis and treatment of this disease. Polyvinyl alcohol cryogel (PVA-C) is a non toxic biomaterial that has been shown to mimic tissue properties simultaneously in various imaging modalities [2]. The use of phantoms is crucial in the construction, preclinical testing, and optimization of new imaging techniques to be used in the early diagnosis of cancer. The purpose of this study is to examine the usefulness of PVA-C as an optical imaging phantom and to use PVA-C to confirm the methodology of the ComfortScan™ system's detection of benign and malignant lesions.

Several materials can be used as optical phantoms: engineered tissue, ex vivo tissue, agar gels, polyacrylamide gel, epoxy resin, polyurethane resin, silicone, PVA-C, and Play-Doh™ [3]. To customize the absorption and scattering coefficient of these materials various additives can be used. Typical materials that are used to alter the scattering properties of a phantom are: TiO_2 and Al_2O_3 powders, quartz glass microspheres, whole blood, oil/fat/lipid, Intralipid [3]. Typical materials that are used to alter the absorption properties of a phantom are: India ink, whole blood, molecular dyes, and fluorophores [3].

Polyvinyl alcohol (PVA) is a polymer that can be formulated as a hydrogel with desirable properties for biomedical applications [4, 5]. Attractive features of PVA-C are: 1) that it can be molded to the shape of a variety of anatomies, 2) it has a long shelf-life, 3) it can be simultaneously used in MRI, ultrasound, Electrical Impedance Tomography, Current Density Imaging, and X-ray applications, and 4) its contrast properties within each of these modalities can be modified nearly independently. One method to form a hydrogel using PVA is by using chemicals such as glutaraldehyde or boric acid, however, PVA can be similarly hardened through a process of mesh entanglement by freezing (to -20 °C) and thawing (to +20 °C) resulting in a gel (termed PVA-cryogel or PVA-C) [6]. This process of entanglement is distinctly different from traditional cross-linking and is directly related to the hydrogen bonding of the PVA hydrogel [7]. Tissue mimicking phantoms made from PVA-C have been demonstrated to be suitable for: i) MRI to

simulate normal tissue [2], ii) temperature dosimetry in MRI [8, 9], iii) simulations of ultrasound guided breast biopsy [10], and iv) impedance imaging techniques such as Electrical Impedance Tomography (EIT) [11]. Work on the optical properties of PVA-C is quite limited [12-14]; thus there is a need for the characterization of this material for use in near infrared imaging.

The goal of this project is to fabricate a PVA-C phantom for use in breast cancer research and to evaluate the validity of the ComfortScan™ to diagnosis breast cancer. A requirement for this study is that the phantom mimics the optical properties of tissue for near infrared imaging. The challenge for the present work is to characterize the near infrared properties of PVA cryogel and demonstrate the dynamic nature of the optical contrast employed by the ComfortScan™ system. The first hypothesis is that the optical properties, both the absorption and reduced scattering coefficients, of PVA-C will be comparable to those in human breast tissue.

The first reports of producing a PVA cryogel were reported by Nambu [15] and Watase et al. [16]. Using PVA-C as an MRI specific phantom was first suggested by Mano et al. [17] who examined the T_1 and T_2 relaxation times, which are simply tissue specific MRI properties, in mouse soft tissues. T_1, T_2, and the elastic properties (speed of sound) of 10% PVA-C with 1-4 FTCs were measured by Surry et al. [21]. Over the range of 1 to 4 FTCs there is a large variation in the MRI properties and elastic properties, suggesting that perhaps there would also be a large dynamic range in the optical properties. As the number of freeze thaw cycles increases, so does the stiffness, resulting in an increase in the elastic modulus [18, 19]. It has been suggested [19] that this increase in elastic modulus is caused by an increase in hydrogen bonding. Increasing the number of freeze-thaw cycles increases the crystallinity and transforms the microstructure into a fibrillar network. Also, it has been shown that there is an increase in turbidity as the number of FTCs increases [20]. Increased turbidity would cause the sample to become more opaque and decrease the transmission of light through the sample. Therefore, with an increase in the number of freeze thaw cycles there should be a decrease in the transmission of light through the material.

The most commonly used imaging modality for breast cancer detection, and the accepted standard for screening, is mammography. In mammography, an image is obtained by passing ionizing radiation through the breast to obtain a measure of tissue attenuation. One pitfall of this technique, occurring in women with dense breasts, is that the attenuation of x-rays by dense tissue and tumourous tissue is similar, making it very difficult to differentiate between the two. Dense breasts usually occur in younger women. Young women that are at high risk of breast cancer development, such as HER2 positive patients, are screened at an early age which increases their total lifetime dose. An increased total lifetime dose will increase the risk of a radiation induced breast cancer. For these young HER 2 positive patients it would be beneficial to provide a non-ionizing screen technique that has a high sensitivity even for dense breasts.

The fundamental idea of NIRS involves the measurement of absorption and scattering of near infrared light in a sample. NIR absorption bands are normally [22]: i) broad, ii) overlapping, and iii) 10-100 times weaker than the mid-IR absorption bands. The latter does restrict the sensitivity, but having a low absorption coefficient does allow for better depth penetration and thus, ability to image thicker samples. NIR light can be used in transmission breast imaging up to thicknesses of 10cm [23].

Commonly used light sources are quartz tungsten halogen (QTH) bulbs, light-emitting diodes (LEDs) or lasers. LED sources provide a very narrow spectral range[1], usually between 50-100 nm. Lasers can also be used to provide very specific wavelengths; however, lasers also offer a high energy that can be delivered in ultrashort pulses.

Using NIR light for imaging has been extensively studied [24-49]. Many of these studies involved measurements in tissue mimicking phantoms [15, 16, 21, 25, 28, 30-33, 40, 41, 44, 47]. These studies were used to: i) determine the viability of various NIR imaging techniques, and ii) to improve image quality. Using NIR light to image the breast is relatively new when compared to the other uses of NIR light[50-57]. The work presented in this paper utilizes a PVA-C breast phantom to test the viability of the ComfortScan™ system, building upon the preliminary findings of an earlier pilot study [58]. The

absorption and reduced scattering coefficient of the PVA-C phantoms and inclusions will be measured in this study.

The ComfortScan™ system uses 640 nm light and a novel application of pressure to image the breast. Pressure is used during a mammogram to flatten and immobilize the breast for imaging. The ComfortScan™ system also applies pressure to the breast; however, it does so to enhance tumour contrast. This contrast is achieved by trapping blood in and around the tumour: the blood deoxygenates over time, resulting in dynamically increasing absorption in the proximity of the tumour. Deoxyhemoglobin has a higher attenuation of 640 nm light when compared to oxyhemoglobin [59]. Publications on the ComfortScan™ system are limited [58 (our preliminary findings), 60, 61]. The ComfortScan™ system was originally produced by DOBI medical and is now available through XinAoMDT Technology Co. [XinAoMDT Technology Co.,Hebei, China].

In this study, the hypothesis has two parts: i) PVA-C can be produced to mimic the optical properties of breast tissue, and ii) the ComfortScan™ system is sensitive to small changes in deoxyhemoglobin absorption. For this study, India ink is added to PVA-C in order to simulate breast tissue absorption. The scattering coefficient is controlled by adjusting the FTC profile. These formulations of PVA-C were used to produce phantoms that mimic breast cancer detection using the ComfortScan™ system.

4.2 MATERIALS AND METHODS

Polyvinyl alcohol samples were prepared and used in optical measurements. Measurements were made using 3 different systems: i) a double integrating sphere apparatus [12], ii) steady-state spatially resolved diffuse reflectance, and iii) the NIR ComfortScan™ system. The first two systems were used to evaluate the optical properties of PVA-C, and the third to evaluate a PVA-C breast phantom and validate the ComfortScan™ system for breast imaging.

4.2.1 PVA-C Manufacture

In this study two sets of samples were prepared. Polyvinyl alcohol powder (molecular weight 146 – 186 kDa, 98-99% hydrolyzed, Sigma Aldrich, Oakville, Ontario, Canada) was mixed with de-ionized water to generate 15 percent PVA by weight. Tissue absorption was mimicked using 50μL or 100μL of India ink (Speedball Superblack India Ink, Product No. 3338) in an 850mL solution of 15% PVA. The resulting mixture was heated to 90°C over 2 hours using a standard reflux column and flask combination. A condenser unit was inserted into the top of the reflux column to help eliminate evaporation but the top of the reflux column had to be removed briefly to stir the mixture during heating. The resulting solution was then placed in water-tight, cylindrical shaped molds (homebuilt - 100mm diameter x 100mm high cylinders) and thin film water tight molds (150mm length x 150mm wide x 2mm thick). The thin film PVA-C samples were measured using a double integrating sphere apparatus (described below) to estimate the optical properties. The 100μL India ink cylindrical phantom was used in the ComfortScan™ system. The PVA samples were exposed to 5 FTC in an environment controlled air chamber (Cincinnati Sub-zero model ZH-8-1-H/AC). One FTC consists of decreasing the temperature from 20°C to –20°C at 0.1°C/min, held at -20°C for one hour, and then returning to 20°C at a rate of 0.1°C/min. The end caps for the molds were securely clamped in order to withstand the expansion resulting from the freezing process. The samples were then removed from the molds, stored in tap water, and refrigerated.

4.2.2 Absorption and Reduced Scattering Coefficients

Measurements of the absorption and reduced scattering coefficients were obtained using two different apparatuses. The first was a double integrating sphere and the second was a steady-state spatially resolved diffuse reflectance apparatus. Both the 50μL and 100μL India ink PVA-C thin film phantoms were measured using the double integrating sphere apparatus; only the 100μL India ink cylindrical PVA-C phantom was measured using the spatially resolved system.

4.2.2.i Double Integrating Sphere

The diffuse reflectance and transmittance were measured from a thin sample using two identical integrating spheres in the configuration shown in Figure 1. The integrating spheres were manufactured in house, comprised of 3 mm thick black matte styrene plastic with the interiors coated with Labsphere's 6080 Diffuse White Reflectance Coating (Labsphere Inc., NH, USA) to achieve high reflectance. Both spheres had a diameter of 61mm. Each sphere had 3 ports: i) entrance/exit (10.5 mm diameter), ii) sample (24 mm diameter), and iii) detector (6mm diameter). It should be noted that in the second sphere there was no need for an entrance/exit port and therefore it was covered with a highly reflective plate ($BaSO_4$).

A white light source, HL 2000 FHSA Halogen Lamp (Ocean Optics, FL, USA) was used to perform spectral measurements. Optical fibres (Ocean Optics, FL, USA) were used to couple the light source to the apparatus, and the spheres to the detector, an HR4000 High Resolution Spectrometer (Ocean Optics, FL, USA).

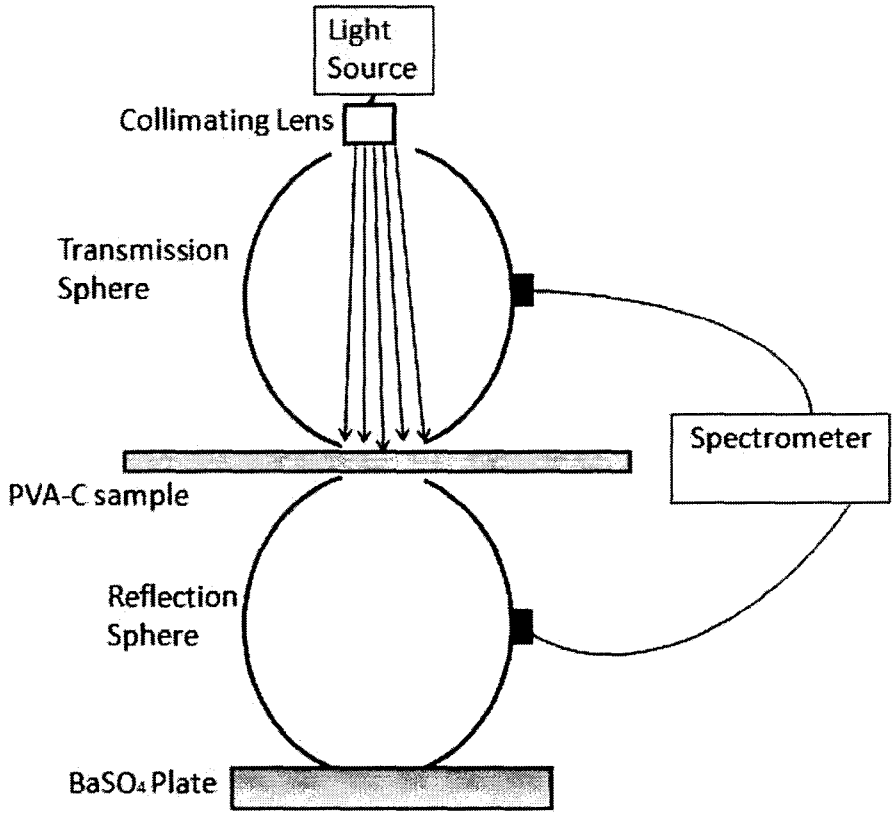

Fig. 1 – Double Integrating Sphere apparatus

Double integrating sphere apparatus that was used to measure the absorption and reduced scattering coefficients of PVA-C samples. Adapted from Counter et al. [12].

A Monte Carlo model of light transport was used to estimate the absorption and reduced scattering coefficients from the measurements of diffuse reflectance and transmittance. Details of the Monte Carlo code and experimental technique are provided elsewhere [12].

4.2.2.ii Steady-State Spatially Resolved Diffuse Reflectance

Secondly, a steady-state spatially resolved diffuse reflectance measurement was performed on the 100μL India ink cylindrical PVA-C sample. This measurement system is described in detail elsewhere [62]. This measurement provides a comparison with the measurement performed by the double integrating spheres, however in this measurement the thicker cylindrical samples were used.

A single source fiber from a flat black multi fiber probe (Fiberguide Industries, NJ, USA) was used for illumination and 25 collection fibers were used for detection (fiber diameter was 100μm, NA=0.22). The probe face was placed on the sample being imaged and a coupling fluid was applied to minimize any artifacts caused by large differences in the index of refraction. In this study, coupling fluid was not needed as the cylindrical PVA-C phantom had a thin film of water on the outside. A 100W quartz-tungsten-halogen (QTH) broadband light source (Oriel Instruments, CT, USA) was coupled into the source fiber and used to illuminate the phantom. Scattered light was collected at 14 distances, ranging from 1-10mm from the source fiber, and sent to a spectrometer (Kaiser Optical Systems, MI, USA) coupled to a charged coupled device (CCD) (Princeton Instruments, NJ, USA). The experimental setup is illustrated in Figure 2.

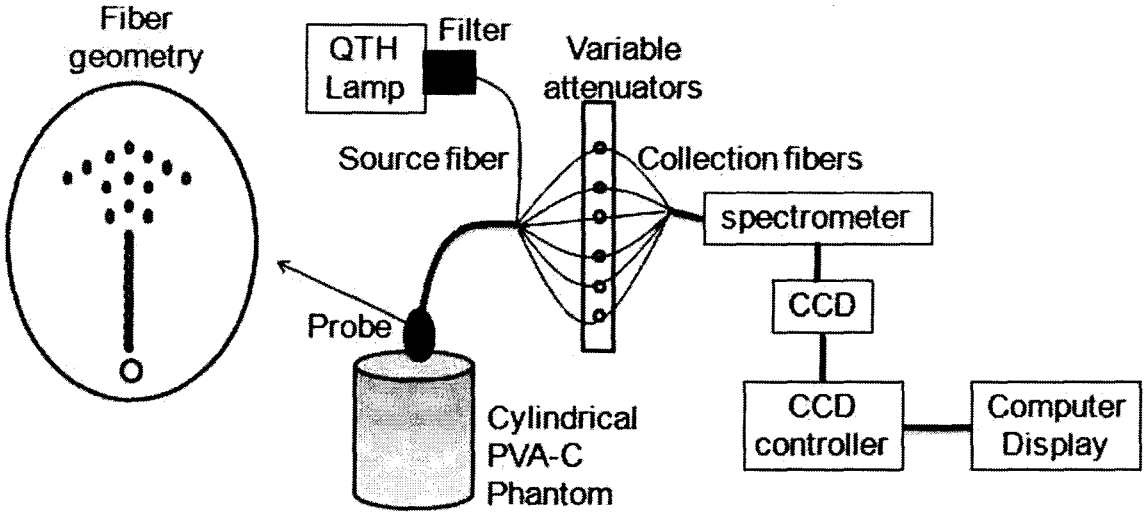

Fig. 2 – Steady-State Spatially Resolved Diffuse Reflectance.

Adapted from Diamond et al. [63].

The absorption and reduced scattering coefficients were estimated using a Monte Carlo simulation that modeled the measurement geometry. The single Monte Carlo simulation scored reflectance as a

function of radial distance in mean-free paths and number of interaction events for a non-absorbing medium. Results for any combination of optical properties could be recovered by appropriately rescaling the simulation. The simulation and method of optical property recovery is described in greater detail in an earlier work by Diamond et al. [63]. A total of 8 independent measurements were performed on the base of the cylindrical PVA-C phantom, and an average was obtained. This was done in case there was any non-uniformity, of either the India ink or the hydrogen bonding, in the cylindrical PVA-C phantom.

4.2.3 ComfortScan™ Imaging

The Dynamic Optical Breast Imaging was performed using the ComfortScan™ system (XinAoMDT Technology Co., LTD, Beijing, China). This system has been tested by other groups and has shown promising results [58, 60] using a different method of image analysis.

The ComfortScan™ system, shown in Figure 3, is a light scanning technique using 640nm red light to image the breast.

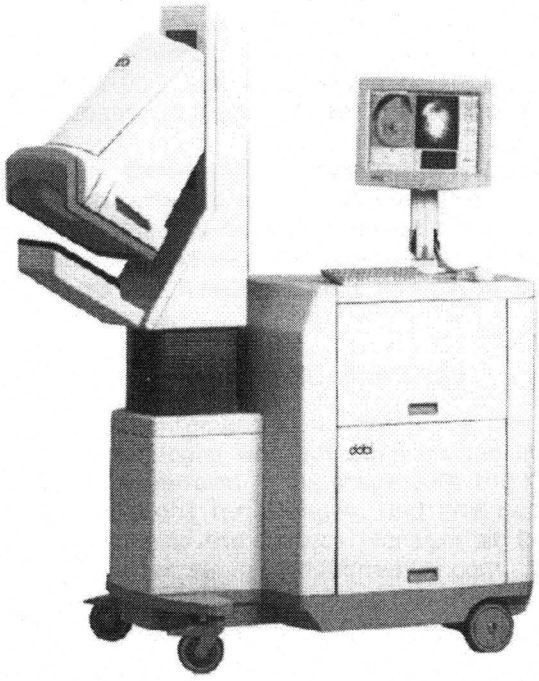

Fig. 3 – ComfortScan System

This figure shows the ComfortScan™ system that was used in this study. The patient is positioned on the left side and the NIR technician stands to the right in front of computer monitor.

The phantom was positioned on the LED array, which is positioned in a square grid and consists of 127 LEDs on a platform angled 30 degrees from the horizontal. A soft air bladder was then lowered onto the top of the phantom. A CCD camera, located within the soft air bladder above the phantom, is used for imaging. A real time positioning image was obtained to check the position of the phantom. Next, an LED check was performed using the ComfortScan™ software in order to ensure all the LEDs are functional, and ensure that the light intensity exiting the phantom was within a normal range. Errors can occur during this LED check if the phantom is either too thick (not enough light is transmitted) or too thin (too much light is transmitted). A suspicious ROI was placed over the area of interest; for the phantom this marker was placed at the cavity. If the phantom was scanned with no cavity the suspicious ROI marker was placed in a

random location near the center of the phantom. The marker is used normally by the reading radiologist to give an approximate area of the suspicious ROI seen in the mammogram. The marker was used in this study to identify the location of the cavity for easier image evaluation.

Standard operating procedure for a patient breast scan was followed. The 640 nm light from the LEDs passed through the phantom and was detected by the sensitive CCD camera. As the scan started, the soft air bladder, made of thin silicon, was inflated to apply gentle pressure (5 mmHg) during the first 15 seconds of the scan. The pressure was then increased to 10 mmHg and images are acquired for the next 30 seconds. During the last part of the scan, the pressure was lowered back to 5 mmHg. A total of 45 images were taken during the 60 second scan, and the initial 5 images were used as a baseline. The 5 initial images are used as I_{ref} in Equation 1. The remaining 40 images make up the dynamic part of the sequence, which takes place during the compression aspect of the scan.

A dynamic signature for every pixel was obtained using Equation 1.

$$DS(x,y,t) = \frac{I(x,y,t) - I_{ref}(x,y)}{I_{ref}(x,y)} \tag{1}$$

where $DS(x,y,t)$ is the dynamic signature used for image production, $I(x,y,t)$ is the intensity of transmitted light at the various positions, and I_{ref} is the light intensity after the breast shape (phantom shape in this study) had stabilized obtained from the reference image ($I_{ref}(x,y)$). The variables x and y represent a two dimensional pixel location, and t represents a point in time related to when the intensity was received by the CCD camera. This dynamic signature is therefore intended to highlight changes in light transmission from the reference image, resulting from changes in pressure of the breast (or phantom).

The dynamic signature was used to produce all 45 images; these images are then shown by the image analysis software as a video. A colour scale applied to the range of dynamic signatures allows for easier image analysis. A green area corresponds to a relatively stable dynamic signature with time, an area of

red/white represents a highly increasing dynamic signature with time, and a purple/black area represents an area of highly decreasing dynamic signatures with time. The dynamic signature is related to the increase or decrease in light attenuation with time, which is directly correlated to the volume of blood at a given position. For example, a highly decreasing dynamic signature represents an area where the transmitted light becomes highly attenuated with time. The videos used in the image analysis show how the dynamic signatures change with respect to time; the more purple/black an area becomes, the higher the likelihood of malignancy. Images in this study represent the static image found at the end of the compression.

4.2.4 Imaging of Full and Half Cylindrical PVA-C Samples

The full cylinder (100μL ink) PVA-C phantom was used as a breast phantom for the ComfortScan™ system; this phantom was measured as outlined in section 3.2.3 of the methods. A full cylinder of PVA-C, as produced for this study, was too opaque for the ComfortScan™ system. For this reason, the phantom was sectioned into two equal halves. The half cylinder of PVA-C was used for all subsequent measurements in this study. Measurements on the ComfortScan™ system on the half cylindrical PVA-C phantom were also performed with a 1cc central cavity (measuring 1cm by 1cm by 1cm); this was done to investigate any changes in the NIR image that were caused by introducing a central cavity.

4.2.5 Oxygenated Equine Blood

Measurements were made using the ComfortScan™ system as per section 3.2.3 (described above) using the half cylindrical PVA-C phantom with 1cc of oxygenated defibrinated equine blood (Hemostat Laboratories, CA, USA) to fill a 1cc central cavity. Equine blood was used because it has been shown previously that the aggregate formation rate and the membrane's anisotropy in horse blood compares well to that of human blood [64]. The oxygenated blood was used to mimic a benign lesion in order to examine the theory of the ComfortScan™ system that oxygenated blood will exhibit a lower attenuation of light than surrounding tissue. The absorption and reduced scattering coefficients of oxyhemoglobin are 0.1 mm^{-1} and

1.8 mm^{-1}, respectively [65]. Using the integrating sphere apparatus measurement, the absorption and reduced scattering coefficients for the PVA-C phantom at 640nm were 0.012 ± 0.002 mm^{-1} and 1.5 ± 0.2 mm^{-1}, respectively. Using the steady state spatially resolved reflectance measurement, the absorption and reduced scattering coefficients for the PVA-C phantom were 0.017 ± 0.005 mm^{-1} and 1.3 ± 0.2 mm^{-1}, respectively. Considering the absorption and the reduced scattering coefficients for oxygenated blood and PVA-C are similar, it is expected that the ComfortScan™ image will having uniform attenuation throughout; unless, the compression used by the ComfortScan™ preferentially affects the region with the oxygenated blood. During the compression aspect of the ComfortScan™ sequence, the oxygenated blood should compress more easily than the surrounding PVA-C material due to tensile strength properties of the two materials. The tensile properties of PVA-C have been shown previously to increase with number of FTCs by our group through use of indentation measurements.

4.2.6 Deoxygenated Equine Blood

Measurements were made using the ComfortScan™ system as per section 3.2.3 (described above) on the half cylindrical PVA-C phantom when deoxygenated defibrinated equine blood was used to fill a 1cc central cavity. The deoxygenated blood was used to mimic the collapse of a malignant lesion's tortuous vasculature causing the deoxygenation of blood during the compression aspect of the scan.

In order to deoxygenate the equine blood, activated yeast was added. A hot plate was used to boil 80mL of water; once boiling, 2 grams of yeast (Fleischmann's Instant Yeast, www.breadworld.com) was added and stirred. When the yeast was completed dissolved in the water, 10mL of the water/yeast mixture was added to 40mL of oxygenated equine blood. Next, 1cc of the blood/water/yeast solution was added to the 1cc central cavity in the PVA-C phantom using a 1cc syringe. The phantom was then immediately positioned on the LED array, and the ComfortScan™ image sequence was started. Various amounts of water, yeast, and blood were used before finding the above mixture which provided the appropriate rate of

deoxygenation needed in order to have the equine blood deoxygenate over the length of the 60 second ComfortScan™ imaging sequence. It was found that using the above mixture deoxygenated all 40mL of equine blood in the appropriate time; adding any more yeast did not have an effect on the deoxygenation process. Previously, Chance et al. have used a mixture of yeast (2-5%) and blood to convert the oxyhemoglobin to deoxyhemoglobin in order to examine change in the absorption of light to simulate anoxia in the brain [66]. The absorption coefficient of Bakers' yeast has been previously measured to be between 0.001 mm^{-1} to 0.003 mm^{-1} for yeast concentrations of 20mg/mL to 50mg/mL, respectively [67]. Considering a concentration of only 5mg/mL was used to deoxygenate the equine blood, there should not be significant light attenuation from the yeast. In this study, previous work by Delpy et al. [59] showed that the attenuation of 640nm light by oxygenated hemoglobin should be less than the attenuation of deoxygenated hemoglobin. The absorption and reduced scattering coefficients of deoxyhemoglobin are 0.95 mm^{-1} and 1.8 mm^{-1}, respectively [65]. Using the integrating sphere apparatus measurement, the absorption and reduced scattering coefficients for the PVA-C phantom at 640nm were 0.012 $\pm$ 0.002 mm^{-1} and 1.5 $\pm$ 0.2 mm^{-1}, respectively. Using the steady state spatially resolved reflectance measurement, the absorption and reduced scattering coefficients for the PVA-C phantom were 0.017 $\pm$ 0.005 mm^{-1} and 1.3 $\pm$ 0.2 mm^{-1}, respectively. This suggests the cavity containing deoxygenated blood should show higher attenuation than the surrounding PVA-C; this helps in providing support that the second hypothesis is true.

4.2.7 Removal of Blood during Compression

Measurements were made using the ComfortScan™ system as per section 3.2.3 (described above) using the half cylindrical PVA-C phantom with 1cc of oxygenated equine blood added to the central 1cc cavity. In this case, however, the cavity was voided of all blood during the compression part of the scan. This was performed by positioning a catheter inside the central 1cc cavity and filling the cavity with oxygenated equine blood, then removing it using a syringe connected to the catheter during the

compression aspect of the scan. This was done to simulate the situation of the vasculature of a malignant tumour collapsing, voiding the region of blood. This was done to test if the increased attenuation seen by the ComfortScan™ system in malignant lesions was a result of the complete removal of blood from the tumourous region during the scan.

4.2.8 Statistics

Standard deviation was performed for the calculations of absorption and reduced scattering coefficients.

4.3 RESULTS

4.3.1 Absorption and Reduced Scattering of PVA-C Phantoms

In Figure 4 the absorption (panel a) and reduced scattering (panel b) coefficients are shown for PVA-C with 50μL of ink measured using the double integrating sphere apparatus.

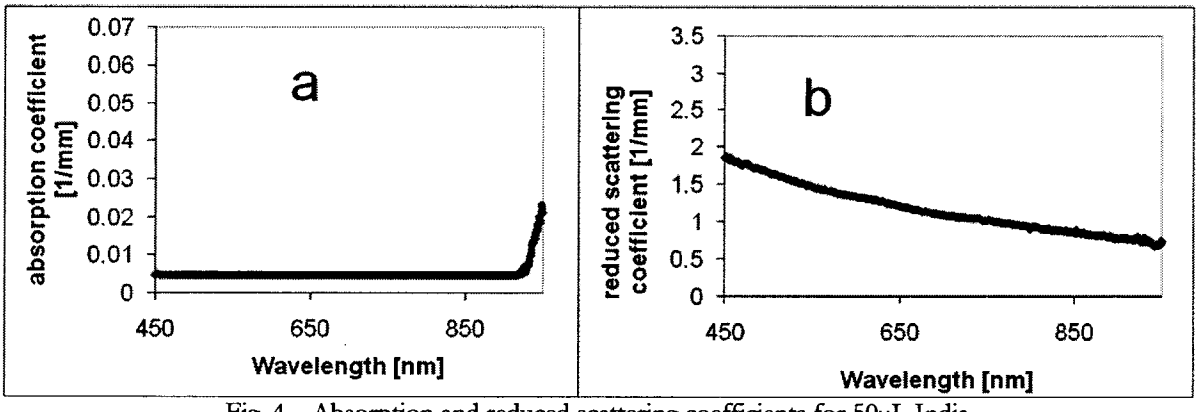

Fig. 4 – Absorption and reduced scattering coefficients for 50μL India ink PVA-C

A figure showing the absorption and reduced scattering coefficients for PVA-C which had 50μL of india ink added to 850mL of distilled water using the double integrating sphere apparatus. The measurements were taken over a range of wavelengths (450nm – 950nm).

Similarly, in Figure 5 the absorption (panel a) and reduced scattering (panel b) coefficients are shown for PVA-C with 100μL of ink measured using the double integrating sphere apparatus.

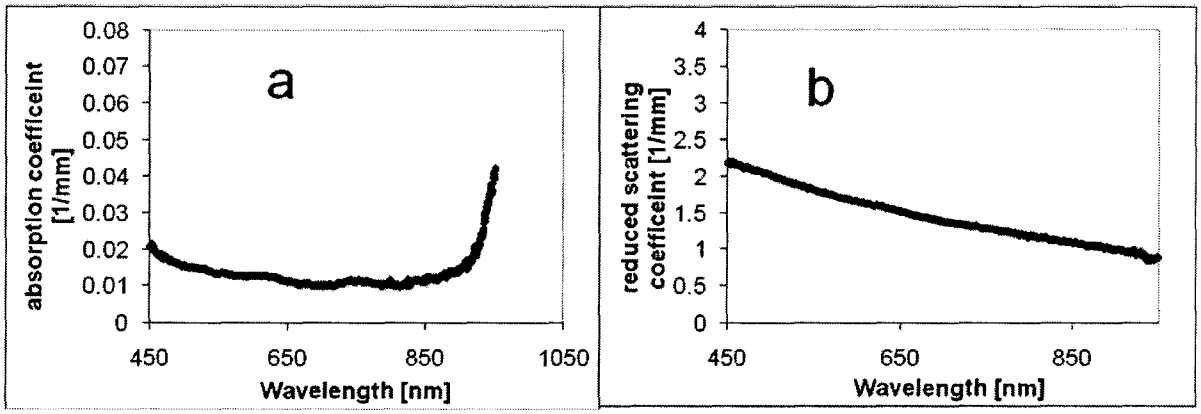

Fig. 5 – Absorption and reduced scattering coefficients for 100μL india ink PVA-C

A figure showing the absorption and reduced scattering coefficients for PVA-C which had 100μL of india ink added to 850mL of distilled water using the double integrating sphere apparatus. The measurements were taken over a range of wavelengths (450nm – 950nm).

Figures 4 and 5 are qualitatively very similar. The only difference is that in Figure 4 there was 50μL of India ink added to the PVA-C, whereas, Figure 5 was PVA-C with 100μL of India ink added. The absorption in Figure 5a demonstrates more variation with wavelength as compared to Figure 4a. It is possible that the measurement depicted in Figure 4a is at the noise level of the Monte Carlo optical property recovery algorithm; for this reason only the 100μL India ink samples will be included in this study.

The absorption of the India ink used in this study has been previous measured [12] to be 5.3 $mm^{-1}/\%$ by volume at 630nm. Devi et al. [13] has shown, at a wavelength of 633nm, that 20% 5 FTC PVA-C resulted in scattering coefficients and reduced scattering coefficients of 5.1 ± 0.1 mm^{-1} and 0.457± 0.038 mm^{-1}, respectively. Similar results have been shown by Kharine et al. [14], 20% 7FTC PVA-C was measured at 1062nm to have scattering coefficient and reduced scattering coefficient of 6.9 ± 0.4 mm^{-1} and 0.62 ± 0.1 mm^{-1}, respectively. These results suggest that the higher number of FTCs, the higher the scattering of light. The results in this study show significantly higher reduced scattering coefficients when compared to the previous work discussed above. This is expected considered the previous work did not provide a controlled freeze/thaw process. In this study the freeze/thaw rate was accurately set to

0.1°C/minute using an air chamber. Our group has shown in the past that the freeze/thaw rate, specifically the thawing process, has dramatic effects on the physical properties of the resultant PVA-C.

Below, Figure 6 shows the absorption and reduced scattering coefficients measured using steady-state spatially resolved diffuse reflectance. The measurement was performed for comparison to the double integrating sphere method and to see if the process of freezing and thawing a larger sample affected the optical properties compared to the thin slabs. Only the 100μL PVA-C sample was used since the 50μL PVA-C sample was below the sensitivity of the double integrating sphere measurement. By comparing Figures 5 and 6, it is seen that the properties of the double integrating sphere are consistent with those of the steady-state spatially resolved diffuse reflectance. In Figure 5, the absorption and reduced scattering coefficients at 640nm were 0.012 ± 0.002 mm^{-1} and 1.5 ± 0.2 mm^{-1} respectively. In Figure 6, the absorption and reduced scattering coefficients at 640nm were 0.017 ± 0.005 mm^{-1} and 1.3 ± 0.2 mm^{-1}, respectively.

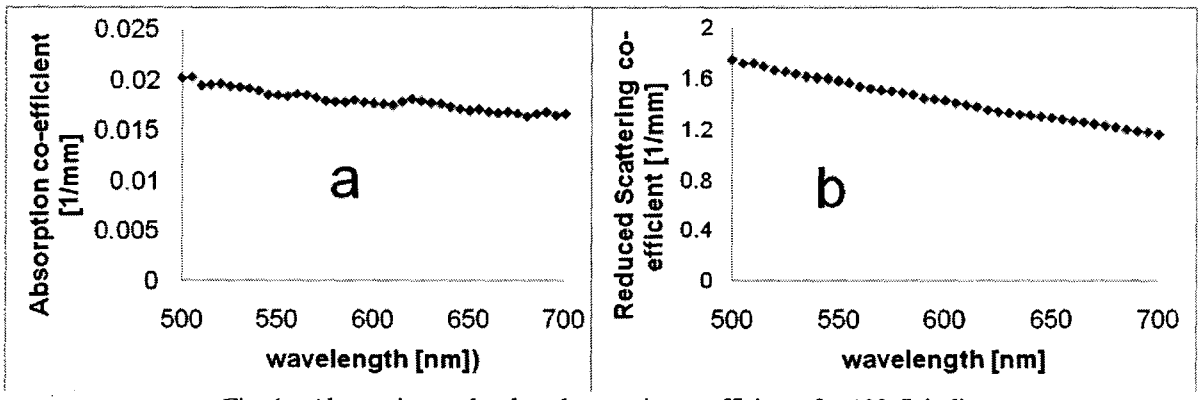

Fig. 6 – Absorption and reduced scattering coefficients for 100μL india ink PVA-C using steady state measurement

A figure showing the absorption and reduced scattering coefficients for PVA-C which had 100μL of india ink added to 850mL of distilled water. The measurements were taken over a range of wavelengths (500nm – 700nm). A steady state spatially resolved diffuse reflectance measurement was performed to provide the above data.

4.3.2 Imaging of PVA-C Samples

It should be noted that all of the ComfortScan™ NIR images in this study are in fact a representative image from the dynamic sequence of images that are outputted from the ComfortScan™ system. The images presented in this publication occur at the end of the compression aspect of the imaging sequence.

"Empty" Cavity

Figure 7 shows a NIR image of a half cylindrical phantom with the central 1cc cavity empty; this cavity should cause there to be less attenuation. As the compression increases during the ComfortScan™ sequence, the size of the cavity is slightly reduced due to the low structural integrity of the empty cavity. With a partial collapse of the cavity there is a smaller path length for the NIR light to travel, and thus, less attenuation and scatter of the NIR light. The white colour represents less light attenuation as compared to the rest of the image. Figure 7 is an image representing approximately the lower 60% of the half cylindrical phantom, including the cavity. The whole phantom could not always be scanned, since in order to satisfy the LED coverage requirement and emulate a true breast, part of the phantom was positioned outside the imaging area.

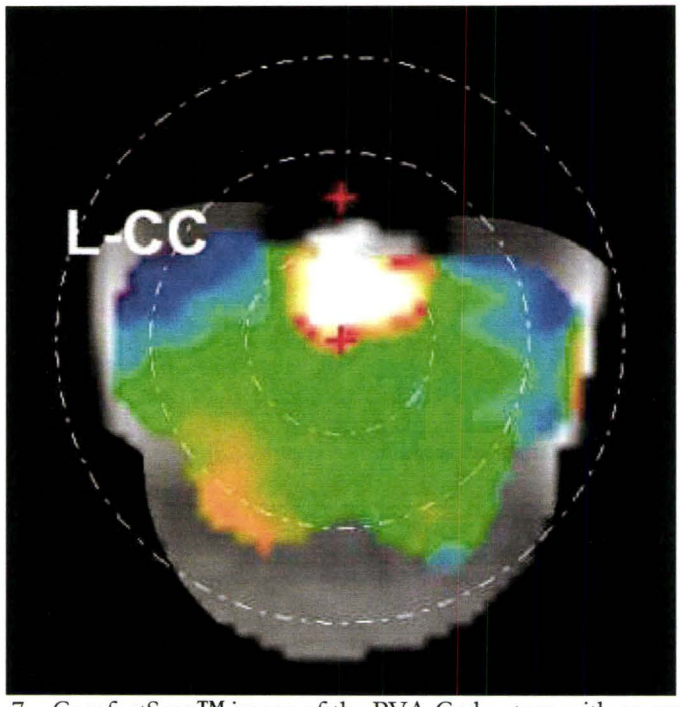

Fig. 7 – ComfortScan™ image of the PVA-C phantom with an empty cavity

This figure shows the PVA-C with an empty 1cc cavity. Note that the cavity is represented by the area in white (less light attenuation has occurred) at the top of the image.

Saline Filled Cavity

Figure 8 shows the effect of adding 1cc of saline to the central cavity of the PVA-C phantom. The result is similar to the result obtained with an empty cavity; there is less attenuation of light in the region of the cavity filled with saline than the surrounding material. The difference in the amount of coloured area in the image is caused by the software reconstruction technique perceives more or less phantom material as real breast tissue.

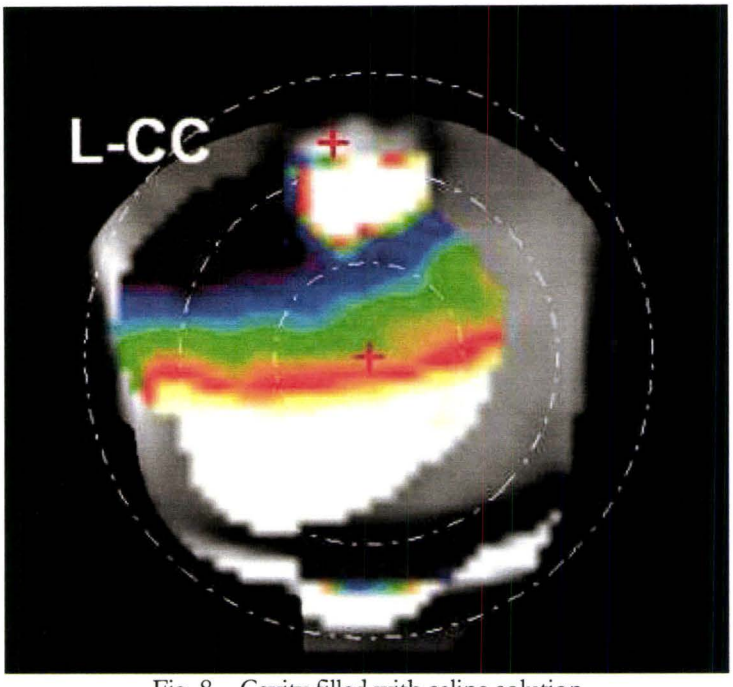

Fig. 8 – Cavity filled with saline solution

This figure shows the effect of adding 1cc of saline in the central cavity of the PVA-C phantom. The central cavity is located at the top of the image and is shown as a white circle. The white colour represents an area of less light attenuation.

4.3.3 Oxygenated Equine Blood

Figure 9 is an image of a half cylindrical phantom with 1cc of equine blood in the central cavity. This image shows less attenuation in the central cavity as compared to the rest of the phantom. The absorption and scattering of blood is primarily caused by hemoglobin. Blood consists of both oxyhemoglobin and deoxyhemoglobin. The absorption and reduced scattering coefficients of oxyhemoglobin are 0.1 mm^{-1} and 1.8 mm^{-1}, respectively [65]. The absorption and reduced scattering coefficients of deoxyhemoglobin are 0.95 mm^{-1} and 1.8 mm^{-1}, respectively [65]. The above results were measure with an HCT of 33.2%. The absorption and reduced scattering coefficients of hemoglobin are similar to those previously mentioned in section 3.3.1 for PVA-C and India ink.

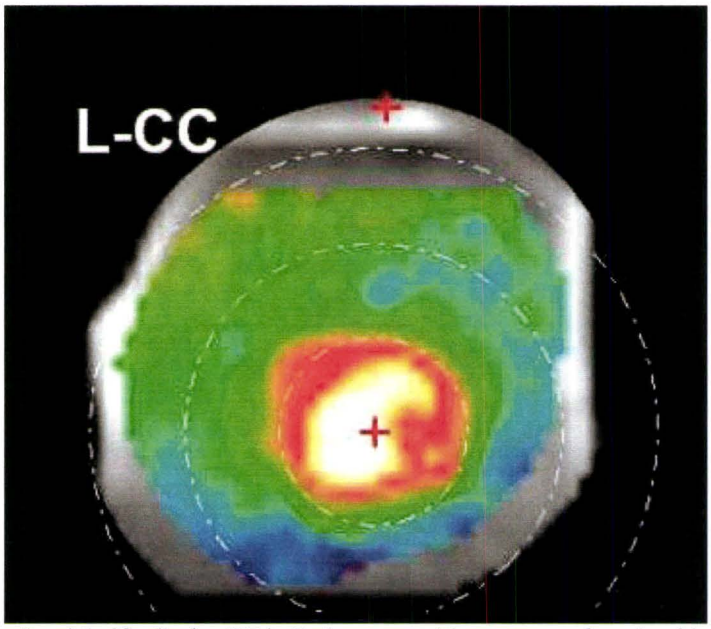

Fig. 9 – A half cylinder PVA-C phantom with oxygenated equine blood filling the 1cc cavity

A figure showing the light attenuation for a PVA-C phantom with 1cc of equine blood in a central cavity. The central region shows less attenuation, represented by the colour white, than the surrounding regions.

4.3.4 Deoxygenated Equine Blood

Figure 10 shows a half cylindrical PVA-C phantom which was filled with a mixture of equine blood and activated yeast. The yeast was used to deoxygenate the equine blood over the course of the scan. This was done to simulate what might occur if the tumourous vasculature was to partially collapse and trap blood in the tumourous region, which would then deoxygenate with time.

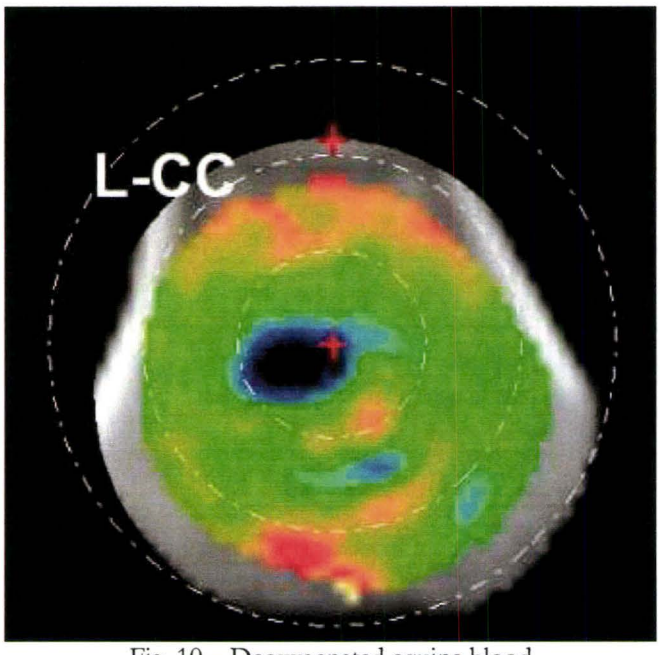

Fig. 10 – Deoxygenated equine blood

This figure shows a cavity that was filled with equine blood and deoxygenated with time using yeast. The deoxygenation process shows a greater attenuation of light (represented by the black/purple colour).

4.3.5 Removal of blood during compression

Figure 11 shows a half cylindrical PVA-C phantom which was filled with oxygenated equine blood and then slowly removed over the course of the scan during compression. This was done to simulate what might occur if the tumourous vasculature was completely collapsed and voided of all blood during the compression. The removal of blood during the compression aspect of the scan did not cause an increase in attenuation. Therefore the complete collapse of the vasculature during the compression aspect of the image sequence should not be responsible for the increased attenuation seen in malignant lesions. This was performed to support the theory that only a partial collapse of the vasculature occurs in malignant lesions.

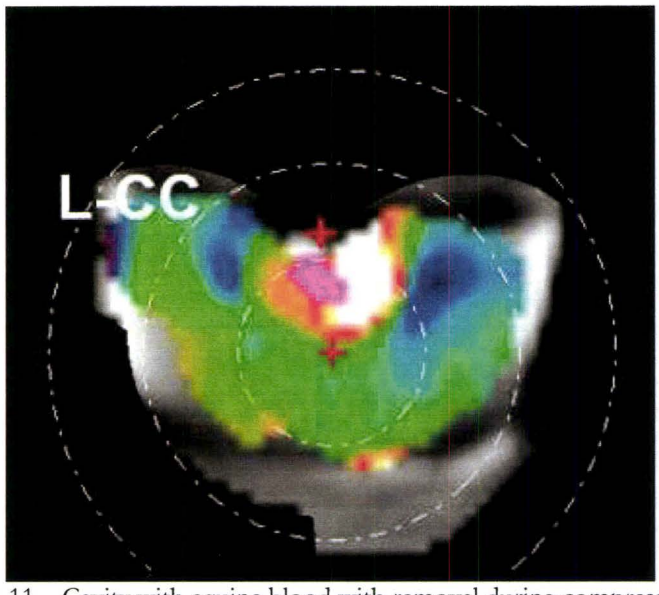

Fig. 11 – Cavity with equine blood with removal during compression

This figure shows the effect of removing the equine blood during the compression part of the scan. The white colour represents less attenuation in the cavity. This was done to demonstrate that the greater light attenuation seen in malignancies is not caused by the removal of blood from the malignant tumour.

4.4 Discussion

The double integrating sphere apparatus was used for the measurements presented in Figures 4 and 5. Figure 4 was a PVA-C mixture that had 50μL of India ink per 850mL and Figure 5 was a PVA-C mixture with 100μL of India ink per 850mL. In Figure 5, the absorption and reduced scattering coefficients at 640nm were 0.012 ± 0.002 mm^{-1} and 1.5 ± 0.2 mm^{-1} respectively. The higher absorption coefficient seen in Figure 5, compared to Figure 4, can be attributed to the larger concentration of India ink. The higher the amount of India ink, the less light is reflected and transmitted. Steady-state spatially resolved diffuse reflectance measurements were performed on the 100μL cylindrical PVA-C sample and the data are shown in Figure 6. It was found that the absorption and reduced scattering coefficients at 640nm were 0.017 ± 0.005 mm^{-1} and 1.3 ± 0.2 mm^{-1}, respectively. These measurements correlate well with the measurements provided by the double integrating spheres, suggesting that the thin film

measurements are a good surrogate for estimating the optical properties of similarly prepared large volume samples. Only the 100μL India ink PVA-C cylinder was measured using the spatially resolved system since the double integrating sphere apparatus was unable to provide useful absorption data for the 50μL India ink PVA-C samples due to poor sensitivity at very low absorption values. The above errors are the standard deviations from multiple independent measurements. Both the absorption and reduced scattering coefficients do not compare well with the previous studies. It has been shown previously that the freeze/thaw rate is a crucial aspect to the mechanical properties of the resultant PVA-C [2]. Both Devi *et al.* and Kharine *et al.* placed the samples in a freezer (-20°C) for 12 hours for the freeze process, and took the samples out and were left at room temperature for the thaw process. We believe the difference in the results is caused by the difference in the freeze/thaw rate. Our study uses a highly controlled freeze/thaw process of 0.1°C/min, whereas, Devi *et al.* and Kharine *et al.* have a highly uncontrolled freeze/thaw process. Our group has found that the freeze/thaw process, specifically the thaw rate, has significant effects on the mechanical properties of the resultant PVA-C.

Figure 7 shows a NIR image of the half cylinder with an empty 1cc cavity located in the middle of the phantom. This depiction reinforces our understanding of the optical absorption and the known geometry of the phantom. A cavity in the PVA-C phantom would cause there to be less material in that region, resulting in a decrease in light attenuation. A decrease in light attenuation is represented by the colour white in the image analysis software. Recall that this image is taken at the end of the dynamic scan, when the 10mmHg pressure has been applied for the longest time. The 10mmHg pressure applied by the soft air bladder of the ComfortScan™ system causes partial collapse of the air filled cavity and a decrease in the path length the NIR light travels. With less material to pass through, the NIR light would exhibit less attenuation during the dynamic aspect of the imaging sequence. Therefore, a cyst would be represented as an area of higher transmission when using the ComfortScan™ system.

Figure 8 shows a ComfortScan™ image of the half cylindrical PVA-C phantom with 1cc of saline in the central cavity. It was seen that there is a lower attenuation from the saline when compared to the surrounding PVA-C material. This would suggest that if the ComfortScan™ encountered a lesion such as a benign cyst it would present as an area of lower attenuation; this theory corresponds to the literature given by DOBI Medical. An area filled with fluid would be structurally weak and when under compression would partially collapse. This partial collapse would cause a smaller path length for the NIR light to travel, resulting in lower light attenuation.

Figure 9 shows a ComfortScan™ image of the half cylindrical phantom with 1cc of oxygenated equine blood in the central cavity. Once again, the image shows a white region where the cavity is situated. The central region with oxygenated blood does not attenuate the light as much of the surrounding PVA-C material. The absorption coefficient of the 100μL PVA-C phantom at 640nm was 0.012 ± 0.002 mm^{-1}, absorption coefficient for normal breast tissue cited by Ghosh et al. to be 0.079 ± 0.008 mm^{-1} at 640nm wavelength [68]. The reduced scattering coefficient found by Wang et al. [52] was approximately 1.2 at a wavelength of 640nm. This compares well to the values of reduced scattering coefficients for PVA-C found using a double integrating sphere measurement, 1.5 ± 0.2 mm^{-1}, and using a steady state spatially diffuse reflectance measurement, 1.3 ± 0.2 mm^{-1}.

By using the same half cylindrical phantom and filling the cavity with a different fluid, any differences seen in the ComfortScan™ image can be attributed to the fluid change. The next part of the experiment used deoxygenating blood, by way of activated Bakers' yeast added to oxygenated blood, to investigate how deoxygenated blood would present using the ComfortScan™ system.

Figure 10 shows a NIR image of the half cylindrical phantom with 1cc of deoxygenating equine blood in the central cavity. Note that the purple colour seen in the cavity region suggests a higher attenuation as compared to the PVA-C material. Recall that oxygenated blood is less attenuating than deoxygenated blood at a wavelength of 640nm [65]. Based on previous work from Kon et al. [69], it can

be inferred that the equine blood would have deoxygenated at a constant oxygen consumption velocity of approximately 2.5 μM/sec over the course of the 60 second scan. This measurement was used to simulate a malignancy which, during the compression aspect of the scan, may collapse the tumourous vasculature causing blood to be trapped and deoxygenate with time.

To ensure that the purple colour in the ComfortScan™ image was in fact a result of a higher concentration of deoxygenated blood, and not the total collapse of the tumourous vasculature, a scan was performed with blood in the cavity during the non-compression aspect and then blood was removed during the compression component of the scan. Figure 11 represents an image where the oxygenated equine blood was removed from the 1cc central cavity during the compression part of the scan. It was seen that the cavity appeared white, showing that there was less attenuation in the cavity as compared to the rest of the phantom. The pink area of the scan was caused by saturated pixels, which was likely due to the catheter that was situated in that region.

The measurements from Figure 10 and 11 were performed in order to determine if the ComfortScan™ system was detecting more attenuation from the presence of deoxygenated blood (as per Figure 10) or detecting more attenuation from the total collapse of the vasculature (as per Figure 11). The results suggest that the higher attenuation seen by the ComfortScan™ system was caused by the presence of trapped deoxygenating blood, rather than the total collapse of the tumourous vasculature.

A qualitative analysis of the ComfortScan™ images was performed to determine the relative signal attenuation for each scan. A quantitative measure was not performed since a different reconstruction algorithm would have been needed and this study was designed to test the current clinically approved algorithm. Three measurements were performed for all results to ensure reproducibility.

Figure 12 shows a sample ComfortScan™ image of a biopsy confirmed malignant lesion in a breast. This image was original published in a previous publication [58].

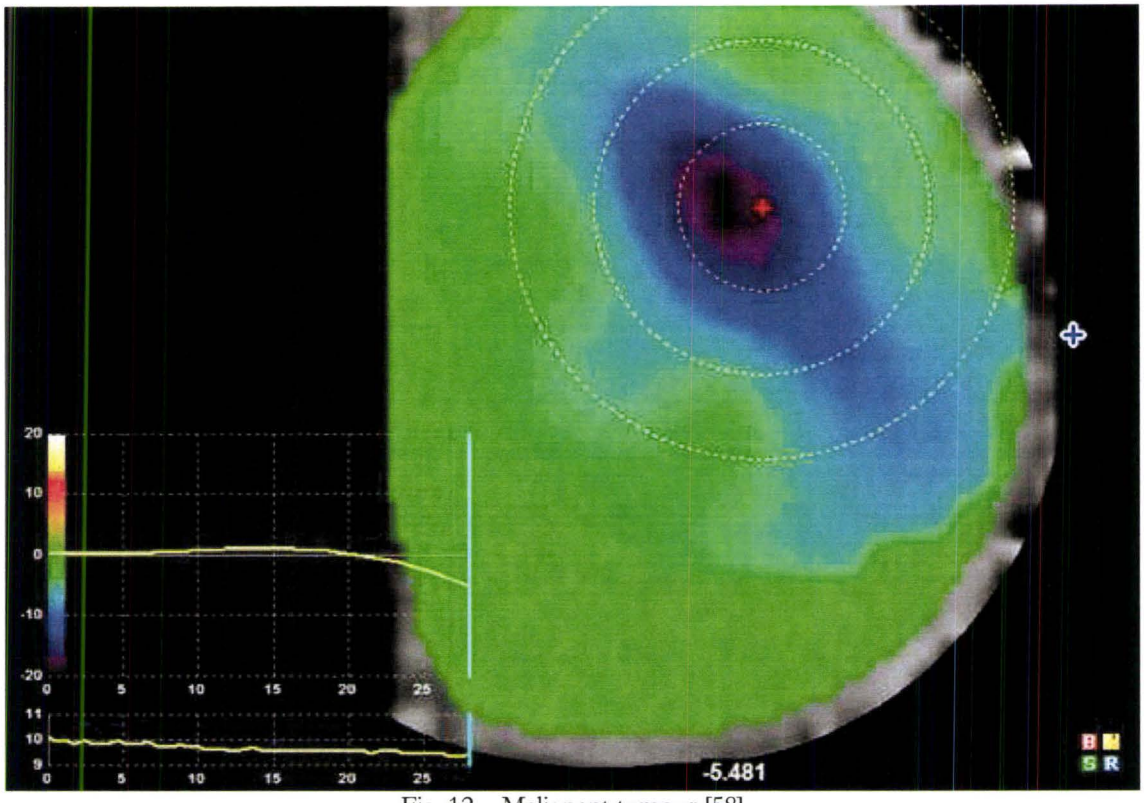

Fig. 12 – Malignant tumour [58]

This figure shows what a ComfortScan™ image of a malignant tumour looks like. The blue marker is the nipple position; the red marker is the suspicious region as identified by the mammogram. The purple region represents a region of higher attenuation, which is representative of the malignant tumour seen in this patient. This image has been provided by a previous publication using the ComfortScan™ system.

By comparing Figures 10 and 11 to how a malignant lesion is presented on the ComfortScan™ system (Figure 12), it can be deduced that although the deoxygenation of trapped blood and total collapse of vasculature may occur at the same time, the trapped blood deoxygenating over time would dominate to produce the higher attenuation of light that is seen in malignant lesions.

4.5 Conclusion

Using the double integrating sphere apparatus, the absorption and reduced scattering coefficients for the 100μL India ink PVA-C sample were 0.012 ± 0.002 mm^{-1} and 1.5 ± 0.2 mm^{-1}, respectively. All of the above optical measurements are quoted for a wavelength of 640 nm, which is the operational wavelength of

the ComfortScan™ system. The 100μL India ink PVA-C measurement was validated by using a steady-state spatially resolved diffuse reflectance apparatus. The latter apparatus found the absorption and reduced scattering coefficients at 640 nm were 0.017 ± 0.005 mm^{-1} and 1.3 ± 0.2 mm^{-1}, respectively. Several conclusions were drawn using a PVA-C breast mimicking phantom in the ComfortScan™ system. First, using saline solution or oxygenated equine blood results in less attenuation when compared to 5 FTC 15% PVA-C material in ComfortScan™ images. Next, the deoxygenation of blood caused higher attenuation of NIR light when compared to 5 FTC 15% PVA-C material in ComfortScan™ images. Lastly, the removal of blood during the compression part of the NIR scan resulted in less attenuation when compared to the surrounding 5 FTC 15% PVA-C material. Therefore the higher attenuation of NIR light seen in ComfortScan™ system images is caused by deoxygenated blood rather than the total collapse of the vasculature. It is postulated that the partial collapse of the tortuous malignant vasculature causes blood to deoxygenate with time and causes the higher attenuation in ComfortScan™ images. The ComfortScan™ system has been shown to be able to detect small changes in oxygenated blood and deoxygenated blood. A decrease of oxygenated blood during compression presented on the ComfortScan™ system as less attenuating than surrounding PVA-C; however, blood that was deoxygenating during the compression presented with greater attenuation.

4.6 Acknowledgements

We would like to thank Horizon Medical for their support with all of the imaging equipment used in this study. Also, we would like to thank George Counter and Julius Pekar for providing the double integrating sphere and the steady-state spatially resolved reflectance measurements, respectively.

4.7 References

1. Canadian_Cancer_Society. Breast Cancer Stats. 2010 [cited 2010 August 11]; Available from: www.cancer.ca

2. Wilson K. Characterization of MRI and Electrical Properties of Polyvinyl Alcohol Cryogel. *M.Sc. Thesis, University of Western Ontario, London, Ontario*, 2006.

3. Pogue BW, Patterson, MS. Review of tissue simulating phantoms for optical spectroscopy, imaging and dosimetry. *Journal of Biomedical Optics.* 2006, 11(4), 041102.

4. Peppas NA: Biomaterials Science: An Introduction to Materials in Medicine. *Academic Press Toronto* 1996.

5. Ratner BD, Hoffman AS: ACS Symposium Series. *American Chemical Society* 1985, 31:14.

6. Willcox PJ, Howie DW, Schmidt-Rohr K, Hoagland DA, Gido SP, Pudjijanto S, Kleiner LW, Venkatraman S: Microstructure of Poly(vinyl alcohol) Hydrogels Produced by Freeze/Thaw Cycling. *J. Polymer. Sci.: Part B: Polymer Physics*, 1999, 37: 3438-3454.

7. Stammen JA, Williams S, Ku DN, Guldberg RE: Mechanical Properties of a Novel PVA Hydrogel in Shear and Unconfined Compression. *Biomaterials* 2001, 22: 799-806.

8. Chu K, Jordan KJ, Battista JJ, VanDyk J, Rutt BK: Polyvinyl alcohol-Fricke Hydrogel and Cryogel: Two New Gel Dosimetry Systems with Low Fe 3 + Diffusion. *Phys. Med. Biol.* 2000; 45: 955-969.

9. Lukas LA, Surry KJ, Peters TM: Temperature dosimetry using MR relaxation characteristics of poly(vinyl alcohol) cryogel (PVA-C). *Magnetic Resonance Medicine* 2001; 46:1006–1013.

10. Surry KJM, Smith WL, Campbell LJ, Mills GR, Downey DB, Fenster A: The development and evaluation of a thre-dimentional ultrasound-guided breast biopsy apparatus. *In proceedings of Medical Image Computing and Computer-Assisted Intervention.* October 20021 6(3): 301-312.

11. Wtorek J, Stelter J, Nowakowski A, Ann NY: Impedance mammograph 3D phantom studies. *In proceedings of 10th International Conference on Electrical Bio-impedance.* April 1998; 873:520-533.

12. Counter, G. M.Sc. thesis McMaster University, Hamilton, Canada. 2010.

13. Devi, C. U., R. M. Vasu, and A. K. Sood. Design, fabrication, and characterization of a tissue-equivalent phantom for optical elastography. *Journal of Biomedical Optics* 2005 10.

14. Kharine, A., S. Manohar, R. Seeton, R. G. M. Kolkman, R. A. Bolt, W. Steenbergen, and F. F. M. De Mul. Poly(vinyl alcohol) gels for use as tissue phantoms in photoacoustic mammography. *Physics in Medicine andBiology.* 2005. 48, 357-370.

15. Nambu M: Japanese patent 56446, 1984

16. Watase M, Nishinari K, Nambu M: Anomalous increase of the elastic modulus of frozen poly(vinyl alcohol) gels. *Cryo-Letters* 1983; 4: 197-200.

17. Mano I, Goshima H, Nambu M, Iio M: New poly(vinyl alcohol) gel material for MRI phantoms. *Magn Reson Med* 1986;3:921–926.

18. Nagura M, Hamano T, Ishikawa H: Structures of poly(vinyl alcohol) hydrogel prepared by repeated freezing and melting. *Polymer* 1989;30: 762–765.

19. Wan W, Campbell G, Zhang Z, Hui A, Boughner D,J: Optimizing the tensile properties of polyvinyl alcohol for the construction of a bioprosthetic heart valve stent, *Biomed. Mater. Res .(Applied Biomater)* 2002, 63:854-861.

20. Peppas NA, Turbidimetric studies of aqueous poly(vinyl alcohol) solutions, Makromol. Chem. 1975. 176, pp. 3433–3440.

21. Surry KJM, Austin HJB, Fenster A, Peters TM: Poly(vinyl alcohol) cryogel phantoms for use in ultrasound and MR imaging. *Phys Med Biol.* 2004;49(24):5529-46.

22. Reich, G., Near-infrared spectroscopy and imaging: Basic principles and pharmaceutical applications. Advanced Drug Delivery Reviews, 2005. 57(8): p. 1109-1143.

23. Brooksby B, Pogue BW, Jiang S, Dehghani H, Subhadra S, Kogel C, Tosteson T, Weaver J, Poplack S, Paulsen K. Imaging breast adipose and fibroglandular tissue molecular signatures by using hybrid MRI-guided near-infrared spectral tomography. PNAS. 2006. 103:23, 8828-8833.

24. Bevilacqua F, Berger AJ, Cerussi AE, Jakubowski D, Tromberg BJ. Broadband absorption spectroscopy in turbid media by combined frequency-domain and steady-state methods. Applied optics. 2000 Dec 1;39(34):6498-507.

25. Cerussi A, Hsiang D, Shah N, Mehta R, Durkin A, Butler J, et al. Predicting response to breast cancer neoadjuvant chemotherapy using diffuse optical spectroscopy. Proceedings of the National Academy of Sciences of the United States of America. 2007 Mar 6;104(10):4014-9.

26. Cerussi A, Shah N, Hsiang D, Durkin A, Butler J, Tromberg BJ. In vivo absorption, scattering, and physiologic properties of 58 malignant breast tumors determined by broadband diffuse optical spectroscopy. Journal of biomedical optics. 2006 Jul-Aug;11(4):044005.

27. Cerussi AE, Berger AJ, Bevilacqua F, Shah N, Jakubowski D, Butler J, et al. Sources of absorption and scattering contrast for near-infrared optical mammography. Academic radiology. 2001 Mar;8(3):211-8.

28. Cerussi AE, Jakubowski D, Shah N, Bevilacqua F, Lanning R, Berger AJ, et al. Spectroscopy enhances the information content of optical mammography. Journal of biomedical optics. 2002 Jan;7(1):60-71.

29. Chance B, Nioka S, Zhang J, Conant EF, Hwang E, Briest S, et al. Breast cancer detection based on incremental biochemical and physiological properties of breast cancers: a six-year, two-site study. Academic radiology. 2005 Aug;12(8):925-33.

30. Chance B, zhao Z, wen S, Chen Y. Simple ac circuit for breast cancer detection and object detection. Rev Sci Instrum. 2006;77:064301.

31. Chen NG, Guo P, Yan S, Piao D, Zhu Q. Simultaneous near-infrared diffusive light and ultrasound imaging. Applied optics. 2001 Dec 1;40(34):6367-80.

32. Chen NG, Huang M, Xia H, Piao D, Cronin E, Zhu Q. Portable near-infrared diffusive light imager for breast cancer detection. Journal of biomedical optics. 2004 May-Jun;9(3):504-10.

33. choe r. Diffuse optical tomography and spectroscopy of breast cancer and fetal brain: University of Pennsulvania; 2005.

34. Durduran T, Choe R, Yu G, Zhou C, Tchou JC, Czerniecki BJ, et al. Diffuse optical measurement of blood flow in breast tumors. Optics letters. 2005 Nov 1;30(21):2915-7.

35. guo p, piao d, Zhu Q, fikiet j. A combined 2-D ultrasound and NIR imaging system. Proceedings of the IEEE 26th annual NE bioengineering conference; 2000 april 8-9; 2000. p. 77-8.

36. Holboke MJ, Tromberg BJ, Li X, Shah N, Fishkin J, Kidney D, et al. Three-dimensional diffuse optical mammography with ultrasound localization in a human subject. Journal of biomedical optics. 2000 Apr;5(2):237-47.

37. Hsiang D, Shah N, Yu H, Su MY, Cerussi A, Butler J, et al. Coregistration of dynamic contrast enhanced MRI and broadband diffuse optical spectroscopy for characterizing breast cancer. Technology in cancer research & treatment. 2005 Oct;4(5):549-58.

38. Jakubowski DB, Cerussi AE, Bevilacqua F, Shah N, Hsiang D, Butler J, et al. Monitoring neoadjuvant chemotherapy in breast cancer using quantitative diffuse optical spectroscopy: a case study. Journal of biomedical optics. 2004 Jan-Feb;9(1):230-8.

39. Jayachandran B, Ge J, Regalado S, Godavarty A. Design and development of a hand-held optical probe toward fluorescence diagnostic imaging. Journal of biomedical optics. 2007 Sep-Oct;12(5):054014.

40. Lanning RT. Non-invasive characterization of breast cancer using near infrared optical spectroscopy. UCI Undergraduate Research Journal II. 1999;2:43-9.

41. Liebert A, Wabnitz H, Steinbrink J, Moller M, Macdonald R, Rinneberg H, et al. Bed-side assessment of cerebral perfusion in stroke patients based on optical monitoring of a dye bolus by time-resolved diffuse reflectance. NeuroImage. 2005 Jan 15;24(2):426-35.

42. Liu Q, Luo Q, Chance B. 2D phased array fluorescence wireless localizer in breast cancer detection 2004.

43. Nioka S, Chance B. NIR spectroscopic detection of breast cancer. Technology in cancer research & treatment. 2005 Oct;4(5):497-512.

44. No K, PH C. Mini-FDPM and heterodyne mini-FDPM: handheld non-invasive breast cancer detectors based on frequency-domain photon migration. IEEE Trans Circuits Syst. 2005;52(December 12):2672-85.

45. No K, Xie Q, Chou P, Kwong R, Cerussi A, Tromberg B. In vivo breast cancer measurement with a handheld laser breast scanner. *The 50th IEEE international Midwest symposium on circuits and systems (MWSCAS).* Montreal Marriott Chateau Champlain Hotel 2007.

46. No K, Xie Q, Kwong R, Cerussi A, Tromberg B, Chou P. HBS: a handheld breast dyne. In Proceedings of IEEE BioCAS; 2006 November 29 - December 1; London: The British Library; 2006.

47. Sao V, Pourrezaei K, Akin A, Ayaz H. Breast tumor imaging using NIR LED based handheld continuous-wave imager. In: Reisman S FR, Mantilla B, editor. IEEE 29th annual NE bioengineering conference; 2003 March 22-23; 2003. p. 55-6.

48. Shah N, Cerussi A, Eker C, Espinoza J, Butler J, Fishkin J, et al. Noninvasive functional optical spectroscopy of human breast tissue. Proceedings of the National Academy of Sciences of the United States of America. 2001 Apr 10;98(8):4420-5.

49. Shah N, Cerussi AE, Jakubowski D, Hsiang D, Butler J, Tromberg BJ. Spatial variations in optical and physiological properties of healthy breast tissue. Journal of biomedical optics. 2004 May-Jun;9(3):534-40.

50. Wang J, Jiang SD, Li ZZ. In vivo quantitative imaging of normal and cancerous breast tissue using broadband diffuse optical tomography. Medical Physics. 2010. 37: 7, 3715-3724.

51. Ardeshirpour Y, Zhu QI. Optical tomography method that accounts for tilted chest wall in breast imaging. Journal of Biomedical Optics. 2010. 15: 4, 041515.

52. Wang YH, Yang HQ, Xie SS. Spectral characteristics of normal breast samples in the 250-850 nm wavelength range. Journal of Biomedical Optics. 2009. 29:10, 2751-2755.

53. Ardeshirpour Y, Huang MM, Zhu Q. Effect of the chest wall on breast lesion reconstruction. Journal of Biomedical Optics. 2009. 14:4, 044005.

54. Ermilov SA, Khamapirad T, Conjusteau A. Laser optoacoustic imaging system for detection of breast cancer. Journal of Biomedical Optics. 2009. 14: 2, 024007.

55. Erickson SJ, Godavarty A. Hand-held based near-infrared optical imaging devices: A review. Medical Engineering & Physics. 2009. 31:5, 495-509.

56. Tanamai W, Chen C, Siavoshi S. Diffuse optical spectroscopy measurements of healing in breast tissue after core biopsy: case study. Journal of Biomedical Optics. 2009. 14:1, 014024.

57. Poellinger A, Martin JC, Ponder SL. Near-infrared laser computed tomography of the breast: First clinical experience. Academic Radiology. 2008. 15:12, 1545-1553.

58. Wilson K, Dhamanaskar K, Minuk T, Moran G. Pilot Study Investigating the Potential use of Dynamic Optical Breast Imaging in Breast Cancer Detection. Accepted - Canadian Association of Radiologists Journal. 2010.

59. Delpy DT, Cope M. Quantification in tissue near-infrared spectroscopy. Philosophical Transactions of the Royal Society B: Biological Sciences. 1997 June: 29; 352(1354): 649-659.

60. Athanasiou A, Vanel D, Balleyguier C, Fournier L, Mathieu MC, Delaloge S, et al. Dynamic optical breast imaging: a new technique to visualise breast vessels: comparison with breast MRI and preliminary results. European journal of radiology. 2005 Apr;54(1):72-9.

61. Fournier LS, Vanel D, Athanasiou A, Gatzemeier W, Masuykov IV, Padhani AR, et al. Dynamic optical breast imaging: a novel technique to detect and characterize tumor vessels. European journal of radiology. 2009 Jan;69(1):43-9.

62. Hyde D E, Farrell T J, PattersonMS andWilson B C. A diffusion theory model of spatially resolved fluorescence from depth-dependent fluorophore concentrations Phys. Med. Biol. 2001. 46 369–83

63. Diamond KR, Farrell TJ, Patterson MS. Measurement of fluorophore concentrations and fluorescence quantum yield in tissue-simulating phantoms using three diffusion models of steady-state spatially resolved fluorescence. Phys Med Biol. 2003;48(24):4135–49.

64. Spengler MI, Bertoluzzo SM, Catalani G, Rasia ML. Study on membrance fluidity and erythrocyte aggregation in equine, bovine, and human species. Clinical Hemorheology and Microcirculation. 2008. 38: 171-176.

65. Friebel M, Netz U, Meinke M. Influence of oxygen saturation on the optical scattering properties of human red blood cells in the spectral range 250 to 2000 nm. Journal of Biomedical Optics. 2009. May-Jun; 14: 3, 034001.

66. Chance B, Leigh JS, Miyake H, Smith DS, Nioka S, Greenfeld R, Finanader M, Kaufmann K, Levy W, Young M, Cohen P, Yoshioka H, Boretsky R. Comparison of time-resolved and –unresolved measurements of deoxyhemoglobin in the brain. Proceedings of National Academy of Science. USA. July 1988. Vol 85, pp 4971-4975.

67. Liu H, Miwa M, Beauvolt B, Wang NG, Chance B. Characterization of absorption and scattering properties of small-volume biological samples using time-resolved spectroscopy. Analytical Biochemistry. 1993. 213, 378-385.

68. Ghosh N, Mohanty SK, Majumder SK, Gupta PK. Measurement of optical transport properties of normal and malignant human breast tissue. Applied Optics. 2001. 40: 1.

69. Kon K, Maeda N, Sekiya M, Shiga T, Suda T. A method for studying oxygen diffusion barrier in erythrocytes: effects of haemoglobin content and membrance cholesterol. Journal of Physiology. 1980. 309, 589-590.

chapter 5

DISCUSSION

5.1 ACHIEVEMENT OF THE OBJECTIVES

The objectives reported earlier in this thesis were accomplished in Chapters 2, 3 and 4. In this section the objectives are examined once again and a summary of the relevant findings is given.

[I] *to investigate whether performing a large clinical trial with the ComfortScan™ system would be warranted to further patient care and diagnostics for breast imaging.*

Based on a preliminary study with 19 patients, Chapter 2 demonstrates that no significant difference in diagnostic information ($p>0.05$) between mammography and ComfortScan™. Anecdotal evidence suggests cases where mammography disagreed with biopsy, whereas ComfortScan™ agreed, though these were not statistically significant. Based on these encouraging results, a large scale clinical trial was launched to investigate the potential widespread use of the ComfortScan™.

[II] *to determine if the ComfortScan™ system will achieve better correlation to biopsy than with mammography alone.*

Mammography agreed with biopsy in 18/33 and the ComfortScan™ system agreed with biopsy in 25/33 cases. By examining all 33 biopsy results, it was found that the sensitivity and specificity for the ComfortScan™ system was 83% and 67%, respectively. The sensitivity and specificity of mammography was 94% and 13%, respectively. Therefore, it was demonstrated that ComfortScan™ achieved a better agreement to biopsy than mammography alone.

[III] *to determine if the ComfortScan™ system would be beneficial as a mainstream method for a radiologist to diagnose breast cancer risk.*

The full study, found in Chapter 3, comprising 126 NIR images demonstrated a statistically significant difference in the diagnostic information from the ComfortScan™ and mammogram assessments ($p<0.05$). While the ComfortScan™ preliminary viability study performed by DOBI Medical International, only included women between 18 and 50 years of age, Chapter 3 has shown that the ComfortScan ™ can successfully image women aged 50 to 78 and correlate to mammogram and biopsy, when available. Furthermore, only BI-RADS 3 and 4 were included in the ComfortScan ™ preliminary viability study, whereas Chapter 3 has shown that inclusion of women with mammograms rated as BI-RADS 1-5 can also successfully correlate to mammography and biopsy, when available. Chapter 3 suggests that the ComfortScan™ could be used as a mainstream adjunct to mammography, providing information of vascularization, with advantages of increased patient comfort and the use of non-ionizing radiation.

[IV] *to evaluate the potential use of PVA-C as a breast mimicking material.*

Chapter 4 demonstrates that the absorption and reduced scattering coefficient of PVA-C matched that of breast tissues. The absorption coefficient of the 100μL PVA-C phantom at 640nm was 0.012 ± 0.002 mm^{-1}, which compares to typical absorption coefficients for tissue reported by Zhang et al. to be between 0.07 and 0.3 mm^{-1} [1]. Considering vascularization affects the optical properties of breast tissue, a good breast mimicking material would have the physical rigidity necessary to hold blood in a cavity and PVA-C has that capability. Furthermore, a properly constructed PVA-C phantom can be successfully recognized by the ComfortScan™ system, as if it were a real breast.

[V] *to validate the suggested mode of action of the ComfortScan™ system for detection of malignancies.*

The mode of action suggested by DOBI Medical for the ComfortScan ™ system is that a malignant tumour will highly attenuate light due to a partial collapse in the tumourous vasculature resulting in an increased deoxygenation over time. Using a PVA-C breast mimicking phantom it was shown that saline solution or oxygenated horse blood in a cavity (representative of a tumour) causes less attenuation than the surrounding phantom material; indicating that the simple presence of more oxygenated blood in a tumour is not causing the ComfortScan™ to register the region as malignant. Furthermore, by deoxygenating horse blood in the same cavity, there was an increase in the attenuation of 640 nm light as compared to the surrounding phantom material; which suggests that the colour representative of malignancies on the ComfortScan™ is caused by deoxygenating blood. It should be noted that by removing oxygenated horse blood during the compression aspect of the scan there was less attenuation than the surrounding phantom material, which means that it is not a change in volume of blood as a result of the compression that is recognized as a malignancy by the ComfortScan™ system. These two pieces of evidence suggest that the ComfortScan™ system is not recognizing a total collapse of the vasculature and subsequent void of blood from the tumour as the trigger for malignant detection. The mode of action suggested by DOBI Medical is supported by our findings.

5.2 Implications and Future Work

We were able to show the usefulness of the ComfortScan™ system as a beneficial adjunct to mammography during routine breast screening examinations. Currently, there are few ComfortScan™ systems clinically available; however, if there was an increase in popularity of the system, patient demand may aid in the introduction of the ComfortScan™ system into the clinical setting. More likely, we suggest the ComfortScan™ system may be more suited to a private fee-for-use environment, where additional voluntary screenings for peace of mind are commodities worth paying for.

More work should be done with randomized, double-blinded, larger scale clinical trials to closer approximate the true sensitivity and specificity for a patient population, before Health Canada would ever consider implementing this imaging modality into its vast public network of hospitals, and pay for the imaging from the public purse. Perhaps once more extensive studies on the ComfortScan™ system continue to demonstrate its effectiveness, it may be introduced into the clinical setting. The ComfortScan™ system's information on the vasculature could be used as a helpful tool to the radiologist to compliment the information obtained from mammography.

5.3 REFERENCES

[1] Zhang L, Wang Z, and Zhou. Determination of the optical coefficients of biological tissue by neural network. Journal of Modern Optics. 2010. 57: 13, 1163-1170.

Appendix I

The Changes in Magnetic Resonance Imaging Properties for Various Formulations of Polyvinyl Alcohol Cryogel at Different Field Strengths

KYLE WILSON[1*], GORDON CAMPBELL[3,4], GERALD R. MORAN[1,2,3], AND R. TERRY THOMPSON[2,3]

[1]*Medical Physics and Applied Radiation Sciences, McMaster University, Hamilton, Ontario, Canada*

[2]*Imaging Division, Lawson Health Research Institute, London, Ontario, Canada*

[3]*Department of Medical Biophysics, University of Western Ontario, London, Ontario, Canada*

[4]*Integrated Manufacturing Technologies Institute, NRC, London, Ontario, Canada*

Word Count: 4982

*Correspondence to: Kyle J. Wilson, Medical Physics and Applied Radiation Sciences, McMaster University, 1280 Main St. W., Hamilton, Ontario L8S 4K1, Canada. Phone: 905 525-9140 Ext. 26876 E-mail: wilsokj2@mcmaster.ca

ABSTRACT

When dealing with quality assurance and sequence development a realistic tissue mimicking MR phantom is extremely valuable. Polyvinyl Alcohol Cryogel (PVA-C) is a non-toxic material that has been shown to have MR relaxation characteristics similar to soft tissue. Our objective is to validate PVA-C as a viable human neonatal phantom material for both white and grey matter. In an attempt to vary the PVA-C relaxation times the percent PVA was varied between 3-30% by weight. These samples all underwent 1 freeze/thaw cycle (FTC). The T_1 and T_2 relaxation times were found to decrease with increasing percent PVA. At 1.89T and 3T the ranges were 0.68 ± 0.04 s$<T_1<1.85 \pm 0.02$ s and 0.058 ± 0.004 s$<T_2<0.47 \pm 0.02$ s. Both the T_1 and T_2 relaxation times showed no significant difference when comparing measurements at 1.89T and 3T. In phase two of the experiment, the concentration of PVA was held at 15% but underwent either: 1, 3, or 6 FTCs. It was shown that increasing the number of FTCs decreased T_1 and T_2 values by approximately 40% and 55%, respectively. To mimic normal neonatal tissue the range of both T_1 and T_2 must be further extended. The use of various additives to the PVA will be explored.

Keywords: PVA, cryogel, MRI, phantom

6.1 INTRODUCTION

Polyvinyl alcohol (PVA) is a material that has shown promise for many biomedical applications. If PVA is combined with water and heated to 90°C and then exposed to a freeze/thaw cycle (FTC) (from 20°C to -20°C then back to 20°C) a cryogel is produced (PVA-C). There is evidence in the literature that PVA-C is particularly well suited for use in imaging modalities such as ultrasound, electrical impedance tomography and magnetic resonance imaging (MRI) (1-3) because of its flexibility in mimicking different parameters. MRI will be the focus in this study.

In PVA-C, the mechanism responsible for cryogel formation is the hydrogen bonding induced by the thaw process (4). As the number of FTCs increases, the molecular motion in the gel is expected to become more restricted and the MR relaxation times (i.e. T_1 and T_2) should be sensitive to these changes. As the concentration of PVA increases, the density of hydrogen atoms available for hydrogen bonding during the thaw process increases. This should have two effects: i) the structure of PVA-C will change as the number of hydrogen bonds between groups change and ii) with the increased hydrogen bonding between the polymer and the water, the polymer structure will be altered, which should be evidenced by changes in the MR relaxation times (both T_1 and T_2). The change in the density of hydrogen atoms should be similar to those changes found in the various human tissues, thereby giving similar relaxation times.

There are large differences when comparing relaxation times of muscle, fat, and adult brain. Typical T_1 and T_2 values can range from 450 ms to 1950 ms and 40 ms to 275 ms, respectively, at 3 T (5-6). Williams et al. (7) found that, at 3 T, neonatal brain relaxation times can reach values as high as 2900 ms for T_1 and 280 ms for T_2 which extends the range even further. Thus in order to mimic the neonatal brain, a phantom must be designed and fabricated to cover a large range of possible relaxation times.

The effects of changing the number of FTC on MR relaxation times have been investigated by Chu and Rutt (8) on 15% (by weight) PVA-C (molecular weight and temperature during measurements were not given) at 1.5 T. The authors found that increasing the number of FTCs from 1 to 10 caused the relaxation times to decrease from approximately 810 ms to 470 ms (for T_1) and 90 ms to 40 ms (for T_2). Further, Mano et al. (9) were able to decrease both T_1 and T_2 by decreasing the percentage water (increasing percentage PVA), with measurements made at 20 MHz (~0.5T) with a sample temperature of 37^{0}C. The authors prepared samples ranging from 70-85 percent water and observed a direct linear relationship between relaxation time (either T_1 or T_2) and percent water. Relaxation times were similar to that of soft tissue (brain, spleen, muscle, liver). Mano et al. (9) did not provide details such as the molecular weight of the PVA used or how the freeze/thaw process was controlled - both of which could potentially affect the relaxation times.

Agarose is a more commonly used MRI phantom material (10-12). PVA-C is thought not only to have potential in mimicking relaxation times, but also in mimicking the electric, ultrasonic, and mechanical properties of tissue. Other work in our lab specifically investigates the use of PVA-C in mimicking electrical properties of tissue. Some promising preliminary electrical impedance results have been published (13). To our knowledge, agarose has not been shown to be able to mimic simultaneously the elastic, MRI, and electrical properties of various tissues. This further increases the potential usefulness of PVA-C. Having a phantom, such as PVA-C, which can mimic a number of different tissue properties would prove to be extremely beneficial.

The main objectives of this present study were to investigate the influence of the following 3 independent variables on relaxation times: (i) changing the number of FTCs from 1-6 for a PVA with a known molecular weight, (ii) changing the percentage PVA from 3-30%, and (iii) imaging at field strengths of 1.89 T and 3 T. The first objective was achieved by preparing 15% PVA-C samples with varying number of FTCs (1, 3, and 6) at controlled freeze-thaw rates and measuring

MR relaxation times (T_1, T_2). The second objective was addressed by preparing a 1 FTC PVA-C with variable percent PVA (3-30%) and measuring MR relaxation times. All measurements in objectives 1 and 2 were performed at both 1.89T and 3T in order to meet the third objective.

6.2 METHODS

6.2.1 PVA-C Manufacture:

In this study two sets of samples were prepared. For the first set, polyvinyl alcohol powder (molecular weight 146 – 186 kDa, 98-99% hydrolyzed, Sigma Aldrich, Oakville, Ontario, Canada) was mixed with de-ionized water to generate 8 concentrations of varying percent PVA: 3, 6, 10, 15, 17, 19, 25, and 30% PVA by weight. Two samples were prepared at each percentage PVA, giving a total of 16 samples. The mixture was heated to 90^{0}C in 2 hours using a standard reflux column and flask combination. A condenser unit was inserted into the top of the reflux column to help eliminate evaporation but the top of the reflux column had to be removed briefly to stir the mixture during heating. The resulting solution was then placed in water-tight, mini-puck shaped molds (homebuilt - 24mm diameter x 21mm high cylinders). The PVA samples were exposed to 1 FTC in a temperature controlled bath (VWR Scientific Products, Model #1187P). One FTC consists of decreasing the temperature from 20^{0}C to –20^{0}C at 0.1^{0}C/min, held at -20^{0}C for one hour, and then returning to 20^{0}C at a rate of 0.1^{0}C/min. The end caps for the molds were securely clamped in order to withstand the expansion resulting from the freezing process. The samples were then removed from the molds, stored in tap water, and refrigerated.

The second set of samples was prepared at a concentration of 15% PVA in a similar fashion as above using: 1, 3, and 6 FTCs. All measurement of MRI properties were made after storage in water for 4 weeks since it has been shown that swelling, as water is drawn into the cryogel matrix, should have equilibrated by this time (14-15).

6.2.2 Magnetic Resonance Imaging

Image based measurements of T_1 and T_2 were performed using separate 1.89 T and 3 T custom built MRI/MRS (Magnex Magnet and SMIS console). Imaging parameters were as follows: 96x96 matrix with 135mm FOV for 1.89T, and 96x96 matrix with a 200mm FOV for 3T. T_1 was measured using a 2D inversion recovery imaging sequence repeated with 30 different inversion times (TI), linearly spaced from 50ms to 4500ms (TR=15sec, TE=16ms). T_1 maps were created using pixel by pixel non-linear least square fit to the equation:

$$S(TI) = S_0 [1-2\exp(-TI/T_1)] \qquad [1]$$

A region of interest (ROI) was selected from the center of each sample and the average T_1 across the ROI was calculated.

T_2 was measured using a spin echo imaging sequence repeated with 20 different echo times (TE), which were linearly spaced from 17ms to 400ms (TR = 6 sec). T_2 maps were created using pixel-by-pixel log-linear least square fit to the equation:

$$S(TE) = S_0 \exp(-TE/T_2) \qquad [2]$$

A ROI was selected from the center of each sample and the average T_2 across the ROI was calculated.

In order to investigate the possible relaxation mechanisms in the PVA-C, both the relaxation times and rates are plotted. All measurements were made at ambient temperature.

6.2.3 Statistics:

Standard deviations were calculated using the ROI's sampled from either T_1 or T_2 maps. Using a linear regression analysis, R1 ($1/T_1$) at 1.89T, R1 at 3T, R2 ($1/T_2$) at 1.89T, R2 at 3T were all compared against percent PVA.

A measure of reliability was performed using an intra-class correlation analysis. This was to facilitate comparisons between R1 values at 1.89 T and 3 T. This means that the R1 values at 1.89 T were compared to the R1 values at 3 T. This analysis was repeated for R2 values at 1.89 T and 3 T. Similarly, this means that the R2 values at 1.89 T were compared to the R2 values at 3 T. All statistical analysis was performed using SPSS Release 13.0 (SPSS, SPSS Inc., Chicago USA). Significance was assumed when $p<0.05$.

Because no field dependence in R2 and R1 was observed, further analysis was performed. First a linear regression analysis was performed on the difference in R1 at 3T and 1.89T (which is called ΔR1 and shown in equation 2.3) against the percent PVA. This was done in order to examine any subtle differences in R1 between the two fields.

$$\Delta R1 = (R1 \text{ at } 3T) - (R1 \text{ at } 1.89T) \qquad [3]$$

A linear regression analysis of the ΔR2 against the percent PVA was executed. Again, this was performed to examine the existence of any subtle differences in R2. The equation for ΔR2 is given below.

$$\Delta R2 = (R2 \text{ at } 3T) - (R2 \text{ at } 1.89T) \qquad [4]$$

To investigate differences in T_1 when comparing field strength or number of FTCs a two-way ANOVA was performed. A two-way ANOVA was also performed to investigate differences in T_2 when comparing field strength and number of FTCs.

6.3 RESULTS

The physical characteristics were noticeably different between various percent PVA samples. At 3% PVA, the PVA-C was very soft (although did hold shape) and nearly transparent, with a jelly-like texture. In contrast, the 30% PVA-C was opaque, bearing a texture similar to rubber.

6.3.1 Relaxation Measurements:

R1 is shown in Figure 1 and R2 in figure 2 at 1.89T and 3T for the various percent PVA samples. There was an increase in both R1 and R2 with increasing percent PVA with significance of $p<0.001$ and $p<0.01$, respectively, at both 1.89T and 3T. These p values were obtained using a correlation analysis between R1 or R2 and percent PVA (first 4 points only). Following this point, there is a discontinuity in the linear approach which may be due to the volume of bound water approaching the free water volume (see discussion), shown in Figures 1 and 2. It was found that the two field strengths (all of the data points) were highly correlated for both R1 and R2 with intraclass correlation values of 0.99 and 0.976, respectively.

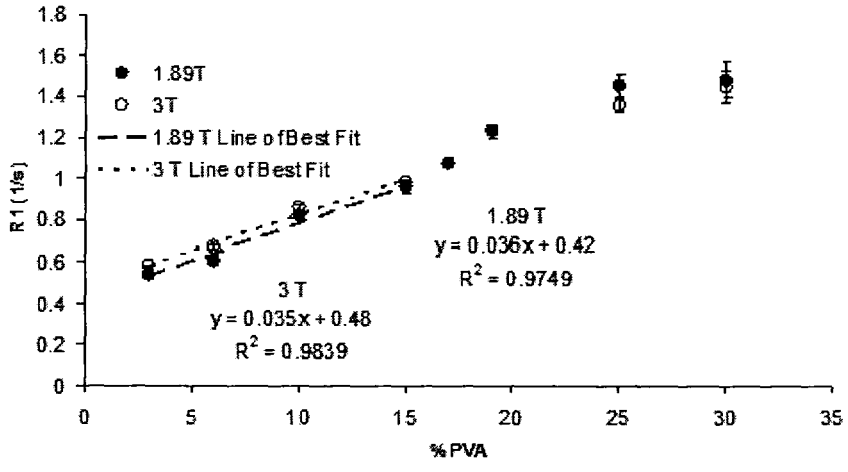

Fig. 1 – Change in R1 with percent PVA for sample set 1 (had undergone 1 FTC). There was an increase in R1 with increasing percent PVA at both 1.89T and 3T. There appeared to be a plateau at high percent PVA where an increase in percent PVA did not cause a rise in R1. Error bars represent ± 1 SD. The lines of best fit for 3-15% PVA samples are given for both field strengths.

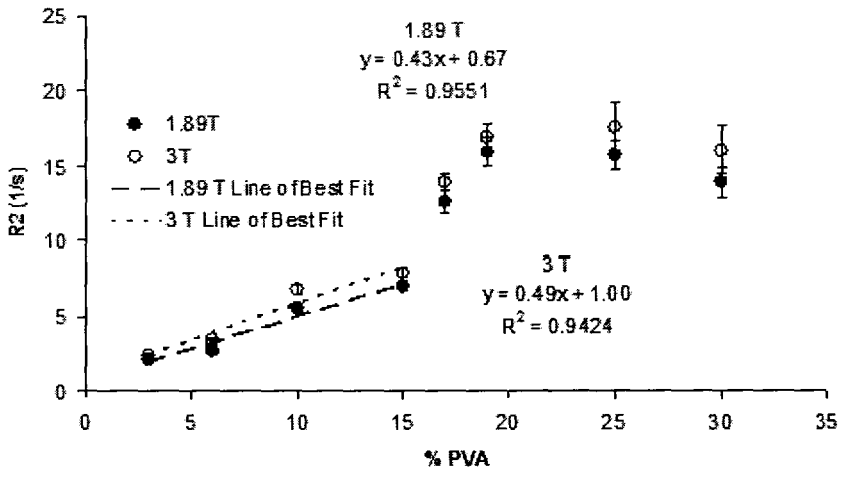

Fig. 2 – Change in R2 with percent PVA for sample set 1 (had undergone 1 FTC). With an increase in percent PVA there is an increase in R2 at both 1.89T and 3T. There was a plateau at high percent PVA, at which further increases in percent PVA did not increase the R2. Error bars represent ± 1 SD. The lines of best fit for 3-15% PVA samples are given for both field strengths.

The changes in relaxation times for all PVA samples are shown in Figures 3 and 4. This is the same data as before but represented as relaxation times rather than relaxation rates. There is a decrease in both relaxation times with increasing percent PVA as expected from the relaxation rate data. Note that there is a change in the linear relationship between 15% and 20% PVA. (See Discussion)

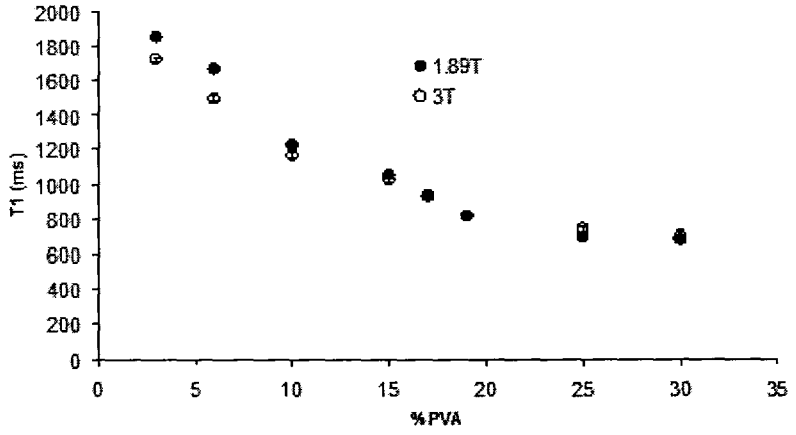

Fig. 3 – Change in T_1 with percent PVA for sample set 1 (1 FTC). With an increase in percent PVA there is a decrease in T_1 at both 1.89T. There appears to be a limit at which increases in percent PVA did not result in further decreases in T_1. Error bars represent ± 1 SD.

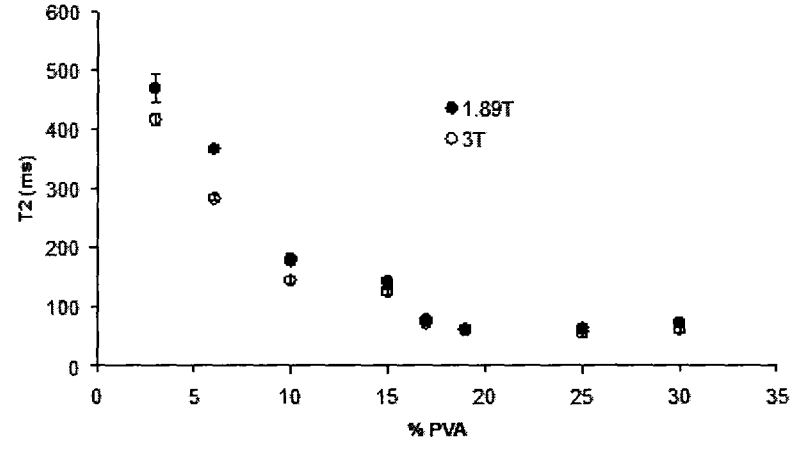

Fig. 4 - Change in T_2 with percent PVA for sample set 1 (1 FTC). There was a decrease in T_1 with increased percent PVA at both 1.89T and 3T. There was a limit at which increases in percent PVA did not result in further decreases in T_1. Error bars represent ± 1 SD.

Figures 5 and 6 show how the relaxation times change with increasing number of FTCs. The relaxation times decrease as the number of FTCs increases at both 1.89 T and 3 T.

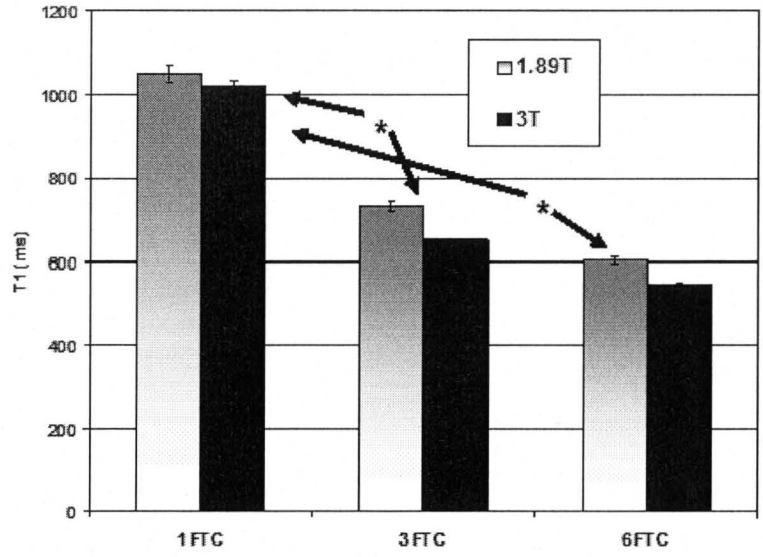

Fig. 5 - T_1 changes with increasing FTC number for a 15% PVA cryogel sample. Error bars represent ± 1 SD. * indicates significant difference at the $p<0.05$ level. There was no significant difference in T_1 for field strength. There was significant difference in T_1 when comparing the 1 FTC data to either the 3 FTC or 6 FTC data at both 1.89 T and 3 T. There was no significant difference in T_1 when comparing the 3 FTC data to the 6 FTC data at 1.89 T and 3 T. Difference was determined using a 2 way ANOVA.

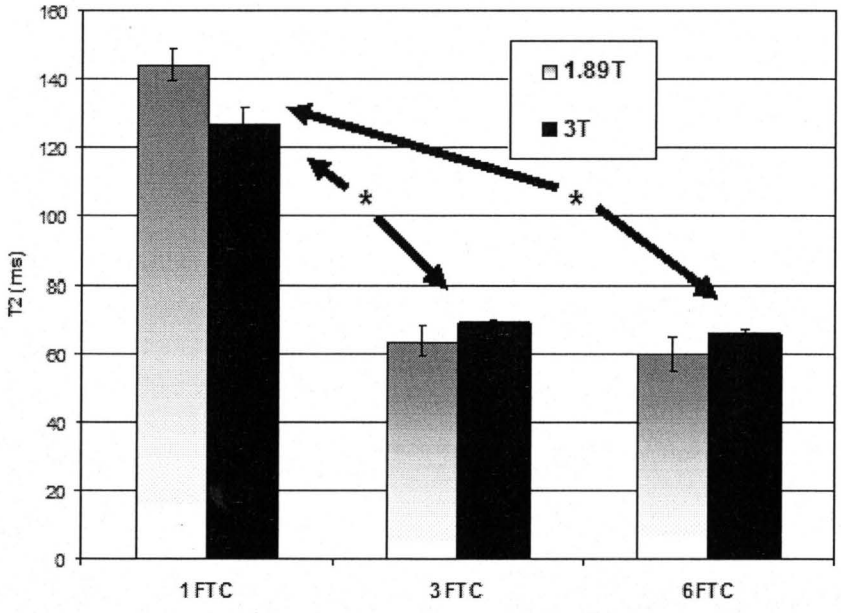

Fig. 6 - T_2 decreased with increasing FTC number for a 15% PVA cryogel sample. Error bars represent ± 1 SD. There was no significant difference in T_2 when comparing field strengths. There was significant difference when comparing the 1 FTC samples with the 3 and 6 FTC samples, but no significant difference in T_2 when comparing 3 and 6 FTCs samples. Difference was determined using a 2 way ANOVA.

Table 1 shows that there were significant linear relationships between the relaxation rates (R1 and R2) and the percent PVA at both field strengths. It also shows that the differences in R1 or R2 were also significantly related to percent PVA.

Table 1

Results of the linear regression analyses of first 4 data points

	Slope mean ± SD	Intercept mean ± SD	r square	Significance
R1 vs %PVA at 1.89T	0.04 ± 0.01	0.42 ± 0.01	0.97	p<0.001
R1 vs %PVA at 3T	0.03 ± 0.03	0.48 ± 0.01	0.98	p<0.001
R2 vs %PVA at 2T	0.43 ± 0.03	0.67 ± 0.07	0.79	p<0.01
R2 vs %PVA at 3T	0.49 ± 0.05	1.00 ± 0.06	0.84	p<0.01
deltaR1 vs %PVA	-0.01 ± 0.02	0.08 ± 0.01	0.72	p<0.01
deltaR2 vs %PVA	0.57 ± 0.04	0.29 ± 0.07	0.8	p<0.01

6.4 DISCUSSION

This is the first study to consider the effects of PVA concentration from 3 - 30% on MR relaxation times. A significant linear relationship was found between percent PVA and both R1 and R2 at 1.89 T and 3 T. Mano et al. (9) showed a similar trend between percent PVA (15-30%) and T_1 and T_2 at 20 MHz (~0.5T). Our values of T_1 and T_2 differ from Mano et al. (9), likely due to one or more of the following factors; FTC rate, Molecular Weight, temperature (Mano et al. (9) used 37 ^{0}C) and the Larmor frequency of the MR measurement. With our experimental parameters a plateau was observed in T_2 above 15% PVA. It appeared that a plateau was beginning to form for T_1 above 25% PVA. Two reasons can be proposed for these plateaus. Perhaps there is a limit to

the degree of entanglement that can occur or perhaps there is a limit to the amount of water that can be trapped within the gel. An experiment with gels of varying percentage water could be used to test the latter, being careful to weigh the samples before and after the freeze/thaw process. This would indicate whether at high percentage PVA the water is not able to be incorporated in the gel matrix and is being lost. Mano et al. (9) did not report any plateaus. All T_1 and T_2 data was fit well using equations 1 and 2, respectively. In order to examine the significance of this plateau in the relaxation rates/times it is useful to consider other work studying relaxation times in gels.

The present work indicated a decrease in relaxation times with increasing percent PVA. One possible mechanism for this decrease is that there is a decrease in bulk water and an increase in surface area for bound water with higher PVA content. In a gel (similar to PVA-C) Derbyshire and Duff (16) found that relaxation times for bound water protons are considerably shorter than those observed for bulk water. For PVA-C, the extent of hydrogen bonding between the carbon and hydrogen chains in the cryogel increases with the percentage PVA content and this likely creates longer chains that afford hydrogen bonding to the nearby water. A second possibility proposes that the structure of water beside a surface is dominated by that surface and the relaxation rates of this surface are modified (17). If there is rapid exchange between the surface layer and the bulk water, an average relaxation rate will result. Since we observe only a mono exponential decay it is likely that fast exchange between the bound and bulk water does occur and the shorter relaxation times of the bound water will greatly influence the measured relaxation time.

To further understand it is useful to look at the work of Derbyshire and Duff (16), who proposed a two compartment model, illustrated by equation [5], to explain the bulk and bound phases in gels. It is important to note that this model applies to situations where the amount of free water is much larger than the amount of bound water as shown by Woessner and Zimmerman (18).

$$\frac{1}{T} = \frac{1}{T_a} + \frac{hc}{1 - hc} \cdot \frac{1}{T_b + \tau_b} \qquad [5]$$

where T is the observed relaxation time, T_a is the relaxation of the bulk water, T_b is the relaxation time of the bound water, h is the amount of water hydrated by unit mass of macromolecule, c is the mass of solute per mass of solvent, and τ_b is the lifetime of the water molecule in the bound phase.

In the fast exchange limit, $\tau_b << T_b$, and in the regime where the concentration of PVA-C is small i.e. $hc << 1$ the equation reduces to:

$$R_{measured} = R_{free} + h \cdot c \cdot R_{bound} \qquad (6)$$

Where the rate (R) is simply the inverse of the relaxation time (T), i.e. (R=1/T). In both R1 ($1/T_1$) and R2 ($1/T_2$), a linear region as indicated by Equation 6 is observed below 15% PVA-C. The linear fit was performed on the samples only up to 15% PVA. Clearly by looking at Figure 2 it can be seen that there is a discontinuity in the linear fit of the data following 15% PVA. This may be the point where the amount of free water is no longer greater than the bound (required condition of the Derbyshire model) and therefore the data was only analyzed up to 15% PVA for both R1 and R2 to be conservative.

Considering the R1 measurements: the y-intercepts for the linear regression (on the 0-15% PVA samples) in Figure 1 for 189T and 3 T are 0.42 ± 0.01 s^{-1} (T_1=2.39 s) and 0.48 ± 0.01 s^{-1} (T_1=2.09 s), respectively. The y-intercept corresponds to the relaxation rate of the bulk or free water. These values are slightly larger than literature values which place the R1 of pure water at approximately 0.37 s^{-1} (T_1= 2.7 s) (19). There is a strong frequency dependence of water reported by Bryant et al. (20) which could account for the differences in relaxation times. Our values might also be slightly higher because the PVA-C samples were stored in tap water, not distilled or de-ionized water. Minute contaminants in tap water might artificially increase (decrease) the relaxation rate (time).

When examining the R2 data there is a significant linear relationship at 1.89 T and 3 T at low percent PVA (3-15%). The y-intercepts (from Figure 2) for the low percent PVA data are 0.67 ± 0.07 s^{-1} (T_1=1.49 s) and 1.00 ± 0.06 s^{-1} (T_1=1.00 s) at 1.89 T and 3 T, respectively. Again, these y-intercepts correspond to the relaxation rate of the free or bulk water. In pure water R1 and R2 would be equal (19) but it is evident that other processes are influencing R2 in the PVA-C as the rates are 50% higher than the R1 values.

The chemical structure of PVA has extensive hydrogen and hydroxyl entanglements that facilitate hydrogen bonding during the freeze/thaw process. An increase in the extent of hydrogen bonding with percent PVA could explain increases in R1 and R2 (decreases in T_1 and T_2). This mechanism has been proposed in a previous work showing a decrease in T_1 and T_2 with increasing number of FTCs (8, 21).

The trend observed in both T_1 and T_2 were similar to the changes seen by Chu et al. (8), but there were differences in the absolute values of the relaxation times. Using the same concentration PVA (15%), we report a range for T_1 and T_2 (602ms<T_1<1049ms; 60ms<T_2<143ms) (at 1.89T) and (546ms<T_1<1049ms; 66<T_2<126ms) (at 3T), produced by varying the number of FTCs between 1 and 6 with measurements taken at room temperature (18 ^{0}C – 24 ^{0}C). Whereas, Chu and Rutt (8) found a range for T_1 and T_2 of (470ms<T_1<810ms; 40ms<T_2<90ms) at 1.5T. Chu and Rutt (8) used freezing and thawing rates of 0.5^{0}C/min and 0.27^{0}C/min, respectively whilst a rate of 0.1^{0}C/min (for both freezing and thawing) was used here. Lukas et al. (22) compared 10% PVA, 1 FTC samples with different thawing rates. Lukas et al. (22) found that as the thawing rate increased the relaxation times (T_1 and T_2) decreased. This would explain why Chu and Rutt (8) found lower relaxation times. Lastly, the molecular weight of the PVA and the sample temperature during measurement were not reported by Chu and Rutt (8).

A significant increase in T_1 with increasing magnetic field was not observed in our study. Previous work (23) has shown that there is a field dependence in T_1 for various types of tissue by comparing measurements at 1.5T and 3T. Stanisz et al. (23) also showed that the percentage increase was different depending on the tissue in question. The percentage increase in T_1 could be as high as 73% (for kidney) or as low as 10% (for cartilage). The quantitative magnetization transfer (MT) data was fitted to a "2 pool" model (24-25) which investigated exchange between an unrestricted liquid pool and a restricted semisolid macromolecular pool. In this model, M_{OB} is the fraction of magnetization residing in the semisolid pool undergoing MT exchange. The M_{OB} for cartilage was the highest (17.1 $\pm$ 2.4%) and for kidney was one of the smallest (7.1 $\pm$ 1.0%). Therefore the larger the semisolid pool the smaller the T_1 field dependence. Just as cartilage demonstrated a smaller T_1 dependence (23) perhaps PVA-C has a larger semisolid pool (a large M_{OB}) and therefore would be expected to behave similarly. It was not done, however it would be very interesting to perform a magnetization transfer (MT) experiment for comparison.

6.5 CONCLUSIONS

At both 1.89T and 3T, it was shown that increasing percentage PVA will result in decreases to both T_1 and T_2 which have been also previously reported. There was evidence for a threshold over which further increases in percent PVA no longer resulted in decreased relaxation times. This plateau began at concentrations in excess of 15% PVA (for PVA-C prepared with 1 FTC and a FTR of 0.1°C/minute). Both the R1 and R2 were found to show no significant difference when comparing measurements at 1.89T and 3T. As the number of FTCs increased from 1 to 6 there was a significant decrease in both T_1 and T_2 values at 1.89T and 3T. It was concluded that there is fast exchange and therefore a mono-exponential for both the T_1 and T_2 relaxation curves. When comparing relaxation times (T_1 and T_2) at 1.89T and 3T, no significant difference was found. By

varying the percent PVA and the number of FTCs, there was a larger range of possible T_1 and T_2 relaxation times. More work is required to increase the T_1 times which would be particularly important when attempting to mimic neonatal brain where relaxation times are quite large. Future work will involve further manipulation of relaxation times, including investigating various additives to the gel matrix, in order to increase the versatility of potential phantoms. It was seen that by changing the percent PVA (from 3 – 30%) and the number of FTCs (1 – 6) it is possible to mimic typical soft body tissues.

6.6 ACKNOWLEDGEMENTS

We would like to thank Multi-Magnetics Incorporated (MMI) for use of MRI time on the 1.89T and 3T MRI facilities in London, Ontario.

6.7 REFERENCES

1. Surry KJ, Austin HJ, Fenster A, Peters TM. Poly(vinyl alcohol) cryogel phantoms for use in ultrasound and MR imaging. *Phys Med Biol* 2004; 49.24: 5529-5546.

2. Oh SH, Lee BI, Woo EJ, Lee SY, Kim TS, Kwon O, Seo JK. Electrical conductivity images of biological tissue phantoms in MREIT. *Physiol Meas* 2005; 26(2): S279-S288.

3. Muftuler LT, Hamamura M, Birgul O, Nalcioglu. Resolution and contrast in magnetic resonance electrical impedance tomography (MREIT) and its application to cancer imaging. *Technol Cancer Res Treat* 2004; 3(6): 599-609.

4. Mori Y, Tokura H, Yoshikawa M. Properties of hydrogels synthesized by freezing and thawing aqueous polyvinyl alcohol solutions and their applications. *Journal of Materials Science* 1997; 32: 491-496.

5. Stanisz GJ, Odrobina EE, Pun J, Escaravage M, Graham SJ, Bronskill MJ, Henkelman RM. T_1, T_2 relaxation and magnetization transfer in tissue at 3T. *Magn Reson Med* 2005; 54(3): 507-12.

6. Rakow-Penner R, Daniel B, Yu H, Sawyer-Glover A, Glover GH. Relaxation times of breast tissue at 1.5T and 3T measured using IDEAL. *J Magn Reson Imaging* 2006; 23(1): 87-91.

7. Williams LA, Gelman N, Picot PA, Lee DS, Ewing JR, Han VK, Thompson RT. Neonatal brain: regional variability of in vivo MR imaging relaxation rates at 3.0 T--initial experience. *Radiology* 2005; 235.2: 595-603.

8. Chu KC and Rutt BK. Polyvinyl alcohol cryogel: an ideal phantom material for MR studies of arterial flow and elasticity. *Magn Reson Med* 1997; 37.2: 314-319.

9. Mano I, Goshima H, Nambu M, Iio M. New polyvinyl alcohol gel material for MRI phantoms. *Magn Reson Med* 1986; 3.6: 921-926.

10. Olsrud J, Nilsson A, Mannfolk P, Waites A, Stahlberg F. A two-compartment gel phantom for optimization and quality assurance in clinical BOLD fMRI. *Magn Reson Imaging.* 2008; 26(2): 279-286.

11. Kato H, Kurado M, Yoshimura K, Yoshida A, Hanamoto K, Kawasaki S, Shibuya K, Kanazawa S. Composition of MRI phantom equivalent to human tissues. *Med Phys.* 2005; Oct: 32(10): 3199-3208.

12. Chen X, Astary GW, Sepulveda H, Mareci TH, Sarntinoranont M. Quantitative assessment of macromolecular concentration during direct infusion into an agarose hydrogel phantom using contrast-enhanced MRI. *Magn Reson Imaging.* 2008; Jun 24, epub.

13. Goharian M, Moran GR, Wilson K, Seymour C, Jegatheesan A, Hill M, Thompson RT, Campbell G. Modifying the MRI elastic stiffness and electrical properties of polyvinyl alcohol cryogel using irradiation. *Nucl Instr and Meth B* 2007; doi:10.1016/j.nimb.2007.04.111.

14. Paliy I, Gelman N, Campbell G, Winter J, Thompson RT. MRI Properties of Polyvinyl Alcohol Cryogel, Potential Material for Neonatal Brain Phantoms. *Proceedings of the International Society Mag Reson Med 13* 2005; 1296.

15. Tamura K, Ike O, Hitomi S, Isobe J, Shimizu Y, Nambu M. A new hydrogel and its medical application. *ASAIO Trans* 1986; 32(1): 605-608.

16. Derbyshire W, Duff ID. N.m.r. of Agarose Gels. *Faraday Discuss Chem Soc* 1974; 57: 243-254.

17. Outhred RK, George EP. A nuclear magnetic resonance study of hydrated systems using the frequency dependence of the relaxation processes. *Biophys J* 1973; 13(2): 83-96.

18. Woessner DE, Zimmerman JR. Nuclear transfer and anisotropic motional spin phenomena: relaxation time temperature dependence studies of water adsorbed on silica gel IV. *J Phys Chem* 1963; 67: 1590-1600.

19. Greenwood A, Bartusiak MF, Burke BA, Edelson E. Science at the Frontier. National Academy Press. Washington D.C. 1992.

20. Bryant RG, Mendelson DA, Lester CC. The magnetic field dependence of proton spin relaxation in tissues. *Magn Reson Med* 1991; 21.1: 117-126.

21. Peppas NA, Stauffer SR. Reinforced uncrosslinked poly(vinyl alcohol) gels produced by cyclic freezing-thawing processes: A short review. *J Controlled Release* 1991; 16: 305-310.

22. Lukas LA, Surry KJ, Peters TM. Temperature dosimetry using MR relaxation characteristics of poly(vinyl alcohol) cryogel (PVA-C). *Magn Reson Med* 2001; 46.5: 1006-1013.

23. Stanisz GJ, Odrobina EE, Pun J, Escaravage M, Graham SJ, Bronskill MJ, Henkelman RM. T_1, T_2 relaxation and magnetization transfer in tissue at 3T. *Magn Reson Med* 2005; 54: 507-512.

24. Henkelman RM, Huang X, Xiang Q-S, Stanisz GJ, Swanson SD, Bronskill MJ. Quantitative interpretation of magnetization transfer. *Magn Reson Med* 1993; 29: 759-766.

25. Morrison C, Stanisz GJ, Henkelman RM. Modeling magnetization transfer for biological-like systems using a semi-solid pool with a super-Lorentzian lineshape and dipolar reservoir. *J Magn Reson B* 1995; 108: 103-113.

Appendix II

MRI and Electrical Properties of Polyvinyl Alcohol Cryogel

KYLE WILSON[1*], MEHRAN GOHARIAN[1], ARAVINTHAN JEGATHEESAN[1], MICHAEL HILL[1], REBECCA E. THORNHILL[1], GORDON CAMPBELL[3,4], GERALD R. MORAN[1,2,3], AND TERRY R. THOMPSON[2,3]

[1]*Medical Physics and Applied Radiation Sciences, McMaster University, Hamilton, Ontario, Canada*

[2]*Imaging Division, Lawson Health Research Institute, London, Ontario, Canada*

[3]*Department of Medical Biophysics, University of Western Ontario, London, Ontario, Canada*

[4]*Integrated Manufacturing Technologies Institute, National Research Council, London, Ontario, Canada*

[*]Correspondence to: Kyle J. Wilson, Medical Physics and Applied Radiation Sciences, McMaster University, 1280 Main St. W., Hamilton, Ontario L8S 4K1, Canada. Phone: 905 525-9140 Ext. 26876 E-mail: wilsokj2@mcmaster.ca

ABSTRACT

Background:

Polyvinyl alcohol (PVA) is a unique polymer: an aqueous solution (hydrogel) of PVA can be stiffened by repeated freeze-thaw cycles (FTCs). The goal of this study was to investigate the effects of repeated FTCs on the MRI and electrical properties of PVA cryogel (PVA-C). The electrical properties of PVA-C were investigated using different molarities of NaCl in order to produce a material that models human tissue electrically.

Methods:

In this study 15% (by weight) of polyvinyl alcohol (molecular weight 146 – 186 kDa) powder was mixed with de-ionized water. Samples were prepared with either: 0 M, 0.1 M, or 1 M NaCl. The PVA samples then underwent either 3 or 6 freeze thaw cycles (FTC) in a temperature controlled bath. Measurements of T_1 and T_2 were performed using a 1.89T and 3T custom built MR systems. An Agilent 4294A Impedance analyzer was used to measure the complex impedance (resistance R, and reactance X), the complex admittance (G and B), and the capacitance were measured between 40Hz and 1MHz. Measurements of conductivity, permittivity and relaxation times were performed on each of the 3 samples to have better confidence in the results. Statistical tests, such as two way ANOVAs and t-tests, were used to determine significance in the results.

Results:

There was a significant decrease in T_1 with increasing FTCs. The T_1 and T_2 relaxation times were found to range from 602 ms – 827 ms and 64 ms – 86 ms, respectively, when looking all data (both 3 and 6 FTCs). The conductivity of 6 FTC PVA-C was significantly lower than 3 FTC PVA-C ($p<0.01$). The range of relative permittivities was

84.5 – $2.32*10^7$ (unitless). The addition of salt (NaCl) caused significant increases in conductivity and decreases in relative permittivity ($p<0.01$).

Conclusions:

Previous work has shown similar values for the relaxation times. Using PVA-C, the possible range of conductivities was 0.026 S/m to 1.07 S/m which compare well with the range in normal breast (0.22 S/m to 0.8 S/m). Similarly, the range of relative permittivities compare well to the range found in normal breast $2*10^4 – 1*10^5$.

7.1 BACKGROUND

Polyvinyl alcohol (PVA) is a polymer that can be formulated as a hydrogel with desirable properties for biomedical applications (1, 2). Although it can be cross-linked by chemical methods using glutaraldehyde or boric acid, PVA can be similarly hardened through a process of mesh entanglement by freezing (to -20 □ C) and thawing (termed PVA-cryogel or PVA-C) (3). This process of entanglement is distinctly different from traditional cross-linking and is directly related to the hydrogen bonding of the PVA hydrogel (4). Tissue mimicking phantoms made from PVA-C have been demonstrated to be suitable for: (a) MRI to simulate normal tissue (5), (b) temperature dosimetry in MRI (6, 7), and (c) simulations of ultrasound guided breast biopsy (8). Different methods of preparation must be attempted in order to improve the versatility of PVA-C. The most obvious are varying the: (a) number of "freeze/thaw cycles" (FTCs), (b) percentage of PVA, (c) freeze/thaw rate (FTR), and (d) molecular weight of PVA. Campbell et al. have further demonstrated that the electrical conductivity of PVA-C can be increased by adding water soluble salts (9). Additionally, PVA-C polymer offers the opportunity to meet the phantom requirements defined by Wtorek et al. (10), suitable for impedance imaging techniques, such as Electrical Impedance Tomography (EIT).

The long term goal of this research is to fabricate PVA-C for use in both medical devices and tissue mimicking phantoms for imaging research. A requirement for the imaging studies is that the phantom constructions mimic the biophysical properties of tissues for MRI and/or electrical impedance imaging modalities. The purpose of the present work is to explore the electrical and the magnetic properties of the PVA cryogel. In particular, we wish to determine how these properties will change as a result of multiple "freeze-thaw cycles" (FTCs).

Nambu (11) and Watase et al. (12) published the first reports of PVA cryogel formation. PVA-C was first proposed as a near-ideal material for MRI phantoms by Mano et al. (13) who examined the T_1 and T_2 relaxation times in relation to mouse soft tissues. It is known (14, 15) that the number of freeze-thaw cycles affects the elastic modulus of PVA-C, making the PVA-C stiffer with increased freeze-thaw cycles. It has been postulated (14) that this increase in elastic modulus is due to an increase in the extent of hydrogen bonding in the cryogel. During the first freeze-thaw cycle, a small proportion of the chain segments crystallize organizing themselves into 3-8 nm primary crystallite junctions with an irregular average spacing of about 30 nm. Increasing the number of freeze-thaw cycles increases the crystalinity and transforms the microstructure into a fibrillar network.

Surry et al. (16) measured T_1, T_2, and the elastic properties (speed of sound) of 10% PVA-C that had undergone one to four freeze-thaw cycles. Although 15% PVA-C will be expected to differ, the relaxation times are predicted to be of the same order of magnitude. In their MRI estimates, Surry and coworkers used inversion times (TI) that ranged from 50-3200ms to measure T_1, and echo times (TE) that ranged from 15-195ms to measure T_2 (16).

In this study, both the electrical and MR properties of PVA-C were investigated. The properties of PVA-C that had undergone 3 and 6 FTCs with various molarities of salt (NaCl) were examined. The hypothesis was that the introduction of different concentrations of salt (NaCl) into the PVA-C matrix will increase its conductivity and decrease its permittivity while the MRI properties will remain unchanged. For this feasibility study, we elected to use two molarities (0.1 M, 1 M) of NaCl that are an order of magnitude apart and bracket the osmolality of normal saline (0.16 M). These measurements are important in order to design a phantom to mimic the electrical properties of tissue, for example to simulate a cancerous tumour surrounded by healthy breast tissue. Given that conductivity is

the ability of a material to conduct electric current and permittivity is a measure of the ability of a material to resist the formation of an electric field within it, both of these properties will be important considerations when constructing an MRI tissue phantom.

In the present work 15%PVA samples subjected to either 3 or 6 FTCs and doped with either: 0 M, 0.1 M, or 1 M NaCl were evaluated in terms of their MR relaxation times, conductivity, and permittivity.

7.2 METHODS

PVA-C Manufacture:

In this study 15% (by weight) of polyvinyl alcohol (molecular weight 146 – 186 kDa) powder was mixed with de-ionized water. Samples were prepared with either: 0 M, 0.1 M, or 1 M NaCl. The mixture was heated to 90^0C in 2 hours with the use of a standard reflux column and flask combination. Contact with air was restricted to less than 3 minutes after removal from the enclosed flask in order to minimize evaporation, which would lead to inaccurate PVA concentration calculations. The resulting solution was then placed in water-tight, puck shaped molds (24mm diameter x 21mm thick cylinder). In the molds, the PVA samples then underwent either 3 or 6 freeze thaw cycles (FTC) in a temperature controlled bath. One FTC consists of decreasing the temperature from 20^0C to -20^0C and then returning to 20^0C at a rate of 0.1^0C/min. All molds were securely clamped in order to withstand the expansion that would otherwise result from the freezing process. The samples were then removed, stored in an air tight container, and refrigerated. It has been observed previously that PVA-C samples swell when stored in water, as water will be drawn into the cryogel matrix. This is an important factor to consider, especially since these samples have NaCl in them. For this reason, it was important to test whether the media in which the samples were stored modified the materials electrical properties. Samples of 3 and 6 FTC

PVA-C were manufactured containing either 0M or 0.1M salt. These samples were then stored in either distilled water or a saline solution (1 M) and the conductivity and permittivity were measured daily for 6 days, and then again at day 30.

MRI:

Measurements of T_1 and T_2 were performed using a 1.89T and 3T custom built MR systems. T_1 was measured using a 2D inversion recovery imaging sequence repeated with 9 inversion times (TI), which ranged from 20 ms to 1000 ms (TR=5.5 sec, TE=20 ms). Regions of interest (ROI) were drawn in the center of each sample and the average signal intensity at each TI was fitted to the equation:

$$S(TI) = S_o [1-2\exp(-TI/T_1)] \quad (1)$$

T_2 was measured using a spin-echo imaging sequence repeated with 6 echo times (TE), which ranged from 25 ms to 500 ms (TR=5.5 sec). ROIs were selected from the center of each sample and T_2 measurements were made by sampling the signal intensities at the various echo peaks and fitting to the following equation:

$$S(TE) = S_o \exp(-TE/T_2) \quad (2)$$

Impedance Analysis:

An Agilent 4294A Impedance analyzer (Agilent Technologies, Mississauga, ON) was first calibrated using a short fixture compensation as directed in the Agilent 16452A liquid test fixture manual. The liquid test fixture was assembled using a home-built 10mm spacer designed to accommodate the PVA-C samples. The PVA-C samples were washed in distilled water, then placed between the electrodes in the fixture, and the fixture sealed.

The impedance analyzer operates in the frequency range of 40Hz to 110MHz, however the liquid test fixture only operates accurately up to 30MHz. These initial tests were performed only between 40Hz and 1MHz to match the frequency range of interest in EIT experiments (1kHz to 1MHz).

Using the impedance analyzer, the complex impedance (resistance R, and reactance X), the complex admittance (G and B), and the capacitance were measured between 40Hz and 1MHz. The interface to the computer was via a LAN connection of the 4294A and the computer's Ethernet card using a home built LAN cross-over cable. Software was written in Excel 2002 (Service Pack 3) using a VisualBasic (version 6.3) script (Microsoft, Redmond, WA) to handle the calls to the impedance analyzer using Windows sockets.

The conductivity, σ, was calculated using:

$$\sigma = t / (AR_p) \qquad [3]$$

where t is the spacing between the electrodes, A is the electrode area (radius = 38.0mm), and R_p is the (parallel) resistance measured.

The permittivity, ε (the real part of the complex relative dielectric constant), was calculated using:

$$\varepsilon = (t\, C_p)/(A\, \varepsilon_o) \qquad [4]$$

where C_p is the parallel capacitance measured in the liquid fixture, and ε_o is the permittivity of free space.

Both the conductivity and the permittivity were measured four times in each of three identical samples (15). The data presented represents an average of these measurements.

Statistics:

Measurements of conductivity, permittivity and relaxation times were performed on each of the 3 samples to have better confidence in the results. Unless otherwise specified

the errors represent standard deviations. Standard deviations were calculated from averaging the 3 samples from each distinct PVA preparation. The specific measurements of the conductivity, permittivity and relaxation times were performed as described previously. Two 3 way ANOVAs were performed to investigate differences in relaxation times (T_1 and T_2) when examining effects of: salt concentration, number of FTCs, and field strength. For the storage media data, conductivities were calculated using equation 3, three or more times, and the standard deviation calculated. T-tests were then performed to evaluate significant difference. A two way ANOVA was performed to investigate the differences in permittivity, examining the effect of freeze thaw cycle and the addition of salt. The statistics were performed using MINITAB Release 13.32 (Minitab, Minitab Inc., Pennsylvania USA) and Microsoft Excel (Microsoft, Microsoft Canada Co., Ontario, Canada).

7.3 RESULTS AND DISCUSSION

The PVA-C samples that had undergone 6 FTCs were observed to be stiffer and more opaque than those that had undergone 3 FTCs. The MRI relaxation time measurements are summarized in Figures 1 and 2.

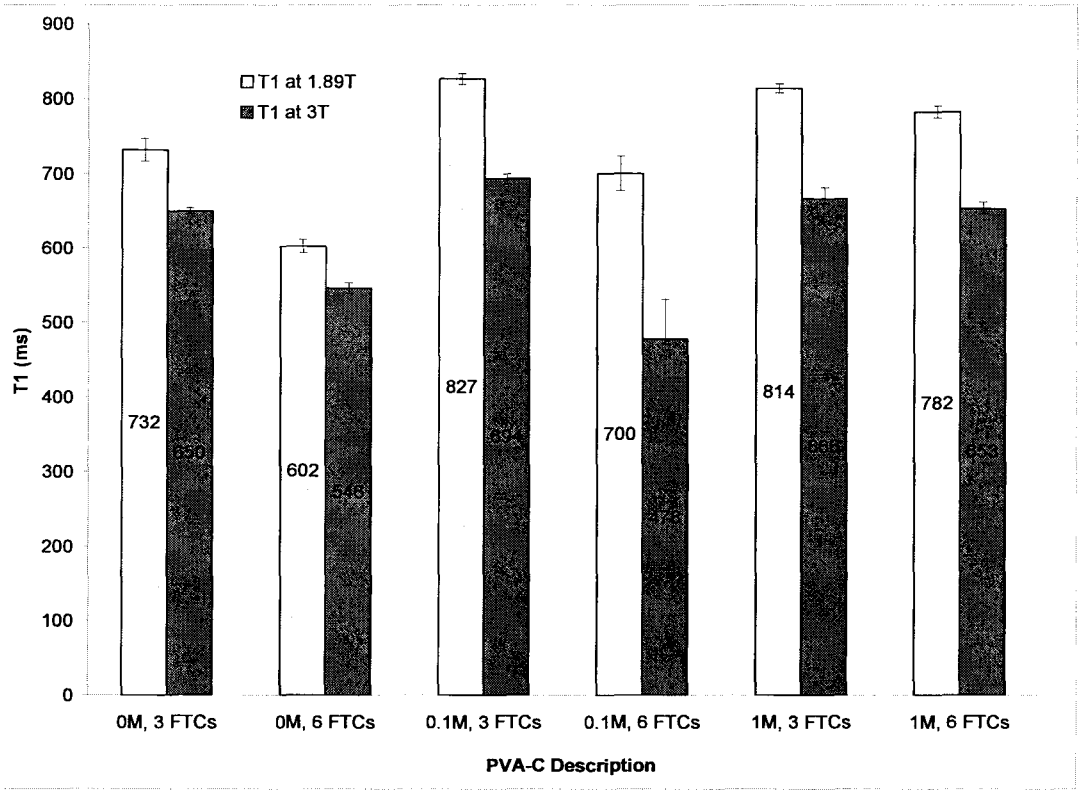

Figure 1: *T1 Relaxation time shown for 3FTC (Freeze Thaw Cycles) and 6FTC for 0M, 0.1M, and 1M salt concentrations, and both 1.89T and 3T.*

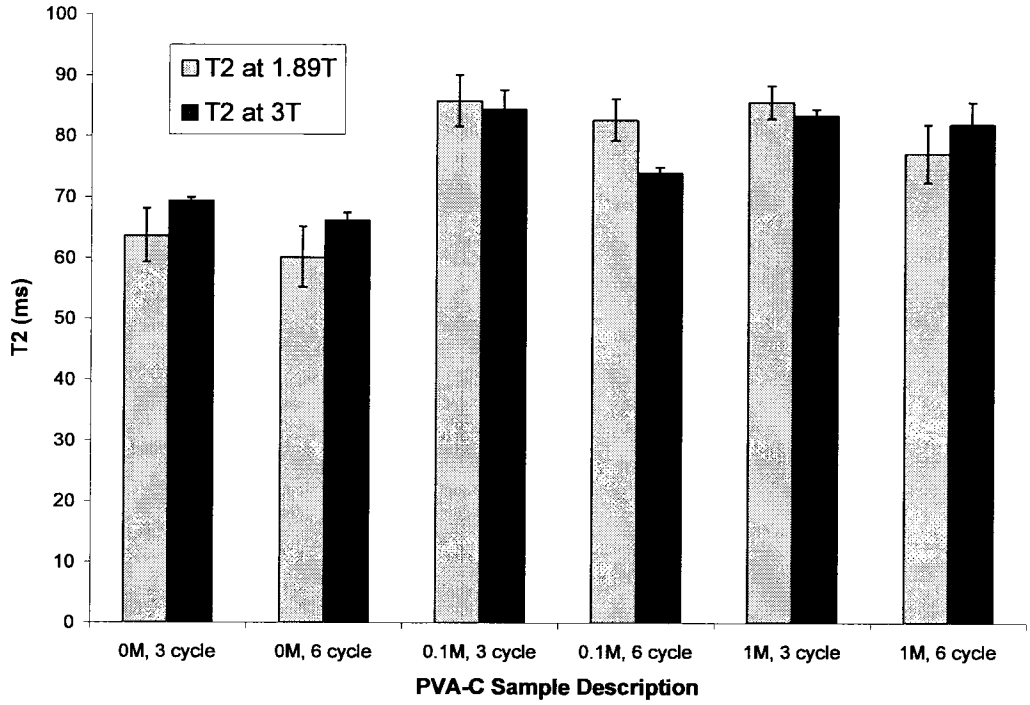

Figure 2: *T2 Relaxation time shown for 3FTC (Freeze Thaw Cycles) and 6FTC for 0M, 0.1M, and 1M salt concentrations, and both 1.89T and 3T.*

The T_2 relaxation time does not change within the error of the measurement with increased freeze-thaw cycles; however, overall T_1 significantly decreased ($p<0.05$) from 3 FTCs to 6 FTCs (values shown in Figures 1 and 2).

An ANOVA showed that salt concentration had a significant effect on T_1 value when comparing the 0M, 0.1M, and 1M 3 FTC samples ($p<0.01$). The effects of both the number of FTCs and the field strength on T_1 were significant ($p<0.01$ for each). The T_1 values at 1.89T ranged from 732 ± 29ms to 827 ± 13ms for 3 FTCs and 602 ± 18ms to 782 ± 16ms for 6 FTCs. The T_1 values at 3T ranged from 650 ± 8ms to 694 ±11ms for 3 FTCs and 478 ± 70ms to 653 ± 17ms for 6 FTCs.

An ANOVA showed that salt concentration also had a significant effect on T_2 values. There was significant difference in T_2 value when comparing the salt concentrations ($p<0.01$). Yet unlike T_1, neither field strength nor the number of FTCs had a significant effect on T_2. The T_2 values at 1.89T ranged from 64 $\pm$ 9ms to 86 $\pm$ 8ms for 3 FTCs and 60 $\pm$ 10ms to 83 $\pm$ 7ms for 6 FTCs. The T_2 values at 3T ranged from 69 $\pm$ 1ms to 84 $\pm$ 6ms for 3 FTCs and 66 $\pm$ 2ms to 82 $\pm$ 7ms for 6 FTCs.

The conductivity measurements of the samples before storage in any media are summarized in Figures 3 and 5. It can be seen from this plot that there is clearly a significant decrease in the conductivity with an increase in freeze thaw cycles from 3C to 6C ($p<0.05$). The conductivities of the 1M samples were significantly greater than either the 0 M or 0.1 M samples ($p<0.01$). The conductivities ranged from 0.026 $\pm$ 0.003 S/m to 1.07 $\pm$ 0.03 S/m for the 3 FTC samples. The conductivity does change less with frequency within the range from 40 kHz to 1 MHz however.

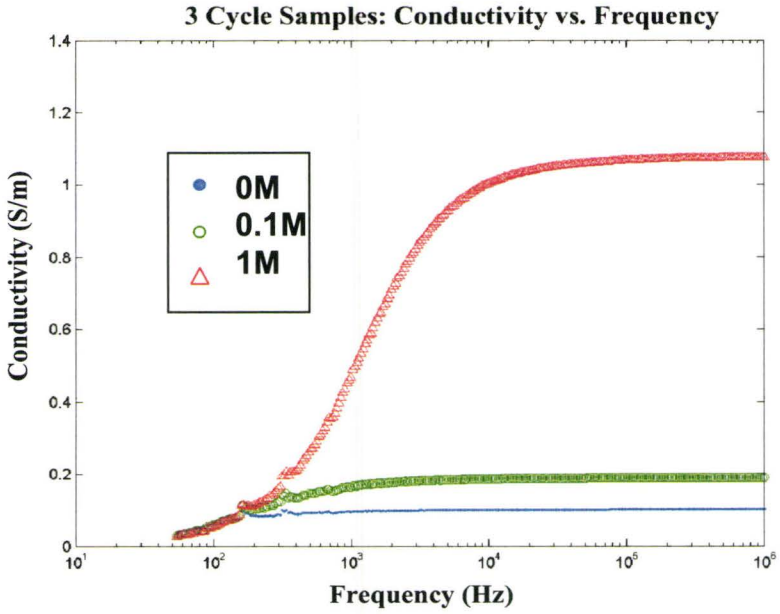

Figure 3: *Conductivity of 3FTC samples versus frequency. Shown here is a comparison of the 3 salt concentrations (0M, 0.1M, and 1M). Data shown is the mean of at least 3 different PVA samples. The standard deviation is within the size of the data marker.*

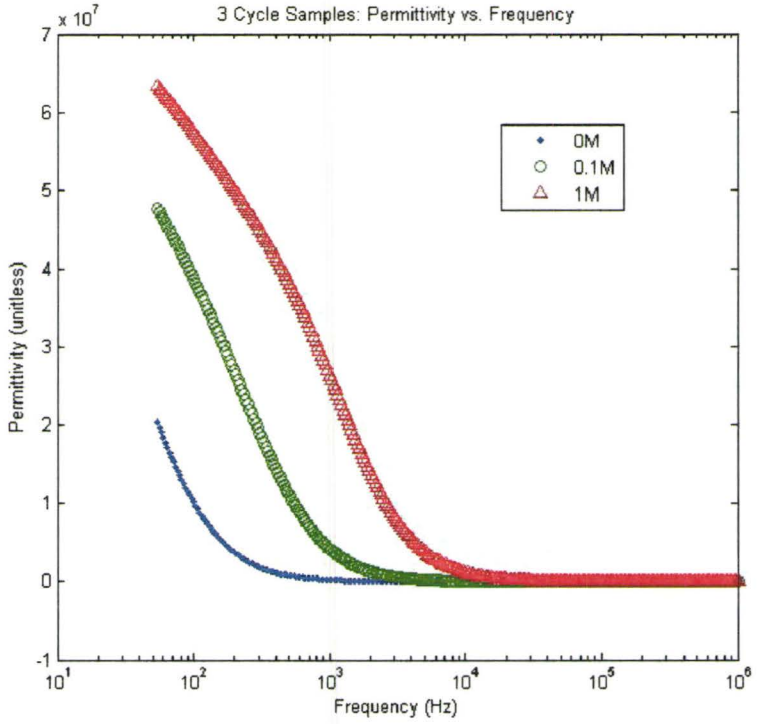

Figure 4: *Permittivity of 3FTC samples versus frequency. Shown here is a comparison of the 3 salt concentrations (0M, 0.1M, and 1M). Data shown is the mean of at least 3 different PVA samples. The standard deviation is within the size of the data marker.*

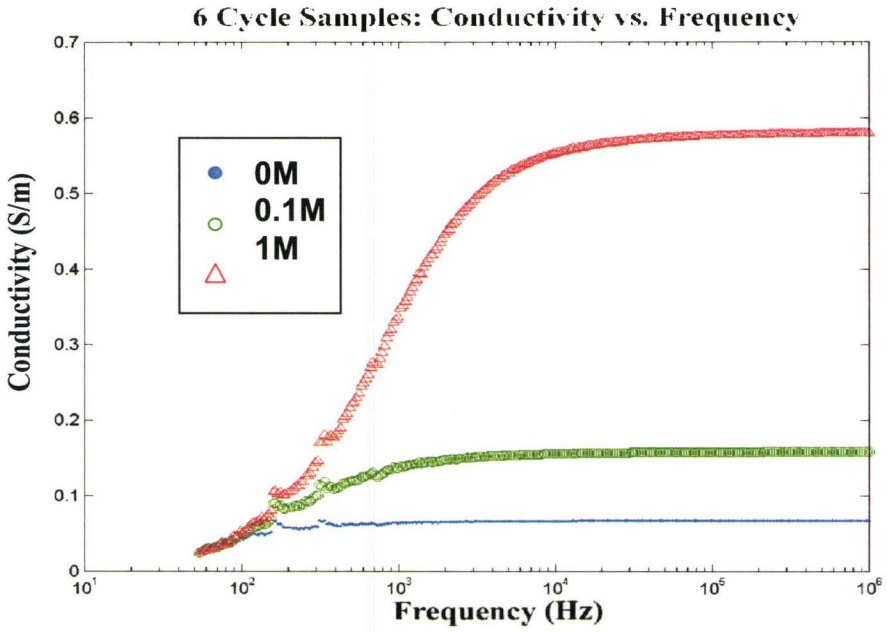

Figure 5: *Conductivity of 6FTC samples versus frequency. Shown here is a comparison of the 3 salt concentrations (0M, 0.1M, and 1M). Data shown is the mean of at least 3 different PVA samples. The standard deviation is within the size of the data marker.*

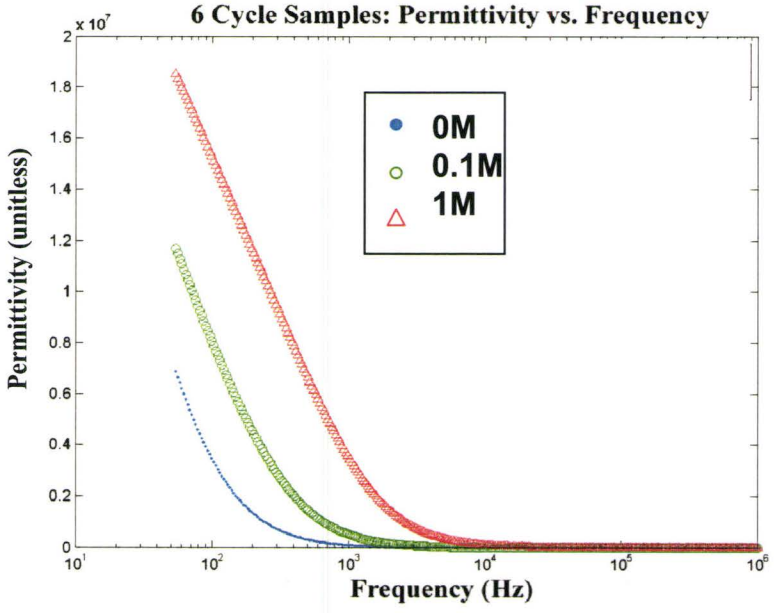

Figure 6: *Permittivity of 6FTC samples versus frequency. Shown here is a comparison of the 3 salt concentrations (0M, 0.1M, and 1M). Data shown is the mean of at least 3 different PVA samples. The standard deviation is within the size of the data marker.*

In Figures 4 and 6, the relative permittivity (unitless) for these same samples is plotted versus frequency. Note that in these figures, the permittivity spans several orders of magnitude. There appears to be a small decrease in the relative permittivity with increasing number of FTCs, but it is not significant. There was a significant increase in the permittivity with the addition of salt ($p<0.01$). At 1kHz, a two-way ANOVA indicates that there is not a significant change with freeze-thaw cycle, but that the change in permittivity is significant ($p<0.01$). For all samples the permittivity approached zero at high frequency (>2 kHz for 0 M and 0.1 M or >10 kHz for 1 M,). The permittivities ranged from 95.1 ± 0.1 to $(2.32 \pm 0.03)*10^7$ for the 3 FTC samples.

In Figures 7 and 8, the electrical data resulting from the storage of the samples in the two different media (water and saline) is presented.

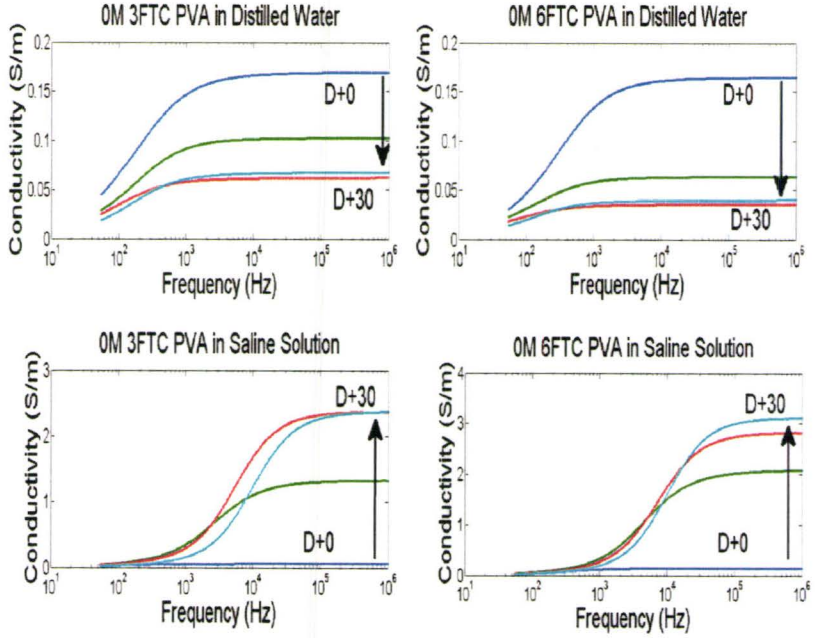

Figure 7: *"Storage Media Test A." In this set of figures, PVA manufactured without salt (0M 3FTC and 6FTC) are placed in either distilled water (top 2 subplots) or in 1M saline solution (bottom 2 subplots). Curves represent measurements taken before being placed in the medium, and day 2, day 6, and day 30 following. Note that the conductivity decreases slightly, probably by the uptake of water (top plots), however when placed in saline (bottom) the conductivity drastically increases.*

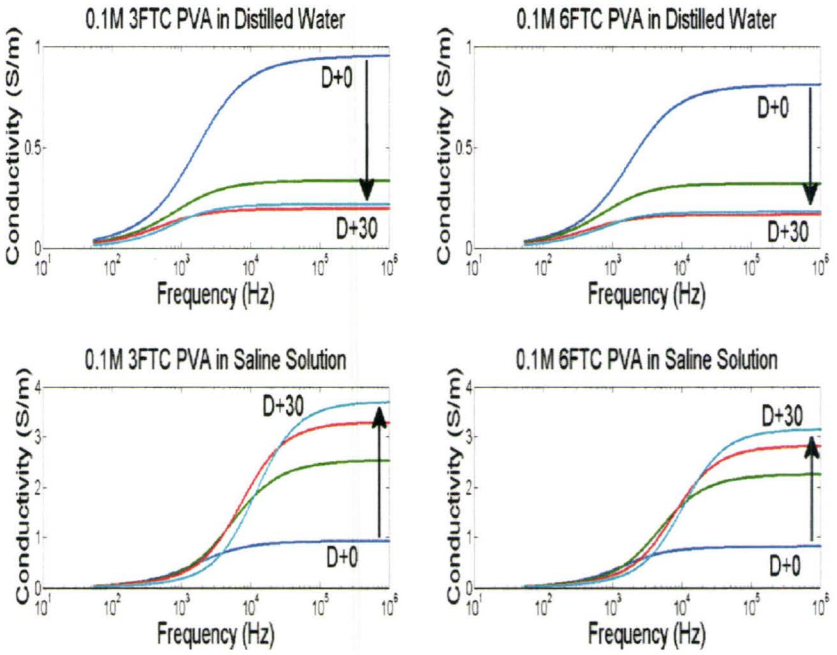

Figure 8: *"Storage Media Test B." In this set of figures, PVA manufactured with salt (0.1M 3FTC and 6FTC) are placed in either distilled water (top 2 subplots) or in 1M saline solution (bottom 2 subplots). Curves represent measurements taken before being placed in the medium, and day 2, day 6, and day 30 following. Note that the larger initial conductivity (as compared to Figure 7) decreases when placed in distilled water (top 2 subplots). However when placed in the saline solution (bottom subplots), these samples demonstrate an increase in conductivity approaching that of day 30 in figure 7.*

Figure 7 shows the 0M NaCl, 3 and 6 FTC PVA-C samples that are either stored in distilled water or saline solution. To enhance the readability of these plots, only the data from days 0,2,6 and 30 are presented. For both the 3 and 6 FTC samples that are stored in distilled water there is a significant decrease ($p < 0.05$) in conductivity from Day 1 to Day 30. This may indicate that water is diffusing into the cryogel making the sample less conductive, or that salt is diffusing out of the gel. For both the 3 and 6 FTC samples that are stored in saline solution there is a significant increase ($p < 0.05$) in conductivity from Day 1 to Day

30. This seems to indicate that in these samples, salt is diffusing into the cryogel to increase its conductivity.

Figure 8 shows the 0.1M NaCl, 3 and 6 FTC PVA-C samples that are either stored in distilled water or saline solution. For both the 3 and 6 FTC that are stored in distilled water there was a significant decrease ($p < 0.05$) in conductivity from Day 1 to Day 30. For both the 3 and 6 FTC samples that were stored in saline solution there is a significant increase ($p < 0.05$) in conductivity from Day 1 to Day 30.

Clearly the results indicate a change in the MRI and the electrical properties of PVA-C between 3 and 6 freeze thaw cycles (shown in Figures 1-6). The gel was found to be less conductive following 6 FTCs, relative to 3 FTCs. Figure 1 demonstrates that increasing the number of FTCs decreases the T_1 value, which is consistent with what has been demonstrated previously (17). There was a significant ($p<0.05$) decrease in T_1 value when comparing the 3 FTC and 6 FTC samples. This was true for samples of any salt concentration. These results also show that by adding salt to the PVA-C there are significant increases in the T_1 values for the 6FTC samples.

The standard deviation of the T_1 for the 6 FTC, 0.1M samples was quite large compared to the other measurements in Figure 1. This indicates a larger variability in the T1 of these samples. This may be due to non-uniformity of relaxation times throughout the samples or a non-uniform sample preparation. An increase/decrease in relaxation time could have been caused by random air bubbles within the sample.

The decrease in T_2 as the number of FTCs increased was not significant ($p>0.01$) for all NaCl concentrations. It has been observed that larger variation in the PVA-C properties occurs during the initial few FTCs (17). Increasing the number of FTCs beyond 3 is

expected to cause less variation in the T_2 value. A plateau in relaxation times as a function of FTC was observed by Chu and Rutt (17).

It may not be intuitive why the simple addition of salt should affect the relaxation times. When salt is added to the water there is a change in the molecular structure which changes the mobility of the protons and thus a change in relaxation time. Work for example by Park & Fayer (18) showed that the structure of a water-ion network in a NaBr solution is very different than a hydrogen bond network in pure water.

Previous work has shown similar values for the relaxation times (5, 16, 17). The numbers are similar, not identical, since there are various factors affecting the final PVA-C product that were different from earlier studies. The number of FTCs, rate of freeze/thaw, %PVA, MRI field strength, temperature of measurement, and molecular weight of PVA are all important factors to be considered when trying to compare relaxation times to previous work.

Part of our motivation for conducting this work is to use PVA-C as a tissue mimicking phantom. One model system of interest for example is the human breast. In the human breast, estimates for healthy tissue yield a T_1 of 900-1000ms (19), and typical T_2s are in the order of 50-100ms. It has been demonstrated that these values are achievable using PVA-C (16) for the purpose of an anthropomorphic breast phantom.

Merchant et al. (20), used a multiecho spin echo interleaved with a multiecho inversion recovery sequence at 1.5T to estimate T_1 and T_2 in the healthy and the diseased breast. They found T_1 and T_2 values in normal breast tissue (n = 23) of 795.64 ± 21.12 and 62.82 ± 4.06 ms, respectively. In benign breast tissue (n = 17), the respective values were 1049.02 ± 40.31 and 89.15 ± 8.33 ms, while in malignant breast lesions (n = 11), they were 876.09 ± 27.83 and 74.76 ± 3.90 ms.

Clearly PVA-C has MRI relaxation times comparable to those observed in normal and diseased breast tissue. Here we have shown T_1 values ranging from 602 ± 18 ms to 827 ± 13 ms and T_2 values from 64 ± 9 ms to 86 ± 8 ms. It would be beneficial to obtain a larger range for both T_1 and T_2 values in order to encompass the entire range of normal values described above. Relaxation times for PVA-C can be changed by altering the percentage PVA and therefore this provides an easy way to obtain NaCl doped samples with the required T_1 and T_2. Changing the percentage PVA has been previously performed and shown to have the correct range of relaxation times to mimic most normal tissue (5).

One possible interpretation of these changes induced by additional freeze-thaw cycles is that indeed the PVA-C becomes more hydrogen bonded with an increased number of freeze-thaw cycles. This idea of increased hydrogen bonding with increasing number of FTCs is supported by Kobayashi et al. (21). Water present within the gel, or possibly channels of water, become more restricted and hence display a reduced conductivity. If this is indeed the case, then water in the cryogel behaves more like "bound water" than "free water." In general, there exists a relationship between MRI relaxation time, and mobility of water. For example, assuming that water in the cryogel with 1 freeze thaw cycle is relatively mobile since the sample has limited crystallinity, then the MRI relaxation times define a position on the molecular mobility axis as indicated perhaps by the arrow in Figure 9. A pure substance, water for example, would have such a characteristic plot and would have a T1 minimum at the Larmor frequency. As the number of freeze thaw cycles increases, then the mobility of water decreases (moving to left on x-axis) suggesting a decrease in T_1 and T_2. This is not an exact analogy as the plot in Figure 9 is intended to describe a pure substance, not a complex material such as a cryogel. However it does illustrate the expected behaviour of the MRI relaxation times as the mobility changes.

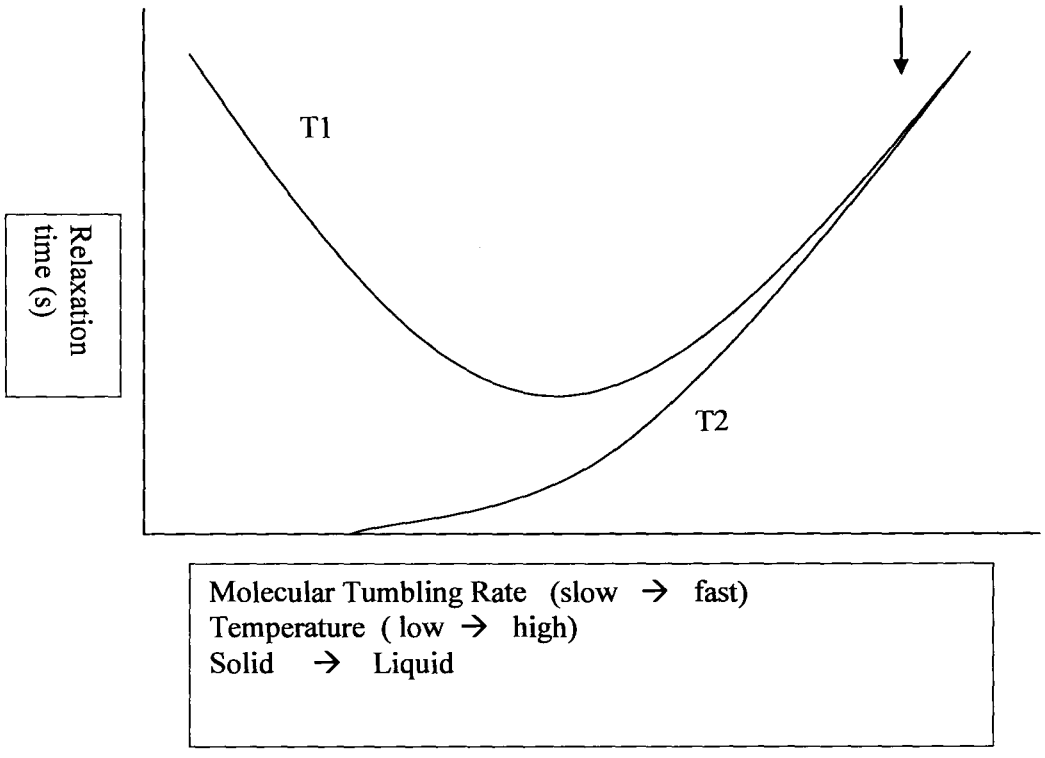

Figure 9: *MR Relaxation Times (T_1 and T_2) as a function of frequency for a pure substance, demonstrating the expected trend for the relaxation times as a function of water mobility. Water at room temperature would be relatively mobile, and may be closer to the position indicated by the arrow. In consideration of a cryogel with reduced water mobility, this plot would suggest a decrease in T_1 and T_2.*

In summary, it was shown here that increasing from 3 to 6 FTCs significantly decreased the T_1 relaxation time but T_2 was left relatively unchanged. It was also shown that the addition of salt significantly increased the relaxation times.

As expected with increasing salt concentration there is an increase in the conductivity. The salt ions allow for better conductivity. As the frequency increases so does the conductivity. At higher frequencies the increase in conductivity begins to slow. The peak conductivity for the 0.1M samples is approximately one tenth that of the 1M samples. The conductivity increased by approximately ten-fold with a commensurate increase in salt

concentration. This linear relationship between molarity and conductivity is expected since a linear relationship has been previously reported (22). Also note that there were sharp increases in the conductivity values between 100 and 1000Hz for all samples. This reflects a limitation of the measurement method. Often when using fixtures in combination with network analyzers, an open-short compensation (23) is required. This procedure requires a measurement of the fixture in the open and short circuit geometries. For some frequencies, this generated a divergence in the compensated equations that was not completely removed, because the capacitance being measured in the parallel geometry becomes very small at these frequencies. This is partially exaggerated because of the large space in the parallel plate fixture required to fit the large PVA-C pucks.

In Figure 4 the permittivity measurements of the 3 FTC samples is shown. The permittivity is a measure of how well a material is able to resist the formation of an electric field within it. All permittivities decreased with increasing frequency. At larger frequencies the permittivities all approached zero. The 0 M and the 0.1 M samples approached zero at a frequency of approximately 2 kHz whereas the 1 M samples approached zero at approximately 10 kHz.

Conversely, the conductivity of the 6 FTC PVA-C samples increased with salt concentration. The peak value of the 0.1M samples was approximately 25% of the 1M measurements. This suggests a different relationship than that which was observed for the 3 FTC samples. Here there was not a tenfold increase in conductivity, as seen previously with the 3 FTC samples. Therefore the number of FTCs must be taken into account as well as the concentration of salt in order to obtain a desired conductivity.

Permittivity is observed to increase with increasing salt concentration. Once again, at higher frequencies the permittivity approached zero for all samples. The 0 M, 0.1 M, and 1 M samples approached zero at approximately 1 kHz, 2 kHz, and 9 kHz, respectively.

The conductivities ranged from 0.026 to 1.07 S/m for the 3 FTC samples. The conductivities ranged from 0.068 to 0.581 S/m for the 6 FTC samples. Kato et al. (24) found that values for conductivity ranged from 0.0295 S/m to 0.744 S/m depending on the tissue type. Therefore it is possible to mimic most tissue types by changing the number of FTCs and the concentration of NaCl (from 0 M – 1 M).

The permittivities ranged from 95.1 to $2.32*10^7$ for the 3 FTC samples. The permittivities ranged from 84.5 to $1.85*10^7$ for the 6 FTC samples. Past studies (25-29) have shown that various human tissues have permittivities in the range of $40 – 40*10^7$. Therefore it is seen that the permittivity measured using PVA-C does not encompass the entire desired range. Further work employing other additives is being performed to be able to mimic the entire range.

The common application of this impedance technology is to measure the dielectric spectrum of a sample to examine the various relaxation processes in a liquid or a polymer. There are two main effects which are "nuisances" in this regard. One is the DC part of the conductivity which we are trying to exploit here. The DC conductivity manifests at the lower frequencies and can overwhelm the signal below 1kHz. The other effect is the electrode polarization (23, 30), which also manifests at the lower frequencies. It is instructive to consider the conductivity at a frequency, say 10kHz-1MHz, where the signal is much less affected by the electrode polarization effect. Clearly at 10kHz the conductivity decreases with an increase in the number of FTC's from 3C to 6C, so this change is independent of any electrode polarization effects.

The electrode polarization is a problem in salt solutions (23). For conducting polymers and materials like ethanol it is not a large contribution and the conductivity can still be extracted from the signal. We have begun to examine samples doped with NaCl solutions. Hence there exist both DC conductivity and electrode polarization effects. It is interesting to note however that clear evidence of the electrode polarization effect appears to be lacking in the PVA-C measurements. Perhaps there is some effect of the PVA-C matrix which inhibits the formation of a polarization layer on the electrode surface. Regardless, further research is being performed to investigate this phenomenon.

The conductivity measurements of the 3C and 6C in this study are about 100 times higher than the AC (frequency range from 10^{-1} to 10^{9} Hz) conductivity reported by Pissis et al (31) for poly(hydroxyethyl acrylate) (PHEA) hydrogel with lower water contents (maximum of 32%). Pissis et al. (31) also report permittivity only for higher temperatures (30 ^{0}C to 90 ^{0}C). At 30 ^{0}C compared to Pissis et al. (31), the PVA-C permittivity is reduced from 6 times down to only 2 times that of PHEA in the frequency range of 10^{2} to 10^{6} Hz. Therefore the electrical impedance properties of PVA cryogel are different from the PHEA hydrogel.

In Figures 7 and 8 there is an obvious change in the conductivity by simply adding 0.1M NaCl to the PVA-C. Also it can be seen that if the desired storage media is either distilled water or saline there will be a transfer of NaCl to or from the PVA-C as an equilibrium of the NaCl and water takes place. Therefore NaCl is not a suitable solute for changing the conductivity when storing samples in a liquid. This diffusion would also make it unsuitable for use in complex phantom structures. Other techniques need to be investigated, such as conducting polymer or MICA or graphite, to manufacture stable 3D conductivity distribution in the PVA-C phantoms.

7.4 CONCLUSION

It has been shown that increasing the number of FTCs from 3 to 6 significantly shortens the T_1 values for 15% PVA-C. There was no significant decrease in the T_2 values when comparing 3 and 6 FTCs. The addition of NaCl caused significant differences in both relaxation times (T_1 or T_2). The conductivity of the 3 and 6 FTC PVA-C was found to increase proportionally with increasing salt concentration. There was a significant difference in the conductivity when comparing the 0 M or 0.1M with the 1M samples for both 3 and 6 FTCs. A plateau in the conductivity was reached with increasing frequency, such that further increases in frequency no longer appeared to affect the conductivity. The permittivities for the 3 and 6 FTC PVA-C samples were found to decrease with increasing frequency. The permittivity for all samples approached zero as the frequency increased. It was shown that the conductivities and permittivities of most human tissue can be mimicked by using PVA-C in a frequency range of 40 Hz – 1 MHz.

These results indicate that with an increase in the number of FTC's, the hydrogen bonding restricts the water in the gel. This therefore implies a reduction in the mobility of the water in the gel.

For the construction of complex phantoms the idea of leaching should be considered. It was shown that the molarity of both the PVA-C sample and the storage solution will tend to equilibrate over time.

In the future, impedance measurements at higher (MRI) frequencies will be used to assess the dielectric effect from loading the MRI coil.

LIST OF ABBREVIATIONS

ANOVA	analysis of variance
EIT	electrical impedance tomography
FTC	freeze thaw cycle
FTCs	freeze thaw cycles
MRI	magnetic resonance imaging
NaCl	sodium chloride
PHEA	poly(hydroxyethyl acrylate)
PVA	polyvinyl alcohol
PVA-C	polyvinyl alcohol cryogel
TE	echo time
TI	inversion time

DECLARATION OF COMPETING INTERESTS

The authors declare that they have no competing interests.

AUTHORS' CONTRIBUTIONS

KW was involved in experimental design, acquisition of data, analysis and interpretation of data, drafting of manuscript, incorporating various revisions to manuscript, submission of all materials for publication. MG, AJ, MH, RT were involved in acquisition of data, analysis and interpretation of data; also, have been involved in drafting of the manuscript. GC was involved in designing and manufacturing of all PVA-C materials and contributed to manuscript revisions and interpretation of data. GM and TT were involved in design of the experiments, acquisition and interpretation of data, writing of the

manuscript, and all revisions of the manuscript. All authors read and approved the final manuscript.

7.5 ACKNOWLEDGEMENTS

We would like to acknowledge funding support from an NSERC grant awarded to G.R. Moran, and to thank Multi-Magnetics Incorporated (MMI) for the use of MRI time on the 2T and 3T MRI facilities in London, Ontario.

7.6 REFERENCES

1. Peppas NA: **Biomaterials Science: An Introduction to Materials in Medicine.** *Academic Press Toronto* 1996.

2. Ratner BD, Hoffman AS: **ACS Symposium Series.** *American Chemical Society* 1985, 31:14.

3. Willcox PJ, Howie DW, Schmidt-Rohr K, Hoagland DA, Gido SP, Pudjijanto S, Kleiner LW, Venkatraman S: **Microstructure of Poly(vinyl alcohol) Hydrogels Produced by Freeze/Thaw Cycling.** *J. Polymer. Sci.: Part B: Polymer Physics*, 1999, 37: 3438-3454.

4. Stammen JA, Williams S, Ku DN, Guldberg RE: **Mechanical Properties of a Novel PVA Hydrogel in Shear and Unconfined Compression.** *Biomaterials* 2001, 22: 799-806.

5. Wilson K. **Characterization of MRI and Electrical Properties of Polyvinyl Alcohol Cryogel.** *M.Sc. Thesis, University of Western Ontario, London, Ontario*, 2006.

6. Chu K, Jordan KJ, Battista JJ, VanDyk J, Rutt BK: **Polyvinyl alcohol-Fricke Hydrogel and Cryogel: Two New Gel Dosimetry Systems with Low Fe 3 + Diffusion.** *Phys. Med. Biol.* 2000; 45: 955-969.

7. Lukas LA, Surry KJ, Peters TM: **Temperature dosimetry using MR relaxation characteristics of poly(vinyl alcohol) cryogel (PVA-C).** *Magnetic Resonance Medicine* 2001; 46:1006–1013.

8. Surry KJM, Smith WL, Campbell LJ, Mills GR, Downey DB, Fenster A: **The development and evaluation of a thre-dimentional ultrasound-guided breast biopsy apparatus.** *In proceedings of Medical Image Computing and Computer-Assisted Intervention.* October 20021 6(3): 301-312.

9. G Campbell. **Controlled Technical Report IMTI-CTR-077 (2003/07)**, *National Research Council*, 2003.

10. Wtorek J, Stelter J, Nowakowski A, Ann NY: **Impedance mammograph 3D phantom studies.** *In proceedings of 10th International Conference on Electrical Bio-impedance.* April 1998; 873:520-533.

11. Nambu M: **Japanese patent 56446,** 1984

12. Watase M, Nishinari K, Nambu M: **Anomalous increase of the elastic modulus of frozen poly(vinyl alcohol) gels.** *Cryo-Letters* 1983; 4: 197-200.

13. Mano I, Goshima H, Nambu M, Iio M: **New poly(vinyl alcohol) gel material for MRI phantoms**. *Magn Reson Med* 1986;3:921–926.

14. Nagura M, Hamano T, Ishikawa H: **Structures of poly(vinyl alcohol) hydrogel prepared by repeated freezing and melting.** *Polymer* 1989;30: 762–765.

15. Wan W, Campbell G, Zhang Z, Hui A, Boughner D,J: **Optimizing the tensile properties of polyvinyl alcohol for the construction of a bioprosthetic heart valve stent**, *Biomed. Mater. Res .(Applied Biomater)* 2002, 63:854-861.

16. Surry KJM, Austin HJB, Fenster A, Peters TM: **Poly(vinyl alcohol) cryogel phantoms for use in ultrasound and MR imaging.** *Phys Med Biol.* 2004;49(24):5529-46.

17. Chu K, Rutt B: **Polyvinyl alcohol cryogel: an ideal phantom material for MR studies of arterial flow and elasticity,** *Magn. Reson. Med.* 1997; 37:314-319.

18. Park S, Fayer MD: **Hydrogen Bond Dynamics in Aqueous NaBr Solutions.** *PNAS* 2007; 104(43):16731-16738.

19. Delille JP, Slanetz PJ, Yeh ED, Kopans DB, Garrido L: **Physiologic Changes in Breast Magnetic Resonance during the Menstrual Cycle: Perfusion Imaging, Signal Enhancement, and Influence of the T1 Relaxation Time of the Breast Tissue.** *Breast J* 2005; 11(4):236-241.

20. Merchant TE, Thelissen GRP, Graaf PWD, .Nieuwenhuizen CW, Kievit HC, Den Otter W: **Application of a mixed imaging sequence for MR imaging characterization of human breast disease.** *Acta Radiol* 1993; 34:356–61.

21. Kobayashi M, Ando I, Ishii T, Amiya S: **Structural Study of Poly(vinyl alcohol) in the Gel State by High-Resolution Solid-State ^{13}C NMR Spectroscopy.** *Macromolecules.* 1995; 28:6677-6679.

22. Tirado M, Grosse C: **Conductivity dependence of the polarization impedance spectra of platinum black electrodes in contact with aqueous NaCl electrolyte solutions.** *Colloids and Surfaces A: Physicochem. Eng. Aspects.* 2003; 222:293-299.

23. Grosse C, Tirado M: **Improved Calibration of Impedance Analyzers for Measurements on Highly Conductive Liquids.** *IEEE Transactions on Instrumentation and Measurement* 2001; 50(5): 1329-1333.

24. Kato H, Kuroda M, Yoshimura K, Yoshida A, Hanamoto K, Kawasaki K, Shibuya K, Kanazawa S: **Composition of MRI Phantom Equivalent to Human Tissues.** *Med. Phys.* 2005; 32 (10):3199–3208.

25. Gabriel C: **Tissue Equivalent Material for Hand Phantoms.** *Phys. Med. Biol.* 2007; 52(14): 4205-4210.

26. Nopp P, Rapp E, Pfutzner H, Nakesch H, Ruhsam C: **Dielectric Properties of Lung Tissue as a Function of Air Content.** *Phys. Med. Biol.* 1993; 38(6): 699-716.

27. Schafer M, Kirlum HJ, Schlegel C, Gebhard MM: **Dielectric Properties of Skeletal Muscle during Ischemia in the Frequency Range from 50 Hz to 200 MHz.** *Ann. N. Y. Acad. Sci.* 1999; 20(873): 59-64.

28. Schepps JL, Foster KR: **The UHF and Microwave Dielectric Properties of Normal and Tumour Tissues: Variation in Dielectric Properties with Tissue Water Content.** *Phys. Med. Biol.* 1980; 25 (6): 1149-1159.

29. Osterman K, Kerner T, Williams D, Hartov A, Poplack S, Paulsen K: **Multifrequency electrical impedance imaging: preliminary in vivo experience in breast.** *Physiol. Meas* 2000; 21:99-109.

30. M. Tirado. C. Grosse: **Low-frequency dielectric spectroscopy of colloidal suspensions.** *Journal of Non-Crystalline Solids* 2002; 305: 386–392.

31. Pissis P, Kyritsis A: **Electrical conductivity studies in hydrogels.** *Solid State Ionics* 1997; 97: 105-113.